Doctoral theses at NTNU, 2023:193

Aravinda Perera

Enhanced Sensorless Control of Electric Drivetrains for Deep-Sea Mining Vehicles

Equipped with Three-Phase and Six-Phase IPMSM

Doctoral thesis

NTNU
Norwegian University of Science and Technology
Thesis for the Degree of Philosophiae Doctor
Faculty of Information Technology and Electrical Engineering
Department of Electric Energy

NTNU
Norwegian University of Science and Technology

Aravinda Perera

Enhanced Sensorless Control of Electric Drivetrains for Deep-Sea Mining Vehicles

Equipped with Three-Phase and Six-Phase IPMSM

Thesis for the Degree of Philosophiae Doctor

Trondheim, June 2023

Norwegian University of Science and Technology
Faculty of Information Technology and Electrical Engineering
Department of Electric Energy

NTNU
Norwegian University of
Science and Technology

NTNU
Norwegian University of Science and Technology

Thesis for the Degree of Philosophiae Doctor

Faculty of Information Technology and Electrical Engineering
Department of Electric Energy

ISBN 978-82-326-7088-8 (printed ver.
ISBN 978-82-326-7087-1 (electronic ver.
ISSN 1503-8181 (printed ver.
ISSN 2703-8084 (online ver.

Doctoral theses at NTNU, 2023:193

Printed by NTNU Grafisk senter

Dedicated to my wife,
Raneshi

And to my two kids,
Améli and Rahél

"The highest education is that which does not merely give us information but makes our life in harmony with all existence."

- Rabindranath Tagore

Abstract

THE thesis deals with sensorless control methods for three-phase and six-phase Interior Permanent Magnet Synchronous Machine (IPMSM) drives, targeted for deep-sea mining vehicles (DMVs).

Rapid growth in the demand for earth minerals, and the increasing limitations on their supply, has driven the search for new mineral sources, among which deep-sea appears to be promising. However, among other challenges, the lack of sustainable technology for environmentally friendly and cost-effective mineral harvesting has deterred explorations in deeper waters. Thus, the need to bridge this technology gap has become the motivation behind this doctoral research.

Electric drivetrains have become the centerpiece of modern deep-sea mining vehicles, which are developed with the aim of reaching water depths beyond three kilometers. Reliability, efficiency, and power density have been identified as the features of merit regarding these electric drives. From this perspective, mechanical sensorless, multiphase IPMSM drives have emerged as a strong contender owing to the elimination of failure-prone sensors, their inherent fault-tolerance, higher efficiency and superior power-to-volume ratio, among other appealing features.

Online identification of machine parameters can enhance the drive performance and stability and supplement it with additional features like sensorless temperature, health, and condition monitoring. A method that employs an open-loop current predictor is proposed herein, which yields a prediction error that is sensitive to model parametric discrepancies. Analytical expressions for the steady-state prediction error are developed, which provides insights into the interplay between the mechanical states, stator currents, and parameters. These expressions become instrumental in online and offline experiment designs for parameter identification. The prediction errors are further utilized to develop prediction gradients w.r.t. model parameters that allow the adoption of gradients-based recursive algorithms. The thesis subsequently presents the application of three such algorithms to identify all electric parameters of IPMSM, including the stator leakage inductance in six-phase IPMSM. Additionally, offline experiment methods are proposed to identify machine inductances, which then are compared against the inductances obtained from the finite element model. The predictor model stability is analyzed both in continuous and discrete domains. As an alternative option to the processor-based solution, the predictor model is implemented in the FPGA to assess its performance with shorter integration time steps.

From the parameter identification, the research proceeds to incorporate these identification schemes into state estimation. The reliance on model parameters makes the performance of the model-based state observers vulnerable to parametric deviations.

The proposed online parameter estimator, a more sensitive scheme for parametric deviations, functions in parallel to provide the observer with the real-time updated model parameters. To circumvent the rank-deficiency challenge without compromising the performance, the IPMSM inductances are identified offline using the same open-loop model and used in real-time with the aid of either a look-up table or analytical functions. This thesis shows that, by incorporating the proposed schemes, model-based observers can be made more stable, precise, and robust to parameter variations as compared to those observers without parameter adaptation.

All concepts are tested and validated for both three-phase and six-phase IPMSM drives, with the use of Matlab/Simulink simulation environments as well as the FPGA-based real-time simulation. The latter is developed, as part of the research, using a Xilinx Zynq System-on-Chip-based industrial control platform. The same control hardware and software are later applied to the newly developed laboratory prototypes for validation. The experimental results demonstrate the effectiveness of the proposed online and offline identification schemes. The open-loop model along with the prediction gradients-premised algorithms succeed in tracking temperature-sensitive parameters within a few seconds while showing good asymptotic stability. The experimental results further exhibit how rotor speeds as low as 1% can be reached by incorporating the proposed identification schemes. In the same low-speed region, the steady-state average rotor position error was reported below two electrical degrees, for both three-phase and six-phase IPMSM drives. The feasibility of realizing sensorless control at very low speeds without test signal injection can make the proposed schemes attractive for a variety of deep-sea mining-associated and similar reliability-critical applications that do not require persistent operations around the rotor standstill.

Index terms: Embedded real-time simulator, multiphase IPMSM drives, parameter identification, state observer.

Preface

THIS doctoral thesis results from my research between 2018 and 2022, under the guidance of Prof. Roy Nilsen, my main supervisor, at the Department of Electric Energy, NTNU, Trondheim. The project is affiliated to the NTNU Oceans pilot program on deep-sea mining, headed by Prof. Steinar Ellefmo. The total research period was constituted of approximately 50% research and course work, 30% prototype development, and 20% teaching and dissemination.

During my time in industry, I began to realize that power electronics product development becomes excessively challenging because of its multi-disciplinary nature and cross-competence involvement. For example, a novel drive product development demands the understanding of electric machines and flux models, semiconductor physics and modulation, motor control/estimation methods, discrete domain modeling, and software/firmware programming apart from the application know-how. The absence of a single engineer proficient in these diverse disciplines can yield significant ramifications, amplifying the impact on both development time and costs, as well as the inherent ingenuity of the product. In addition to my fascination with power electronics, to become a solution to this cross-competence scarcity in industry was my motivation to select this topic.

This motivation truly became an action plan as soon as Roy, with his decades of industrial drive experience, rejoined the university as a full-time professor in 2017. My decision to go back to school from industry did incur a penalty which, however was outweighed by the possibility of filling my doctoral degree wish-list full of hands-on targets, which could not have been accomplished without the supervision of someone of Roy's calibre. Today, my gratitude to Roy is immeasurable and compounding, not only because he trusted me with the position and guided me to unravel the physical interplay behind the complex mathematical formulations, but also for the life changing inspirations. I am also thankful to my co-supervisor, Prof. Dimosthenis Peftitsis, for the encouragement and advises provided throughout. I wish many more collaborations with them in my career.

Publish or perish, they say, yet one can conveniently perish in the modern-day publishing saga during a fixed-term tenure. In this regard, I owe much gratitude to Prof. Gilbert Bergna Diaz and my good colleague, Babak Abdolmaleki, for imparting clever techniques to "bulletproof" a manuscript. Prof. Emiretus Tore Undeland, Prof. Elisabetta Tedeschi, Dr. Salvatore D'Arco, Prof. Robert Nilssen, Dr. Zhaoqiang Zhang, Dr. Hossein Ehya, and Kjell Ljøkelsøy are also acknowledged with gratitude, for their insightful discussions, of which some were extended into co-authored papers. Dr. Anirudh Acharya deserves a special mention for imparting his FPGA knowledge

generously to me in addition to being a good mentor. Dr. Stef Kapusniak and Dr. Simon Graham of Soil Machine Dynamics, UK are gratefully acknowledged for their invaluable information about deep-sea mining machinery. I am also very much grateful to my fellow colleagues, Erik and Spyros, for sharing and supporting with the thesis template.

A pandemic in a global scale patiently awaited its moment for decades to break out just when I began to discover a breakthrough in the research field. The immediate consequence was a lock-down that compelled me to persist in the research at home with my two playful kids. Sigrid Norman-Hansen did not take much time to realize this debacle, and offered her apartment in Tyholt as a temporary office while she was away. That period turned out to be one of the more fruitful episodes of the doctoral study, for which I express my heartiest gratitude to dear friend, Sigrid. Amidst the global chaos, the clock was ticking faster than ever and the laboratory preparation took the largest blow. Thomas Haugan and Aksel Hanssen along with Bård, Dominik and Morten from the service lab are acknowledged for their services in prototype building and tolerating my occasional nagging under the time pressure, which was somewhat alleviated at the end, thanks to the contract extension from the faculty. I would be marking a hollow in the preface, if I failed to acknowledge the administration staff who often went the extra yard in their services. Among them, Koharu, Silje, and Bodil, some of the most service-oriented public servants I have come across, are gratefully remembered.

If a virtue of philosophical nature has been instilled in me by the doctoral training, that perhaps results from the intriguing, intense and inspiring coffee breaks with my colleagues. Our cultural diversity blended with cheerful bonds of friendship helped us address a wide range of sensitive topics, from Kim Jong-un to Kim Kardashian, especially, when I was grappling with my own research topic. The memories of Raghbendra, Gard, Andreas, Babak, Tobias, Venkat, Dan El, Prabhat, Erik, Spyros, multiple Daniels, and many other nice colleagues shall I fondly cherish in the years to come. In general, the impact NTNU has made in my life is enormous, and therefore, it is truly satisfying to leave behind two state-of-the-art drive prototypes which were byproducts of my research, as an act of gratitude to this great institution.

Last but never the least, I must thank our families, particularly, Felician, my father-in-law, for being an immense strength during the difficult times. I am equally grateful to our friend circle in Trondheim for offering a helping hand during my travels. If not for the perpetual trust, support and love of my wife, Raneshi, this research completion would not have been possible. I cannot thank enough to my two beautiful kids for accepting my absence during our usual playtimes and story-telling sessions. Your dividends will be paid lavishly, as promised. In essence, this thesis is a collaborative effort of many. Moreover, it is also a result of a collection of decisive events, like Roy's rejoining with impeccable timing. I attribute these to the act of the universal energy, whom I'd also call God. I proclaim His miracles and wisdom showered upon me in the last five years, just as it was since the beginning. He continues to raise me up to more than I can be.

Contents

Nomenclature

Acronyms

ac	Alternating current
ADC	Analog to digital converter
AF	Active flux
DAC	Digital to analog converter
dc	Direct current
DMV	Deep-sea mining vehicle
DSP	Digital signal processor
DSRF	Double synchronous reference frame
DTP	Dual three-phase
EKF	Extended Kalman filter
ERTS	Embedded real-time simulator
FE	Fundamental excitation
FOC	Field-oriented control
FPGA	Field programmable gate array
GIPC	Generic intellectual property core
GNA	Guass-Newton algorithm
HFSI	High frequency signal injection
HWE	Hardware emulator
IGBT	Insulated-gate bipolar transistor
IP core	Intellectual property core
IPMSM	Interior permanent magnet synchronous machines
KF	Kalman filter
LPF	Low-pass filter
LUT	Look-up table
MOSFET	Metal–oxide–semiconductor field-effect transistor
MRAS	Model reference adaptive system
MTPA	Maximum torque per ampere
OPE	Online parameter estimator
PhyInt	Physically interpretative method
PI	Proportional integral
PLL	Phase-locked loop
PMSM	Permanent magnet synchronous machines
pu	Per-unit
RLS	Recursive least squares
RPEM	Recursive prediction error method
SGA	Stochastic gradient algorithm
Si	Silicon
SiC	Silicon Carbide
SMS	Seafloor massive sulphides
SoC	System on chip
SoM	System on module
SSRF	Single synchronous reference frame
VSD	Variable speed drive
XSG	Xilinx System Generator

Roman symbols

$\boldsymbol{I}$	Identity matrix
$\boldsymbol{L}$	Estimator gain-matrix
$\boldsymbol{R}()$	Vector Hessian matrix
$\boldsymbol{T}$	Transformation matrix
$\boldsymbol{x}_s$	Stator reactance matrix
$\mathscr{M}$	Model set
$\mathscr{M}(\underline{\theta})$	Model set corresponding to $\underline{\theta}$
$\mathscr{M}_i$	Current model
$\mathscr{M}_{u\theta}$	Full-order model
$\mathscr{M}_{ui}$	Voltage-current model
$\mathscr{M}_u$	Voltage model
$D_{\mathscr{M}}$	Parameter space describing the model set
D_s	Parameter space for stable predictors
f_{sw}	Switching frequency
h	Time step
I	Current [A]
i	Current [pu]
i_α	α-axis current
i_β	β-axis current
i_d	d-axis current
i_q	q-axis current
i_s	Stator current
i_{01}	0_1-axis current
i_{02}	0_2-axis current
i_{d1}	d_1-axis current
i_{d2}	d_2-axis current
i_{q1}	q_1-axis current
i_{q2}	q_2-axis current
i_{z1}	z_1-axis current
i_{z2}	z_2-axis current
j	Imaginary operator
k	Sample number
K_i	Integral gain
K_p	Proportional gain
L	Inductance [H]
l	Inductance [pu]
L_d	d-axis inductance
L_q	q-axis inductance
$L_{s\sigma}$	Stator leakage inductance
N	Rotor speed [rms]
n	Rotor speed [pu]
n_{lim}	Rotor speed limit for r_s-identification scheduling
p	Number of pole pairs
$r()$	Scalar Hessian function
R_s	Stator winding resistance [Ω]
r_s	Stator winding resistance [pu]
T_d	d-axis time-constant
T_q	q-axis time-constant
T_{FPGA}	FPGA clock
T_{samp}	Sampling time
T_{step}	Solver clock in FPGA
$tr()$	Trace of a matrix
U	Voltage [V]
u	Voltage [pu]
u_α	α-axis voltage
u_β	β-axis voltage
u_d	d-axis voltage
u_q	q-axis voltage
u_s	Stator voltage
u_{01}	0_1-axis voltage
u_{02}	0_2-axis voltage
u_{comp}	Compensation voltage
u_{d1}	d_1-axis voltage
u_{d2}	d_2-axis voltage
u_{dc}	DC-link voltage
u_{q1}	q_1-axis voltage
u_{q2}	q_2-axis voltage
u_{z1}	z_1-axis voltage
u_{z2}	z_2-axis voltage

V_N	Criterion function
$x = \omega_n \cdot l$	Reactance [pu] or inductance [pu] at nominal speed
x_d	d-axis reactance
x_q	q-axis reactance
x_{md}	d-axis magnetizing reactance
x_{mq}	q-axis magnetizing reactance
$x_{s\sigma}$	Stator leakage reactance

GREEK SYMBOLS

$\mathbf{\Psi}^T$	Prediction gradient matrix
$\delta\underline{i}$	Current error vector
$\delta\underline{\theta}$	Parametric error vector
γ	Gain sequence
$\gamma_{0,LK}$	Gain sequence for gain computation
$\gamma_{0,rK}$	Gain sequence for Hessian computation
Λ	Covariance matrix
λ	Eigenvalue
ω_n	Nominal rotational speed
Ψ	Flux linkage [Wb]
ψ	Flux linkage [pu]
ψ_α	α-axis flux linkage
ψ_β	β-axis flux linkage
ψ_d	d-axis flux linkage
ψ_m	Magnet flux linkage
ψ_q	q-axis flux linkage
ψ_s	Stator flux linkage
ψ_T	Active flux linkage
ψ_{01}	0_1-axis flux linkage
ψ_{02}	0_2-axis flux linkage
ψ_{z1}	z_1-axis flux linkage
ψ_{z2}	z_2-axis flux linkage
τ	Torque [pu]
τ_e	Electromagnetic torque
τ_l	Load torque
$\underline{\epsilon}$	Prediction error vector
$\underline{\theta}$	Motor parameter vector
ϑ	Rotor electrical angle
ϑ_s	Displacement angle between the winding groups
ϑ_{mech}	Rotor mechanical angle

Part I

PROLOGUE

Chapter 1

Introduction

Abstract

This introductory chapter will provide a comprehensive overview of the doctoral thesis. The motivation for deep-sea mining and its opportunities and challenges are discussed to formulate the research questions in brief. Subsequently, the contributions from the research is outlined giving reference to the 12 publications that resulted as part of the doctoral research. For the readers' convenience, the contributions, their relevance, and interlinks are visualized. The chapter concludes with the thesis outline to assist the navigation through the thesis contents.

1.1 Motivation of the Research

1.1.1 Increase in Minerals Demand

THE uses of minerals including the rare earth elements are widespread, ranging from fertilizers to medicines to ice cream [1]. The worldwide demand for earth minerals is rising at a dramatic rate which can be attributed to several reasons. One major cause is population growth owing to extended life expectancy. Secondly, the increased standards of living across many parts of the globe has escalated the minerals consumption per capita. For example, there are approximately over two billion mobile phone users today, and they tend to change their phones, on average, every 11 months. These modern phones are a repository of many rare earth minerals. To put this into context, one million mobile phones contain nearly 16 tons of copper, 350 kg of silver, 34 kg of gold and 15 kg of palladium [2]. Watches, digital cameras, and computers are just a few of the other consumer electronics that require minerals to manufacture. To exemplify the need for new materials for modern-day needs, strontium, a mineral that was barely known before the 1960s, has now become a key element in the television industry to develop the technology that prevents radiation emission from color picture tubes [3].

One of the other main causes of the minerals demand surge is the significant emphasis on decarbonisation of the industry to tackle global warming [4]. Consequently,

the attention has shifted toward solar, wind, and other renewable energy sources to replace the conventional coal and thermal power plants. Iron, copper, aluminium, silicon, and titanium are some of the commonly required minerals [5, 6] that enable this green-shift in the power generation. Similarly, the electrification of the transportation sector has become a mega trend and a substantial driving factor for the rise in minerals demand. Several European countries have already pledged to sell only carbon emission-free new vehicles within the next two decades [7]. Automotive batteries, fuel cells, and electric drivetrains are rich with lithium, cobalt, silicon, aluminium, and copper. In essence, these radical measures to tackle global warming are giving rise to mineral demand hikes at an unprecedented rate.

1.1.2 Depletion in Minerals Supply

On the other hand, the adequacy of mineral reserves in the land-based mining sites is in question. Some studies [3] claim that minerals supply will suffer major shortages by 2050, if new deposits are not discovered. Moreover, the Western countries have a significant dependency on metal imports [8]. This dependency leads to a high risk of supply crisis. Moreover, China holds a monopoly on global supply of rare earth minerals which amounts to 97% of the market share [8] and for unknown reasons, it has restricted exports since 2010 [1]. Due to the potential risk of a supply crisis, and geopolitical reasons, industrial countries see a paramount importance in diversifying their mineral supply chains.

1.1.3 Opportunities in Deep-Sea Mining

As such, minerals demand is growing exponentially, while the supply is stagnating and monopolized. Under these circumstances, deep-sea mineral mining is rapidly becoming inevitable.

Land-based mining is becoming increasingly costly due to the depletion of mineral reserves. Digging deeper and in longer latitudes is necessary to access remotely trapped resources, which introduces high production costs. On the contrary, since the deep-water seabeds have not yet been exploited, high concentration fields are not rare. To take the example of cobalt, global land reserves and resources represent around 13 million tons, while it is estimated there is approximately 50 million tons in the cobalt-rich crusts of the Prime Crust Zone and 44 million tons in the polymetallic nodules of the Clarion Clipperton Zone1, both located in the Pacific Sea [9].

To provide another example, copper grade in the Solwara 1 offshore field is about 10% whereas land-based field yields a maximum of 1% [10]. Most of these seabed sediments are on the surface, therefore deep excavation is unnecessary; at least, at the early phase of explorations. As a result, the mining and recovery technologies do not require deep drilling of the seabed. Therefore, the concept of deep-sea mining already appears promising and is gradually becoming cost-competitive in comparison

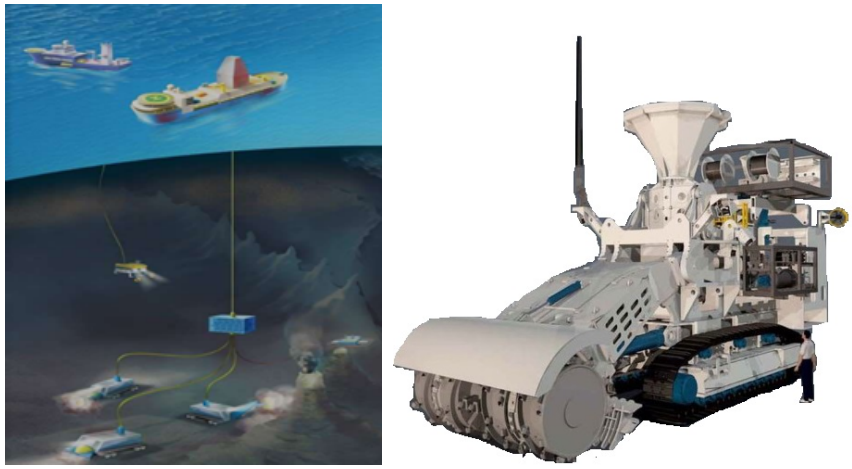

(a) (b)

Figure 1.1. (a) A product support vessel from the top side supplying energy to multiple deep-sea mining vehicles. (b) A state-of-art deep-sea mining vehicle.

to on-land mining [9, 11]. Figure 1.1 gives insight into one of the leading approaches and most promising technologies for deep-sea mining.

Dependable and productive technology is a key enabler for the deep-sea mining. Albeit, given the state of ocean mining technology and its readiness level for sustainable deployment, the economic feasibility of deep-sea mining is questionable [1, 8].

1.2 Identification of Research Questions

Oceanic mining technology is still emerging and only a handful of industrial players currently exist [12]. This implies a lack of technology state-of-art for deep-sea mining and a void in the relevant literature. This absence is identified as the first research question. Answering this question necessitates the identification of the application-specific challenges, and thus the requirements to develop productive and sustainable mining technology. Chapter 2 is dedicated to outlining the answers to this question.

In answering the above question, it becomes apparent that economic profit is considered to be the largest driver behind deep-sea mining [13]. The breakdown of the equipment on the seabed far from the shore, and unplanned stoppage for repair, and maintenance are some of the highly undesirable events that would hinder profitability. Thus, technology that can be relied on, is identified as the foremost important, application-specific research question. Not only because of the efforts toward decarbonization but also due to the energy crisis Europe is experiencing at the time of writing, energy-efficient technology is needed today as never before. When deep-sea mining technology is the focus, the energy efficiency in the mining equipment has a major impact on the profitability of the industry (see Section 2.4). Thus, efficient

technology for mining is identified as another dimension of the research question. The ease of maneuverability, the large capacity for payload, and the lightness of the mining equipment influence the size of vessels and the capacity of lifting equipment. Consequently, the high power density of the mining equipment becomes the third facet of the research question.

To summarize, after identifying the application-specific requirements, the research question formulated is: which mining technology will satisfy the three requirements in the priority order: 1) reliable, 2) efficient, and 3) power-dense technology for deep-sea mining? The research that follows attempts to answer this question.

1.3 Main Contributions from the Research

The main contribution from the research is an improved rotor-position estimation scheme for three-phase and six-phase PMSM electric drivetrains, aimed at mission-critical applications like deep-sea mining drives. The elimination of the failure-prone mechanical position sensor with the aid of a position estimation is targeted to improve the reliability. The enhancement of the position estimation not only improves the motor control precision, but also contributes to enhance the efficiency of the electric drivetrain. These features are implemented in both three-phase and six-phase machines, a more reliable machine configuration, to reinforce the system reliability. The type of machine chosen to implement these schemes is the Interior Permanent Magnet Synchronous Machine (IPMSM); that is best in class regarding operational efficiency in the medium power range. To the best of the author's knowledge, the main scientific contributions can be elaborated in terms of existing literature, as follows:

Generalized Framework that formulates a step-by-step procedure for parameter identification. Analytical expression for steady-state error that provides insight into the physical interlinks among parameters, rotor speed, and stator currents, thereby helping to design experiments for identification. Chapter 3 discloses this framework. Additionally, the publications **[J01]** and **[C02]** discuss the framework.

Open-loop model-based predictor and prediction gradients-based algorithms show their effectiveness in online and offline identifications of electric parameters of the IPMSM, including the stator leakage inductance of the six-phase IPMSM. Chapters 3 and 6 unveil the identification methods and results for three-phase and six-phase IPMSM, respectively. **[J01]**, **[C01]**, **[C02]**, **[C03]** and **[C07]** discuss different algorithms and implementation concerns for three-phase IPMSM drives. **[J03]** and **[C08]** disclose the same for six-phase IPMSM.

Enhanced sensorless control of three-phase and six-phase IPMSM with the aid of the proposed online parameter adaptations schemes, in the presence of varying parameters. The experiments demonstrated that, by incorporating the proposed

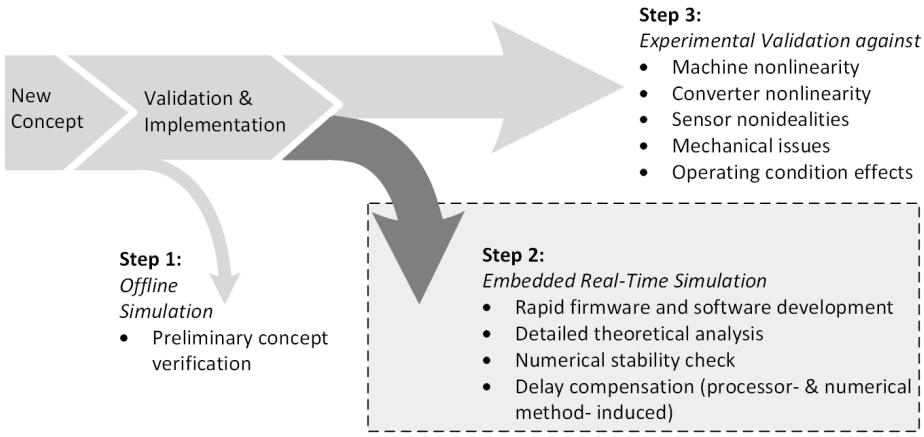

Figure 1.2. Introduction of an intermediary step with the use of ERTS, which can eliminate many of the development bugs and issues, before implementing the concepts in the power hardware, such that the challenges arising from the power hardware can be isolated.

estimation schemes, the model-based observers can be made more stable, precise, and robust to parameter variations as compared to the observer without parameter adaptation. The achievable lower speed limit without test signal injections is as low as 1%, which makes the combined sensorless control schemes for both three-phase and six-phase drives, an attractive solution for the applications that do not have sustained operations around the rotor standstill.

Embedded Real-Time Simulator (ERTS) development in an industrial System-on-Module (SoM). The ERTS becomes a resourceful tool in developing and debugging the motor drive software and firmware without having access to power hardware in the drive system. This intermediary step allows one to pre-filter a number of potential issues that could otherwise confuse the debugging process and delay the laboratory validation. In other words, the use of ERTS improves the technology readiness level and accelerates the development time. Figure 1.2 illustrates this benefit. **[C06]** discusses the design details of the ERTS.

Drives research laboratory: the contribution in procurement of machines and components, project coordination in hardware and software development, machine characterization, and debugging of the firmware and software culminated in a state-of-the-art drives research lab that is now equipped with four electric drive experimental setups, namely separately excited DC machine drive, three-phase IPMSM, six-phase IPMSM, and six-phase induction machine. These experimental prototypes are showed in Figure 3.14 and Figure 7.11.

More details of the contributions are outlined in their respective chapters.

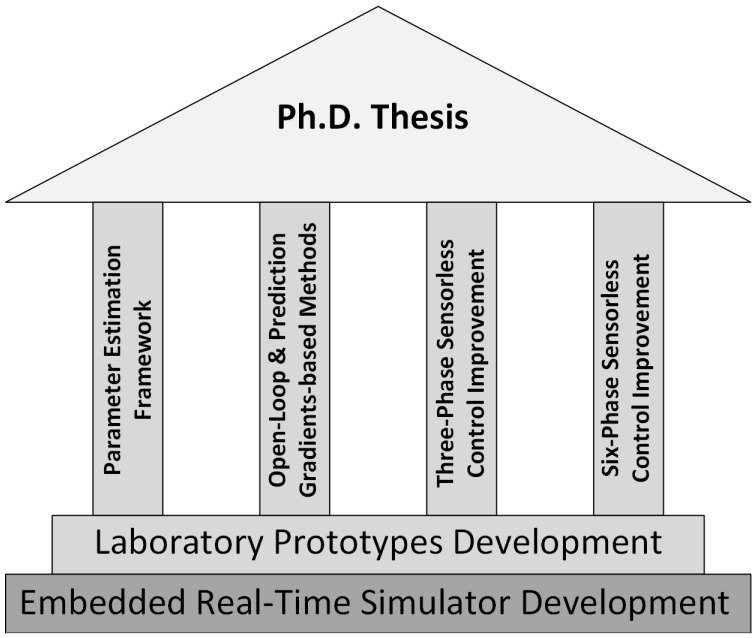

Figure 1.3. Visualization of contributions: The thesis is supported by four main pillars of contributions. These contributions are reinforced by the laboratory validations. The foundation on which to validate the concepts and develop the laboratory has been the Embedded Real-Time Simulator.

1.4 Publications

1.4.1 List of Publications

The list of publications, constituted of journal articles (J), conference proceedings (C), and poster presentations (P), is as follows:

[J01] **A. Perera** and R. Nilsen, "Recursive Prediction Error Gradient-Based Algorithms and Framework to Identify PMSM Parameters Online," in *IEEE Transaction in Industry Application*, 2022

[J02] **A. Perera**, R. Nilsen, Z. Zhang "Multi-Parameter Identification using Open-Loop Current-Prediction Error and Gradients to Augment Sensorless IPMSM Drive," in *IEEE Transaction in Industry Application*, (Submitted, 10 Jan. 2023, under revision)

[J03] **A. Perera**, R. Nilsen, T. Haugan "Open-Loop Predictor-Based Multi-Parameter Identification to Enhance Dual Three-Phase Sensorless IPMSM Drive ," in *IEEE Transaction in Power Electronics*, (Submitted, 30 Nov. 2022, under revision)

[C01] **A. Perera** and R. Nilsen, "A Recursive Prediction Error Method with Effective Use of Gradient-Functions to Adapt PMSM Parameters Online," in *IEEE Industry Applications Society Annual Meeting*, (Detroit, USA), pp.2–6, IEEE, 2020.

[C02] **A. Perera** and R. Nilsen, "A Framework and an Open-Loop Method to Identify PMSM Parameters Online," in *International Conference on Electrical Machines and Systems, ICEMS*, (Hamamatsu, Japan), pp.1945–1950, IEEE, 2020.

[C03] **A. Perera** and R. Nilsen, "Gauss-Newton: A Prediction-Error-Gradient based Algorithm to Track PMSM Parameters Online," in *IEEE International Conference on Power Electronics, Drives and Energy Systems*, (Jaipur, India), p. 8., IEEE, 2020.

[C04] **A. Perera** and R. Nilsen, "A Sensorless Control Method for IPMSM with an Open-Loop Predictor for Online Parameter Identification," in *International Conference on Electrical Machines and Systems, ICEMS*, (Hamamatsu, Japan), pp.1983–1988, IEEE, 2020.

[C05] **A. Perera** and R. Nilsen, "Full Speed Range Sensorless IPMSM Drive Enhanced with Online Parameter Identification," in *IEEE International Electric Machines & Drives Conference, IEMDC*, (Hartford, USA), p. 6., IEEE, 2021.

[C06] **A. Perera**, R. Nilsen, T. Haugan and K. Ljøkelsøy "A Design Method of an Embedded Real-Time Simulator for Electric Drives using Low-Cost System-on-Chip Platform," in *PCIM Europe digital days*, (Nuremberg, Germany), p. 8., 2021.

[C07] **A. Perera**, R. Nilsen and T. Haugan "Investigation of Open-Loop Predictor Implementation Methods for Online Parameter Estimation of IPMSM," in *PCIM Europe*, (Nuremberg, Germany), pp. 1225-1232, 2022.

[C08] **A. Perera** and R. Nilsen, "Online Identification of Six-Phase IPMSM Parameters Using Prediction-Error Sensitivities to Model Parameters," in *International Power Electronics Conference, IPEC-ECCE Asia*, (Himeji, Japan), p. 6., IEEE, 2022.

[P01] **A. Perera** and R. Nilsen, "Electric motor drive system for highly reliable and productive mining machines for deep-sea," Poster presented at *Underwater Mining Conference, UMC*, (Bergen, Norway), 2018.

The doctoral candidate authored the 12 publications with the support and guidance of Prof. Roy Nilsen. Dr. Z. Zhang contributed with the finite element analysis and its description in **[J02]**. Mr. T. Haugan contributed in ERTS development/integration to realize **[C06]**, **[C07]** and prototype development including EnDat encoder integration to realize **[J03]**. The carrier board development and critical review was the contribution from Mr. K. Ljøkelsøy for **[C06]**.

1.4.2 *Publications in Context*

The focus area of each publication is, from the perspective of propulsion drive system, as shown in Figure 1.4). It is evident that the majority of the publications revolve around parameter identification. In combination, the articles range across the control, estimation, and digital implementation scope of an electric drive.

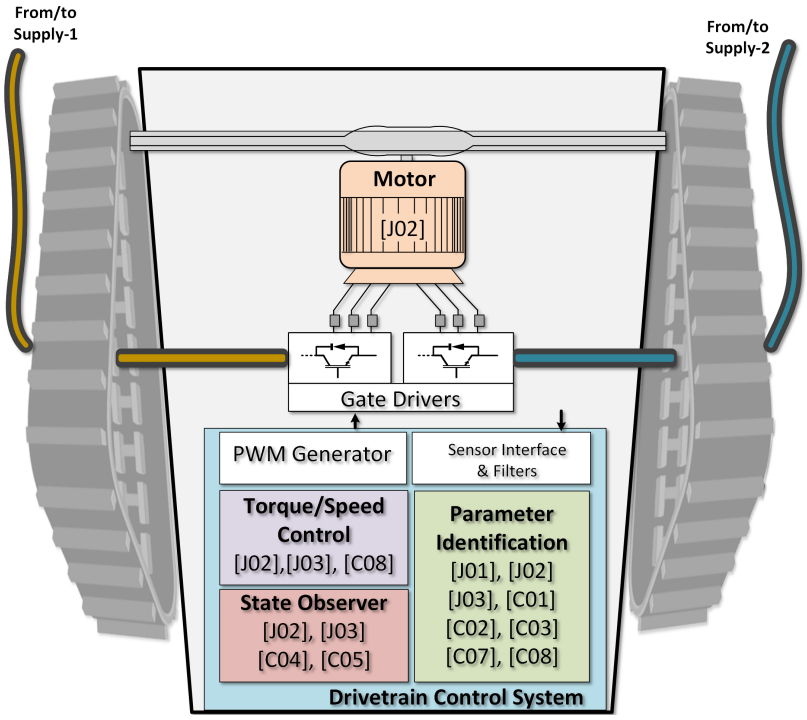

Figure 1.4. The focus of attention of the publications from the perspective of a simplified propulsion drive in a mining vehicle.

1.5 Outline of the Thesis

The thesis contains 8 chapters which are classified into four parts. Part 1 contains the background and contextual content of the research, presented in Chapter 1 and Chapter 2. Part 2 and Part 3 contain the core of the scientific work. The former is dedicated to three-phase drives, of which Chapter 3 and 4 contain the parameter and enhanced state estimation research, respectively. Similarly, Part 3 is comprised of six-phase drives-related research work, in which, Chapter 6 and Chapter 7 contain parameter estimation and enhanced sensorless control schemes, respectively. Chapter 5 contains the ERTS design details with a focus on three-phase drives. The main conclusions from each of these chapters are drawn in Chapter 8 to conclude the thesis. Extensive

derivations are presented in appendices, to leave only the resultant expressions in the relevant chapters. Figure 1.5 presents short descriptions of each chapter.

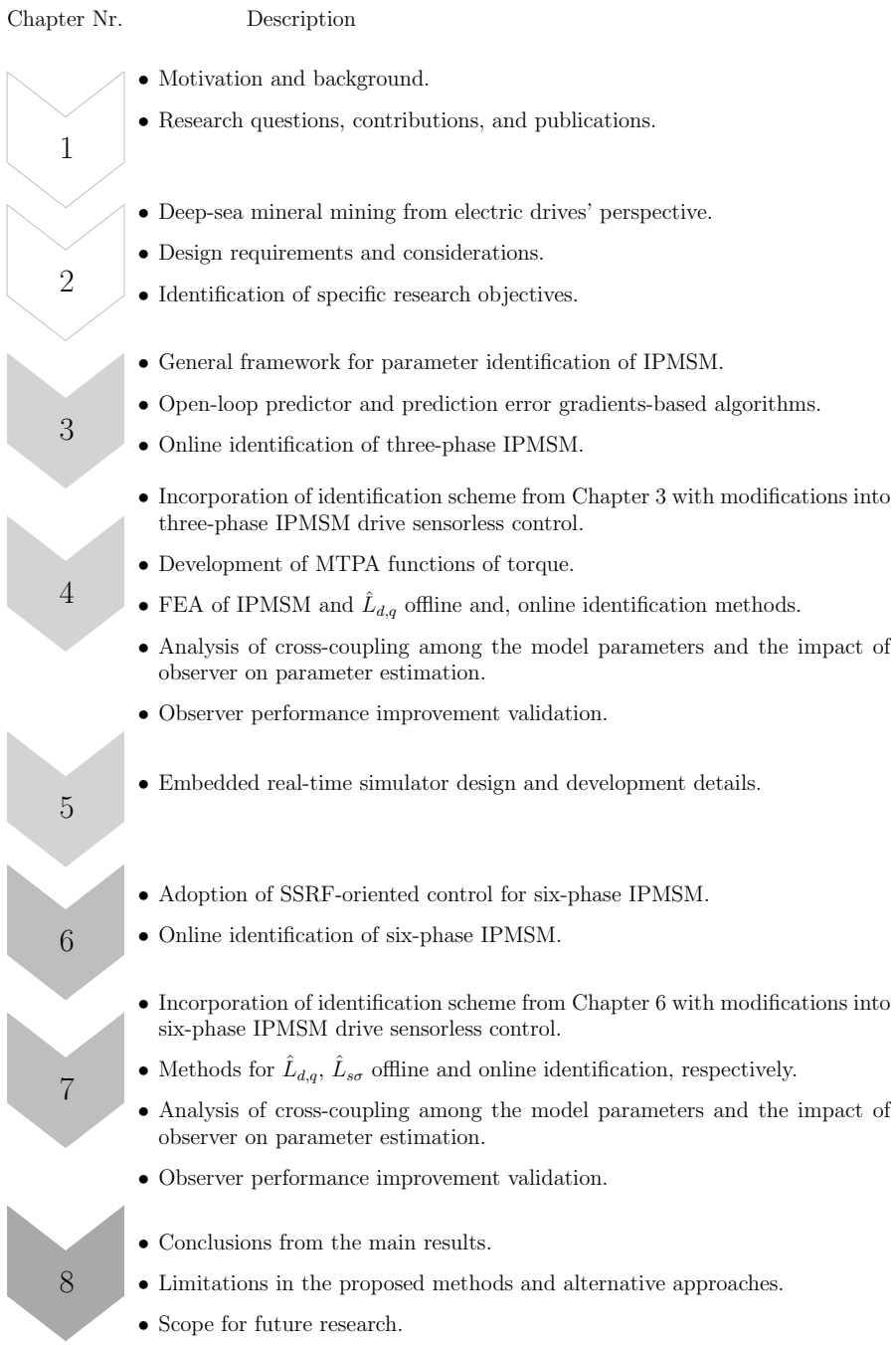

Figure 1.5. The outline of the thesis.

1.6 References

[1] V. Balaram. Rare earth elements: A review of applications, occurrence, exploration, analysis, recycling, and environmental impact. *Geoscience Frontiers* **10** (4), 1285–1303 (2019). ISSN 16749871. doi: 10.1016/j.gsf.2018.12.005. URL https://doi.org/10.1016/j.gsf.2018.12.005. Cited on page/s 3, 4, 5.

[2] Bianca Nogrady. Your old phone is full of untapped precious metals (5 2016). URL http://www.bbc.com/future/story/20161017-your-old-phone-is-full-of-precious-metals. Cited on page/s 3.

[3] S.E Kesler. Mineral supply and demand into the 21st century. *Proceedings, Workshop on Deposit Modeling, Mineral Resource Assessment, and Sustainable Development* pages 55–62 (2007). ISSN 1067084X. URL http://pubs.usgs.gov/circ/2007/1294/reports/paper9.pdf. Cited on page/s 3, 4.

[4] Norman Toro, Pedro Robles, and Ricardo I. Jeldres. Seabed mineral resources, an alternative for the future of renewable energy: A critical review. *Ore Geology Reviews* **126** (July), 103699 (2020). ISSN 01691368. doi: 10.1016/j.oregeorev.2020.103699. URL https://doi.org/10.1016/j.oregeorev.2020.103699. Cited on page/s 3.

[5] Muhammad Badar Hayat, Danish Ali, Keitumetse Monyake, Lana Alagha, and Niaz Ahmed. Solar energy - a look into power generation challenges and a solar-powered. *International Journal of Energy Research* **43** (3), 1049–1067 (2018). doi: DOI:10.1002/er.4252. URL https://onlinelibrary.wiley.com/doi/10.1002/er.4252. Cited on page/s 4.

[6] Alaa A.F. Husain, Wan Zuha W. Hasan, Suhaidi Shafie, Mohd N. Hamidon, and Shyam Sudhir Pandey. A review of transparent solar photovoltaic technologies. *Renewable and Sustainable Energy Reviews* **94** (January 2017), 779–791 (2018). ISSN 18790690. doi: 10.1016/j.rser.2018.06.031. Cited on page/s 4.

[7] U Kramer, F Ortloff, and S Stollenwerk. Defossilizing the Transportation Sector: Options and Requirements for Germany. Technical report FVV Prime, Movers Technologies Frankfurt, Germany (2018). Cited on page/s 4.

[8] Ecorys. Study to investigate state of knowledge of deep sea mining. Technical Report March European Commission - DG Maritime Affairs and Fisheries Rotterdam/Brussels (2014). URL https://webgate.ec.europa.eu/maritimeforum/sites/default/files/FGP96656DSMInterimreport280314.pdf. Cited on page/s 4, 5.

[9] Marie Navarre, Heloise Lammens, and ESG Analysis. Opportunities of deep-sea mining and ESG risks. Technical Report August (2017). Cited on page/s 4, 5.

[10] S. Davies. Mining the depths. *Engineering and Technology* **5** (15), 36–39 (2010). doi: 10.1049/et.2010.1504. Cited on page/s 4.

[11] Paripurnanda Loganathan, Gayathri Naidu, and Saravanamuthu Vigneswaran. Mining valuable minerals from seawater: a critical review. *Environmental Science: Water Research & Technology* **3** (1), 37–53 (1 2017). ISSN 2053-1400. doi: 10.1039/C6EW00268D. URL http://xlink.rsc.org/?DOI=C6EW00268D. Cited on page/s 5.

[12] Autorite des Marches Financiers (AMF) and Technip. Reference Document including the Annual Financial Report. Technical report AMF (2010). Cited on page/s 5.

[13] L Egorov, H Elosta, N.L. Kudla, S Shan, and K Yang. Sustainable Seabed Mining: Guidelines and a new concept for Atlantis II Deep volume 4. (2012). ISBN 9780854329496. URL http://eprints.soton.ac.uk/349891/. Cited on page/s 5.

Chapter 2

Deep-Sea Mineral Mining: Insight into the Application

Abstract

The aim of this chapter is to investigate deep-sea mining from the application perspective of electric drivetrains, to formulate the application-oriented research objectives. Thus, this chapter will provide the reader with the technology state-of-art, requirements, and considerations in designing electric drives for sustainable and productive deep-sea mineral mining. The chapter concludes with a solution proposal that entails the definite objectives to be accomplished by the doctoral research.

2.1 Deep-Sea Minerals and Surrounding Conditions

THE mineral deposits on the seabed are typically found in water depths ranging from 1 to 6 km. Depending on the characteristics of the deposits, they can be categorized into three groups [1]:

1. Seafloor Massive Sulphides (SMS)
2. Polymetallic (or Manganese) nodules
3. Ferromanganese crusts

Of these, SMS deposits have attracted most of the early attention from a commercial point of view [2, 3]. SMS are concentrated deposits resulting from hydrothermal activity on the seabed [4]. In the Norwegian context, such deposits are identified in Loki's Castle in the Norwegian extended continental shelf (see Figure 2.1). This deposit is rich with copper, zinc, and silicon and a basis to evaluate its economic worth is developed in [5].

The minerals are deposited about a 2,400-m water depth, and the temperatures of fluids around the deposits have been measured as high as 317 °C [6]. The ocean conditions are expected to be harsh with sea waves as high as 1.5 m [4]. This suggests the tools to harvest these deposits will undergo high temperatures, shock and vibration.

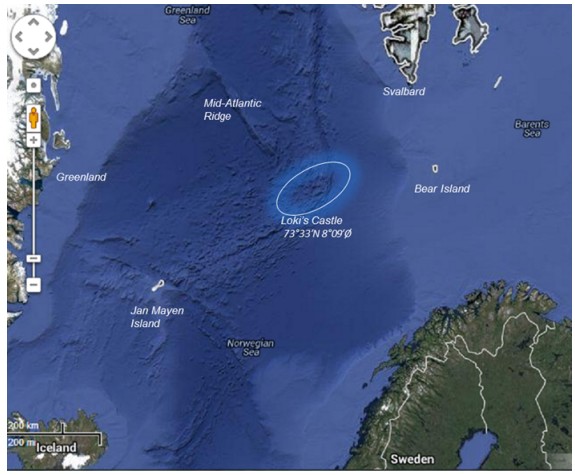

Figure 2.1. Overview map showing the location of the Loki's Castle occurrence.

2.2 Mining Technology State-of-Art

2.2.1 Mining Methodologies

Technology for deep-sea mineral mining is still under development with only a handful of industrial players existing at present. The deployment of multiple Deep-sea Mining Vehicles (DMV), also known as Seafloor Production Tools (SPT) with different functions [3], or single SPT with exchangeable heads [2], is one prevalent line of approaches. Figure 2.2 illustrates what this approach looks like. A floating vessel that supplies energy to the SPT(s), will retrieve the ore that is pumped back from the seabed. An alternative approach known as vertical trench cutting has been reported where, a cutter is submerged vertically from a topside floater to the seabed instead of complete mobile machines [7].

2.2.2 Hydraulic vs. Electric Drives

Hydraulic and more recently, hydraulic-electric motor drive systems have become the state-of-the-art in the mining tools both in terrestrial and deep-sea mineral mining [8]. A typical hydro-electric system incorporates electric drives to drive the hydraulic power unit in combination with an electric pump. The hydraulic technology is mature, offers excellent power-to-weight ratio [8], and has plenty of know-how, spare parts, and support services in the market. With the aim of improving the energy efficiency and due to low-emission requirements, more-electric mining tools have been emerging recently. The same trend is seen in the offshore mining industry due to the following concerns:

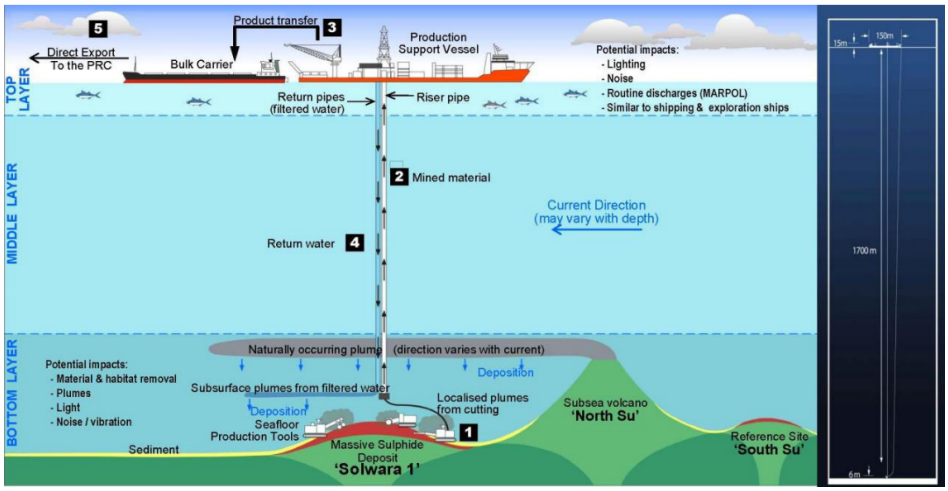

FIGURE 2.2. Seabed Mining Vehicle deployment approach, powered by Production Support Vehicle [3].

1. **Energy efficiency and related concerns**
   One of the major drawbacks of hydraulic drive systems is their poor energy efficiency [9, 10]. This is due to its inherent nature of several energy conversion stages from the source to the actuator. Several of the actuators in a typical DMV generate reverse energy during braking actions and this amounts, in some actuators over to 20% of its forward energy consumption. Feasible solutions to recover this reverse energy in the hydraulic systems are still under development [11]. Consequently, a hydraulic drive train would have a poorer efficiency by over 20% in comparison to its electrical counterpart [12]. Moreover, certain loads in mining machines, like dredging, fluctuating significantly [13], meaning, hydraulic drives yield even worse operating efficiencies. Low energy efficiency means higher energy consumption for the same useful output, and thus, energy storage in the Production Support Vessel will be exhausted faster to shorten the operations. The heat generation due to the losses and cooling design can also become demanding and can have implications in the overall power density and power-to-weight ratio.

2. **Energy cost**
   In assessing the energy bill and overall operating and maintenance costs, studies show that more-electric drive systems are more cost-effective than their counterpart. For instance, [14] claims that the overall cost saving in production per oil well is USD 200,000 (during total operational life) when systems were converted from hydraulic to electric. Another study [15] in a Canadian terrestrial mining site claims that the energy cost of a fully electric mining shovel is about 50% the cost per cubic meter of a hydraulic shovel. Studies [16] and [17] reinforce the same argument.

3. **Potential environmental cost**
   In addition to the high emissions owing to the lower efficiencies, hydraulic drives pose a persistent threat in potential hydraulic fluid leakage in the sea. Such undesirable outcomes can not only damage the sea habitation, but also will incur major penalties to the operators, which will hamper the profitability of the deep-sea explorations.

4. **Coping with the ambient conditions**
   The sensitivity of the hydraulic fluid to temperature could be another challenge in the attempt to reach deep-sea mining reserves that are in the proximity of volcanic chimneys where temperatures could be high, as explained in Section 2.1. This has an impact in the performance and reliability of the overall system. The hydro-electric systems are considerably bulky due to the fluid tank and hydraulic pressure unit. One option is to leave the bulky components on the top-side and transmit fluid to the seabed. Such arrangement will, however, lead to limitations to the depths that a DMV can reach.

AC motors with variable speed drives, on the other hand, provide solutions to many of these concerns. Advanced electric drives offer much better overall energy efficiencies and fast energy recovery possibilities with integrated battery solutions. The technology know-how is escalating rapidly thanks to the booming electric mobility industry. There are multiple success stories in relation to deep-sea oil and gas explorations, from which the mining industry can learn several lessons. Another key driving factor for the electrification of deep-sea mining is condition monitoring, plus the diagnostic capability that enhances the reliability and the predictability of the operations [18]. Power-to-weight ratio can still be one drawback for particular actuators. For example, hydraulic drives are difficult to compete with when linear actuators are concerned, in realizing lifting or crushing motions. From a broader perspective, the benefits of using more-electric DMVs can outweigh their shortcomings in comparison to the traditional hydro-electric drive systems. Thus, the future of deep-sea mining seems to be inclining toward mining vehicles that are equipped with more and more electric motor drive systems.

2.2.3 Topside vs. Seabed Electric Drives

For electric motor-equipped MW-level DMVs, a question emerges regarding whether or not to install the Voltage Source Inveters (VSI) on the DMV itself or retain the VSI on the Production Support Vehicle and deliver power to the DMV using long subsea cables. There are several advantages of the latter approach. When the VSI is on the sea surface rather than on the seabed, such drives technology is already proven and mature, time and cost of product development, and installation and commissioning will be reduced. Moreover, their access is much easier for repair and maintenance, and they offer the possibility of realizing lighter mining vehicles. However, [19] points out that

the topside drive approach becomes unfeasible in the face of modern DMVs, which contain multiple electric motors and are targeted for sea depths beyond 1 km. The primary driving factor in this investigation is the number of expensive subsea cables and the power losses in the cables. Consequently, it becomes necessary and important to install the complete electric drive, including the VSI, on the DMV itself.

There are two methods to realize medium power electric drive trains in hyperbaric conditions:

1. **Submerge the electronics in an enclosure filled with electrically neutral and compressible fluid.**

   The enclosure will then be designed with a pressure compensator such that the differential pressure across the enclosure wall is maintained at minimum close to zero. The advantages are in abundance. The wall thickness of the enclosures can be minimum, which allows lighter and less expensive packages. The ingress protection at the connectors and seals will also be simpler. Secondly, due to the ambience in the enclosure being fluidic, the natural convection will support heat transfer out of the hot spots. Thin walls in the enclosure will also support convenient heat transfer from inside to outside the enclosure. Certain fluids claim to have higher breakdown strength than air, and therefore, the distances among the sub-components could be reduced to achieve further power density. The main challenge with this approach is, however, the requirement to qualify the components and subsystems for their operability in such fluidic ambience over a long period, ideally across the operational life. The presence of fluid in the ambience poses threats in device and sensor properties and air pockets that can be detrimental in the depressurization. Workmanship during the system assembly, wiring, and cable connection also needs to be extremely meticulous to avoid human error, otherwise, it could lead to critical failures that are undetectable until the occurrence.

2. **Enclose the (power) electronics in a canister that has 1-atm air inside.**
   Most of the challenges associated with the first method can be overcome under this approach. The off-the-shelf components can then be directly utilized in the circuitry, which will accelerate the product development. The challenge is then that the canister weight and cost will increase with the operational depth. Heat transfer may become challenging as well, and therefore special designs for heat exchange and/or forced-cooling may become necessary.

The design choice, again, is dependent on multiple variables as such as the power consumption of the target system, the investment cost, and mean-time between maintenance. The first generation of mining machines used to have motor drives enclosed with are air-filled chambers. When the overall reliability, cost of manufacturing, and transportation are regarded for DMVs, the liquid-filled, pressure-compensated enclosures can be more favourable [20], thus the power converters and auxiliary systems

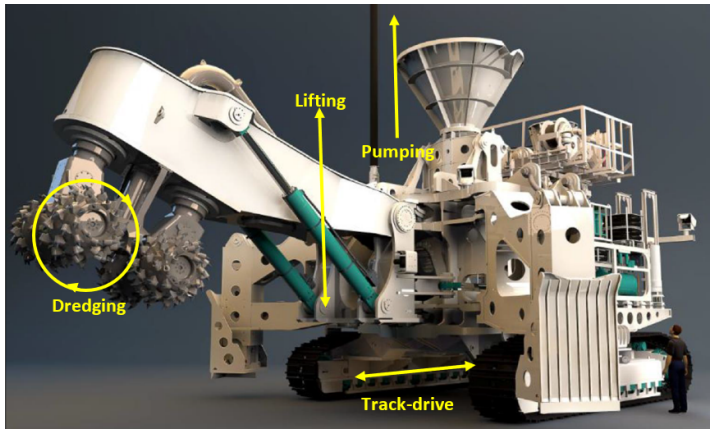

Figure 2.3. DMV known as Auxilliary Cutter developed by SMD for Solwara Project-1 [3].

will be exposed to pressurized fluid.

2.3 More-Electric Mining Drives

A modern DMV that features more electric drives than a conventional mobile mining machine is displayed in Figure 2.3. In this machine, either electric or hydroelectric drive units are employed for different functions. Table 2.1 contains the drive types used in the various actuators and their nature obtained from the machine manufacturer, SMD.

Table 2.1. Typical motor drive applications in a DMV operated under 1,500 m below the sea level.

Task	Dredging	Pumping	Collection	Track-drive	Lifting
Max continuous power [kW]	1,200	650	150	200	100
Power consumption of total	52%	28%	7%	9%	4%
Overload	30%	0%	0%	10%	0%
Drive type	2 x IM drive	1 x IM drive	1 x Hydraulic drive	2 x Hydraulic drive	2 x Hydraulic drive
Load/speed dynamics	High	Low	Relatively low	Low	Relatively high
Control mode	Torque	Speed	Torque	Speed	Position
Rotation	Forward, reverse	Forward	Forward	Forward, reverse	Forward, reverse

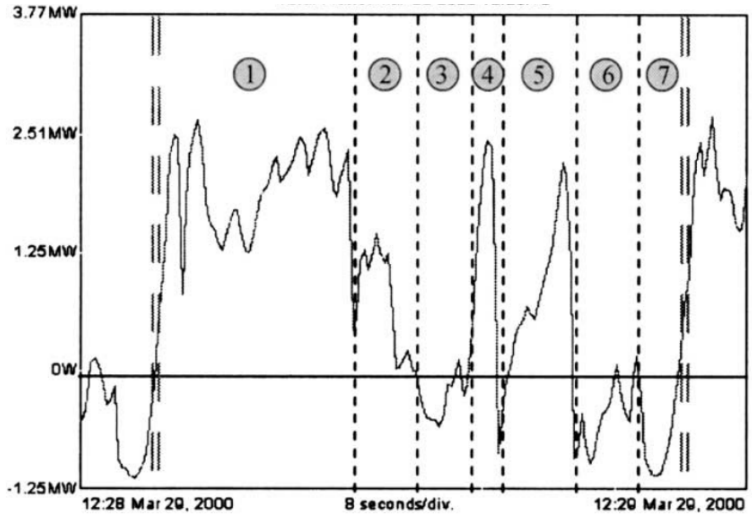

FIGURE 2.4. Shovel active power consumption during a truck loading cycle [13].

Accordingly, such vehicles have a combination of hydraulic and electric motor drive systems. High-power, high-speed applications like dredging are driven by electric drives. Hydraulic drives are preferred for lifting that can benefit from a high power-to-weight ratio. The power consumption values given in Table 2.1 are for 1,500 m water depth, and these values vary in proportion to the depth of deployment, nature of the terrain, and soil hardness, among other factors. The nature of the load profiles varies. The exact load profiles for such machines are difficult to obtain. However, the load profiles of similar machines used in the terrestrial mining industry can provide a close approximation. Figure 2.4 from [13] shows the active power profile of a 100-ton shovel across three loading cycles. Different movements in these loading cycles are given in Table 2.2.

TABLE 2.2. Different movements corresponding to Figure 2.4, during the loading cycle of a shovel [13].

Loading Action	Movement
1	The dipper is fully loaded with rocks.
2	The revolving frame rotates toward the truck.
3	Braking of the revolving frame (regeneration).
4	Mineral discharge and dipper lift.
5	The revolving frame rotates toward mineral side.
6	Braking of the revolving frame (regeneration).
7	Dipper lowered down (regeneration).

Similarly, [21] contains estimated load profiles for swing, hoist, and crowd drives of a terrestrial mining shovel, which appear to be not as demanding as in Figure 2.4. From

this perspective, one can expect the motor drives for dredging can experience highly dynamic speeds and loads. The pump loads will see relatively lower speed variations in a short time interval (~ 1 minute). In summary, the following load characteristics can be expected in the electric drives used in the DMV;

1. Certain actuators will face high-speed dynamics whereas the others will see only mild dynamics.
2. Motoring and regenerating operations are part of the load profiles of many actuators.
3. Dredging actuators can experience high fluctuations in speed and load.
4. Stall-torque can be an operating point for certain actuators like those used for dredging.

2.4 Design Requirements for Deep-Sea Mining Drives

Well-established terrestrial mining and the decades-old offshore oil and gas industry offer plenty of lessons as found in [18, 22], from which it can be inferred the following objectives for Deep-sea Mining Vehicles:

(i) Maximize the amount of minerals mined per unit time.

(ii) Minimize the cost per unit minerals.

(iii) Minimize the environmental footprint.

To satisfy the above objectives for mining vehicles, the following design requirements at a system level can be identified for their subsea motor drive systems:

1. **Increased reliability to increase the predictability and availability.**
   Sudden breakdown in electric drives and the cost of retrieval of deep-sea mining vehicles for unscheduled repair may sometimes cost more than the cost of the system itself [20]. Therefore, high reliability and fault resilience to elongate the system availability is essential to the success of electric drives in DMVs.
2. **High power density.**
   Maximizing the available power in the electric drive and the torque in the rotating machines per volume would increase the payload per empty vehicle volume ratio. Consequently, the DMVs not only will be lighter to ease the maneuvering but will also be less expensive to fabricate.
3. **High power efficiency.**
   The benefits of high-power efficiency are two-fold; reduced losses mean the heat dissipation is lower thus the cooling is simpler and the drive becomes more

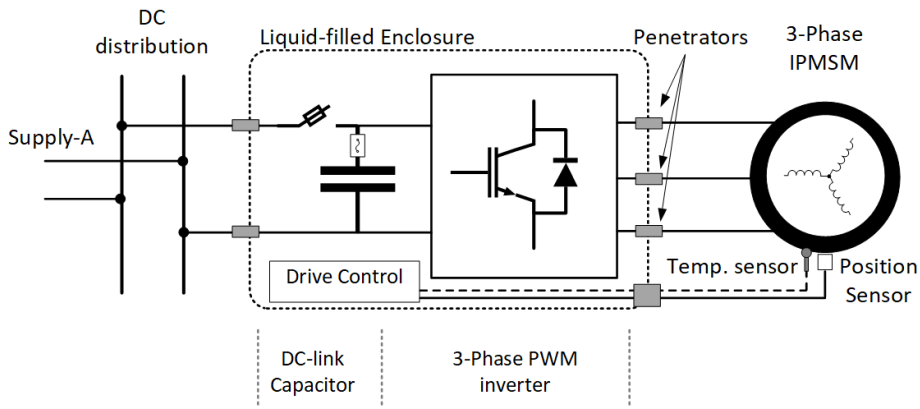

Figure 2.5. Simplified circuit diagram of the two-level, three-phase, IGBT-based inverter enclosed in a pressure-compensated and liquid filled tank in a deep-sea mining vehicle. VSI output breakers should be in place, typically inside the enclosure.

compact. Secondly, the energy usage per unit material will be reduced, and thus the operating cost will be reduced. Particularly when the energy budget is stringent in the topside floating vessel, high efficiency means longer periods of operation.

2.5 Design Considerations for Deep-Sea Mining Drives

From the previous section, it is evident that reliability is the most essential feature that these drives must possess. In this section, the general design considerations of the electric drives will be investigated by examining their subsystems/sub-components. Figure 2.5 presents a simplified three-phase medium power motor drive system in the deep-sea mining vehicle. Here, a DC distribution is assumed, from which each drive receives its input power. AC distribution can be an alternative approach. The pros and cons of different power distribution configurations for DMVs are investigated in [19]. The classical, two-level, three-phase, PWM, IGBT-based inverters are considered in this drive. It is also assumed that the state-of-the-art approach is followed where the inverter and related electronics are submerged in a liquid-filled, pressure compensated tank. For the operating conditions given in Section 2.1, the following components can be identified as the most vulnerable [23–25] in electric drives in the DMVs:

1. **IGBT modules in three-phase PWM inverter.**
   An industry-based survey presented in [26] claims that about 38% of the failure that occur in variable speed drives are caused by failure in their power electronic devices. the main causes of failure are reported to be high temperature variations within a short span of time and high mean temperature in devices. Cooling can become challenging when the inverter is enclosed in a tank where heat exchange

from inside to outside is hampered by thick walls. On the other hand, the device properties can change over time in the highly pressurized fluidic atmosphere, due to the fluid leakage inside the power modules. Thus, the power devices or modules must be designed or selected meticulously.

2. **DC-link capacitors–short circuit due to failure in self-healing system.**
The power capacitors are among the most fragile components, statistically being second only to power electronic devices [26]. Due to a number of reasons outlined in [27], film capacitor type is the most reliable choice to provide capacitance at the dc-link. However, when the inverter is submerged in a dielectric fluid, self-healing in the film capacitors must be specially treated and customized [23, 28]. It is understood that the power capacitors are equally or more susceptible for failure than IGBTs in pressurized liquid environments.

3. **Sensors, control electronics and gate drivers.**
Several sensors are used in a motor drive system for torque/speed control and condition monitoring from remote locations. Among them, rotor speed- or position-sensor is one of the weaker links in such a system due to the wear and tear. Modern drives incorporate estimation and identification strategies such that, the drive can either run without a mechanical sensor (known as sensorless control) or can fail safely and "limp" home if the mechanical sensor fails. The digital electronics that contain the firmware, control/estimation logic, and protection algorithms are critical components that need special attention in system design for reliability and robustness. IGBT gate driver circuits are a critical component from a reliability point of view. In the event of a short circuit in the output of the inverter, gate-drivers are the first line of defence that can turn-off the circuit. Secondly, they can be used effectively in the accurate acquisition of output voltage of the VSI. Because of these reasons, the reliable design and operation of gate drivers become critical.

4. **Penetrators–risk of water intrusion through the mating point.**
Insulation failure due to seawater intrusion is one of the largest risks to which subsea power systems are exposed.

5. **Dielectric fluid – change of fluid characteristics.**
Deterioration of the favorable characteristics of the dielectric fluid is another major threat when design approach 1 in Section 2.2.3 is being used. Under this design approach, the cooling of the electrical components strongly relies on the natural fluidic convection that has direct relations with the viscosity of the fluid. Also, if the breakdown strength of the dielectric fluid is reduced due to aging or contamination, the risk of partial discharge increases.

2.5.1 Inverter Design Considerations

Inverter design for deep-sea mining drives needs special attention to ensure longer life time and predictable behavior of the drive. Mission-profile-based design methods [29] provide a comprehensive approach in this regard, that consider environmental, drive system-level, converter-level, and component-level mission profiles. The medium voltage converters are preferred for MW-level electric drives due to their high power density and good efficiencies [30].

Two-level, 690 V topology is the most common choice regarding the power level of interest, owing to its simplicity and relatively low number of parts. Additionally, three-level Neutral Point Clamped (NPC) converter topology can also be a favorable choice for MW-level drives due to the excellent efficiencies and low Total Harmonic Distortion (THD) [31]. Subsequently, variants of the NPC topology have been proposed, namely, Active NPC (ANPC) and Fault-Tolerant ANPC (FT-ANPC), which offer better thermal distribution among the devices and failure tolerance against successive device failure [32].

Selection of the power electronic devices or modules and their types of packaging requires attention too, as they become vulnerable under harsh mission profiles like the dredging in the DMVs. The Silicon (Si) IGBT has been the state-of-the-art device for medium voltage drives owing to their technology maturity over several decades and ruggedness. Silicon Carbide (SiC) MOSFETs have been emerging as a competitive alternative. In [33], the two devices are compared for PMSM drives and the authors conclude, owing to the higher efficiency by about 1%, lesser temperature rise in the heat sink by 2-3 °C, and increased power density, the SiC MOSFETs are the more favourable of the two choices. However, mainly due to the limitation of the understanding of the device physics, gate-design and packaging related issues, and their brittleness concerns [34–36], SiC MOSFETs can still be a bold choice for electric drives in mission-critical applications like the DMVs that cannot afford to compromise the reliability of the electric drivetrain.

2.5.2 Motor Choice and Design Considerations

In alignment with the design criteria outlined in Section 2.4, the gear in the drive system, despite its usefulness in improving the torque density of the motor, will significantly hurt the overall reliability, power density, and efficiency [37, 38], and therefore, the direct drive solutions become more appealing in deep-sea mining applications.

In the handful of successful trial runs on the seabed for mineral mining, the Permanent Magnet Synchronous Motor (PMSM) has been chosen as their drive machine. The main motive behind this choice is the high torque-to-current and torque-to-volume ratios PMSMs offer compared to its closest contender, the induction motor in the medium power ranges [39, 40]. When the reliability of the motor is concerned, the motor bearing and the stator winding are among the weak links [41]. For PMSMs,

the permanent magnets should also be added to that list [42]. The subsea motors are liquid-filled in their construction to compensate for the pressure difference between the internal and external environments. This leads to increased friction and winding losses because the air gap now becomes a liquid gap. Unlike in an induction motor, PMSMs can support larger air gaps because of the strong permanent magnet fields, and therefore the friction loss can be further reduced. Also, due to the absence of current conduction in the rotor, the PMSM generates much less heat. Consequently, the stator winding insulation in the PMSM will undergo lesser thermal stress [43]. Due to these reasons, the PMSMs offer superior efficiency in a wide speed range in comparison to the standard induction motors. In electrical submersible pump applications, the difference in efficiency could be as large as 20% at nominal speed [43]. In an overall evaluation, the PMSM appears to have an advantage by a fair margin over induction machines in subsea operations. A key design consideration of the PMSM is the axial flux versus the radial flux structures, particularly when the axial length is limited [44]. By burying the magnets inside the rotor core, one can achieve more reluctance torque in addition to the synchronous torque, particularly in the flux-weakening regions. Such machines, known as Interior PMSMs (IPMSMs), are particularly suitable for traction applications, and they provide additional information about the rotor position when saliency-based position extraction is concerned, because of its rotor magnetic anisotropy.

The adoption of electric machines with more than three phases (multiphase) is one proven approach to enhance the fault tolerance of the electric drivetrain at the failure of an inverter leg or capacitor bank or even one isolated power supply, depending on the circuit arrangement. The concentrated windings in the multiphase machines can be a desirable option over the distributed windings, owing to fewer coupling between the winding sets that offer more resilience at a fault in one three-phase group [45].

All in all, multiphase, IPMSM direct drives appear to be a promising and robust solution for the application being studied and thus are chosen for this research.

2.6 Proposed Electric Drivetrains and Research Scope

There is a multitude of possible research directions regarding electric drives for deep-sea mining vehicles. A certain level of research focuses already exists whereby component-level reliability is regarded in NTNU research environment as seen in [23, 24]. Therefore, it was decided to give emphasis on the control aspects of electric drives in this doctoral research.

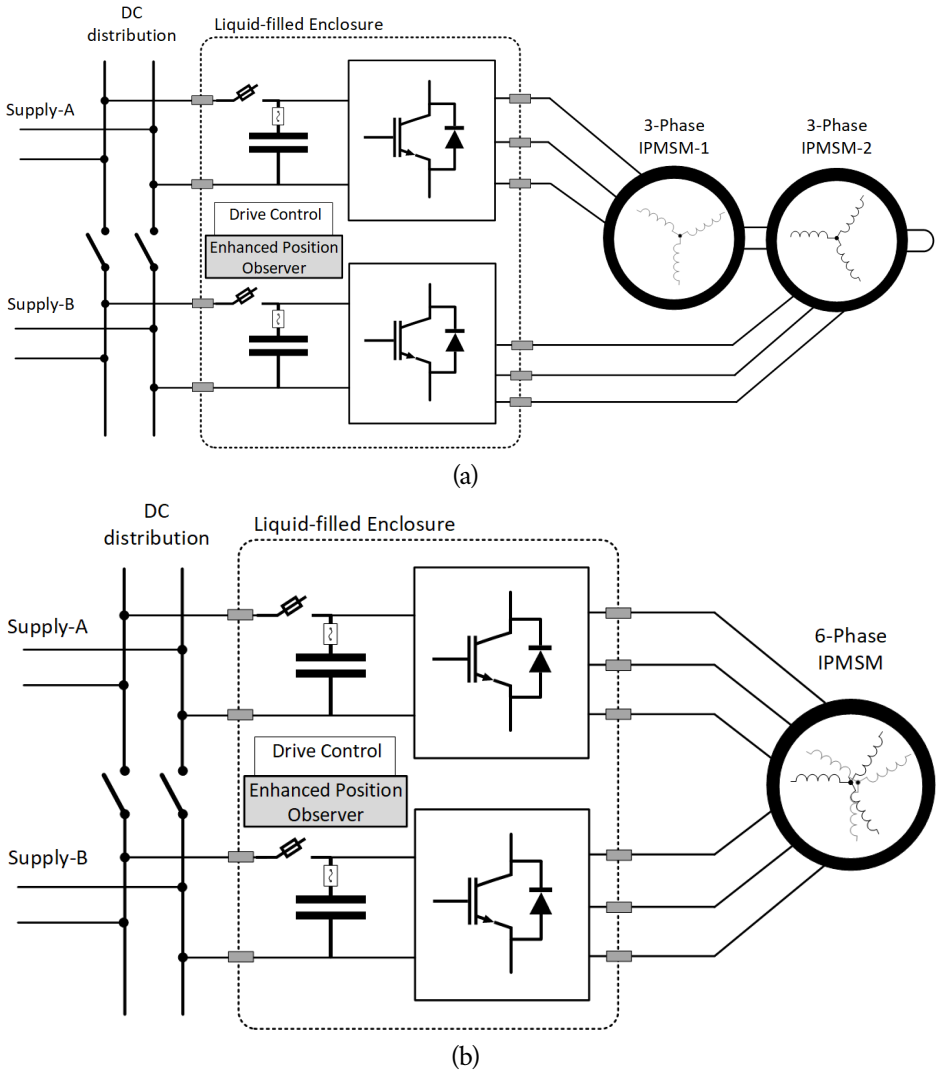

FIGURE 2.6. Sensorless electric drivetrain solutions for DMVs, composed of two units of two-level, three-phase VSI with (a) three-phase IPMSM (b) six-phase IPMSM.

1. **Three-phase and six-phase IPMSM drives**
   A six-phase drive encompassing two units of three-phase IGBT-based inverters is the main system of interest. See Figure 2.6(b). Here, the machine is arranged in a dual three-phase winding configuration with their star points isolated from each other. This solution is targeted to provide hardware redundancy to the electric drive, considering the vulnerability of the IGBTs and the capacitor banks, as revealed in Section 2.5. Another reliability improvement targeted with such a system configuration is in relation to supply failure. If supply-A fails, supply-B can still supply to the second inverter which can yield at least 50% of the rated

power to the load. Chapter 6 and Chapter 7 provide more details of such machines.
Nonetheless, three-phase electric motors can still be applied in many applications in the DMV drives, either in the solutions as shown in Figure 2.6(a) or in stand-alone applications. Thus, both three-phase and six-phase drives are taken into consideration in this thesis.

2. **Position sensorless control**
The elimination of the mechanical position sensor of the IPMSM drives, with the aid of a state-of-art observer, is targeted. Fundamental excitations-based observers are used in a wide speed range, and they have been reviewed in Chapter 4 and Chapter 7. One of their common drawbacks is their performance dependence on the model parameters. This drawback invites researchers to find solutions for a stable and precise observer performance, irrespective of the parameter behavior. Consequently, that leads to the next component of the research scope.

3. **Online parameter adaptation**
Section 2.5 explained that the temperatures of the mining terrains can vary and also can be quite high, particularly in the vicinity of seabed volcanic occurrences. System and component temperature is a key indicator of the health and condition of the electric drivetrain. Moreover, the temperature variations induce variations in the machine parameters, which can degrade the torque/speed control of the machine and sometimes lead to faults, if not taken into account. On the other hand, sensor-based temperature and parameter tracking is cumbersome, expensive, and can degrade overall reliability. As mentioned before, accurate information of machine parameters will also assist the model-based observers in their performance. After evaluating the overall benefits and realizable features, online parameter tracking becomes the third research component.

In essence, this doctoral research attempts to realize the control system that is proposed in Figure 2.6(b).

2.7 Conclusion and Summary

This chapter disclosed key insights into the deep-sea mineral mining from the technology perspective. The water depths can be, in average, 3 km and the temperatures, particularly for seafloor massive sulphide deposits, can be harsh. The adoption of more-electric mining vehicles may become mandatory under these circumstances and owing to the shortcomings in the conventional hydraulic mining vehicles. Reliability, efficiency, and power density are identified to be the features of merit for deep-sea mining vehicles. For subsea environments, the voltage source inverters including the capacitor banks and the mechanical sensors are identified to be the weak links that

can threaten the overall system reliability. Silicon IGBT-based two-level, three-phase inverter technology is adopted, due to its technology maturity and proven robustness. The IPMSM has been the preferred choice for the machine because it can accommodate larger air gaps to reduce friction losses in liquid-filled environments, in addition to its inherent superior efficiency, and torque density in a wide speed range. Thereby, the research scope for the doctoral research is identified, comprising; position sensorless, three-phase and six-phase IPMSM drive, assisted by online parameter adaptation.

2.8 References

[1] Rahul Sharma. Approach towards deep-sea mining: current status and future prospects. In Rahul Sharma, editor, *Perspectives on Deep-Sea Mining* chapter 2. Springer Cham, Switzerland (2021). ISBN 9783030879815. Cited on page/s 13.

[2] Nobuyuki Okamoto, Satoshi Shiokawa, Seiya Kawano, Norihiro Yamaji, Hironobu Sakurai, and Masaomi Kurihara. World's first lifting test for seafloor massive sulphides in the okinawa trough in the EEZ of Japan. *Proceedings of the International Offshore and Polar Engineering Conference* **1**, 1–7 (2019). ISSN 15551792. Cited on page/s 13, 14.

[3] Nautilus Minerals Niugini Ltd. Preliminary Economic Assessment of the Solwara Project, Bismarck Sea, PNG. Technical Report February (2018). Cited on page/s 13, 14, 15, 18.

[4] Steinar L. Ellefmo. Conceptual 3D modeling and direct block scheduling of a massive seafloor sulfide occurrence. In Rahul Sharma, editor, *Perspectives on Deep-Sea Mining* chapter 16. Springer Cham, Switzerland (2021). Cited on page/s 13.

[5] Maxime Lesage, Cyril Juliani, and Steinar L. Ellefmo. Economic block model development for mining seafloor massive sulfides. *Minerals* **8** (10) (2018). ISSN 2075163X. doi: 10.3390/min8100468. Cited on page/s 13.

[6] M Ludvigsen, K Aasly, Steinar L. Ellefmo, A Hilario, E. Ramirez-Llodra, and F Søreide. MarMine Cruise report Arctic Mid-Ocean Ridge (AMOR) 15.08.2016 - 05.09.2016. Technical report NTNU Trondheim (2016). Cited on page/s 13.

[7] Giovanni Spagnoli, Sape A. Miedema, Christian Herrmann, Johann Rongau, Leonhard Weixler, and Julien Denegre. Preliminary Design of a Trench Cutter System for Deep-Sea Mining Applications Under Hyperbaric Conditions. *IEEE Journal of Oceanic Engineering* **41** (4), 930–943 (10 2016). ISSN 0364-9059. doi: 10.1109/JOE.2015.2497884. URL http://ieeexplore.ieee.org/document/7347479/. Cited on page/s 14.

[8] Rajesh Siva, P Muthuvel, A A Gnanaraj, B O Vishvanath, K Gopakumar, and G A Ramadass. Adaptation of land based hydraulic pump for deep sea applications: testing and qualification. In *OCEANS* pages 0–4 Chennai (2022). IEEE. ISBN 9781665418218. Cited on page/s 14.

[9] Panu Sainio, Matti Heiska, Teemu Lehmuspelto, and Jussi Suomela. Comparison of packaging hydraulic and electric components in a HEV power line. **3**, 777–786 (2009). Cited on page/s 15.

[10] W Pawlus and M Choux M R Hansen. Hydraulic vs . Electric : A Review of Actuation Systems in Offshore Drilling Equipment. **37** (1), 1–17 (2016). doi: 10.4173/mic.2016.1.1. Cited on page/s 15.

[11] Milos Vukovic, Roland Leifeld, and Hubertus Murrenhoff. Reducing fuel consumption in hydraulic excavators - a comprehensive analysis. *Energies* **10** (5) (2017). ISSN 19961073. doi: 10.3390/en10050687. Cited on page/s 15.

[12] D.W. Williams, C.M. McBride, and S.C. Kinnaman. Deep ocean mining - technology transfer from and to the offshore drilling industry. *IN: PROC. 9TH ANNUAL OFFSHORE TECHNOL. CONF. (HOUSTON, U.S.A.: MAY 2-5, 1977).* **1 , Dallas**, 395–402 (1977). Cited on page/s 15.

[13] José Rodríguez, Luis Morán, Jorge Pontt, José Espinoza, Rodrigo Díaz, and Eduardo Silva. Operating experience of shovel drives for mining applications. *IEEE Transactions on Industry Applications* **40** (2), 664–671 (2004). ISSN 00939994. doi: 10.1109/TIA.2004.824508. Cited on page/s 15, 19.

[14] M. Rivenbark, S. Khater, W. Dietz, and S. Barnes. An Innovative All Electric Well Production System. In *Proceedings - SPE Production Operations Symposium* pages 283–291 (2001). Cited on page/s 15.

[15] Rodion Andreev. Evaluation of hydraulic excavator and rope shovel major maintenance cost in operation. *PhD thesis*. University of Alberta (2015). Cited on page/s 15.

[16] V. S. Isakov, V. P. Maksimov, and Y. V. Maksimov. Justification of an adaptive working body of a cable excavator. *Procedia Engineering* **129** (8635), 910–914 (2015). ISSN 18777058. doi: 10.1016/j.proeng.2015.12.130. Cited on page/s 15.

[17] V K Slobodyanyuk and Yu Yu Turchin. RATIONAL USE OF HYDRAULIC EXCAVATORS IN IRON ORE PITS Statement of the problem and its connection with practical tasks. **60**, 2–7 (2017). Cited on page/s 15.

[18] K.M. Elgsaas, T. Hjertvikrem, W. Hua, S. Tryti, and T. Glomsaker. All-Electric subsea systems - Intelligence on demand. In *Proceedings of the Annual Offshore Technology Conference* volume 2 pages 1233–1243 (2018). ISBN 9781510862531. Cited on page/s 16, 20.

[19] Razieh Fard and Elisabetta Tedeschi. Investigation of AC and DC power distributions to seafloor mining equipment. In *Oceans* Aberdeen (2017). IEEE. URL https://brage.bibsys.no/xmlui/bitstream/handle/11250/2475776/PID4856857.pdf?sequence=2&isAllowed=y. Cited on page/s 16, 21.

[20] Vedachalam Narayanaswamy. Review of challenges in reliable electric power delivery to remote deep water enhanced oil recovery systems. *Applied Ocean Research* **43**, 53–67 (2013). ISSN 01411187. doi: 10.1016/j.apor.2013.07.008. URL http://dx.doi.org/10.1016/j.apor.2013.07.008. Cited on page/s 17, 20.

[21] Matias Valenzuela and M. Anibal Valenzuela. Payload estimation in AC electric mining shovels using drive signals. *IEEE Transactions on Industry Applications* **52** (5), 4470–4479 (2016). Cited on page/s 19.

[22] Gerald M. Brown, Bernard J. Ebacher, and Walter G. Koellner. Increased productivity with AC drives for mining excavators and haul trucks. In *Conference Record - IAS Annual Meeting (IEEE Industry Applications Society)* volume 1 (2000). Cited on page/s 20.

[23] Magnar Hernes and Riccardo Pittini. Enabling pressure tolerant power electronic converters for subsea applications Keywords Identification of problems and priority settings for the research. (7465), 1–10 (). Cited on page/s 21, 22, 24.

[24] Astrid Petterteig, Riccardo Pittini, Magnar Hernes, and Øystein Holt. Pressure tolerant power IGBTs for subsea applications. In *13th European Conference on Power Electronics and Applications* pages 1–10 Barcelona (2009). IEEE. ISBN 9789075815009. Cited on page/s 21, 24.

[25] H.S.-H. Chung, H. Wang, F. Blaabjerg, and M. Pecht. Reliability of power electronic converter systems. (2016). ISBN 9781849199025. doi: 10.1049/PBPO080E. Cited on page/s 21.

[26] Shaoyong Yang, Angus Bryant, Philip Mawby, Senior Member, Dawei Xiang, Li Ran, Senior Member, Peter Tavner, and Senior Member. An Industry-Based Survey of Reliability in Power Electronic Converters. **47** (3), 1441–1451 (2011). Cited on page/s 21, 22.

[27] Il Yop Chung, Wenxin Liu, David A. Cartes, Emmanuel G. Collins, and Seung Il Moon. Control methods of inverter-interfaced distributed generators in a microgrid system. *IEEE Transactions on Industry Applications* **46** (3), 1078–1088 (2010). ISSN 00939994. doi: 10.1109/TIA.2010.2044970. Cited on page/s 22.

[28] Fredrik Aarskog. Removing faults from a self-healing film capacitor (2017). ISSN 2004001828. Cited on page/s 22.

[29] Frede Blaabjerg, Huai Wang, Ionut Vernica, Bochen Liu, and Pooya Davari. Reliability of Power Electronic Systems for EV / HEV Applications. *Proceedings of IEEE* **109** (6), 1060–1076 (2021). doi: 10.1109/JPROC.2020.3031041. Cited on page/s 23.

[30] Ferreira Victor De Nazareth, Gabriel Alves Mendonca, Anderson Vagner Rocha, Robson Silva Resende, and Braz De Jesus Cardoso Filho. Mission Critical Analysis and Design of IGBT-Based Power Converters Applied to Mine Hoist Systems. *IEEE Transactions on Industry Applications* **53** (5), 5096–5104 (2017). ISSN 00939994. doi: 10.1109/TIA.2017.2709719. Cited on page/s 23.

[31] Dietmar Krug, Mariusz Malinowski, and Steffen Bernet. Design and comparison of medium voltage multi-level converters for industry applications. In *Conference Record - IAS Annual Meeting (IEEE Industry Applications Society)* pages 781–790. IEEE (2004). ISBN 0780384865. Cited on page/s 23.

[32] Anderson V. Rocha, Sidelmo M. Silva, Igor A. Pires, Alysson A P Machado, Fernando V. Amaral, Victor N. Ferreira, Helder De Paula, and Braz J. Cardoso Filho. A new fault-tolerant realization of the active three-level NPC converter. In *2014 IEEE Energy Conversion Congress and Exposition (ECCE)* pages 3483–3490 (2014). ISBN 9781479956982. doi: 10.1109/ECCE.2014.6953874. Cited on page/s 23.

[33] Haihong Qin, Haotian Xie, Zhu Ziyue, Nie Xin, Huajuan Xu, and Dafeng Fu. Comparisons of SiC and Si devices for PMSM drives. *2016 IEEE 8th International Power Electronics and Motion Control Conference, IPEMC-ECCE Asia 2016* pages 891–896 (2016). doi: 10.1109/IPEMC.2016.7512404. Cited on page/s 23.

[34] Paula Diaz Reigosa, Francesco Iannuzzo, Haoze Luo, and Frede Blaabjerg. A short-circuit safe

operation area identification criterion for SiC MOSFET power modules. *IEEE Transactions on Industry Applications* **53** (3), 2880–2887 (2017). ISSN 00939994. doi: 10.1109/TIA.2016.2628895. Cited on page/s 23.

[35] L Yu, S Araujo, D Pappis, and P Zacharias. Short-circuit capability: benchmarking SiC and GaN devices with Si-based technologies. *Proceedings of PCIM Europe 2015; International Exhibition and Conference for Power Electronics, Intelligent Motion, Renewable Energy and Energy Management* (May), 1–5 (2015). Cited on page/s 23.

[36] T Kimoto, H Niwa, N Kaji, T Kobayashi, Y Zhao, S Mori, and M Aketa. Progress and Future Challenges of SiC Power Devices and Process Technology. pages 3–6 (2017). Cited on page/s 23.

[37] W.G. Koellner, G.M. Brown, J. Rodriguez, J. Pontt, P. Cortes, and H. Miranda. Recent Advances in Mining Haul Trucks. *IEEE Transactions on Industrial Electronics* **51** (2), 321–329 (4 2004). ISSN 0278-0046. doi: 10.1109/TIE.2004.825263. URL http://ieeexplore.ieee.org/document/1282020/. Cited on page/s 23.

[38] M Combes, C Dirscherl, and T Roesch. Increasing Availability through Advanced Gearless Drive Technology. In *46th Annual Canadian Mineral Processors Operators Conference* Ottawa, Ontario (2014). URL https://www.ceecthefuture.org/wp-content/uploads/2016/01/CMP2014_Increasing-Availability-through-Advanced-Gearless-002.pdf. Cited on page/s 23.

[39] Gilberto Cunha, Adalberto Jos, Joable Andrade Alves, and Eduardo Cardoso. Control of Permanent Magnet Synchronous Machines for Subsea Applications. **54** (2), 1899–1905 (2018). doi: 10.1109/TIA.2017.2785764. Cited on page/s 23.

[40] Mounir Zeraoulia, Mohamed El Hachemi Benbouzid, and Demba Diallo. Electric Motor Drive Selection Issues for HEV Propulsion Systems: A Comparative Study. *IEEE Transactions on Vehicular Technology* **55** (6), 1756–1764 (11 2006). ISSN 0018-9545. doi: 10.1109/TVT.2006.878719. URL http://ieeexplore.ieee.org/document/4012550/. Cited on page/s 23.

[41] Olav Vaag Thorsen and Magnus Dalva. A Survey of Faults on Induction Motors in Offshore Oil Industry, Petrochemical Industry, Gas Terminals, and Oil Refineries. *IEEE Transactions on Industry Applications* **31** (5), 1186–1196 (1995). ISSN 19399367. doi: 10.1109/28.464536. Cited on page/s 23.

[42] Kai Li Yang and Qiang Song. Study on Influencing Factors on Reliability of Permanent Magnet Synchronous Motor System in Electric Vehicle. *Advanced Materials Research* **544**, 151–158 (6 2012). ISSN 1662-8985. doi: 10.4028/www.scientific.net/AMR.544.151. URL https://www.scientific.net/AMR.544.151. Cited on page/s 24.

[43] Thomas R Brinner, Life Member, Robert H Mccoy, and Trevor Kopecky. Induction Versus Permanent-Magnet Motors for Electric Submersible Pump Field and Laboratory Comparisons. *IEEE Transactions on Industry Applications* **50** (1), 174–181 (2014). doi: 10.1109/TIA.2013.2288203. Cited on page/s 24.

[44] A Cavagnino, Mario Lazzari, Francesco Profumo, and Alberto Tenconi. A comparison between the axial flux and radial flux structures for PM synchronous motors. *IEEE Trans. on Industry Applications* pages 1517 – 1524 (2002). Cited on page/s 24.

[45] Emanuele Fornasiero, L Alberti, Nicola Bianchi, and Silverio Bolognani. Considerations on selecting fractional-slot nonoverlapped coil windings. *IEEE Trans. on Industry Applications* pages 1316–1324 (2013). Cited on page/s 24.

Part II

THREE-PHASE DRIVES

Chapter 3

Online Parameter Identification: Framework and Algorithms

Abstract

Real-time acquisition of accurate machine parameters is of significance to achieving high performance in electric drives, particularly for mission-critical applications. Unlike the saturation effects, the temperature variations are difficult to predict, and thus it is essential to track temperature-dependent parameters online. In this chapter, a unified framework is developed for online parameter identification of rotating electric machines, premised on the Recursive Prediction Error Method (RPEM). Secondly, the prediction gradient ($\boldsymbol{\Psi}^T$)-based RPEM is adopted for identification of the temperature-sensitive parameters, i.e., the permanent magnet flux linkage (Ψ_m) and stator-winding resistance (R_s) of the IPMSM. Three algorithms, namely Stochastic Gradient (SGA), Gauss-Newton (GNA), and the physically interpretative method (PhyInt), are investigated for the estimation gains computation. A speed-dependent gain-scheduling scheme is used to decouple the inter-dependency of Ψ_m and R_s. With the aid of offline simulation methods, the main elements of RPEM such as $\boldsymbol{\Psi}^T$ are analyzed. The concept validation and the choice of the optimal algorithm is made with the use of the System-on-Chip (SoC)-based Embedded Real-Time Simulator (ERTS). Subsequently, the selected algorithms are validated with the aid of a 3-kW, IPMSM drive where the control and estimation routines are implemented in the SoC-based industrial embedded control system. The experimental results reveal that $\boldsymbol{\Psi}^T$-based RPEM, in general, can be a versatile technique in temperature-sensitive parameter adaptation, both online and offline.

3.1 Introduction

In the wake of increasing electrification in operational reliability and safety-critical applications such as surface transport, aerospace, and seabed mining, the dependability of the electrical systems becomes of major significance. Also, the increasing urge to reduce the carbon footprint calls for more efficient power systems. IPMSM-

equipped electric drives have become a frontrunner in this context, owing to some of their inherent features such as superior efficiency and power density, and thus ease of cooling, design capability for fault-tolerance, and good control dynamics in a wide torque-speed range [1].

In realizing a high-performance electric drive, knowing the exact machine parameters is essential for multiple reasons [2], yet this information is often unknown across the operating range. Therefore, it is useful to identify the machine parameters of the electric drive, and thus a variety of online and offline identification methods, as reviewed in [2, 3], have gained attention in recent years. Out of the electric parameters, i.e., Ψ_m, R_s, and d- and q- axis inductances L_d, L_q, the first two are temperature-dependent and display slow dynamics due to the thermal capacity. L_d and L_q can vary rapidly as they are iron core-saturation dependent, a phenomenon that is dictated by the stator current. Nevertheless, simultaneous identification of more than two unknown parameters is prohibited by the rank-deficiency problem of IPMSM [4] unless extra efforts are exerted. Adoption of two time-scale routines for fast- and slow- dynamic parameter-sets [5] or High-Frequency Signal Injection (HFSI) [6], or a combination of such methods [7], or the use of special instrumentation for online computation of inductances as reported in [8], have been employed to solve the rank-deficiency challenge. Alternatively, some of the electric parameters can be identified offline and updated online. The stator current, which affects the inductances, is a measured quantity in electric drives,and thus, the model inductances can be updated with reference to stator current in real-time, using the offline identified inductances with the aid of a Look-Up Table (LUT) or analytical functions [9]. Sensor-based R_s and Ψ_m acquisition have also been reported both with and without contact [10, 11]. Sensor-based stator temperature monitoring is a more common industrial approach, from which R_s and Ψ_m can be back-calculated in real-time. Although, such sensor-based acquisitions are associated with considerable integration and reliability concerns and will also have implications for the space requirement and the overall costs [12]. Online tracking of R_s and Ψ_m can be a more versatile solution from this perspective. Based on this premise of the two-fold benefits, R_s and Ψ_m are identified online and the inductances are identified offline and updated online, in the scope of this chapter, which will enable us to solve the rank deficiency problem in addition to drive performance enhancement.

3.1.1 Literature Review

The RPEM is a set of parameter identification methods presented by Ljung [13], in which it is indicated that several well-known techniques like the Recursive Least Squares (RLS) and the Extended Kalman Filter (EKF) methods can be viewed as its subsets. Among these, RLS, perhaps the most widely adopted, is used in [5] for the identification of all electric parameters of PMSM. Ref [14] the use of RLS to improve the performance of the Model Predictive Controlled PMSM by recursively updating the prediction models. In sensorless drives, the position-estimation accuracy is enhanced

using RLS in [15, 16]. A combination of a signal injection scheme and the RLS method is applied in [7] to identify IPMSM parameters of a Direct Torque Control drive. The EKF, another popular member of the RPEM family discussed for online parameter adaptation [17, 18], offers decent performance at the cost of increased computational burden. An alternative method in the RPEM-family that exploits the sensitivity of the predicted currents to the model parameters has been discussed in [13], which calls this approach the prediction gradient ($\boldsymbol{\Psi}^T$)-based Recursive Prediction Error Method (RPEM). $\boldsymbol{\Psi}^T$-based RPEM offers more consistent estimations [19], and the global convergence is more often guaranteed [20, 21] compared to EKF-based identification. Additionally, in contrast to the RLS or EKF methods, the digital implementation of $\boldsymbol{\Psi}^T$-based RPEM can be less demanding due to the possibility of avoiding tedious computations like matrix inversions. Model Reference Adaptive System (MRAS)-based parameter identification has been adopted in [22, 23]. Apart from its known stability issues and design complexities [2], the reference model is assumed to emulate the plant, which may not be the case if its parameters mismatch with the physical counterparts, and thus the prediction error may not represent the true parameter discrepancy. A variety of artificial intelligence applications like different forms of neural network (NN) models and evolutionary algorithms like the Particle Swamp Optimization (PSO) have been reported in connection to the parameter estimation of PMSM [24, 25]. To overcome their known stability and convergence issues [26], more advance methods, for example, with self-learning capability, have emerged lately. However, adoption of these are hampered by longer model-training time or demand of high expertise in design and implementation [26].

3.1.2 Research Gaps and Contribution

Despite the merits of $\boldsymbol{\Psi}^T$-based RPEM, it has not been investigated for electric drives in recent decades, and thus omitted in the recent reviews [2, 3]. Another notable research gap in the RPEM-related literature is the absence of the basis and underlying principles behind the choices of estimation gains. This chapter attempts, firstly, to adopt the $\boldsymbol{\Psi}^T$-based RPEM for online parameter identification of IPMSM, an investigation that has not been done before, to the author's best knowledge. Three algorithms, namely SGA, GNA and PhyInt become applicable under this context [13, 27]. The SGA- and GNA -based Ψ_m and R_s identification using the offline simulation tools, presented in [28], will be extended with the real-time simulation and experimental validation in this chapter. Additionally, PhyInt is also explored for Ψ_m and R_s identification. Eventually, the performances with different algorithms are compared to draw conclusions regarding the optimal algorithm to compute estimation-gains for $\boldsymbol{\Psi}^T$-based RPEM. Secondly, to address the absence of an elaborate procedure to identify estimation-gains in the drives domain, a general approach outlined in [13] is tailored for electric drives with the aim of formulating a thorough and physically insightful framework for RPEM-based identification. The step-by-step sequence [13], put explicitly, is: 1) Choice of Model-Set,

$\mathscr{M}$; 2) Choice of experimental conditions; 3) Choice of criterion function; 4) Choice of search direction using prediction gradient and 5) Choice of gain-sequence and initial values. In order to focus this chapter to parameter identification, a mechanical position-sensor is assumed to obtain the rotor position although the incorporation of position-sensorless schemes within the same scope is possible as shown in Chapter 4. A Zynq System-on-Chip (SoC)-based ERTS and a 3 kW-IPMSM experimental setup is used for simulation and experimental validation.

3.2 IPMSM Modeling and Control

In this section, the dynamic model of the IPMSM and its control method is outlined. The mathematical model of the electrical part of the machine is in the rotor co-ordinates when given in the per-unit (pu) system as per [29]:

$$\begin{aligned} \underline{u}_s^r &= r_s \cdot \underline{i}_s^r + \frac{1}{\omega_n} \cdot \frac{\mathrm{d}\underline{\psi}_s^r}{\mathrm{d}t} + \mathbf{j} \cdot n \cdot \underline{\psi}_s^r \\ \underline{\psi}_s^r &= \mathbf{x}_s^r \cdot \underline{i}_s^r + \underline{\psi}_m^r \end{aligned} \tag{3.1}$$

$$\begin{aligned} \underline{i}_s^r &= \begin{bmatrix} i_d & i_q \end{bmatrix}^T, \quad \underline{\psi}_m^r = \begin{bmatrix} \psi_m & 0 \end{bmatrix}^T \\ \mathbf{x}_s^r &= \begin{bmatrix} x_d & 0 \\ 0 & x_q \end{bmatrix}, \quad \mathbf{j} = \begin{bmatrix} 0 & -1 \\ 1 & 0 \end{bmatrix} \end{aligned}$$

u, i, ψ, l, n, and ω_n are voltage, current, flux linkage, inductance, electric speed, and nominal angular frequency, respectively in pu. Reactance in pu, $x = l$ at rated speed, and thus x is more often used. ϑ is the electrical angle of the mechanical position ϑ_{mech} whose relationship with ϑ is given by $\vartheta = p \cdot \vartheta_{mech}$ where p is the number of pole pairs. Throughout the chapter, the superscript and subscript denote the reference frame and the location of the quantity (s-stator, r-rotor, m-magnet), respectively. The notation $\hat{}$ and superscript * indicate the estimated and the reference quantities, respectively.

The block diagram of the three-phase, vector-controlled, IPMSM drive enhanced by the Online Parameter Estimator (OPE) is given in Figure 3.1. The classical two-level, three-phase, Insulated-Gate Bipolar Transistor (IGBT), Voltage Source Inverter (VSI) is supplied by dc-link capacitors, in which the voltage U_{dc} is measured and used to estimate the stator winding voltages while compensating for the dead-time and the device on-stage voltage drop as given in [30]. $\underline{I}_s$ is measured at the output of the VSI. The OPE estimates the model parameter vector $\hat{\underline{\theta}}$ that is fed into the reference calculator and Proportional-Integral (PI) controllers. Based on the given torque command τ_e^*, either from the Human Machine Interface (HMI) or from the speed controller, i_d^*, i_q^* are calculated to fulfill either MTPA or the field-weakening strategy at high-speed operations as described in [31].

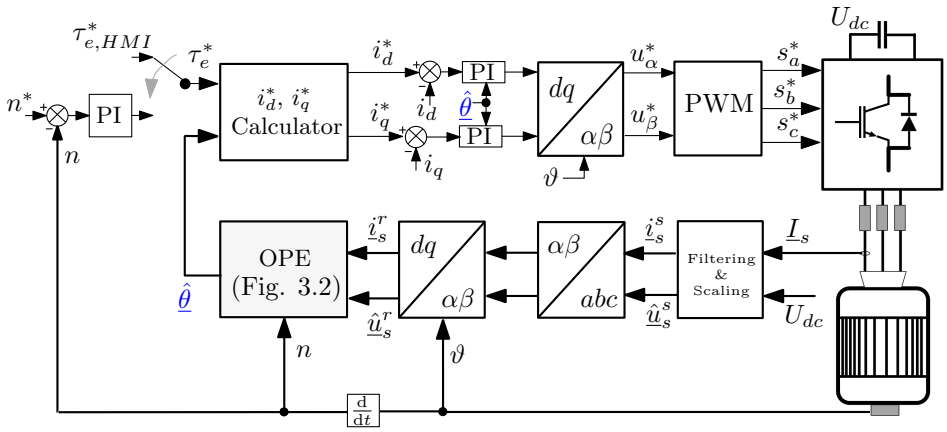

FIGURE 3.1. Block diagram of the vector controlled-IPMSM drive enhanced with the online parameter estimator.

3.3 PROPOSED FRAMEWORK AND DEVELOPMENT OF Ψ^T-BASED RPEM

The generalized RPEM, in discrete form of a pure integrator, becomes:

$$\hat{\underline{\theta}}[k] = \left[\hat{\underline{\theta}}[k-1] + \mathbf{L}[k, \hat{\underline{\theta}}] \cdot \underline{\epsilon}[k, \hat{\underline{\theta}}]\right]_{D_{\mathscr{M}}} \tag{3.2}$$

Here, $\boldsymbol{L}$ is the gain-matrix, and $\underline{\epsilon}$ is the criterion function that is attempted to minimize and eventually nullify, by choosing appropriate $\boldsymbol{L}$. Among the various approaches to computing $\boldsymbol{L}$, $\boldsymbol{\Psi}^T$-based methods are adopted. In contrast to the common practice, in this section, the author attempts to reveal the underlying principles of computing $\boldsymbol{L}$ by adopting the step-by-step approach from [13] for online identification of three-phase IPMSM parameters.

3.3.1 *Choice of Model-Set, $\mathscr{M}(\underline{\theta})$*

The Full-Order Model, $\mathscr{M}_{u\theta}$, can be expressed as:

$$\begin{aligned} \frac{\mathbf{x}^r_s(\underline{i}_s)}{\omega_n} \frac{\mathrm{d}\hat{\underline{i}}^r_s(t, \hat{\underline{\theta}})}{\mathrm{d}t} &= \underline{u}^r_s(t) - \hat{r}_s(t) \cdot \hat{\underline{i}}^r_s(t, \hat{\underline{\theta}}) \\ &\quad - \mathbf{j} \cdot n(t) \cdot \mathbf{x}^r_s(\underline{i}_s) \cdot \hat{\underline{i}}^r_s(t, \hat{\underline{\theta}}) - \mathbf{j} \cdot n(t) \cdot \underline{\psi}^r_m(t) \\ \underline{i}^r_s &= \mathbf{T}^r_{ss}(\vartheta) \cdot \underline{i}^s_s, \qquad \underline{u}^r_s = \mathbf{T}^r_{ss}(\vartheta) \cdot \underline{u}^s_s \end{aligned} \tag{3.3}$$

$\mathscr{M}_{u\theta}$ is chosen in the proposed method because it incorporates the electric parameters of interest. $\mathscr{M}_{u\theta}$ is used to construct a predictor to predict the stator current, $\hat{\underline{i}}^r_s$. The prediction error, $\underline{\epsilon}^r_s$ is then generated using the measured and the predicted currents, which can be expressed in discrete form as $\underline{\epsilon}^r_s = \underline{i}^r_s[k] - \hat{\underline{i}}^r_s[k, \hat{\underline{\theta}}]$. It is assumed that the

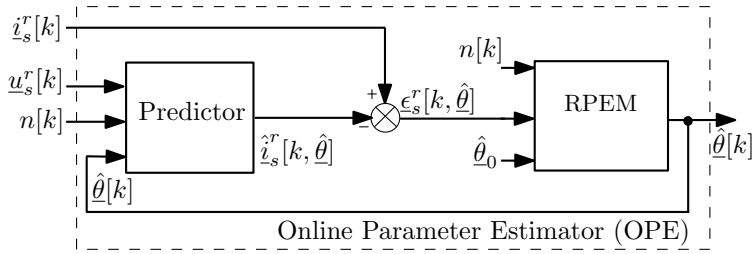

Figure 3.2. Block diagram of the open-loop online parameter estimator.

sole cause for nonzero $\underline{\epsilon}_s^r$ is the difference between the physical and model parameters. The block diagram of the $\mathscr{M}_{u\theta}$-based OPE is given in Figure 3.2. $\underline{\epsilon}_s^r$ is fed forward with no correction in contrast to a closed-loop/observer, where the error is corrected using a feedback loop. Therefore, this open-loop predictor arrangement enriches $\underline{\epsilon}_s^r$ with parametric error information, a feature that is attempted to capitalize on computing the prediction gradients under this method. $\underline{\epsilon}_s^r$ is discussed in detail in section 3.3.3. This choice, however, requires a separate Model-Set for parameter estimation, unlike the MRAS-based approaches [22, 23], in which both parameter- and state-estimations can be integrated within one Model-Set. Thus, for low-cost processor-based or high-speed drives, the designers should be cautious about the additional time taken by the proposed scheme in the processor.

$$\lambda \cdot I_2 - A = \begin{bmatrix} \lambda + \frac{1}{\hat{T}_d} & \frac{-n \cdot x_q \cdot \omega_n}{x_d} \\ \frac{-n \cdot x_d \cdot \omega_n}{x_q} & \lambda + \frac{1}{\hat{T}_q} \end{bmatrix} \tag{3.4a}$$

$$\lambda_{1,2} = -\frac{1}{2} \cdot \left(\frac{1}{\hat{T}_d} + \frac{1}{\hat{T}_q} \right) \pm \sqrt{\left[\frac{1}{2} \cdot \left(\frac{1}{\hat{T}_d} + \frac{1}{\hat{T}_q} \right) \right]^2 - \left[\left(\frac{1}{\hat{T}_d \cdot \hat{T}_q} \right) + (\omega_n \cdot n)^2 \right]} \tag{3.4b}$$

$$\hat{T}_d = \frac{x_d}{\hat{r}_s \cdot \omega_n}, \qquad \hat{T}_q = \frac{x_q}{\hat{r}_s \cdot \omega_n} \tag{3.4c}$$

$$\hat{\underline{i}}_s^r[k,\hat{\underline{\theta}}] = \hat{\underline{i}}_s^r[k-1,\hat{\underline{\theta}}] + \frac{T_{samp}}{2} \left(\underline{g}_c \left(\hat{\underline{i}}_s^r[k,\hat{\underline{\theta}}], \underline{u}_s^r[k], n[k] \right) + \underline{g}_c \left(\hat{\underline{i}}_s^r[k-1,\hat{\underline{\theta}}], \underline{u}_s^r[k-1], n[k-1] \right) \right) \tag{3.5}$$

$\mathscr{M}_{u\theta}$ is a second-order system in which the linearized system matrix **A** and the eigenvalues, $\lambda_{1,2}$ are given in (3.4a) and (3.4b), respectively, where $\hat{T}_d$, $\hat{T}_q$, expressed in (3.4c) are

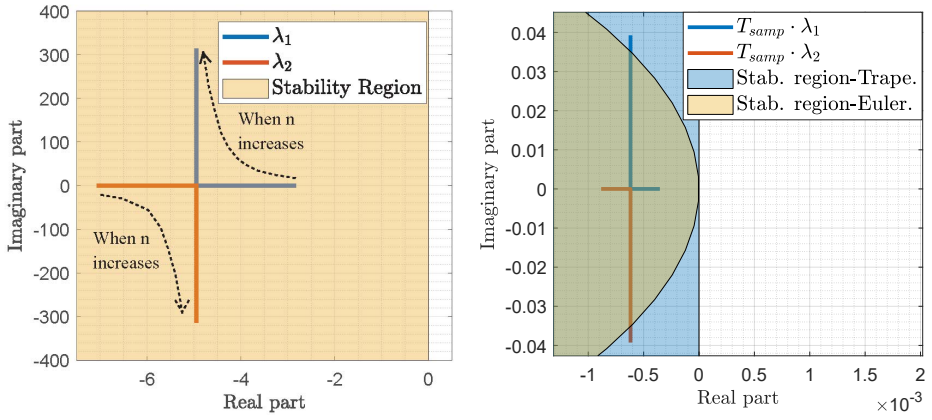

FIGURE 3.3. Eigenvalue trajectories and stability regions (a) in continuous time domain (b) when discretized using trapezoidal method, in $\lambda \cdot T_{samp}$ plane.

d, q- axes time-constants. To linearize the nonlinear IPMSM model, only the electrical equations are considered, in which, n is treated as a measured and slow-varying parameter. Figure 3.3(a) plots the trajectories of $\lambda_{1,2}$ against the increasing rotor speed from standstill for the IPMSM given in Table 3.1. It is evident that the $\mathscr{M}_{u\theta}$ is stable across the full speed range, yet $\hat{\underline{i}}_s^r$ can contain oscillations and their frequency is expected to increase in proportion to the rotor speed. Due to this speed-dependency, the numerical method adopted to discretize $\mathscr{M}_{u\theta}$ as well as the integration time-step of the digital controller can influence the stability of the digitally implemented predictor. Unlike the explicit Euler method, the trapezoidal rule-based numerical method has a much larger stability region (entire left-half plane) in the $\lambda \cdot T_{samp}$-plane [32], which can guarantee the full speed-range stability of the $\mathscr{M}_{u\theta}$-based open-loop predictor when implemented in a processor at sampling times T_{samp} corresponding to IGBT-based drives. Figure 3.3(b) illustrates how eigenvalues escape the Euler-based stability region in $\lambda \cdot T_{samp}$-plane, yet are well within that of the trapezoidal rule, when $T_{samp} = 125\ \mu s$. Eq. (3.5) expresses the predicted currents when discretized using the trapezoidal rule-based numerical method, in which $\hat{\underline{i}}_s^r[k]$ must be explicitly solved as a function of $\hat{\underline{i}}_s^r[k-1]$ and other variables.

3.3.2 *Choice of Experimental Conditions*

$$\hat{\underline{\theta}} = \begin{bmatrix} \hat{\psi}_m & \hat{r}_s \end{bmatrix}^T, \qquad \hat{\underline{\theta}} \in D_{\mathscr{M}}, \qquad D_{\mathscr{M}} \in D_s \tag{3.6a}$$

$$D_{\mathscr{M}} = \left\{ \begin{matrix} \hat{\psi}_{m,min} \leq \hat{\psi}_m \leq \hat{\psi}_{m,max} \\ \hat{r}_{s,min} \leq \hat{r}_s \leq \hat{r}_{s,max} \end{matrix} \right\} \tag{3.6b}$$

The choice of experimental conditions imply *when* and *which* data are collected from the process for identification. The input signals for the OPE model are identified as $\underline{u}_s^r, \underline{i}_s^r, n$ as illustrated in Figure 3.2. An online identification method, both at the start of the drive and during its operation, is chosen as the means to acquire the input signals to identify Ψ_m and R_s. Henceforth, $\hat{\underline{\theta}}$ becomes as in (3.6a). In [13] it is shown that to guarantee global convergence, the $\hat{\underline{\theta}}$ must be bounded by the parameter-space D_s, which defines the stable region of the $\mathscr{M}_{u\theta}$-based predictor. To facilitate faster tracking, a narrower parameter-subspace, $D_{\mathscr{M}}$ can be defined as given in (3.6b).

In addition to the input signals to the OPE, ϑ needs to be accurately identified, because of the required reference frame transformations, particularly in the OPE, among other instances.

3.3.3 Choice of Criterion Function, $V_N(\hat{\underline{\theta}})$

$V_N(\hat{\underline{\theta}})$ and its asymptotic properties are influenced by the choice of $\mathscr{M}(\underline{\theta})$. If a Gaussian distribution of the prediction errors is assumed, $V_N(\hat{\underline{\theta}})$ becomes a scalar quadratic criterion [13] as given below, in which Λ is the covariance matrix of the prediction error:

$$V_N(\hat{\underline{\theta}}) = \frac{1}{2}\underline{\epsilon}_s^{rT}(t, \hat{\underline{\theta}}) \cdot \Lambda^{-1} \cdot \underline{\epsilon}_s^r(t, \hat{\underline{\theta}}) \tag{3.7}$$

Assuming that the Λ is known and independent of the model parameters, and the prediction error is based on the current measurement, Λ is chosen as the Identity Matrix.

The sensitivity of the prediction error to all four parametric errors can be evaluated by deriving an expression for the steady-state $\underline{\epsilon}_s^r$, as follows, when assuming the same voltage inputs to the physical system and the predictor:

$$\begin{aligned} u_d &= \underbrace{r_s \cdot i_d - n \cdot x_q \cdot i_q}_{\text{Physical}} = \underbrace{\hat{r}_s \cdot \hat{i}_d - n \cdot \hat{x}_q \cdot \hat{i}_q}_{\text{Model}} \\ u_q &= \underbrace{r_s \cdot i_q + n \cdot x_d \cdot i_d + n \cdot \psi_m}_{\text{Physical}} \\ &= \underbrace{\hat{r}_s \cdot \hat{i}_q + n \cdot \hat{x}_d \cdot \hat{i}_d + n \cdot \hat{\psi}_m}_{\text{Model}} \end{aligned} \tag{3.8}$$

The detailed derivation is revealed in Appendix A.1. Accordingly, the prediction error,

in component form, becomes:

$$
\begin{aligned}
\epsilon_d = &-\left(\frac{n^2 \cdot \hat{x}_q}{\hat{r}_s^2 + n^2 \cdot \hat{x}_d \cdot \hat{x}_q}\right)\delta\psi_m \\
&-\left(\frac{\hat{r}_s}{\hat{r}_s^2 + n^2 \cdot \hat{x}_d \cdot \hat{x}_q} \cdot i_d + \frac{n \cdot \hat{x}_q}{\hat{r}_s^2 + n^2 \cdot \hat{x}_d \cdot \hat{x}_q} \cdot i_q\right)\delta r_s \\
&-\left(\frac{n^2 \hat{x}_q}{\hat{r}_s^2 + n^2 \cdot \hat{x}_d \cdot \hat{x}_q} \cdot i_d\right)\delta x_d \\
&+\left(\frac{n \cdot \hat{r}_s}{\hat{r}_s^2 + n^2 \cdot \hat{x}_d \cdot \hat{x}_q} \cdot i_q\right)\delta x_q
\end{aligned}
$$

$$
\begin{aligned}
\epsilon_q = &-\left(\frac{n \cdot \hat{r}_s}{\hat{r}_s^2 + n^2 \cdot \hat{x}_d \cdot \hat{x}_q}\right)\delta\psi_m \\
&-\left(\frac{\hat{r}_s}{\hat{r}_s^2 + n^2 \cdot \hat{x}_d \cdot \hat{x}_q} \cdot i_q - \frac{n \cdot \hat{x}_d}{\hat{r}_s^2 + n^2 \cdot \hat{x}_d \cdot \hat{x}_q} \cdot i_d\right)\delta r_s \\
&-\left(\frac{n \cdot \hat{r}_s}{\hat{r}_s^2 + n^2 \cdot \hat{x}_d \cdot \hat{x}_q} \cdot i_d\right)\delta x_d \\
&-\left(\frac{n^2 \cdot \hat{x}_d}{\hat{r}_s^2 + n^2 \cdot \hat{x}_d \cdot \hat{x}_q} \cdot i_q\right)\delta x_q \\
\delta\psi_m = \psi_m - \hat{\psi}_m, &\qquad \delta r_s = r_s - \hat{r}_s \\
\delta x_d = x_d - \hat{x}_d, &\qquad \delta x_q = x_q - \hat{x}_q
\end{aligned}
\tag{3.9}
$$

Let us assume the model inductances are in alignment with their physical counterparts, thus $\delta x_d, \delta x_q = 0$ in (3.9). Therein, the prediction error sensitivities can be visualized in the four-quadrant speed-torque plane for a 10% underestimation in $\hat{\psi}_m$ in Figure 3.4 (a) and a 10% underestimation in $\hat{r}_s$ in Figure 3.4 (b). In connection to (3.9) and Figure 3.4, the following observations can be made:

Remark 1: When $\delta\psi_m$, δr_s becomes zero, $\epsilon_{d,q}$ also go to zero.

Remark 2: Regarding $\delta\psi_m$ (see Figure 3.4 (a)), ϵ_d is consistently well-condition with $\delta\psi_m$ beyond very low rotor speeds. When n increases, $\epsilon_d \approx \frac{-1}{\hat{x}_d} \cdot \delta\psi_m$. On the contrary, the sensitivity of ϵ_q to $\delta\psi_m$ across the operating range is weak and inconsistent to make ϵ_q redundant information for ψ_m-identification.

Remark 3: Regarding δr_s (see Figure 3.4 (b)), both ϵ_d and ϵ_q become dominant at and around zero-speed to carry rich-conditioned information for r_s-identification.

Remark 4: When δr_s is concerned, $\epsilon_{d,q}$ are also stator current dependent, meaning, even at standstill, $\underline{\epsilon}_s^r$ carries information to identify r_s if stator current is present.

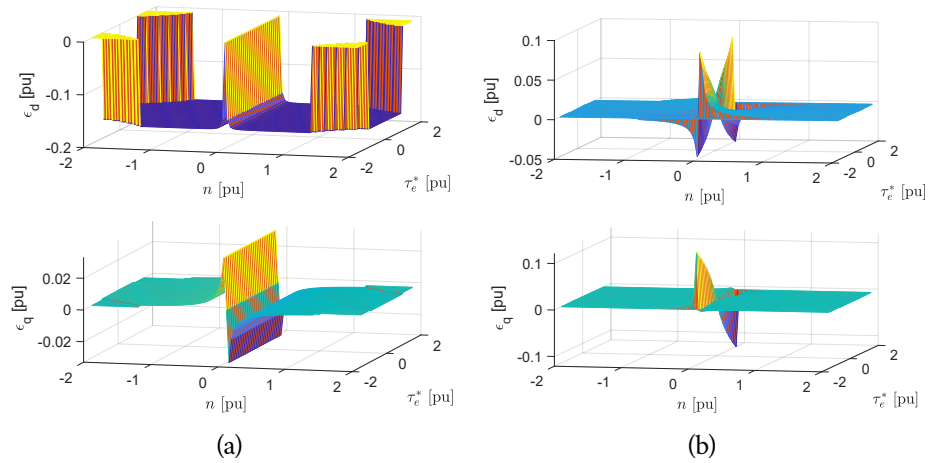

FIGURE 3.4. Prediction-errors in four-quadrant speed-torque plane when estimate is 10% lower than respective physical quantity w.r.t. (a) $\hat{\psi}_m$ (b) $\hat{r}_s$.

Remark 5: $\epsilon_{d,q}$ becomes more sensitive to $\delta\psi_m$ and δr_s in mutually exclusive speed regions. The dominance of δr_s-sensitivity is at and around zero speed, and this is the very region, the accuracy of $\hat{r}_s$ becomes critical.

3.3.4 *Choice of Search Direction using Prediction Gradient,* Ψ^T

Once V_N is chosen, the correct direction to minimize V_N is discovered using a search direction algorithm. In this section, the development of $\boldsymbol{\Psi}^T$-based algorithms that are used to discover the search direction, will be disclosed.

One well-known numerical minimization approach is the use of the gradient of the criterion function. Ljung shows in [13] that in the pursuit of ∇V, the prediction-error gradient, $\frac{\mathrm{d}\underline{\epsilon}_s^r}{\mathrm{d}\hat{\underline{\theta}}}$, becomes the actual gradient of interest when the quadratic criterion is assumed. The prediction-error gradient becomes the negative of the prediction gradient, $\boldsymbol{\Psi}^T$, deduced as follows:

$$\begin{aligned}\frac{\mathrm{d}\underline{\epsilon}_s^r[k,\hat{\underline{\theta}}]}{\mathrm{d}\hat{\underline{\theta}}} &= \frac{\mathrm{d}\underline{i}_s^r[k,\vartheta]}{\mathrm{d}\hat{\underline{\theta}}} - \frac{\mathrm{d}\hat{\underline{i}}_s^r[k,\hat{\underline{\theta}}]}{\mathrm{d}\hat{\underline{\theta}}} \\ \frac{\mathrm{d}\underline{\epsilon}_s^r[k,\hat{\underline{\theta}}]}{\mathrm{d}\hat{\underline{\theta}}} &= -\frac{\mathrm{d}\hat{\underline{i}}_s^r[k,\hat{\underline{\theta}}]}{\mathrm{d}\hat{\underline{\theta}}} = -\boldsymbol{\Psi}^T[k,\hat{\underline{\theta}}]\end{aligned} \tag{3.10}$$

$$\begin{aligned}\frac{\mathrm{d}}{\mathrm{d}\hat{\underline{\theta}}}\left(\frac{\mathrm{d}\hat{\underline{i}}_s^r(t,\hat{\underline{\theta}}))}{\mathrm{d}t}\right) &= \frac{\mathrm{d}}{\mathrm{d}t}\left(\frac{\mathrm{d}\hat{\underline{i}}_s^r(t,\hat{\underline{\theta}}))}{\mathrm{d}\hat{\underline{\theta}}}\right) \\ &= \frac{\mathrm{d}}{\mathrm{d}\hat{\underline{\theta}}}\left(\underline{f}_{-c}\left(t,\hat{\underline{i}}_s^r(t,\hat{\underline{\theta}}),\underline{u}_s^r(t),n(t);\hat{\underline{\theta}}\right)\right)\end{aligned} \tag{3.11}$$

The dynamic forms of the $\boldsymbol{\Psi}^T$ can be derived by derivation of (3.3) w.r.t. $\hat{\psi}_m$ and $\hat{r}_s$. Such derivation can be generalized as in (3.11), in which f_c is a function equivalent to the right-hand side of (3.3).

$$\frac{\mathrm{d}\left(\frac{\mathrm{d}\hat{i}_d}{\mathrm{d}\hat{\psi}_m}\right)}{\mathrm{d}t} = \frac{\omega_n}{\hat{x}_d}\left(-\hat{r}_s \cdot \frac{\mathrm{d}\hat{i}_d}{\mathrm{d}\hat{\psi}_m} + \hat{x}_q \cdot n \cdot \frac{\mathrm{d}\hat{i}_q}{\mathrm{d}\hat{\psi}_m}\right) \tag{3.12a}$$

$$\frac{\mathrm{d}\left(\frac{\mathrm{d}\hat{i}_q}{\mathrm{d}\hat{\psi}_m}\right)}{\mathrm{d}t} = \frac{\omega_n}{\hat{x}_q}\left(-\hat{r}_s \cdot \frac{\mathrm{d}\hat{i}_q}{\mathrm{d}\hat{\psi}_m} - \hat{x}_d \cdot n \cdot \frac{\mathrm{d}\hat{i}_d}{\mathrm{d}\hat{\psi}_m} - n\right) \tag{3.12b}$$

$$\frac{\mathrm{d}\left(\frac{\mathrm{d}\hat{i}_d}{\mathrm{d}\hat{r}_s}\right)}{\mathrm{d}t} = \frac{\omega_n}{\hat{x}_d}\left(-\hat{r}_s \cdot \frac{\mathrm{d}\hat{i}_d}{\mathrm{d}\hat{r}_s} + n \cdot \hat{x}_q \cdot \frac{\mathrm{d}\hat{i}_q}{\mathrm{d}\hat{r}_s} - \hat{i}_d\right) \tag{3.13a}$$

$$\frac{\mathrm{d}\left(\frac{\mathrm{d}\hat{i}_q}{\mathrm{d}\hat{r}_s}\right)}{\mathrm{d}t} = \frac{\omega_n}{\hat{x}_q}\left(-\hat{r}_s \cdot \frac{\mathrm{d}\hat{i}_q}{\mathrm{d}\hat{r}_s} - \hat{x}_d \cdot n \cdot \frac{\mathrm{d}\hat{i}_d}{\mathrm{d}\hat{r}_s} - \hat{i}_q\right) \tag{3.13b}$$

By solving (3.11), one can arrive at the respective gradient functions as shown in (3.12) and (3.13) The detailed derivations are presented in Appendix A.2. The dynamic forms of the prediction gradients w.r.t. $\hat{x}_d, \hat{x}_q$ can be presented as follows:

$$\frac{\mathrm{d}\left(\frac{\mathrm{d}\hat{i}_d}{\mathrm{d}\hat{x}_d}\right)}{\mathrm{d}t} = \frac{\omega_n}{\hat{x}_d}\left(-\hat{r}_s \cdot \frac{\mathrm{d}\hat{i}_d}{\mathrm{d}\hat{x}_d} + \hat{x}_q \cdot n \cdot \frac{\mathrm{d}\hat{i}_q}{\mathrm{d}\hat{x}_d} + \frac{\hat{r}_s}{\hat{x}_d} \cdot \hat{i}_d - \frac{\hat{x}_q \cdot n}{\hat{x}_d} \cdot \hat{i}_q - \frac{u_d}{\hat{x}_d}\right) \tag{3.14a}$$

$$\frac{\mathrm{d}\left(\frac{\mathrm{d}\hat{i}_q}{\mathrm{d}\hat{x}_d}\right)}{\mathrm{d}t} = \frac{\omega_n}{\hat{x}_q}\left(-\hat{r}_s \cdot \frac{\mathrm{d}\hat{i}_q}{\mathrm{d}\hat{x}_d} - \hat{x}_d \cdot n \cdot \frac{\mathrm{d}\hat{i}_d}{\mathrm{d}\hat{x}_d} - n \cdot \hat{i}_d\right) \tag{3.14b}$$

$$\frac{\mathrm{d}\left(\frac{\mathrm{d}\hat{i}_d}{\mathrm{d}\hat{x}_q}\right)}{\mathrm{d}t} = \frac{\omega_n}{\hat{x}_d}\left(-\hat{r}_s \cdot \frac{\mathrm{d}\hat{i}_d}{\mathrm{d}\hat{x}_q} + n \cdot \hat{x}_q \cdot \frac{\mathrm{d}\hat{i}_q}{\mathrm{d}\hat{x}_q} + n \cdot \hat{i}_q\right) \tag{3.15a}$$

$$\frac{\mathrm{d}\left(\frac{\mathrm{d}\hat{i}_q}{\mathrm{d}\hat{x}_q}\right)}{\mathrm{d}t} = \frac{\omega_n}{\hat{x}_q}\left(-\hat{r}_s \cdot \frac{\mathrm{d}\hat{i}_q}{\mathrm{d}\hat{x}_q} - \hat{x}_d \cdot n \cdot \frac{\mathrm{d}\hat{i}_d}{\mathrm{d}\hat{x}_q} + \frac{\hat{r}_s}{\hat{x}_q} \cdot \hat{i}_q - \frac{\hat{x}_d \cdot n}{\hat{x}_q} \cdot \hat{i}_d - \frac{u_q}{\hat{x}_q}\right) \tag{3.15b}$$

The above dynamic forms of $\boldsymbol{\Psi}^T$ share the same eigenvalues with $\mathscr{M}_{u\theta}$, and thus the concerns regarding the digital implementation discussed in the section 3.3.1 apply

to these as well. The corresponding steady-state $\boldsymbol{\Psi}^T$ forms can be derived by equalizing the the left-hand side of each of the above equations to zero. The final derivations are given in (3.16) and (3.17) w.r.t. $\hat{\psi}_m$ and $\hat{r}_s$, which can, in fact, be obtained by partially deriving (3.9) w.r.t. each parameter estimate. The steady-state $\boldsymbol{\Psi}^T$-functions are plotted in Figure 3.5.

$$\begin{aligned}
\frac{\mathrm{d}\hat{i}_d}{\mathrm{d}\hat{\psi}_m} &= -\frac{n^2 \cdot x_q}{\hat{r}_s^2 + n^2 \cdot x_q \cdot x_d} \\
\frac{\mathrm{d}\hat{i}_q}{\mathrm{d}\hat{\psi}_m} &= -\frac{n \cdot \hat{r}_s}{\hat{r}_s^2 + n^2 \cdot x_q \cdot x_d}
\end{aligned} \tag{3.16}$$

$$\begin{aligned}
\frac{\mathrm{d}\hat{i}_d}{\mathrm{d}\hat{r}_s} &= -\frac{\hat{r}_s \cdot \hat{i}_d}{\hat{r}_s^2 + n^2 \cdot x_q \cdot x_d} - \frac{n \cdot x_q \cdot \hat{i}_q}{\hat{r}_s^2 + n^2 \cdot x_q \cdot x_d} \\
\frac{\mathrm{d}\hat{i}_q}{\mathrm{d}\hat{r}_s} &= -\frac{\hat{r}_s \cdot \hat{i}_q}{\hat{r}_s^2 + n^2 \cdot x_q \cdot x_d} + \frac{n \cdot x_d \cdot \hat{i}_d}{\hat{r}_s^2 + n^2 \cdot x_q \cdot x_d}
\end{aligned} \tag{3.17}$$

Based on the steady-state functions and corresponding plots, the following remarks can be made:

Remark 1: $\boldsymbol{\Psi}^T$-steady state forms hold the same shapes as their respective ϵ-plots given in Figure 3.4. Their relationship can be explained by (3.10). However, unlike ϵ, $\boldsymbol{\Psi}^T$ is independent from $\delta\psi_m$ and δr_s.

Remark 2: $\boldsymbol{\Psi}^T$ w.r.t. $\hat{\psi}_m$ is excited by n. See (3.16). In observing the low derivative due to the inertia, the n-excitation can be assumed to be quite slow, and thus, in computation of $\boldsymbol{L}$ for $\hat{\psi}_m$ identification, the use of steady-state form of $\boldsymbol{\Psi}^T$ given in (3.16) will be adequate [33].

Remark 3: $\boldsymbol{\Psi}^T$ w.r.t. $\hat{r}_s$ is excited by both n and $\underline{\hat{i}}_s^r$. See (3.17). The dynamic counterparts of $\boldsymbol{\Psi}^T$ in (3.13) can offer some sort of a filtering effect in the computed $\boldsymbol{L}$ owing to the $\hat{T}_d, \hat{T}_q$, while yielding faster adaptation. However, to avoid oscillations in the gain, the steady-state forms can be used instead [33].

Now that the $\boldsymbol{\Psi}^T$-functions have been developed, what remains is the choice of the $\boldsymbol{\Psi}^T$-based algorithm. Three algorithms become relevant in this context, namely 1) stochastic gradient, 2) Gauss-Newton, and 3) physically interpretative method, which will be discussed next. The choice of the algorithm is determined by the rate of convergence and the asymptotic accuracy they offer and at which cost of computational tediousness. Note that Λ is omitted from the respective expressions due to the same basis associated with (3.7).

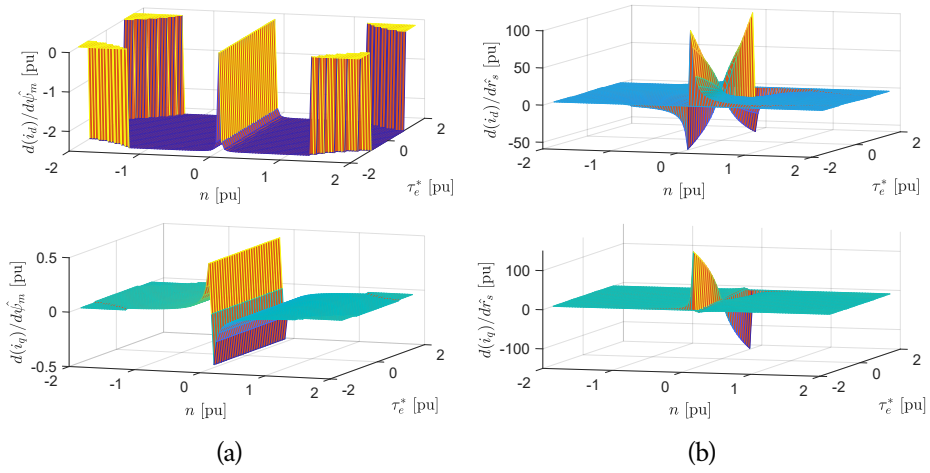

FIGURE 3.5. Prediction Gradient in steady-state in four-quadrant speed-torque plane w.r.t. (a) $\hat{\psi}_m$ (b) $\hat{r}_s$.

Stochastic Gradient Algorithm

$$\underline{\hat{\theta}}[k] = \underline{\hat{\theta}}[k-1] + \mathbf{L}[k] \cdot \underline{\epsilon}_s^r[k], \quad \mathbf{L}[k] = \gamma[k] \frac{1}{r[k]} \boldsymbol{\Psi}[k] \tag{3.18a}$$

$$r[k] = r[k-1] + \gamma[k] \left(tr \left\{ \boldsymbol{\Psi}[k] \cdot \boldsymbol{\Psi}^T[k] \right\} - r[k-1] \right) \tag{3.18b}$$

$r[k]$, in steady-state, appears as follows:

$$tr \left\{ \boldsymbol{\Psi}[k] \boldsymbol{\Psi}^T[k] \right\} = \left(\frac{\mathrm{d}\hat{i}_d}{\mathrm{d}\hat{\psi}_m} \right)^2 + \left(\frac{\mathrm{d}\hat{i}_q}{\mathrm{d}\hat{\psi}_m} \right)^2 + \left(\frac{\mathrm{d}\hat{i}_d}{\mathrm{d}\hat{r}_s} \right)^2 + \left(\frac{\mathrm{d}\hat{i}_q}{\mathrm{d}\hat{r}_s} \right)^2 \tag{3.19}$$

This is a rather simple $\boldsymbol{L}$-computation method given in (3.18a) from [13]. The algorithm adopts a first-order approximation, i.e., $\boldsymbol{\Psi}^T$, to identify the search direction with gains $\gamma[k]$ (introduced later) and $r[k]$, the scalar variant of Hessian Function. Thus, in effect, the Stochastic Gradient can be viewed as a modification to the classical gradient descent method. Close inspection of (3.18b) indicates that $r[k]$ is a first-order filtered version of the traces, (*tr*). Such filtering becomes useful, particularly when dynamic variants of $\boldsymbol{\Psi}^T$ are applied in computing the *tr*, to prevent undesirable fluctuations in the estimates. Another use with such filtered $r[k]$ is the ability to amplify the estimation gains at the start of adaptation, by selecting smaller initial values.

Gauss-Newton Algorithm

This is, unlike the previous method, a second-order iterative minimization technique, which minimizes the criterion function more efficiently, particularly in the vicinity

of the minimum. This algorithm from [13], after simplifying for the same reason associated with V_N, becomes as follows:

$$\underline{\hat{\theta}}[k] = \underline{\hat{\theta}}[k-1] + \mathbf{L}[k] \cdot \underline{\epsilon}_s^r[k],\ \mathbf{L}[k] = \gamma[k]\mathbf{R}^{-1}[k]\boldsymbol{\Psi}[k] \tag{3.20a}$$

$$\mathbf{R}[k] = \mathbf{R}[k-1] + \gamma[k]\Big(\boldsymbol{\Psi}[k] \cdot \boldsymbol{\Psi}^T[k] - \mathbf{R}[k-1]\Big) \tag{3.20b}$$

Here, the vector form of Hessian, $\boldsymbol{R}[k]$, is employed. In steady-state, $\boldsymbol{R}[k] = \boldsymbol{\Psi}[k] \cdot \boldsymbol{\Psi}^T[k]$, where the elements of $\boldsymbol{R}[k]$ become as in:

$$\mathbf{R}=\begin{bmatrix} \Psi_{11}^2 + \Psi_{12}^2 & \Psi_{11} \cdot \Psi_{21} + \Psi_{12} \cdot \Psi_{22} \\ \Psi_{11} \cdot \Psi_{21} + \Psi_{12} \cdot \Psi_{22} & \Psi_{21}^2 + \Psi_{22}^2 \end{bmatrix} \tag{3.21}$$

Owning to the relatively small order of the Hessian, computation of its inverse matrix can be made convenient as follows, by adopting an algebraic manipulation:

$$R^{-1} = \frac{1}{|\mathbf{R}|}\begin{bmatrix} R_{22} & -R_{12} \\ -R_{21} & R_{11} \end{bmatrix}$$

$$|\mathbf{R}| = \Psi_{11}^2\Psi_{22}^2 + \Psi_{12}^2\Psi_{21}^2 - 2 \cdot \Psi_{11}\Psi_{12}\Psi_{21}\Psi_{22} \tag{3.22}$$

In general, Hessian is a function of prediction gradients, and it is independent from $\underline{\epsilon}_s^r$. At zero-speed, $|\boldsymbol{R}|$ becomes zero and so are the elements of $\boldsymbol{R}$ except R_{22}, and thus the inverse yields zero-divided-by-zero scenarios in three of its elements. To tackle the challenge with a non-existent inverse matrix due to these singularities at zero-speed, a mathematical method called Moore-Penrose pseudoinverse (MPP) is applied to find a pseudoinverse matrix that has most of the properties of $\boldsymbol{R}^{-1}$[28]. To compare with SGA, the scalar- and the determinant of the matrix- Hessians, which are the denominators of the SGA and GNA, are plotted in the speed-torque plane in Figure 3.6. In connection to the GNA formulae and Figure 3.6, the following remarks can be made:

Remark 1: Both denominators hold similar shapes except at and around zero speed and torque. Despite the similarity in shape, $|\boldsymbol{R}|$ is several times smaller by up to ten times at most at lower speeds, to facilitate faster adaptation with GNA in the lower speed and torque region.

Remark 2: At and around zero speed, $r = \psi_{21}^2 + \psi_{22}^2$, which is its peak. Conversely, $|\boldsymbol{R}|$ holds very low values (theoretically zero, but in practice, limited to very low values) to create a cleavage between the peak wedges. In summary, $|\boldsymbol{R}|$ is expected to offer a larger boost in gain-computation in the lower speed/torque region.

$$\boldsymbol{L}[k] = \frac{\gamma[k]}{|\mathbf{R}|}\begin{bmatrix} \psi_{11}R_{22} - \psi_{21}R_{12} & \psi_{12}R_{22} - \psi_{22}R_{12} \\ \psi_{21}R_{11} - \psi_{11}R_{12} & \psi_{22}R_{11} - \psi_{12}R_{12} \end{bmatrix} \tag{3.23}$$

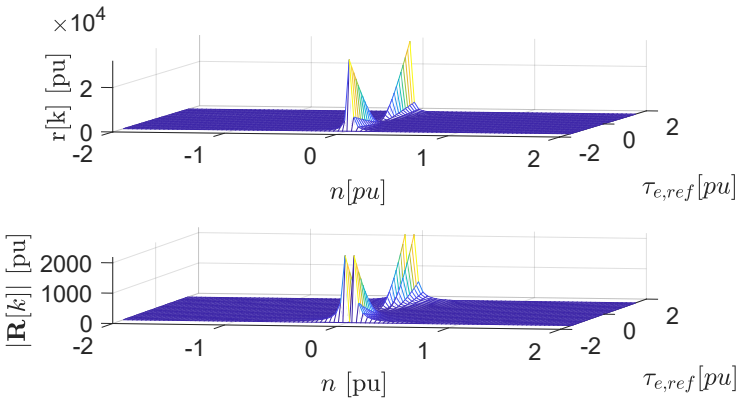

FIGURE 3.6. Scalar Hessian, r and the determinant of Matrix Hessian, $|\boldsymbol{R}|$ in four-quadrant speed-torque plane.

From inspection of (3.23), all the elements in the $\boldsymbol{L}$ become zero at standstill. This does not influence the $\hat{\psi}_m$- adaptation as the $\underline{\epsilon}_s^r$ does not carry respective information anyway. However, $\underline{\epsilon}_s^r$ does carry information about δr_s at zero speed (if $\underline{i}_s^r \neq 0$), thus forcing L_{21}, L_{22} to null at this point, prevents possible $\hat{r}_s$-adaptation at standstill. This phenomenon indicates an inherent drawback in the implementation of GNA in comparison to SGA.

Physically interpretative method

In this method, the estimation-gains are attempted to obtain by physically interpreting the steady-state behaviour of $\underline{\epsilon}_s^r$ in (3.9), s.t. $\boldsymbol{L} \cdot \epsilon \approx \delta\theta$. Author capitalizes the physical interpretations in *Remark 2* and *Remark 5* in section 3.3.3 to identify the estimation-gains. Accordingly, $\hat{\psi}_m$ estimation-gain becomes:

$$L_{11}[k] = -\gamma[k] \cdot \hat{x}_d, \qquad \hat{\psi}_m[k] = \hat{\psi}_m[k-1] + L_{11}[k] \cdot \epsilon_d[k] \tag{3.24}$$

Similarly, the estimation gains for $\hat{r}_s$-estimation become as follows:

$$\begin{aligned} L_{21} &= \gamma[k] \left(\frac{\hat{r}_s^2 + n^2 \cdot \hat{x}_d \cdot \hat{x}_q}{-\hat{r}_s \cdot \hat{i}_d - n \cdot \hat{x}_q \cdot \hat{i}_q} \right) \\ L_{22} &= \gamma[k] \left(\frac{\hat{r}_s^2 + n^2 \cdot \hat{x}_d \cdot \hat{x}_q}{-\hat{r}_s \cdot \hat{i}_q + n \cdot \hat{x}_d \cdot \hat{i}_d} \right), \qquad \underline{\hat{i}}_s[k] \neq 0 \\ \hat{r}_s[k] &= \hat{r}_s[k-1] + L_{21}[k] \cdot \epsilon_d[k] + L_{22}[k] \cdot \epsilon_q[k] \end{aligned} \tag{3.25}$$

Close inspection of (3.24) and (3.25) will reveal that L_{11}, L_{21}, and L_{22} are nothing but the estimation gains obtained from SGA in steady-state, when only the prediction gradient of concern is applied in the respective Hessian formulation. When digital implementation is concerned, SGA, GNA, and PhyInt require a minimum value for

their denominators (r, $|\boldsymbol{R}|$, or $\hat{\underline{i}}_s$) at the very low torque/speed region, to avoid large $\boldsymbol{L}$, and thus to prevent noise amplification.

3.3.5 Choice of Gain Sequence and Initial Values

Gain-sequence, γ can be viewed as a memory-coefficient. It can also be viewed as integral- or filter-time constant. Larger γ enables faster tracking by 'forgetting' the older ϵ in preference to the more recent ones however, at the expense of increased noise sensitivity. In the context of tracking slowly varying parameters, it is shown in [13] that $\gamma[k]$ is often chosen to be a constant, γ_0, which can be expressed as follows;

$$\hat{\underline{\theta}}[k] = \hat{\underline{\theta}}[k-1] + \frac{T_{samp}}{T_0} \cdot \boldsymbol{\Psi}[k] \cdot \underline{\epsilon}[k], \quad \gamma_0 = \frac{T_{samp}}{T_0} \tag{3.26}$$

Thus, γ_0 is nothing but an integral time constant, in which, T_0 is, in fact, the chosen variable. T_0 should be chosen such that the estimated parameters are almost constant over a period of length T_0. When temperature-sensitive parameters are concerned, T_0 could be in the range of a few seconds such that it still produces a fast enough algorithm to track slow-varying parameters, yet not too fast to prevent being sensitive to noise.

Having accurate initial values can circumvent a fundamental challenge with the gradient-based minimization algorithms that can be mislead by local minima. By using offline methods and identification runs during the commissioning, initial machine parameters can be identified accurately.

3.4 Gain-Scheduling Scheme

In this section, the impact of the simultaneous adaptation that demonstrates the requirement of having a decoupling mechanism will be analyzed. Subsequently, the implementation of the gain-scheduling scheme is disclosed.

3.4.1 Impact of Simultaneous Adaptation

The possibility of simultaneous adaptation can be favorable in many ways. However, it was emerged in the *Remark 5* in section 3.3.3, the sensitivity of $\underline{\epsilon}$, hence $\boldsymbol{\Psi}^T$ w.r.t. $\hat{\psi}_m$ and $\hat{r}_s$ is prominent in exclusive speed regions. This suggests that the $\hat{\psi}_m$-adaptation will be successful mostly beyond very low speeds, whereas $\hat{r}_s$-adaptation will be successful during very low speeds. These sensitivities are illustrated in Figure 3.9, in which it is seen that there are also overlapping regions. As such, it is interesting to examine how an error in one parameter influences the other when the rotor speed is in a speed zone where the erroneous parameter is less sensitive, but the other is more sensitive.

The influence from δr_s on the $\hat{\psi}_m$ is investigated first. Due to the influence from the q-component on $\hat{\psi}_m$-adaptation is negligible, the analysis is performed only in

relation to the d-component. Accordingly, from (3.9), an expression as below can be derived to express unfairly adapted $\hat{\psi}_m$ in steady-state due to δr_s, by setting $\epsilon_d = 0$:

$$\hat{\psi}_m = \psi_m + \frac{\left(\hat{r}_s \cdot i_d + n \cdot \hat{x}_q \cdot i_q\right)}{n^2 \cdot \hat{x}_q} \cdot \delta r_s \approx \psi_m + \frac{i_q}{n} \cdot \delta r_s \tag{3.27}$$

It's worth noting that in a typical IPMSM, $\psi_m \gg r_s$, $r_s \ll 1$ in pu. In this context, the expression says that the impact of δr_s becomes significant only when $n \ll 1$, given that the stator current is present. To eliminate this undue impact during very low speeds, a requirement to halt the $\hat{\psi}_m$-adaptation may arise in this speed region.

Similarly, the influence from $\delta\psi_m$ on the $\hat{r}_s$ can be analyzed. Unlike the previous discussion, here it should be considered the influence from both ϵ_d, ϵ_q, thus two expressions as follows can be derived from (3.9):

$$\begin{aligned} \hat{r}_s &= r_s + \frac{n^2 \cdot \hat{x}_q}{\left(\hat{r}_s \cdot i_d + n \cdot \hat{x}_q \cdot i_q\right)} \cdot \delta\psi_m \\ \hat{r}_s &= r_s + \frac{n \cdot \hat{r}_s}{\left(n \cdot \hat{x}_q \cdot i_d - \hat{r}_s \cdot i_q\right)} \cdot \delta\psi_m \end{aligned} \tag{3.28}$$

In view of $\psi_m \gg r_s$ and $r_s \ll 1$, these expressions reveal that as the rotor speed increases, the impact from $\delta\psi_m$ dramatically increases to unduly adapt $\hat{r}_s$, and thus it signifies a mandatory requirement to cut-off the $\hat{r}_s$-adaptation beyond very low speeds.

3.4.2 *Impact of Hessian Choices*

The choice of Hessian function, $r[k]$, in formulating the respective SGA can have an impact in tracking behaviours, particularly during simultaneous adaptation. Because $r[k]$ is in the denominator in L-computation, its magnitude can determine the parameter tracking speed. One can choose the full trace [13] or only the relevant prediction gradient(s) in computing $r[k]$. Thus, in steady-state, $r[k]$ can be computed with either of the following options:

$$r_n[k] = \psi_{11}^2 + \psi_{12}^2 + \psi_{21}^2 + \psi_{22}^2 \tag{3.29a}$$
$$r_{\psi m}[k] = \psi_{11}^2 + \psi_{12}^2 \tag{3.29b}$$
$$r_{rs}[k] = \psi_{21}^2 + \psi_{22}^2 \tag{3.29c}$$
$$r_{rd}[k] = \psi_{21}^2 \tag{3.29d}$$
$$r_{rq}[k] = \psi_{22}^2 \tag{3.29e}$$

To assess their behaviours, each of the traces in (3.29) are plotted in Figure 3.7 and Figure 3.8. The former shows that, when the full trace is chosen, $r[k]$ can be quite high around standstill to yield high damping of the online estimations. This choice can become problematic with regard to $\hat{\psi}_m$-adaptation, because, during the same speed

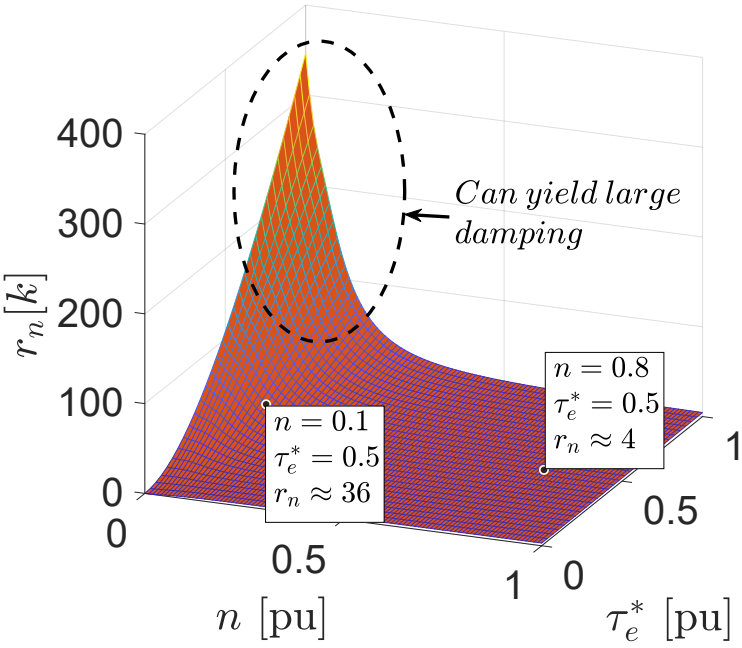

Figure 3.7. $r_n[k]$ behaviour in the torque-speed plane.

region, its prediction gradients are quite weak, that will result in very small estimation gains, to render very slow tracking. Thus, a much smaller $r[k]$ can be suitable for $\hat{\psi}_m$-adaptation, which can be achievable with $r_{\psi m}$ as seen in Figure 3.8(a), subplot-1. In contrast to the previous case, with $r_{\psi m}$ as the denominator, L_{11} can be many folds larger at lower speeds. Both these Hessians, however, become comparable beyond low speeds, owing to the rapid decay in $\psi_{21,22}$. Nevertheless, one drawback with $r_{\psi m}$ is that it becomes very low and eventually zero at the rotor standstill. Very small denominator can amplify noise, and division by zero is prohibited. Therefore, when using $r_{\psi m}$, the denominator must be limited around zero-speed.

Figure 3.8(a), subplot-2 shows the r_{rs} behaviour. This is comparable to r_n, particularly in the lower speed region, because, at the same speeds, $\psi_{21,22}$ are the dominant elements in the full trace. As an alternative to r_{rs}, one can choose either r_{rd} or r_{rq} (See Figure 3.8(b)) as the Hessians for L_{21} and L_{22} computations, respectively. It is however, interesting to note that r_{rd} contains a dip to yield $r[k] = 0$ at $n = 0.01$ pu. Therefore, its application demands caution, to prevent zero division events and noise amplification. In general, the Hessians can be useful in adjusting the convergence speeds, particularly during simultaneous adaptation of both $\hat{\psi}_m$ and $\hat{r}_s$, which is further investigated in section 4.4.3 with the aid of real-time simulation.

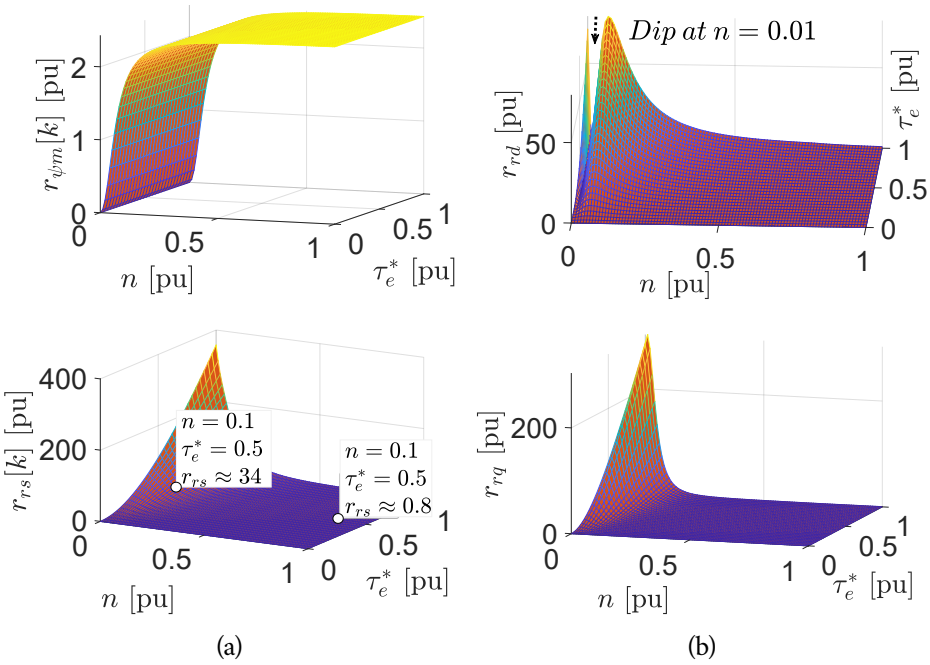

FIGURE 3.8. Behaviours of different choices for Hessians: (a) subplot-1 $r_{\psi m}$, subplot-2 r_{rs} (b) subplot-1 r_{rd}, subplot-2 r_{rq}.

3.4.3 Gain-Scheduler

Based on the requirements identified, a simple gain-scheduler is proposed to limit the respective adaptations to their own sensitive speed zones as shown in the Figure 3.9. Such zonal adaptation can provide reasonable adaptations of $\hat{\psi}_m$ and $\hat{r}_s$ in their respective sensitive speed-zones. Thus, the respective gains are scheduled as given below, where $x = 1, 2$ and $|n_{lim,1}| > |n_{lim,2}|$:

$$L_{1,x} = \begin{cases} L_{1,x}, |n| > |n_{lim,1}| \\ 0, \ otherwise \end{cases}, \qquad L_{2,x} = \begin{cases} L_{2,x}, |n| < |n_{lim,2}| \\ 0, \ otherwise \end{cases} \tag{3.30}$$

Chapter 4 introduces a modification to this gain-scheduler, that assists simultaneous adaptation during Zone-$\hat{r}_s$. More advanced gain-scheduling schemes may also be developed, for example, by adopting speed-dependent γ_0, that can facilitate simultaneous adaptation.

3.5 REAL-TIME SIMULATION-BASED VALIDATION

In this section, attempts are made to make a choice among the three $\mathbf{\Psi}^T$-based algorithms with the aid of a Xilinx Zynq System on Chip-based ERTS. $\hat{\psi}_m$ and $\hat{r}_s$ are

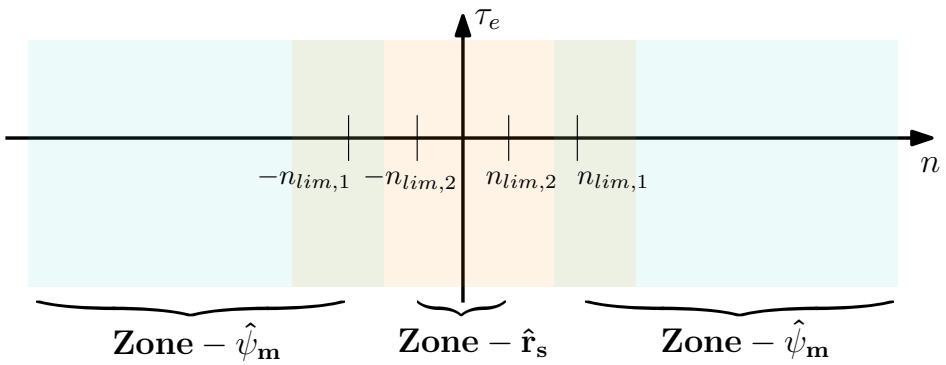

Figure 3.9. Illustration of a simple zonal adaptation of $\hat{r}_s$ and $\hat{\psi}_m$ implemented using the gain-scheduling scheme.

identified online when the respective physical values undergo a step-change of -8%. The model inductances are updated online using the offline identified values, and thus it is assumed that there is no discrepancy between the model and physical counterparts. A step-change in motor parameters allows us to assess the stability and the tracking speed of the proposed method, despite it being unusual for temperature-sensitive parameters. The overview of the ERTS is illustrated in Figure 3.10. The power hardware components of the drive are programmed in the Field-Programmable Gate Array (FPGA) fabric of the SoC to achieve real-time emulation at a time-step of 1 μs. The control, state-, and parameter-estimation algorithms, and likewise relatively slower processes are programmed in the on-chip processor at the PWM double-update time-step of 125 μs. The design details and the validation of this ERTS against the Matlab/Simulink-based offline simulation are given in [34] and Chapter 5. Two-level VSI with asymmetrical modulation and 3$^{\text{rd}}$ harmonic injection is used to drive the machine. A speed-dependent gain-scheduler is applied to restrain the $\hat{r}_s$-adaptation between -10 to 10 rpm and $\hat{\psi}_m$-adaptation beyond |100| rpm. Table 3.1 tabulates the experimental plant data.

The respective gain-sequence values for $\hat{\psi}_m$ and $\hat{r}_s$ -adaptation using SGA, GNA, and PhyInt are tabulated in Table 3.2. These values are chosen in order to demonstrate comparable, yet sufficiently rapid tracking performances among these algorithms.

Table 3.2. Gain-sequences for online estimation.

Symbol	Parameter	γ_0[pu] SGA, PhyInt	γ_0[pu] GNA
	For $\hat{\psi}_m$-estimation		
$\gamma_{0,rk}$	Gain-sequence for Hessian	6.25×10^{-4}	6.25×10^{-4}
$\gamma_{0,Lk}$	Gain-sequence for Gain	3.25×10^{-4}	3.25×10^{-4}
	For $\hat{r}_s$-estimation		
$\gamma_{0,rk}$	Gain-sequence for Hessian	6.25×10^{-4}	6.25×10^{-5}
$\gamma_{0,Lk}$	Gain-sequence for Gain	6.25×10^{-5}	7.5×10^{-6}

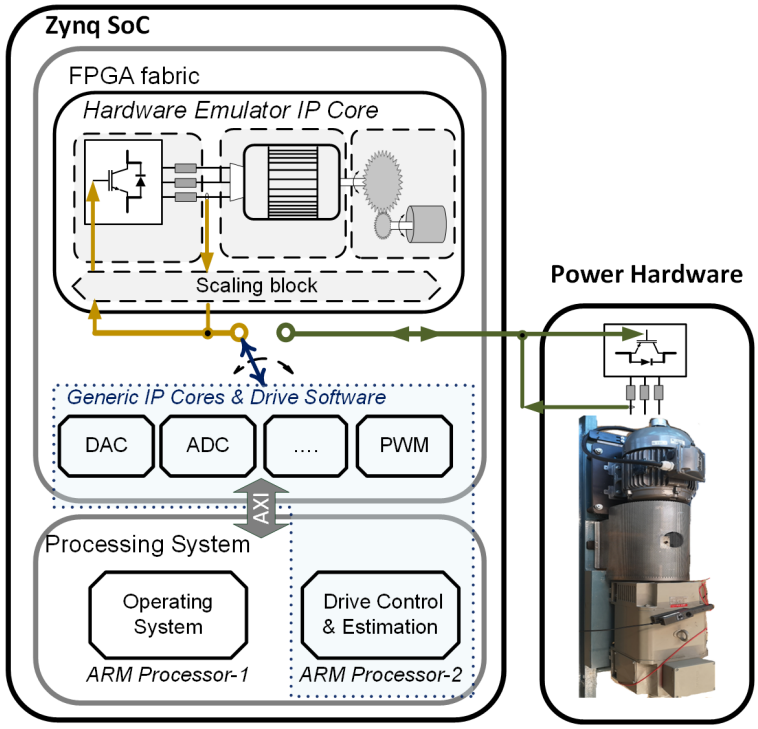

FIGURE 3.10. Overview of the Embedded Real-Time Simulator designed for simulation and implementation of three-phase IPMSM Drive.

3.5.1 *Steady-State vs. Dynamic-State Prediction Gradients*

This section investigates the behaviors of steady-state and dynamic-state variants of the prediction gradients. ψ_{11}, i.e., corresponding to $\hat{\psi}_m$ is chosen as an example and Figure 3.11 presents these behaviors. It is evident that the dynamic variant contains oscillations and eventually converges with its steady-state counterpart. Adoption of the dynamic variant can induce these oscillations in the respective estimation gains, which can lead to oscillatory tracking in the model parameter. On the other hand, the averages of both these variants appear to be the same, and therefore, there is no particular favor in selecting one or the other when boosting is concerned. Consequently, to avoid potential oscillations, steady-state forms of the $\boldsymbol{\Psi}^T$ are, thus, adopted to formulate the RPEM algorithms and corresponding Hessians. are used where applicable [33].

3.5.2 *Algorithms Comparison for Online Tracking*

Figure 3.12 contains ψ_m online tracking trajectories overlaid when the three algorithms are adopted at different speeds and loads. Figure 3.12 (a) and (b) are when the rotor

Table 3.1. Parameters of the Experimental Plant.

Symbol	Parameter	Value
U_n	IPMSM rated voltage	400 V
I_n	IPMSM rated current	4.93 A
P_n	IPMSM rated power	3 kW
N_n	IPMSM rated speed	1000 rpm
T_n	IPMSM rated torque	32.6 Nm
p	IPMSM number of pole-pairs	3
R_s	Stator resistance (offline)	2.25 Ω
Ψ_m	Permanent magnet flux linkage (offline)	1.14 Wb
L_d	IPMSM d-axis inductance (rated load)	0.0953 H
L_q	IPMSM q-axis inductance (rated load)	0.206 H
U_{dc}	DC bus voltage	220 V
f_{sw}	Power device switching frequency	4 kHz
T_{samp}	Sampling period	125 μs

Table 3.3. Processor execution times of the different algorithms.

Algorithm	Execution Time (μs)
SGA	~5.2
GNA	~5.6
PhyInt	~5.0

speeds are negative. In case (a), the load-torque τ_{el} is zero and in (b), τ_{el} = 0.2, meaning the machine will be in generating mode. Under these conditions, both SGA and PhyInt yield stable and noise-free tracking. GNA, too, succeeds in convergence but seems to be overly excited along the way. At low loads, the $\mathbf{R}-$elements in (3.22) become very small, which can excessively boost $\mathbf{L}$. This effect is what causes the oscillations in the GNA-trajectories in (a) and (b). At higher loads, as in Figure 3.12 (c) and (d), GNA yields smoother adaptation like the SGA and PhyInt.

Similarly, the R_s-adaptation related to the three algorithms is presented in Figure 3.13. In this case, to achieve stable tracking with GNA, γ_0 needed to be made nearly one-tenth of that for SGA or PhyInt. This hinders the GNA-tracking speed as it is made evident in all cases. PhyInt, on the other hand, while offering noise-free tracking, has a significantly lower convergence speed in comparison to SGA.

In general, SGA and PhyInt consistently display stable adaptations. These two algorithms become the same in steady-state if $r[k]$ in the SGA is computed using only the respective prediction gradient instead of the full trace, i.e., given in (3.19). One advantage of SGA over PhyInt is the ability to use the dynamic/filtered $r[k]$ (3.18b) which allows initialization and the choice of γ_{rk}, that can determine the magnitude and length of adaptation-boosting. This facilitates faster and filtered estimations, particularly at the start of the routines. In comparison to the execution times of the three algorithms, there is very little to differentiate between the algorithms, as one can see in Table 3.3, owing to the powerful floating-point processor in the SoC. The computational burden posed by GNA can, however, be increased when the rank of $\mathbf{L}$ increases, which will involve the demanding task of real-time matrix inversion.

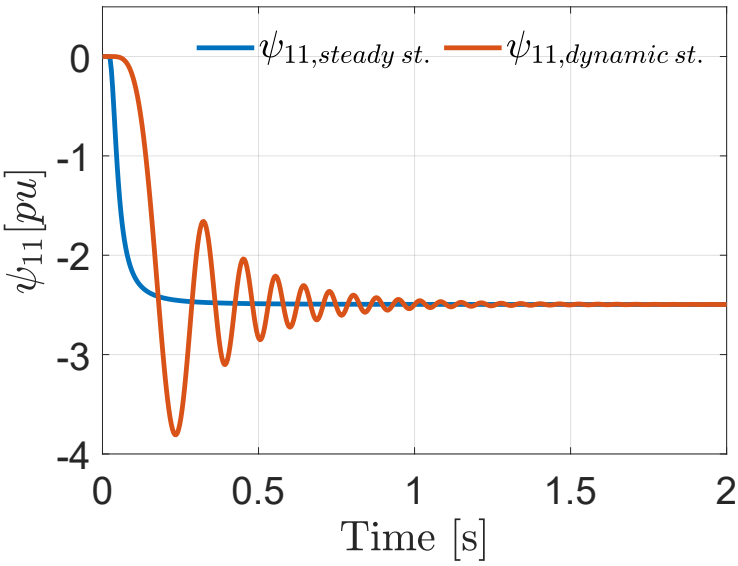

Figure 3.11. Comparison of steady-state vs. dynamic-state variants of ψ_{11}.

3.6 Experimental Validation

Here, the $\mathbf{\Psi}^T$-based RPEM algorithms for parameter identification are attempted to validate using an experimental setup shown in Figure 3.14 of which the data is given in Table 3.1. It was evident in the previous section that PhyInt can be viewed as a less flexible variant of SGA, thus, it will be omitted in this experimental validation. The same digital controller that houses the ERTS is used to control the motor drive setup. The γ_0-values tabulated in Table 3.2 are applied here. The gain-scheduling scheme proposed in 3.4.3 is applied and herein, it is assumed only one model parameter is erroneous at a time, to demonstrate the concept. Simultaneous parametric errors and adaptations are discussed in Chapter 4.

3.6.1 Ψ_m-Tracking Validation

During the experiments, it was identified that the dynamic forms of the ψ_{21} and ψ_{22} cause to superimpose the current-sensor noise in the GNA-based tracking trajectories, particularly at the event of no-load. This could have been mitigated by using a much smaller $\gamma_{0,Lk}$ for GNA than what is tabulated in Table 3.2, however at the price of slower convergence. Also, these oscillations disappear as soon as the IPMSM is loaded. Instead, in order to achieve a comparable convergence speed, the steady-state forms of ψ_{11} and ψ_{12} are chosen in both SGA and GNA computations. The performance of the online adaptation of $\hat{\psi}_m$ using these algorithms at various rotor speeds and

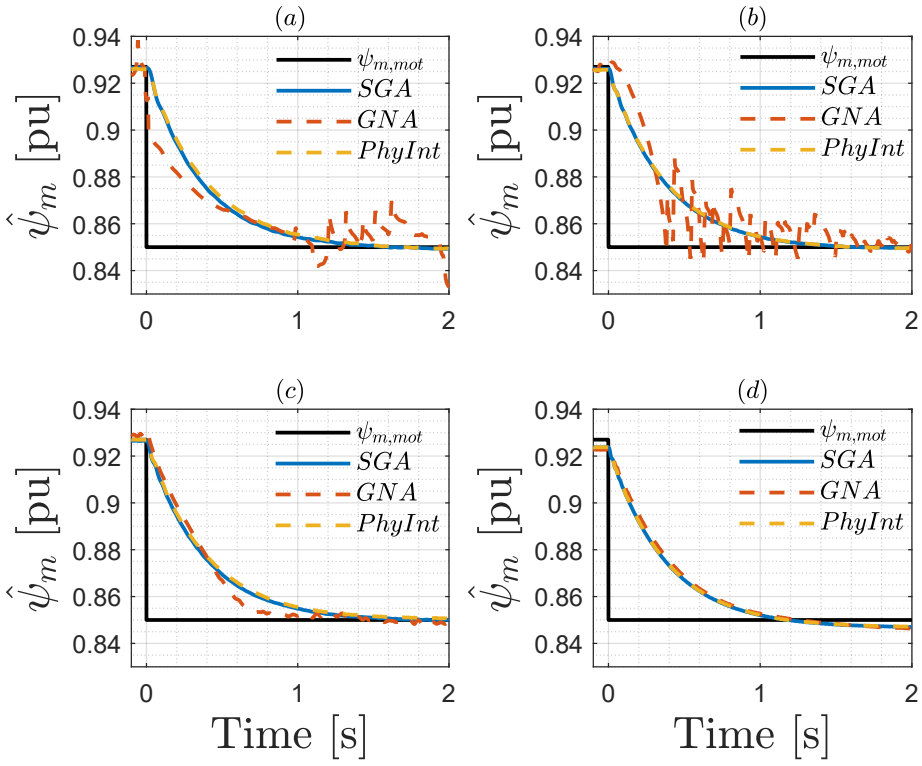

FIGURE 3.12. $\hat{\psi}_m$ online adaption with SGA, GNA, and PhyInt (a) $n = -0.2\ pu$, $\tau_{el} = 0\ pu$ (b) $n = -0.4\ pu$, $\tau_{el} = 0.2\ pu$ (c) $n = 0.4\ pu$, $\tau_{el} = 0.2\ pu$ (d) $n = 0.8\ pu$, $\tau_{el} = 0.4\ pu$.

load torques are plotted in Figure 3.15. The reference (Ref) in the plot is the offline identified $\psi_m = 0.895\ pu$. The no-load adaptation with GNA is slightly quicker than that with the SGA, at the price of a 6% overshoot, as per Figure 3.15(a). When the IPMSM is loaded with 0.4 pu load-torque, the adaptation between the algorithms is nearly identical as seen in Figure 3.15(b). Irrespective of the load, at the given speed, the convergence occurs within 2 seconds, which is sufficient for a temperature-induced ψ_m-variation.

Figure 3.15(c) and (d) show how the $\hat{\psi}_m$ behaves upon a step-change in the speed reference and load-torque respectively. In the first case, the speed varies from -0.3 to +0.3 pu speed, during which $\hat{\psi}_m$ remains stable. When a step-change in the load-torque occurs from -0.4 pu to +0.4 pu, i.e., when the sign of the i_q changes, again the $\hat{\psi}_m$ remains stable with the SGA. With regard to GNA, the $\hat{\psi}_m$ oscillates when the rotor speed is unsettled, yet converges afterward. A summary of the performance is tabulated in Table 3.4.

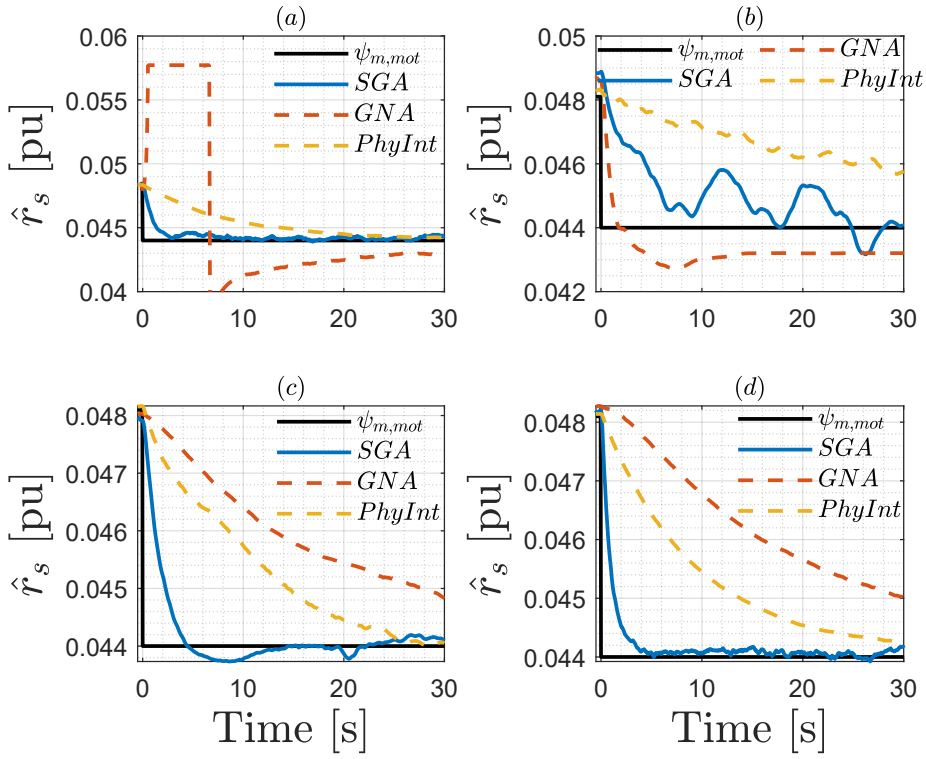

FIGURE 3.13. $\hat{r}_s$ online adaption with SGA, GNA and PhyInt (a) $n = -0.05\ pu$, $\tau_{el} = 0.2\ pu$ (b) $n = 0\ pu$, $\tau_{el} = 0.2\ pu$ (c) $n = 0\ pu$, $\tau_{el} = 0.6\ pu$ (d) $n = 0.05\ pu$, $\tau_{el} = 0.6\ pu$.

3.6.2 R_s-Tracking Validation

As in the previous case, the steady-state forms of the ψ_{21} and ψ_{22} are incorporated when GNA gains are computed. The respective experimental validations are presented in Figure 3.16. The adaption performances at standstill and at 0.005 pu speed are in Figure 3.16 (a) and (b), respectively when the load-torque is 0.4 pu. In both cases, the performance differences between the algorithms are marginal. The convergence performances upon a speed reference and load-torque step-change are plotted in Figure 3.16(c) and (d), respectively. Despite the steady-state behaviors being indistinguishable, it is seen that the SGA yields more stable tracking during the load (and thus the rotor-speed) transient. At low speeds, a speed ripple is evident in the rotor shaft, which is superimposed on the estimate-trajectories as seen in Figure 3.16(b) and (c).

A summary of the performance is tabulated in Table 3.4. The time taken by the SoC to process SGA and GNA routines is nearly the same as given in Table 3.4, which is well within the interrupt service routine for IGBT-based drives, and thus, the computational burden is not a matter of concern.

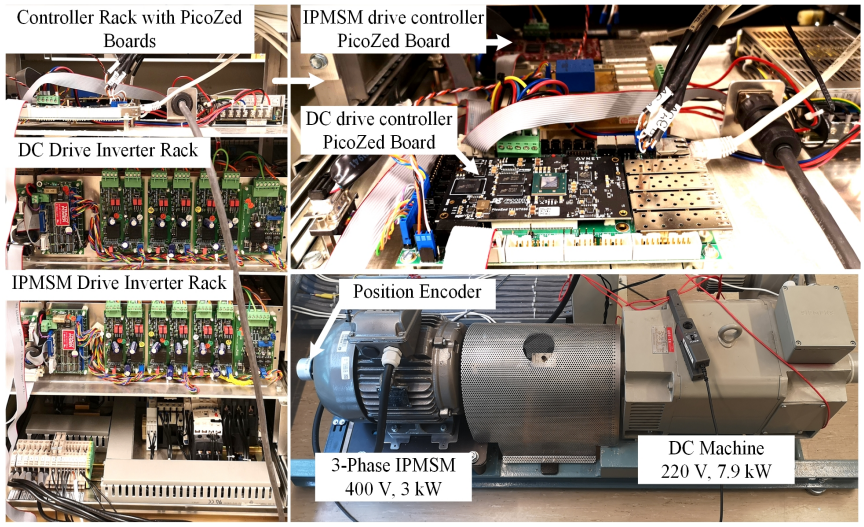

FIGURE 3.14. Experimental Setup having IPMSM as the drive machine and DC machine as the load machine mounted on the same shaft.

TABLE 3.4. Performance comparison summary between SGA and GNA.

Case	SGA	GNA
W.r.t. $\hat{\psi}_m$-estimation		
Convergence speed ($\tau_l = 0, n = 0.3\,pu$)	~2 s	~0.5 s
Convergence speed ($\tau_l = 0.4, n = 0.3\,pu$)	~1.5 s	~1.5 s
Steady-state error ($\tau_l = 0, n = 0.3\,pu$)	(-)0.5%	0.5%
Steady-state error ($\tau_l = 0.4, n = 0.3\,pu$)	~0%	~0%
W.r.t. $\hat{r}_s$-estimation		
Convergence time ($\tau_l = 0.4, n = 0\,pu$)	8 s	8 s
Convergence time ($\tau_l = 0.4, n = 0.005\,pu$)	6 s	4 s
Steady-state error ($\tau_l = 0.4, n = 0\,pu$)	0	0
Steady-state error ($\tau_l = 0.4, n = 0.005\,pu$)	~0	~0

3.7 CONCLUSION AND SUMMARY

This chapter proposed a prediction-gradients-assisted RPEM-based framework and three algorithms to identify parameters of electric machines, and the methods were demonstrated and validated using an IPMSM by identifying temperature-sensitive parameters online. The predictor is arranged in an open-loop, and thus the prediction error is enriched with parametric errors, a feature that is exploited by deriving prediction gradients, which becomes the main element in the estimation gains in this context. With the aid of real-time simulation, a performance comparison of the three algorithms was executed across the operating range. Experimental results show that both the SGA and GNA offer reasonable tracking performance. Despite the latter being able to offer faster tracking in principle, it becomes overly excited at lower torque/speed region and inherently prevents R_s-tracking at zero-speed, unlike the

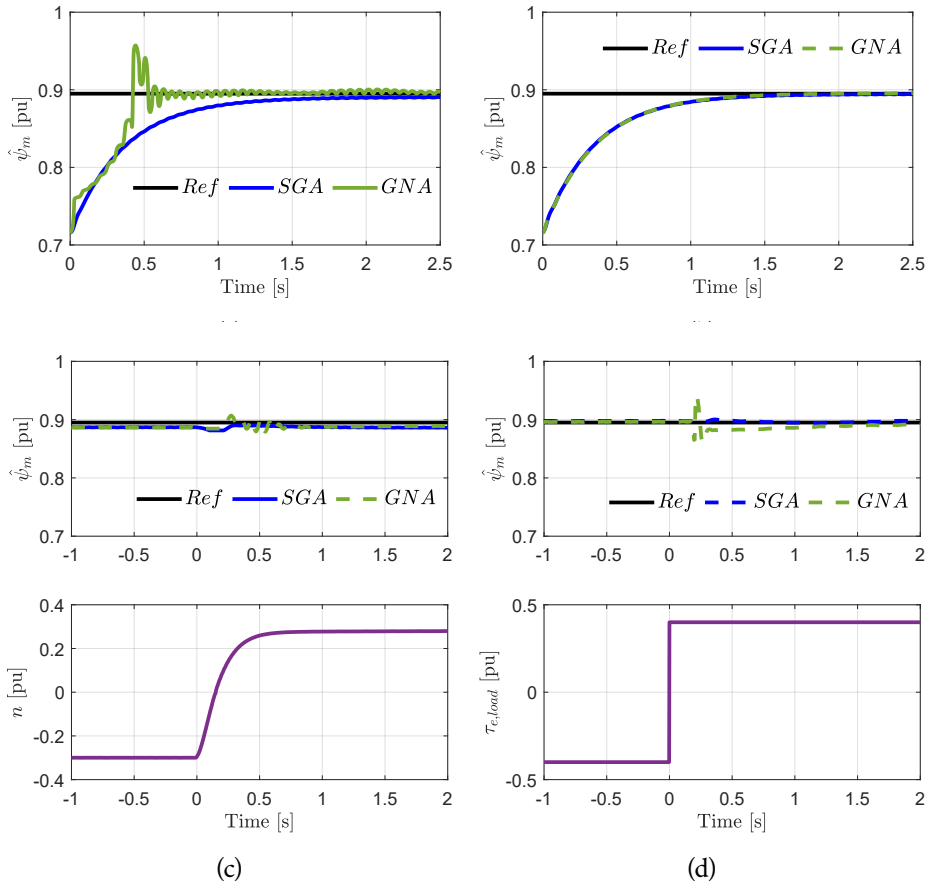

Figure 3.15. Experimental validations of $\hat{\psi}_m$ -online adaptation with SGA and GNA when (a) no-load at 0.3 pu speed (b) 0.4 pu load-torque at 0.3 pu speed (c) speed reference step-change from -0.3 to 0.3 at 0.4 pu load-torque (d) load step-change from -0.4 to +0.4 pu load-torque at 0.3 pu speed.

other two methods. Moreover, very fast adaptation has little use when large thermal time constants are concerned. Due to the attributes of the dynamic hessian, SGA offers controllable tracking speeds at the start, unlike the PhyInt. Given the stable, flexible, and consistent performance and the simplicity in the implementation, RPEM with SGA can be a practical solution for temperature-sensitive parameter estimation of electrical machines. In the next chapter, this parameter adaptation scheme is incorporated within a sensorless control scheme, with the purpose of enhancing the sensorless control of the three-phase IPMSM drive.

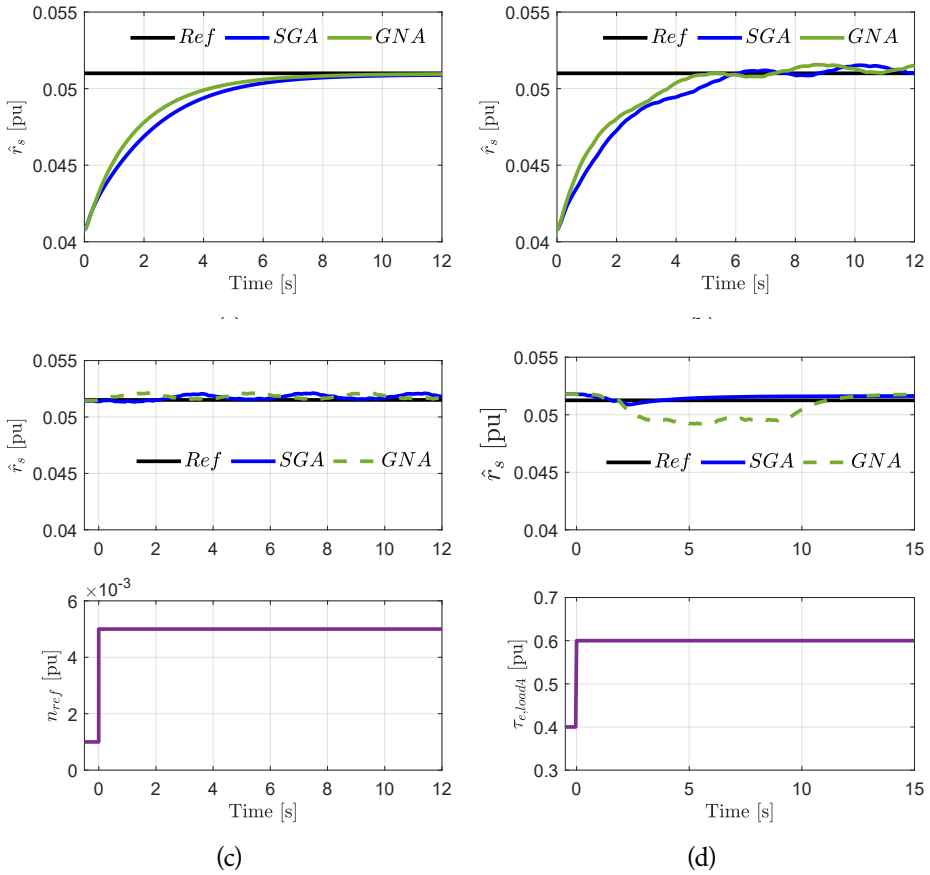

Figure 3.16. Experimental validations of $\hat{r}_s$ -online adaptation with SGA and GNA when (a) 0.4 pu load-torque at standstill (b) 0.4 pu load-torque at 0.005 pu speed (c) speed reference step-change from 0.001 to 0.005 pu at 0.4 pu load-torque (d) load step-change from 0.4 to 0.6 pu load-torque at standstill.

3.8 References

[1] Emine Bostanci, Mehdi Moallem, Amir Parsapour, and Babak Fahimi. Opportunities and challenges of switched reluctance motor drives for electric propulsion: a comparative study. *IEEE Transactions on Transportation Electrification* **3** (1), 58–75 (2017). ISSN 23327782. doi: 10.1109/TTE.2017.2649883. Cited on page/s 34.

[2] Z. Q. Zhu, Dawei Liang, and Kan Liu. Online parameter estimation for permanent magnet synchronous machines : an overview. *IEEE Access* **9**, 59059–59084 (2021). doi: 10.1109/ACCESS.2021.3072959. Cited on page/s 34, 35.

[3] Muhammad Saad Rafaq and Jin Woo Jung. A Comprehensive review of state-of-the-art parameter estimation techniques for permanent magnet synchronous motors in side speed range. *IEEE Transactions on Industrial Informatics* **16** (7), 4747–4758 (2020). ISSN 19410050. doi: 10.1109/TII.2019.2944413. Cited on page/s 34, 35.

[4] Pavel Vaclavek, Petr Blaha, and Ivo Herman. AC drive observability analysis. *IEEE Transactions on Industrial Electronics* **60** (8), 3047–3059 (2013). ISSN 02780046. doi: 10.1109/TIE.2012.2203775.

Cited on page/s 34.

[5] Samuel J. Underwood and Iqbal Husain. Online parameter estimation and adaptive control of permanent-magnet synchronous machines. *IEEE Transactions on Industrial Electronics* **57** (7), 2435–2443 (2010). ISSN 02780046. doi: 10.1109/TIE.2009.2036029. Cited on page/s 34.

[6] Qiwei Wang, Gaolin Wang, Nannan Zhao, Guoqiang Zhang, Qingwen Cui, and Dianguo Xu. An impedance model-based multiparameter identification method of PMSM for both offline and online conditions. *IEEE Transactions on Power Electronics* **36** (1), 727–738 (2021). ISSN 19410107. doi: 10.1109/TPEL.2020.3000896. Cited on page/s 34.

[7] Wei Xu and Robert D Lorenz. High-frequency injection-based stator flux linkage and torque estimation for DB-DTFC implementation on IPMSMs considering cross-saturation effects. *IEEE Transactions on Industriy Applications* **50** (6), 3805–3815 (2014). Cited on page/s 34, 35.

[8] Uwe Schaible and Barna Szabados. Dynamic motor parameter identification for high speed flux weakening operation of brushless permanent magnet synchronous machines. *IEEE Transactions on Energy Conversion* **14** (3), 486–492 (1999). ISSN 08858969. doi: 10.1109/60.790901. Cited on page/s 34.

[9] Shih Wei Su, Christoph M. Hackl, and Ralph Kennel. Analytical prototype functions for flux linkage approximation in synchronous machines. *IEEE Open Journal of the Industrial Electronics Society* **3** (March), 265–282 (3 2022). ISSN 26441284. doi: 10.1109/OJIES.2022.3162336. Cited on page/s 34.

[10] Stjepan Stipetic, Marinko Kovacic, Zlatko Hanic, and Mario Vrazic. Measurement of excitation winding temperature on synchronous generator in rotation using infrared thermography. *IEEE Transactions on Industrial Electronics* **59** (5), 2288–2298 (2012). ISSN 02780046. doi: 10.1109/TIE.2011.2158047. Cited on page/s 34.

[11] Daniel Fernandez, David Reigosa, Tsutomu Tanimoto, Takashi Kato, and Fernando Briz. Wireless permanent magnet temperature & field distribution measurement system for IPMSMs. *2015 IEEE Energy Conversion Congress and Exposition, ECCE 2015* pages 3996–4003 (2015). doi: 10.1109/ECCE.2015.7310224. Cited on page/s 34.

[12] Oliver Wallscheid. Thermal monitoring of electric motors: state-of-the-art review and future challenges. *IEEE Open Journal of Industry Applications* **2** (June), 204–223 (2021). doi: 10.1109/ojia.2021.3091870. Cited on page/s 34.

[13] Lennart Ljung and Torsten Soderstrom. Theory and Practice of Recursive Identification. The MIT Press Cambridge, Massachusetts 2nd edition (1985). ISBN 0-262-12095-X. Cited on page/s 34, 35, 37, 40, 42, 45, 46, 48, 49.

[14] Anian Brosch, Sören Hanke, Oliver Wallscheid, Joachim Böcker, and Senior Member. Data-driven recursive least squares estimation for model predictive current control of permanent magnet synchronous motors. *IEEE Transactions on Power Electronics* **36** (2), 2179–2190 (2021). Cited on page/s 34.

[15] Shigeo Morimoto, Masayuki Sanada, and Yoji Takeda. Mechanical sensorless drives of IPMSM with online parameter identification. *IEEE Transactions on Industry Applications* **42** (5), 1241–1248 (2006). ISSN 00939994. doi: 10.1109/TIA.2006.880840. Cited on page/s 35.

[16] Yukinori Inoue, Yasunori Kawaguchi, Shigeo Morimoto, and Masayuki Sanada. Performance improvement of sensorless IPMSM drives in a low-speed region using online parameter identification. *IEEE Transactions on Industry Applications* **47** (2), 798–804 (2011). ISSN 00939994. doi: 10.1109/TIA.2010.2101994. Cited on page/s 35.

[17] Lennart Harnefors and Hans Peter Nee. Adaptive sensorless control of induction motors for improved low-speed performance. *Conference Record - IAS Annual Meeting (IEEE Industry Applications Society)* **1**, 278–285 (1996). ISSN 01972618. doi: 10.1109/ias.1996.557030. Cited on page/s 35.

[18] Xinyue Li and Ralph Kennel. General formulation of kalman-filter-based online parameter identification methods for VSI-fed PMSM. *IEEE Transactions on Industrial Electronics* **68** (4), 2856–2864 (2021). ISSN 15579948. doi: 10.1109/TIE.2020.2977568. Cited on page/s 35.

[19] Torsten Soderstrom and Petre Stoica. System Identification. Prentice Hall International Uppsala (2001). ISBN 0-13-881236-5. Cited on page/s 35.

[20] H Børsting, M Knudsen, H Rasmussen, and P Vadstrup. Estimation of mechanical signals in

induction motors using the recursive prediction error method. In *EPE* pages 455–460 (1993). Cited on page/s 35.

[21] Dag Ljungquist and Jens G. Balchen. Recursive prediction error methods for online estimation in nonlinear state-space models. *Proceedings of the IEEE Conference on Decision and Control* **1**, 714–719 (1993). ISSN 01912216. doi: 10.4173/mic.1994.2.4. Cited on page/s 35.

[22] Antti Piippo, Marko Hinkkanen, and Jorma Luomi. Adaptation of motor parameters in sensorless PMSM drives. *IEEE Transactions on Industry Applications* **45** (1), 203–212 (2009). ISSN 00939994. doi: 10.1109/TIA.2008.2009614. Cited on page/s 35, 38.

[23] Sai Shiva Badini and Vimlesh Verma. A new stator resistance estimation technique for vector-controlled PMSM drive. *IEEE Transactions on Industry Applications* **56** (6), 6536–6545 (2020). ISSN 19399367. doi: 10.1109/TIA.2020.3025265. Cited on page/s 35, 38.

[24] Zhao Hua Liu, Hua Liang Wei, Qing Chang Zhong, Kan Liu, Xiao Shi Xiao, and Liang Hong Wu. Parameter estimation for VSI-Fed PMSM based on a dynamic PSO with learning strategies. *IEEE Transactions on Power Electronics* **32** (4), 3154–3165 (2017). ISSN 08858993. doi: 10.1109/TPEL.2016.2572186. Cited on page/s 35.

[25] Zitan Wang, Jianyun Chai, Xuewei Xiang, Xudong Sun, and Haifeng Lu. A novel online parameter identification algorithm designed for deadbeat current control of the permanent-magnet synchronous motor. *IEEE Transactions on Industry Applications* **58** (2), 2029–2041 (2022). ISSN 19399367. doi: 10.1109/TIA.2021.3136807. Cited on page/s 35.

[26] Shuai Zhao, Frede Blaabjerg, and Huai Wang. An overview of artificial intelligence applications for power electronics. *IEEE Transactions on Power Electronics* **36** (4), 4633–4658 (2021). ISSN 19410107. doi: 10.1109/TPEL.2020.3024914. Cited on page/s 35.

[27] Roy Nilsen and Marian P Kazmierkowski. Reduced-order observer with parameter adaption for fast rotor flux estimation in induction machines. *IEE Proceedings* **136** (1), 35–43 (1989). Cited on page/s 35.

[28] Aravinda Perera and Roy Nilsen. Gauss-Newton: A prediction-error-gradient based algorithm to track PMSM parameters online. In IEEE, editor, *9th IEEE International Conference on Power Electronics, Drives and Energy Systems, PEDES 2020* Jaipur, India (2020). ISBN 9781728156729. doi: 10.1109/PEDES49360.2020.9379424. Cited on page/s 35, 46.

[29] Hansruedi Buhler. Einfuhrung in die Theorie Geregelter Drehstromantriebe. Birkhauser Basel 6 edition (1977). ISBN 3-7643-08337-0. Cited on page/s 36.

[30] Peter Weichbold and Thomas von Raumer. Influence of dead time effects of PWM-VSI on current control. In IEEE, editor, *EPE* page 8 Graz (2001). Cited on page/s 36.

[31] Shigeo Morimoto, Masayuki Sanada, and Yoji Takeda. Wide-speed operation of interior permanent magnet synchronous motors with high-performance current regulator. *IEEE Transactions on Industry Applications* **30** (4), 920–926 (1994). Cited on page/s 36.

[32] J.D. Lambert. Computational Methods in Ordinary Differential Equation. John Wiley & Sons, Inc Hoboken (1973). Cited on page/s 39.

[33] Aravinda Perera and Roy Nilsen. A recursive prediction error method with effective use of gradient-functions to adapt PMSM parameters online. In *IEEE Industry Applications Society Annual Meeting* pages 2–6 Detroit, USA (2020). IEEE. ISBN 9781728171920. doi: 10.1109/IAS44978.2020.9334744. Cited on page/s 44, 53.

[34] Aravinda Perera, Roy Nilsen, Thomas Haugan, and Kjell Ljøkelsøy. A design method of an embedded real-time simulator for electric drives using low-cost system-on-chip platform. In *PCIM Europe digital days* Nuremberg, Germany (2021). Cited on page/s 52.

Chapter 4

Enhanced Position Sensorless Control of Three-Phase Drives

Abstract

This chapter proposes an open-loop predictor-based scheme to identify all electric parameters, with the aim of enhancing the performance of sensorless three-phase IPMSM drives. An active flux (AF)-based observer is employed to estimate the rotor position and speed. The full-order model-premised open-loop predictor and prediction gradients-based SGA disclosed in Chapter 3 are exploited to identify the temperature-sensitive parameters, i.e., permanent magnet flux linkage Ψ_m and stator resistance R_s. The estimation gains are chosen by providing physical insights into the basis of choices. The SoC-based real-time simulator is used to assess the cross-coupling among the estimates. Dedicated prediction error components and Hessian function modifications are proposed to optimize the simultaneous identifiability of Ψ_m and R_s. The inductances are updated online with the aid of a Look-Up Table (LUT) that contains the inductance-current mapping identified offline. This offline experimental method is also premised on the exact open-loop predictor and its results are in acceptable agreement with the inductances obtained from the Finite Element Model (FEM). The laboratory drive prototype used in the previous chapter is used to conduct the experimental validations. The results show that, by incorporating the proposed schemes, the observer is made more stable, precise, and robust to parameter variations as compared to the observer without parameter adaptation. Under the proposed scheme, the steady-state average rotor position error reported is below 2° and could reach speeds as low as 1%.

4.1 Introduction

POSITION sensorless IPMSM drives are becoming state-of-art in high-performance and mission-critical applications attributing to multiple attractive features [1, 2], among which, superior efficiency, high power density, and enhanced reliability are prominent. The sensorless control algorithms can be classified into two main categories: fundamental excitation (FE)-based methods and inductance variation tracking

methods [3, 4]. While the former is the standard method for a wide speed range, the latter is applied to extract the rotor position, typically in the low-speed region. High-Frequency Signal Injection (HFSI)-premised rotor magnetic saliency tracking is the most prevalent in this category [5]. Injected signals, however, increase the acoustic noise and tend to deteriorate the motor performance as the rotor gains traction, hence it is beneficial to exploit the FE-based position extraction as close as possible to zero speed. Besides, many industrial drives, like marine propulsion or pump drives, do not demand persistent operation around zero speed and thus can be realized with only FE-based techniques.

4.1.1 Literature Review

A variety of FE-based state observers, as reviewed in [3, 4], are prevalent for rotor position estimation from either the back Electromotive Force (EMF) or electromagnetic flux linkages. Despite this, they can be categorized into either Luenberger-form, Disturbance, or Filter type observers by assessing their mathematical equivalence [6] or alternatively into full-order or reduced-order observers depending on the order of the observer gain-matrix [7]. In parallel, concepts known as Extended EMF [8] and Active Flux [9] have been developed to ease the complexities of the IPMSM mathematical model that arises from its saliency.

One drawback of such observers is their performance and stability dependency on the precision of the identified machine parameters (hereafter known as the model parameters). R_s and Ψ_m are temperature dependent whereas L_d, L_q can vary due to the electromagnetic saturation and cross-coupling. The impact of inaccurate model parameters on the FE-based position estimation is discussed in [10], and the effects can lead to poor torque/speed control, reduced efficiency, and increased torque ripples and sometimes faults [11]. Despite the full-order observers being claimed to show more robustness to parameter variations over their reduced-order counterparts [12], the performance of an observer that is assisted by online parameter adaptation is far superior [13, 14]. Moreover, online parameter tracking can be exploited to identify the stator and rotor temperatures, which is a more reliable, less expensive, and much less cumbersome approach than sensor-based temperature monitoring [15].

Consequently, online parameter adaptation has gained attention with proven and emerging methods discussed in Chapter 3. Improvements to the AF observer are attempted using the offline identified R_s and analytically modeled $\hat{L}_q$ in [16]. The same observer is augmented with inductance and R_s -identifications using dc-voltage and signal-injections along with additional hardware for stator voltage measurement in [17]. In [18], the full-order observer's residual information is used to adapt R_s and Ψ_m online in the low and higher speed regions, respectively. Ref [19–22] propose the combination of EEMF-based reduced-order observer and Recursive Least Squares (RLS) method to enhance sensorless control of IPMSM. Forms of injected signals are used in [23, 24] to identify multiple parameters of PMSM sensorless drive. Modifications of the Kalman

Filter for nonlinear system identification are adopted in [25, 26] for either or both parameter and position estimations of PMSM.

4.1.2 Research Gaps and Contribution

A set of recursive algorithms using an open-loop predictor model and prediction error gradients $\boldsymbol{\Psi}^T$ for PMSM identification is proposed in Chapter 3. This method is yet to be investigated in combination with sensorless control, for its ability in enhancing the observer's performance, and overall stability. The steady-state gradients for inductance identification and in-depth analysis of the Hessian functions for effective adaptation are, however, not revealed in the previous chapter. Moreover, a variety of similar identification methods [19–22, 27] have been proposed to enhance the reduced-order observers previously, nevertheless, their choice of gains matrix for parameter identification is not well clarified. These gaps are attempted to be addressed by this chapter, with the purpose of realizing relatively simple state estimation without compromising the performance due to observer simplicity or by using test signals.

The main contribution of this chapter is to adopt the open-loop predictor and current prediction error-based gradients to identify all electric parameters, with the aim of enhancing the sensorless IPMSM drive. Active flux observer is chosen due to its prevalence, and relative ease of design, although, it is believed that any observer that relies on model parameters can fit into the proposed combined scheme. This identification scheme is expected to be effective because its prediction error is enriched with model parametric discrepancies, as opposed to the closed-loop models [18, 28], in which the parameter sensitivity tends to be reduced by the feedback correction. Estimation gains to identify all electric parameters are explicitly developed by disclosing the model parametric sensitivities across the torque-speed plane. The impact of different Hessian functions on estimation gains is analyzed to choose the combinations for more effective simultaneous online identification. Thereby, R_s and Ψ_m are identified online using $\boldsymbol{\Psi}^T$-based Stochastic Gradient Algorithm (SGA). $\boldsymbol{\Psi}^T$ w.r.t. the inductances as well, are developed, and the respective online identification algorithms are presented. An experimental method based on the same open-loop predictor is also proposed herein for offline identification inductances. FEM is developed for the test machine to compare the offline identifications. This chapter also presents the deduction of an expression to compute Maximum Torque Per Ampere (MTPA) reference currents directly from the torque command, in contrast to the popularly used expressions [29] which are functions of the stator current.

The proposed combined sensorless scheme is aimed to improve sensorless control, particularly at very low speeds and saturation regions without the help of additional sensors or modification to the hardware or test signals, thus potential performance degradation is prevented. The preliminary offline simulation results [30], is extended here with the aid of Zynq System-on-Chip-based real-time simulator. The combined sensorless control scheme is subsequently validated using an experimental prototype.

TABLE 4.1. IPMSM PARAMETERS

Symbol	Parameter	Value
U_n	Rated Voltage	400 V
I_n	Rated Current	4.93 A
P_n	Rated Power	3 kW
N_n	Rated Speed	1000 rpm
T_n	Rated Torque	32.6 Nm
p	Number of pole-pairs	3
R_s	Stator Resistance (offline)	2.25 Ω
Ψ_m	Permanent magnet flux linkage (offline)	1.14 Wb
L_d	d-axis inductance (rated load)	95.3 mH
L_q	q-axis inductance (rated load)	206 mH

4.2 MACHINE MODELS

In this section, the mathematical and finite element models of the IPMSM are detailed.

4.2.1 IPMSM Dynamic Model

The dynamic model of the IPMSM and the notations are as same as in (3.1).

4.2.2 Finite Element Model

The test machine is a three-phase, six-pole, 36-slots IPMSM, and the stator winding is in a single layer. Machine ratings and the electrical parameters are tabulated in Table 4.1. A 2D FEM is developed with ANSYS Maxwell as illustrated in Figure 4.1(b). Motor dimensions are acquired by direct measurement of the motor. Since this motor is an off-the-shelf product, material grades (mainly permanent magnet and laminated steel used in stator and rotor) and material properties after manufacture are unknown. To address this issue, various approaches are taken to characterize the motor, and numerous materials are tried in the FEM in order to determine the materials that bring the FEM results closest to the measurement and motor specification listed in Table 4.1. It is eventually concluded that the permanent magnet can be assumed to be N50M, and the laminated steel in the stator and rotor can be assumed to be 35PN300. With these assumptions, motor inductances of the active part are computed with the frozen permeability approach in 2D FEM computation, and end-winding inductance is computed with an analytical approach. The computed $\hat{L}_d$ and $\hat{L}_q$ vs. I_d and I_q are plotted in Figure 4.2, and they will be used in section 4.3.6 to assess the results from the offline experimental method.

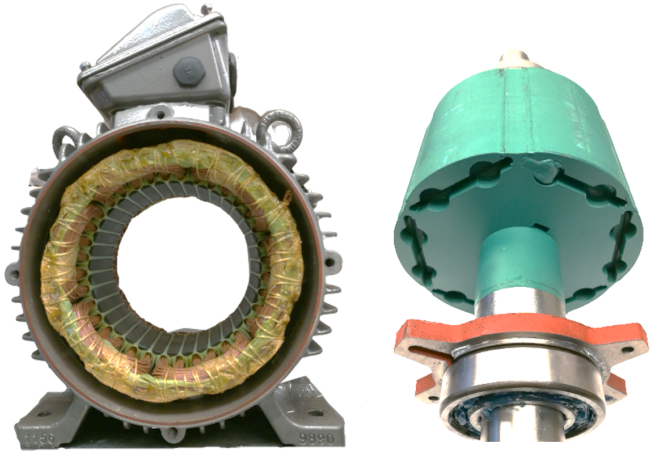

(a)

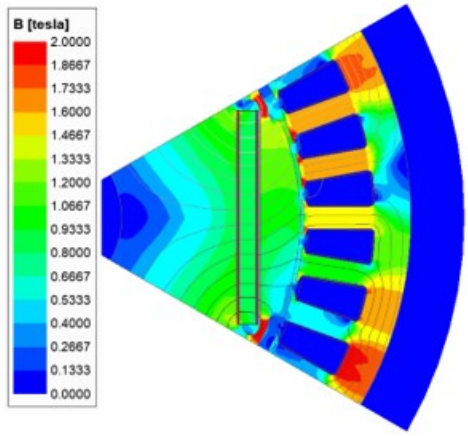

(b)

FIGURE 4.1. IPMSM: (a) stator and rotor (b) 2D Finite Element Model.

4.3 SENSORLESS CONTROL SCHEME

4.3.1 Overview of the IPMSM Drive

The block diagram of the three-phase, current vector controlled, sensorless IPMSM drive enhanced by the parameter identifier is given in Figure 4.3. The classical two-level, three-phase Voltage Source Inverter (VSI) is supplied by dc-link capacitors, in which the voltage U_{dc} is measured and used to estimate the stator winding voltages. $\underline{I}_s$ is measured at the output of the VSI. The parameter identifier provides the model parameter vector $\underline{\hat{\theta}}$ that is fed into the state observer, among others, which estimates

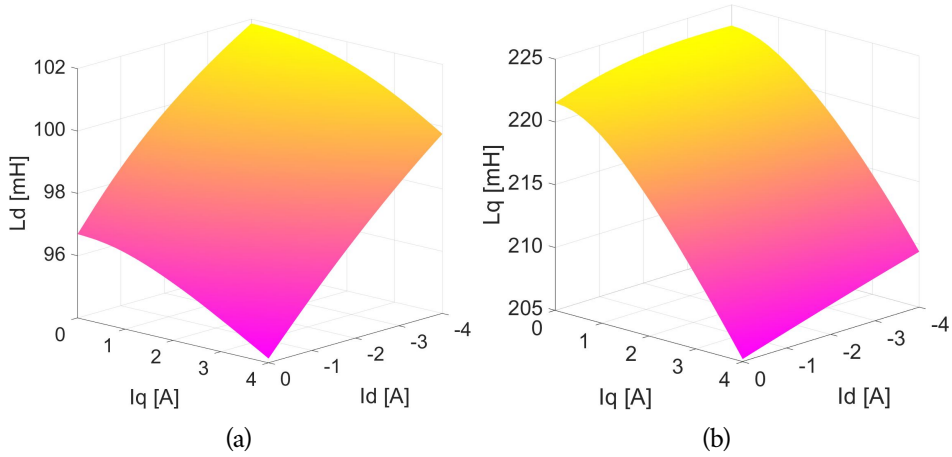

Figure 4.2. Computed inductances of the test machine: (a) L_d (b) L_q.

the rotor position $\hat{\vartheta}$ and speed $\hat{n}$. External torque or speed commands $\tau^*_{e,ext}$, n^*_{ext} can be fed from the top-level control panel like the programmable logic control. When the drive is in the speed-control mode, $\tau^*_{e,ext}$ becomes redundant as the τ^*_e will then be generated from the speed regulator. i^*_d, i^*_q are calculated to fulfill either MTPA with the following expression or the flux-weakening strategy at high-speed operations:

$$i^*_d = \frac{\hat{\psi}_m}{4(\hat{x}_q - \hat{x}_d)} \cdot \sqrt{\left(\frac{\hat{\psi}_m}{4(\hat{x}_q - \hat{x}_d)}\right)^2 + \frac{i_s^2}{2}} \tag{4.1a}$$

$$i^*_q = \pm\sqrt{i^{*2}_d - \frac{\hat{\psi}_m \cdot i^*_d}{(\hat{x}_q - \hat{x}_d)}} \tag{4.1b}$$

From the operator's point of view, it is more practical to feed in a torque command than a stator current reference as required by (4.1a). This motivates to develop an expression to find i^*_d based on $\tau^*_{e,ext}$. From two different expressions, namely from (4.1b) and classical torque expression, i^*_q for MTPA strategy can be found as below:

$$i^*_q = \frac{\tau^*_{e,PLC}}{\hat{\psi}_m - (\hat{x}_q - \hat{x}_d) \cdot i^*_d} = \pm\sqrt{i^{*2}_d - \frac{\hat{\psi}_m \cdot i^*_d}{(\hat{x}_q - \hat{x}_d)}} \tag{4.2}$$

This allows to eliminate i^*_q and develop a 4$^{\text{th}}$ order expression as below:

$$\begin{aligned} 0 = {} & s^3 \cdot i^{*4}_d - 3 \cdot s^2 \cdot \hat{\psi}_m \cdot i^{*3}_d + 3 \cdot s \cdot \hat{\psi_m}^2 \cdot i^{*2}_d - \hat{\psi}^3_m \cdot i^*_d \\ & - s \cdot \tau^*_e; \qquad s = \hat{x}_q - \hat{x}_d \end{aligned} \tag{4.3}$$

The 4$^{\text{th}}$ order term can generally be neglected because the term-$s^3 \cdot i^{*4}_d$ is very small compared to the rest of the terms. After solving the remaining 3$^{\text{rd}}$ order expression,

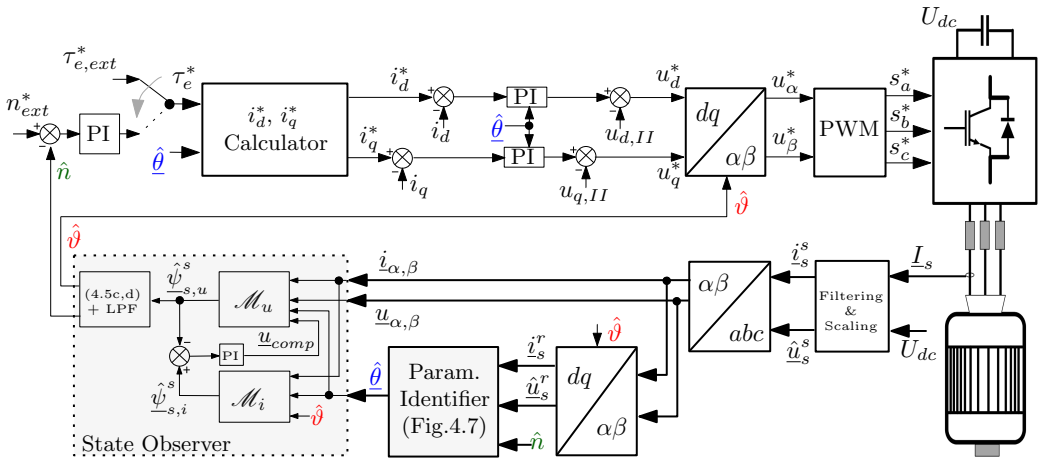

FIGURE 4.3. Block diagram of the vector controlled-IPMSM sensorless drive enhanced with the online parameter estimator.

one can arrive at the following expression [31] to compute i^*_d that is a function of τ^*_e, unlike (4.1a):

$$i^*_d = \frac{\frac{\hat{\psi}_m}{3} - \sqrt[3]{\left(\frac{\hat{\psi}_m}{3}\right)^3 + \frac{(\hat{x}_q - \hat{x}_d)^2 \cdot (\tau^*_e)^2}{3 \cdot \hat{\psi}_m}}}{\hat{x}_q - \hat{x}_d} \tag{4.4}$$

The performance comparison of the classical expression and (4.4) is given in Figure 4.12.

4.3.2 *Active Flux Observer for State Estimation*

AF Concept and Model

Active Flux, $\underline{\psi}_T$ is introduced in [9], aiming to simplify the arithmetic behind the ϑ-extraction. As illustrated in Figure 4.4, $\underline{\psi}_T$ is located in the d-axis of the rotor, thus identifying the phase of $\underline{\psi}_T$ will tell us the rotor position w.r.t. the machine a-axis. From a physical point of view, $\underline{\psi}_T$ is what actively produces the electromagnetic torque, from which it receives name (see (4.5a)). The key result of the AF concept is in (4.5b) which is evident in the vector diagram too, which illuminates that $\underline{\psi}_T$ can be calculated using only $\underline{i}_s$ and x_q. Eventually, $\hat{\vartheta}$ and $\hat{n}$ can be calculated using the components of $\underline{\psi}_T$ via (4.5c) and (4.5d) [16] or alternatively, a Phase-Locked Loop (PLL) as shown in [9, 32]. A 1st order Low Pass Filter (LPF) can be required to eliminate the ripple in the

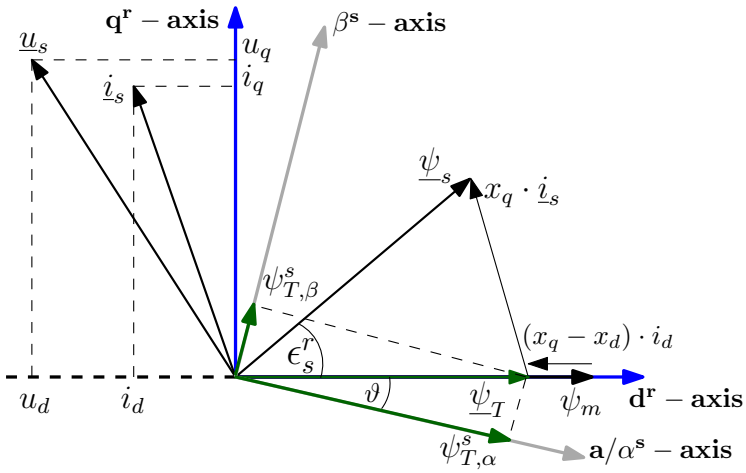

Figure 4.4. Phasor diagram of IPMSM to highlight the Active Flux Vector and its application in position estimation.

speed estimation, typically with a time constant of 3-5 ms.

$$\psi_T = \psi_m - (x_q - x_d)\cdot i_d \tag{4.5a}$$

$$\underline{\psi}_T = \underline{\psi}_s - x_q \cdot \underline{i}_s \tag{4.5b}$$

$$\hat{\vartheta} = \text{atan2}\left(\frac{\psi^s_{T,\beta}}{\psi^s_{T,\alpha}}\right) \tag{4.5c}$$

$$\hat{n} = \frac{\psi^s_{T,\alpha}[k-1]\cdot\psi^s_{T,\beta}[k] - \psi^s_{T,\beta}[k-1]\cdot\psi^s_{T,\alpha}[k]}{T_{samp}\cdot\left(\psi^{s2}_{T,\alpha}[k] + \psi^{s2}_{T,\beta}[k]\right)} \tag{4.5d}$$

$\mathscr{M}_{ui}$-Observer and Design Guidelines

A flux observer is required to estimate the stator flux for $\underline{\psi}_T$-computation. Such an observer can be realized in the conventional Model Reference Adaptive System (MRAS) approach discussed in [9, 16, 32] or using more novel approaches [33]. The conventional MRAS-observer (see Figure 4.3) is adopted, which employs $\mathscr{M}_{ui}$ introduced in [34]. In this type of flux observer, the Voltage Model $\mathscr{M}_u$ is chosen for the stator flux estimation $\hat{\underline{\psi}}^s_{s,u}$ using (4.6a), however, with the feedback correction with reference to the stator flux estimated $\hat{\underline{\psi}}^s_{s,i}$ from the Current Model $\mathscr{M}_i$ using the following:

$$\hat{\underline{\psi}}^s_{s,u} = \omega_n \cdot \int \left(\underline{u}^s_s - r_s\cdot\underline{i}_s + \underline{u}_{comp}\right)\cdot dt \tag{4.6a}$$

$$\hat{\underline{\psi}}^r_{s,i} = \mathbf{x}^r_s \cdot \underline{i}^r_s + \underline{\psi}^r_m \tag{4.6b}$$

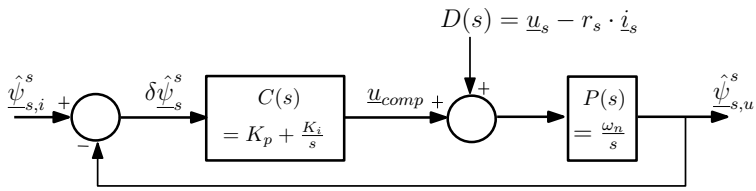

FIGURE 4.5. Control block diagram of the $\mathscr{M}_{ui}$ treating voltages as a disturbance.

$\mathscr{M}_u$ offers reasonable flux estimation across a wide speed range except in the lower speed region, during which the voltage drop across the resistances gradually becomes comparable to the back EMF, and the impact from the unaccounted variations in the stator and device on-state resistances on the estimated flux become significant [34, 35]. Additionally, open-loop flux estimation using $\mathscr{M}_u$ is known for the drift and DC offset issues owing to the open integrator [13]. To eliminate the integrator-related issues and to mitigate the increasing R_s-sensitivity in the low-speed region, $\mathscr{M}_i$ is introduced as a reference to the $\mathscr{M}_u$ which, in combination, forms the $\mathscr{M}_{ui}$ observer. The control block diagram of such an observer while treating the voltages as disturbance can be presented as in Figure 4.5. Accordingly, $\hat{\underline{\psi}}^s_{s,u}$ can be expressed as follows:

$$\hat{\underline{\psi}}^s_{s,u} = \underbrace{\frac{P(s)C(s)}{1+P(s)C(s)}}_{\mathrm{M}} \cdot \hat{\underline{\psi}}^s_{s,i} + \underbrace{\frac{P(s)}{1+P(s)C(s)}}_{\mathrm{N}} \cdot D(s) \tag{4.7a}$$

$$\hat{\underline{\psi}}^s_{s,u} = \frac{K_p \cdot s + K_i}{\frac{1}{\omega_n} \cdot s^2 + K_p \cdot s + K_i} \cdot \hat{\underline{\psi}}^s_{s,i} + \frac{s}{\frac{1}{\omega_n} \cdot s^2 + K_p \cdot s + K_i} \cdot \left(\underline{u}_s - r \cdot \underline{i}_s\right) \tag{4.7b}$$

Here, M is designed as a 2$^{\mathrm{nd}}$ order LPF such that during the low-speed region below the cross-over frequency $|\omega_{cro}|$, $D(s)$ will be rejected such that $\hat{\underline{\psi}}^s_{s,u} = \hat{\underline{\psi}}^s_{s,i}$. In the rotor speeds beyond $|\omega_{cro}|$, N is designed to dominate such that $\mathscr{M}_u$ prevails. This design criterion is illustrated in Figure 4.6(a), in which the intended open-loop gain $P(s)C(s)$ should appear as in the figure. A Proportional-Integral (PI) compensator with the respective gains K_p, K_i can be chosen to achieve such observer performance and for the elimination of steady-state offset, that will yield (4.7b). The PI gains can be computed using the Root-Locus design described in [36]. Accordingly, $K_p,\ K_i = 0.01$, for the machine given in Table 4.1. Damping factor, ζ, and rated frequency, ω_n, are $\frac{1}{\sqrt{2}}$ and $\omega_n = 314.16\, rad \cdot s^{-1}$, respectively. ω_{cro} is chosen to be 15 $rad \cdot s^{-1}$ i.e., equivalent to 0.05 pu.

Parameter Influence on the Observer

The impact of the mistuned model parameters on the FE-based position estimators is investigated in [10]. The key outcome is that x_q influence is present across the full speed range, particularly under the $\underline{\psi}_T$ concept, and the magnitude of the impact is

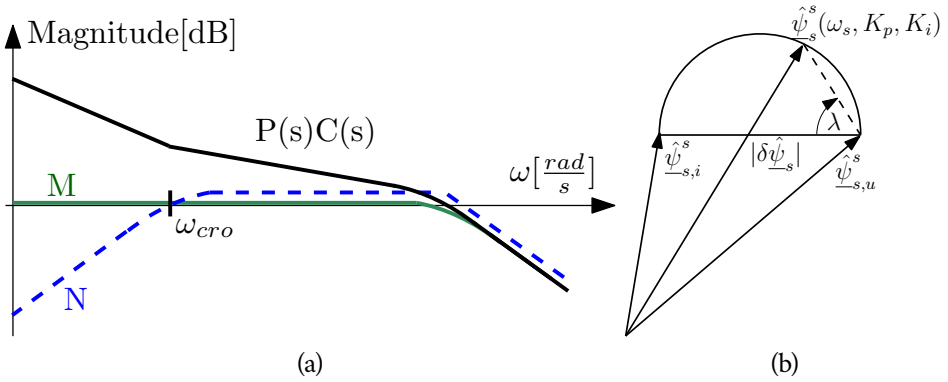

Figure 4.6. (a) Illustration of $\mathscr{M}_{ui}$-observer design criteria using Bode magnitude plot (b) Phasor diagram of estimated stator flux linkages in steady state in $\mathscr{M}_{ui}$ inspired by [34] when machine parameters are not correctly identified.

independent of the rotor speed. x_d-impact, on the other hand, can appear when $\mathscr{M}_i$ is dominant in the observer, i.e., during very low speeds. During this narrow speed region, the mistuned $\hat{\psi}_m$ can also degrade the position estimation. However, the speed region where $\mathscr{M}_u$ dominates in position observers is far wider, and thus R_s-sensitivity is the most critical, particularly below mid speeds [37].

The parameter influence of $\mathscr{M}_{ui}$ is in Figure 4.6(b) that illustrates vector diagrams of the flux quantities involved in the $\mathscr{M}_{ui}$ [34] modified for IPMSM. Here, $\hat{\underline{\psi}}^s_{s,u}$ and $\hat{\underline{\psi}}^s_{s,i}$ are uncorrected flux estimates from the respective models and the gap between them $\delta\hat{\underline{\psi}}_s$ is a result mainly of the poorly tuned $\hat{\underline{\theta}}$ [34]. $\hat{\underline{\psi}}^s_{s,u}(\omega_s, K_p, K_i)$ is the corrected output in Figure 4.5, which will then be used for $\underline{\psi}_T$-computation in (4.5b). Figure 4.6(b) reflects the fact that a well-tuned observer can still yield an approximation of $\hat{\underline{\psi}}^s_s$, at the mercy of the accuracy of the model parameters. This parameter reliance is the motivation to assist the observer with a dedicated scheme for parameter identification, which will be presented next.

4.3.3 RPEM Development using Open-Loop Prediction Error

According to [38], the general form of RPEM can be expressed as:

$$\hat{\underline{\theta}}[k] = \left[\hat{\underline{\theta}}[k-1] + \mathbf{L}[k, \hat{\underline{\theta}}] \cdot \underline{\epsilon}[k, \hat{\underline{\theta}}]\right]_{D_{\mathscr{M}}} \tag{4.8}$$

where

$$\hat{\underline{\theta}} = \begin{bmatrix} \hat{\psi}_m & \hat{r}_s & \hat{x}_d & \hat{x}_q \end{bmatrix}^T,\ \hat{\underline{\theta}} \in D_{\mathscr{M}},\ D_{\mathscr{M}} \in D_s \tag{4.9}$$

$$D_{\mathscr{M}} = \left\{\hat{\underline{\theta}}_{min} \le \hat{\underline{\theta}} \le \hat{\underline{\theta}}_{max}\right\}$$

Here, $\hat{\underline{\theta}}$ is the estimated parameter vector, $\mathbf{L}$ is the gain-matrix, $\underline{\epsilon}$ is the prediction error that is attempted to minimize and eventually nullify, choosing appropriate $\mathbf{L}$. A rank-

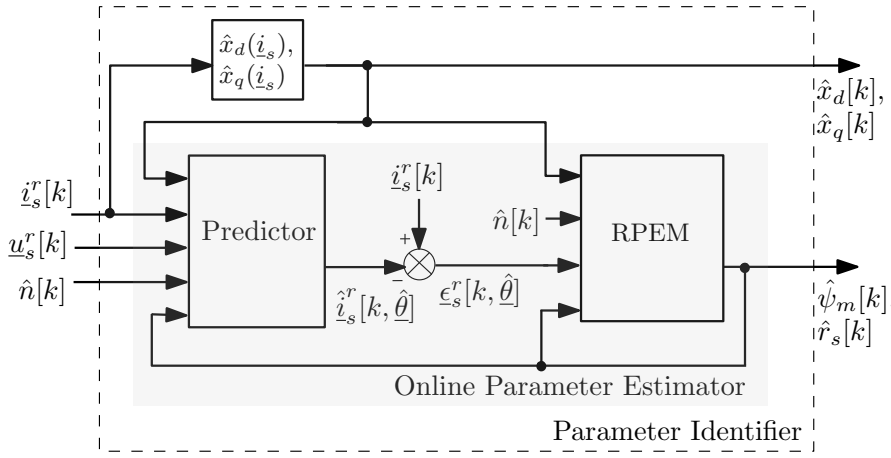

FIGURE 4.7. Block diagram of the parameter identifier and the Online Parameter Estimator with Open-Loop Predictor.

deficiency issue [39] prevents identifying all parameters premised on the FE signals. To circumvent this challenge without compromising the performance, $\hat{\psi}_m$ and $\hat{r}_s$ are identified online and the inductances are identified offline and updated in real-time. Figure 4.7 illustrates the structure of the Parameter Identifier in the proposed scheme.

$$\begin{aligned}\frac{\mathbf{x}_s^r(\underline{i}_s)}{\omega_n}\frac{\mathrm{d}\hat{\underline{i}}_s^r(t,\hat{\underline{\theta}})}{\mathrm{d}t} &= \underline{u}_s^r(t) - \hat{r}_s(t)\cdot\hat{\underline{i}}_s^r(t,\hat{\underline{\theta}}) \\ &\quad -\mathbf{j}\cdot\hat{n}(t,\hat{\underline{\theta}})\cdot\mathbf{x}_s^r(\underline{i}_s)\cdot\hat{\underline{i}}_s^r(t,\hat{\underline{\theta}}) - \mathbf{j}\cdot\hat{n}(t,\hat{\underline{\theta}})\cdot\underline{\psi}_m^r(t)\end{aligned} \tag{4.10}$$

The predictor is designed with the Full-Order Model, $\mathscr{M}_{u\theta}$ given in (4.10), that yields $\hat{\underline{i}}_s^r$. The stability of the predictor in the continuous and discrete-time domains is discussed in [40], which concludes that the trapezoidal rule-based implementation in the DSP guarantees stable prediction across the full-speed range. $\underline{\epsilon}$ becomes $\underline{\epsilon} = \underline{i}_s^r - \hat{\underline{i}}_s^r$ for which a simplified expression in steady-state can be obtained as below, w.r.t. $\hat{\psi}_m$, $\hat{r}_s$ where $\delta\underline{\theta} = \underline{\theta} - \hat{\underline{\theta}}$.

$$\begin{aligned}\epsilon_d &= -\left(\frac{\hat{n}^2\cdot\hat{x}_q}{\hat{r}_s^2+\hat{n}^2\cdot\hat{x}_d\cdot\hat{x}_q}\right)\delta\psi_m \\ &\quad -\left(\frac{\hat{r}_s}{\hat{r}_s^2+\hat{n}^2\cdot\hat{x}_d\cdot\hat{x}_q}\cdot i_d + \frac{\hat{n}\cdot\hat{x}_q}{\hat{r}_s^2+\hat{n}^2\cdot\hat{x}_d\cdot\hat{x}_q}\cdot i_q\right)\delta r_s \\ \epsilon_q &= -\left(\frac{\hat{n}\cdot\hat{r}_s}{\hat{r}_s^2+\hat{n}^2\cdot\hat{x}_d\cdot\hat{x}_q}\right)\delta\psi_m \\ &\quad -\left(\frac{\hat{r}_s}{\hat{r}_s^2+\hat{n}^2\cdot\hat{x}_d\cdot\hat{x}_q}\cdot i_q - \frac{\hat{n}\cdot\hat{x}_d}{\hat{r}_s^2+\hat{n}^2\cdot\hat{x}_d\cdot\hat{x}_q}\cdot i_d\right)\delta r_s\end{aligned} \tag{4.11}$$

It is assumed that δx_d, δx_q are eliminated in real-time by using the offline identified values. The full expression that entails δx_d, δx_q is disclosed in [41]. Eq. (4.11) provides

insight into the interplay among the rotor speed, stator current, and parameter discrepancies. $\underline{\epsilon}$ is also the quantity that carries parametric error information into the RPEM, thus when $\delta\underline{\theta}$ reaches zero, the updating of the model parameter stops naturally. The updating of the model parameter will be weakened (or stopped) also when the drive is in an operating region, where $\underline{\epsilon}$ is not sensitive for the particular $\delta\underline{\theta}$. For example, at a standstill or very low speeds, $\underline{\epsilon}$ is null or poorly conditioned w.r.t. $\delta\psi_m$-information, thus not suitable for $\hat{\psi}_m$-adaptation in the very low-speed region. Similarly, at no- or smaller- stator current conditions, $\hat{r}_s$-adaptation becomes impossible or poor.

$$\mathbf{L}[k] = \gamma_{0,Lk}\frac{1}{r[k]}\boldsymbol{\Psi}[k] \tag{4.12}$$

$$r[k] = r[k-1] + \gamma_{0,rk}\Big(tr\left\{\boldsymbol{\Psi}[k]\cdot\boldsymbol{\Psi}^T[k]\right\} - r[k-1]\Big) \tag{4.13}$$

$$\begin{aligned}\Psi : \frac{\mathrm{d}}{\mathrm{d}\underline{\hat{\theta}}}\left(\frac{\mathrm{d}\underline{\hat{i}}_s^r(t,\underline{\hat{\theta}}))}{\mathrm{d}t}\right) &= \frac{\mathrm{d}}{\mathrm{d}t}\left(\frac{\mathrm{d}\underline{\hat{i}}_s^r(t,\underline{\hat{\theta}}))}{\mathrm{d}\underline{\hat{\theta}}}\right)\\ &= \frac{\mathrm{d}}{\mathrm{d}\underline{\hat{\theta}}}\left(\underline{f}_c\left(t,\underline{\hat{i}}_s^r(t,\underline{\hat{\theta}}),\underline{u}_s^r(t),n(t);\underline{\hat{\theta}}\right)\right)\end{aligned} \tag{4.14}$$

The other main component in (4.8) is $\mathbf{L}$ that can be computed using a few different algorithms, out of which the Stochastic Gradient Algorithm (SGA) appears to be the optimal choice from the perspective of temperature-sensitive parameter identification [41]. SGA can be expressed as in (4.12) [38]. The centerpiece of SGA is $\boldsymbol{\Psi}^T$ of which the generalized dynamic form can be expressed as in (4.14), of which $\underline{f}_c$ is a function equivalent to the right-hand side of (4.10).

$$\Psi_{11} : \frac{\mathrm{d}\hat{i}_d}{\mathrm{d}\hat{\psi}_m} = -\frac{\hat{n}^2\cdot\hat{x}_q}{\hat{r}_s^2+\hat{n}^2\cdot\hat{x}_q\cdot\hat{x}_d} \tag{4.15a}$$

$$\Psi_{12} : \frac{\mathrm{d}\hat{i}_q}{\mathrm{d}\hat{\psi}_m} = -\frac{\hat{n}\cdot\hat{r}_s}{\hat{r}_s^2+\hat{n}^2\cdot\hat{x}_q\cdot\hat{x}_d} \tag{4.15b}$$

$$\Psi_{21} : \frac{\mathrm{d}\hat{i}_d}{\mathrm{d}\hat{r}_s} = -\frac{\hat{r}_s\cdot\hat{i}_d}{\hat{r}_s^2+\hat{n}^2\cdot\hat{x}_q\cdot\hat{x}_d} - \frac{\hat{n}\cdot\hat{x}_q\cdot\hat{i}_q}{\hat{r}_s^2+\hat{n}^2\cdot\hat{x}_q\cdot\hat{x}_d} \tag{4.16a}$$

$$\Psi_{22} : \frac{\mathrm{d}\hat{i}_q}{\mathrm{d}\hat{r}_s} = -\frac{\hat{r}_s\cdot\hat{i}_q}{\hat{r}_s^2+\hat{n}^2\cdot\hat{x}_q\cdot\hat{x}_d} + \frac{\hat{n}\cdot\hat{x}_d\cdot\hat{i}_d}{\hat{r}_s^2+\hat{n}^2\cdot\hat{x}_q\cdot\hat{x}_d} \tag{4.16b}$$

The dynamic forms of the $\boldsymbol{\Psi}^T$ w.r.t. $\hat{\psi}_m$ and $\hat{r}_s$ are presented in Chapter 3. The corresponding steady-state $\boldsymbol{\Psi}^T$ forms can be derived by equalizing the left-hand side of their dynamic forms to zero. The final derivations are given in (4.15a) and (4.16a) w.r.t. $\hat{\psi}_m$ and $\hat{r}_s$. Similarly, the equivalent steady-state gradient functions w.r.t. $\hat{x}_d$ and

$\hat{x}_q$ become:

$$\Psi_{31}: \frac{\mathrm{d}\hat{i}_d}{\mathrm{d}\hat{x}_d} = \frac{\left(\frac{\hat{r}_s^2 - \hat{n}^2 \cdot \hat{x}_d \cdot \hat{x}_q}{\hat{x}_d}\right)}{\hat{r}_s^2 + \hat{n}^2 \cdot \hat{x}_d \cdot \hat{x}_q} \cdot \hat{i}_d - \frac{\frac{\hat{r}_s \cdot \hat{x}_q \cdot \hat{n}}{\hat{x}_d}}{\hat{r}_s^2 + \hat{n}^2 \cdot \hat{x}_d \cdot \hat{x}_q} \cdot \hat{i}_q - \frac{\frac{\hat{r}_s}{\hat{x}_d}}{\hat{r}_s^2 + \hat{n}^2 \cdot \hat{x}_d \cdot \hat{x}_q} \cdot u_d \tag{4.17a}$$

$$\Psi_{32}: \frac{\mathrm{d}\hat{i}_q}{\mathrm{d}\hat{x}_d} = \frac{-2 \cdot \hat{n} \cdot \hat{r}_s}{\hat{r}_s^2 + \hat{n}^2 \cdot \hat{x}_d \cdot \hat{x}_q} \cdot \hat{i}_d + \frac{\hat{n}^2 \cdot \hat{x}_q}{\hat{r}_s^2 + \hat{n}^2 \cdot \hat{x}_d \cdot \hat{x}_q} \cdot \hat{i}_q + \frac{\hat{n}}{\hat{r}_s^2 + \hat{n}^2 \cdot \hat{x}_d \cdot \hat{x}_q} \cdot u_d \tag{4.17b}$$

$$\Psi_{41}: \frac{\mathrm{d}\hat{i}_d}{\mathrm{d}\hat{x}_q} = \frac{2 \cdot \hat{n} \cdot \hat{r}_s}{\hat{r}_s^2 + \hat{n}^2 \cdot \hat{x}_d \cdot \hat{x}_q} \cdot \hat{i}_q - \frac{\hat{n}^2 \cdot \hat{x}_d}{\hat{r}_s^2 + \hat{n}^2 \cdot \hat{x}_d \cdot \hat{x}_q} \cdot \hat{i}_d - \frac{\hat{n}}{\hat{r}_s^2 + \hat{n}^2 \cdot \hat{x}_d \cdot \hat{x}_q} \cdot u_q \tag{4.18a}$$

$$\Psi_{42}: \frac{\mathrm{d}\hat{i}_q}{\mathrm{d}\hat{x}_q} = \frac{\left(\frac{\hat{r}_s^2 - \hat{n}^2 \cdot \hat{x}_d \cdot \hat{x}_q}{\hat{x}_q}\right)}{\hat{r}_s^2 + \hat{n}^2 \cdot \hat{x}_d \cdot \hat{x}_q} \cdot \hat{i}_q - \frac{\frac{\hat{r}_s \cdot \hat{x}_d \cdot \hat{n}}{\hat{x}_q}}{\hat{r}_s^2 + \hat{n}^2 \cdot \hat{x}_d \cdot \hat{x}_q} \cdot \hat{i}_d - \frac{\frac{\hat{r}_s}{\hat{x}_q}}{\hat{r}_s^2 + \hat{n}^2 \cdot \hat{x}_d \cdot \hat{x}_q} \cdot u_q \tag{4.18b}$$

To elaborate on the behaviors of the prediction gradients, the above steady-state functions are visualized in Figure 4.8 and Figure 4.9 in a single quadrant torque-speed plane, from which, the following observations can be made:

Remark 1: Ψ_{11} is clearly more sensitive than Ψ_{12}. Moreover, Ψ_{11} becomes a stronger signal beyond low speeds, 0.1 pu w.r.t. this machine.

Remark 2: In contrast to the above remark, $\Psi_{21,22}$ become stronger at and around zero speed.

Remark 3: $\Psi_{11,12} = 0$ at $n = 0$, yet they are independent from stator current. This means that $\hat{\psi}_m$-adaptation is prohibited at a rotor standstill. Similarly, $\hat{r}_s$-adaptation is prohibited at the absence of stator current.

Remark 4: Ψ_{21} changes its sign at $n = 0.01$, however, Ψ_{22} is consistent with its sign.

Remark 5: Prediction gradients w.r.t. $\hat{x}_{d,q}$ are stator current-dependent, i.e., at lower loads, the gradients become trivial.

Remark 6: The same prediction gradients become null at zero speed. By inspection of (4.17a) and (4.18a), one can observe the same, by applying $\hat{n} = 0$.

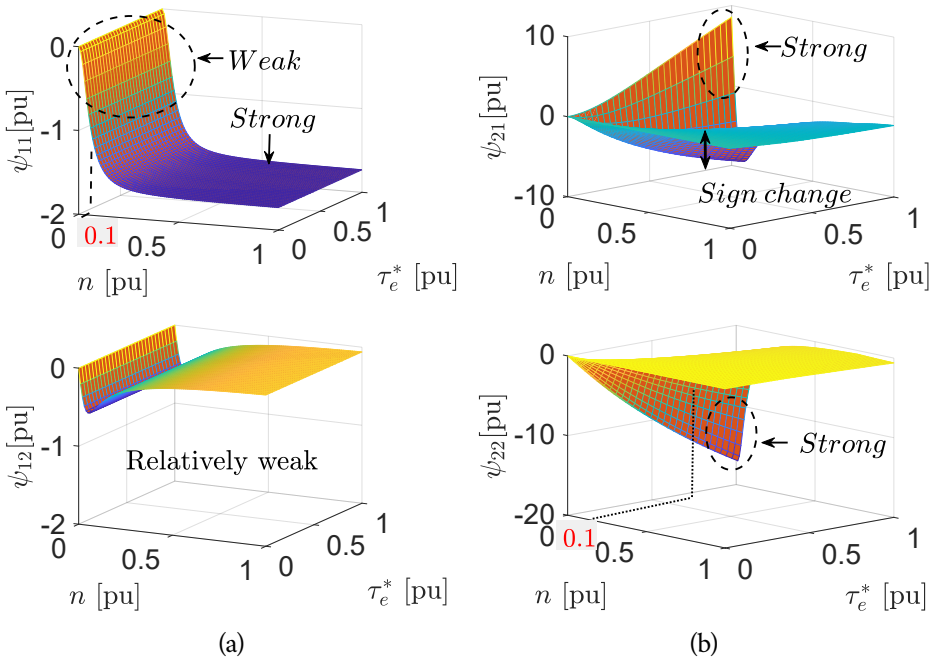

Figure 4.8. Steady-state prediction gradients in the speed-torque plane w.r.t. (a) $\hat{\psi}_m$ (b) $\hat{r}_s$.

Due to the reasons under *Remark 1* and *Remark 2*, it is shown in Chapter 3 that the $\hat{\psi}_m$ and $\hat{r}_s$ -adaptations are successful in exclusive speed regions. For this machine of interest, it appears from Figure 4.8 that beyond $n = 0.1$ pu is a speed region favorable for $\hat{\psi}_m$-tracking, whereas below $n = 0.1$ towards zero speed is attractive for $\hat{r}_s$-tracking.

The next significant element in (4.8) is the Hessian function, $r[k]$, given in (4.13). Different formulations and behaviors of the scalar Hessian function were investigated in section 3.4.2. They will be assessed for their dynamic impact in section 4.4.3.

4.3.4 *Online Method for ψ_m and r_s Identification*

By applying the significant prediction gradient elements into (4.8), the specific algorithms to identify temperature-sensitive parameters online can be developed as follows:

$$\hat{\psi}_m[k] = \hat{\psi}_m[k-1] + \frac{\gamma_{0,Lk}}{r[k]} \left(\Psi_{11}[k] \cdot \epsilon_d[k]\right) \tag{4.19}$$

$$\hat{r}_s[k] = \hat{r}_s[k-1] + \frac{\gamma_{0,Lk}}{r[k]} \left(\Psi_{21}[k] \cdot \epsilon_d[k] + \Psi_{22}[k] \cdot \epsilon_q[k]\right) \tag{4.20}$$

The choice of $r[k]$ can be either (3.29a) or (3.29b) for $\hat{\psi}_m$-adaptation and (3.29a) or (3.29d) or (3.29e) for $\hat{r}_s$-adaptation. This will be investigated in Section 4.4.

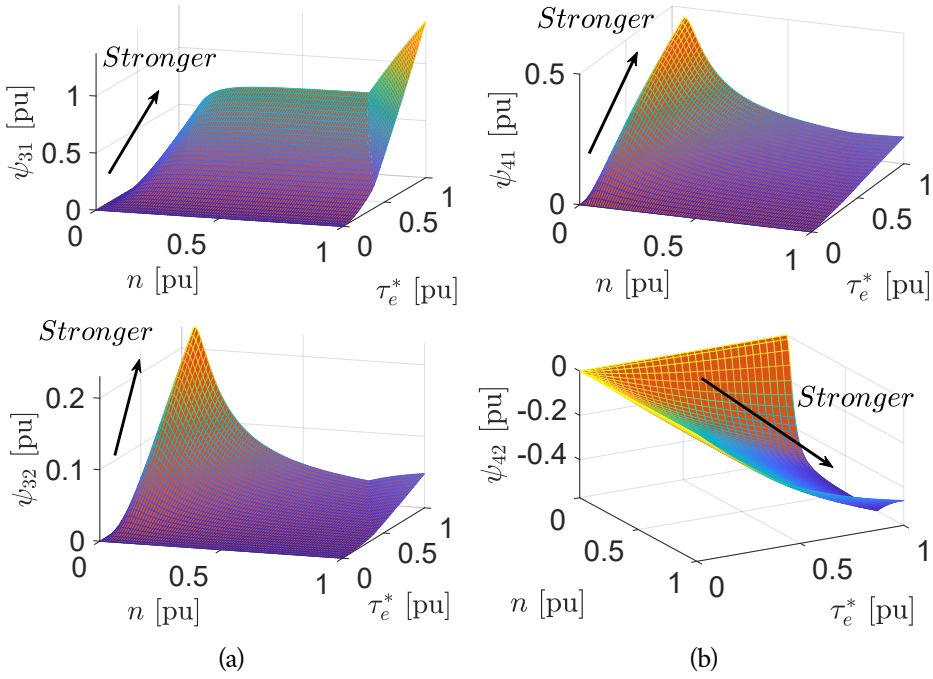

FIGURE 4.9. Steady-state prediction gradients in the speed-torque plane w.r.t. (a) $\hat{x}_d$ (b) $\hat{x}_q$.

4.3.5 *Online Method for x_d and x_q Identification*

The inductances can be identified online using the following expressions:

$$\hat{x}_d[k] = \hat{x}_d[k-1] + \frac{\gamma_{0,Lk}}{r[k]} \left(\Psi_{31}[k] \cdot \epsilon_d[k] + \Psi_{32}[k] \cdot \epsilon_q[k] \right) \tag{4.21}$$

$$\hat{x}_q[k] = \hat{x}_q[k-1] + \frac{\gamma_{0,Lk}}{r[k]} \left(\Psi_{41}[k] \cdot \epsilon_d[k] + \Psi_{42}[k] \cdot \epsilon_q[k] \right) \tag{4.22}$$

One can adopt the two time-scale approach [42, 43] to circumvent the rank-deficiency, such that the current-dependent inductances can be identified in the faster routine while assuming the temperature-sensitive parameters remain constant during their short adaptation time-steps.

4.3.6 *Offline Method for x_d and x_q Identification*

Here, an intuitive method is presented to identify $\hat{x}_d$, $\hat{x}_q$ offline, for real-time usage in the processor. The proposed experimentation is premised on the $\mathscr{M}_{u\theta}$-based Open-Loop Predictor. The method assumes $\hat{\psi}_m$ and $\hat{r}_s$ are correctly identified. It is shown in Chapter 6 that $\hat{\psi}_m$ and $\hat{r}_s$ identifications are unaffected by other parameter discrepancies during no-load and zero speed conditions, respectively. To prevent the influence

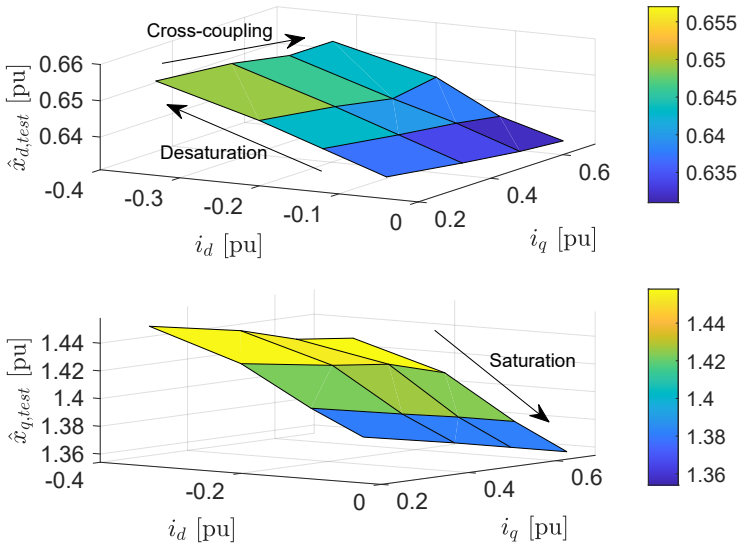

Figure 4.10. Experimentally identified $\hat{x}_d(\underline{i}_s)$, $\hat{x}_q(\underline{i}_s)$ using the proposed offline method.

of temperature-affected variations, the tests must be performed in short runs at regular intervals. It is assumed that no error in the rotor speed acquisition or rotor position offset exists during the experiment. To improve the accuracy of the identification, the IPMSM drive should be operated in the torque mode whereas the load drive is in the speed mode. Under this configuration, the friction and other mechanical losses will be served off by the load drive or can be neglected, and thus the stator currents in the IPMSM can be assumed only for the production of the commanded torque. If the above assumptions are held true and the inductances are correctly identified, the following expressions become valid in steady-state:

$$u_d = \underbrace{r_s \cdot i_d - n \cdot x_q \cdot i_q}_{\text{Physical}} = \underbrace{\hat{r}_s \cdot \hat{i}_d - n \cdot \hat{x}_q \cdot \hat{i}_q}_{\text{Model}}$$

$$u_q = \underbrace{r_s \cdot i_q + n \cdot x_d \cdot i_d + n \cdot \psi_m}_{\text{Physical}} = \underbrace{\hat{r}_s \cdot \hat{i}_q + n \cdot \hat{x}_d \cdot \hat{i}_d + n \cdot \hat{\psi}_m}_{\text{Model}} \tag{4.23}$$

Under these conditions, when there exist differences in actual and predicted currents, i.e. $i_d - \hat{i}_d = \delta i_d \neq 0$ and/or $i_q - \hat{i}_q = \delta i_q \neq 0$, the following expressions can be derived by neglecting the voltage drops across the resistances because $r_s << x_{d,q}$.

$$\delta i_d = \frac{u_q - n \cdot \psi_m}{n \cdot x_q \cdot \hat{x}_q}(\hat{x}_d - x_d), \;\; \delta i_q = \frac{u_d}{n \cdot x_q \cdot \hat{x}_q}(x_q - \hat{x}_q) \tag{4.24}$$

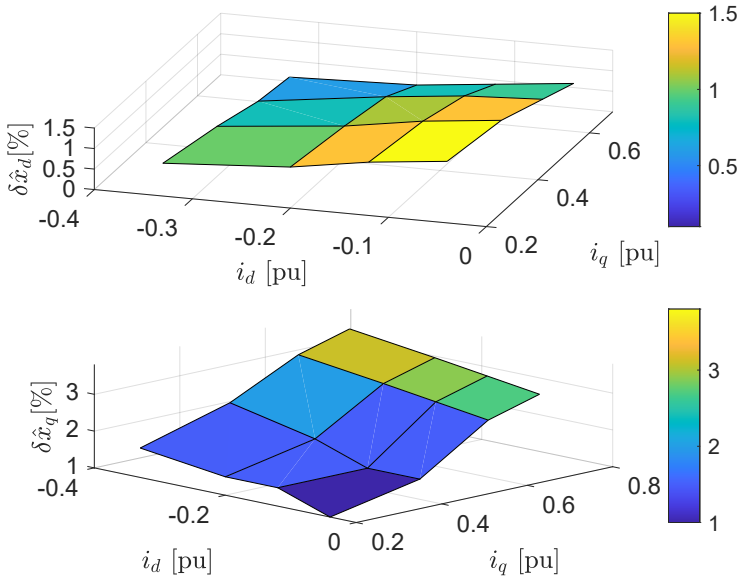

FIGURE 4.11. The deviation of experimentally identified $\hat{x}_d(\underline{i}_s)$, $\hat{x}_q(\underline{i}_s)$ w.r.t. them using FEM.

Eq. (4.24) tells us that, under the given conditions, if the model inductances are correctly tuned, then $\delta i_{d,q}$ will be driven to zero. Based on this criteria, $\hat{x}_d(\underline{i}_s), \hat{x}_q(\underline{i}_s)$ were identified and the experimental results are given in Figure 4.10. The identified $\hat{x}_d$ appears to be slightly increasing as the i_d increases (in the negative direction), a possible outcome in IPMSM, due to desaturation of the d-axis with the increasing i_d that opposes the magnetic flux linkage, to pull the axis out of saturation. It is also noticed mild effects of the cross-coupling from the i_q that cause a slight decline in the $\hat{x}_d$ as the i_q increases. Regarding $\hat{x}_q$, the saturation phenomenon is quite evident as i_q increases.

For the purpose of verification, the difference between the inductances identified using the FEM method and this experimental method as a percentage of the FEM-based values are plotted and shown in Figure 4.11. It turns out that the d-axis values are aligned well with a maximum error of 1.5%. The q-axis values also show satisfactory agreement with a maximum discrepancy of 3.5%. The reasons behind these discrepancies could be; 1) deviation of conditions from some of the assumptions made in the experimental method, 2) assumption of the material properties of the magnet or/and the rotor in the FEM are inaccurate, or 3) the geometric measurements to construct the FEM are inaccurate. These offline identified values are programmed in a LUT in the DSP, such that the appropriate inductances are updated in the algorithms in real-time.

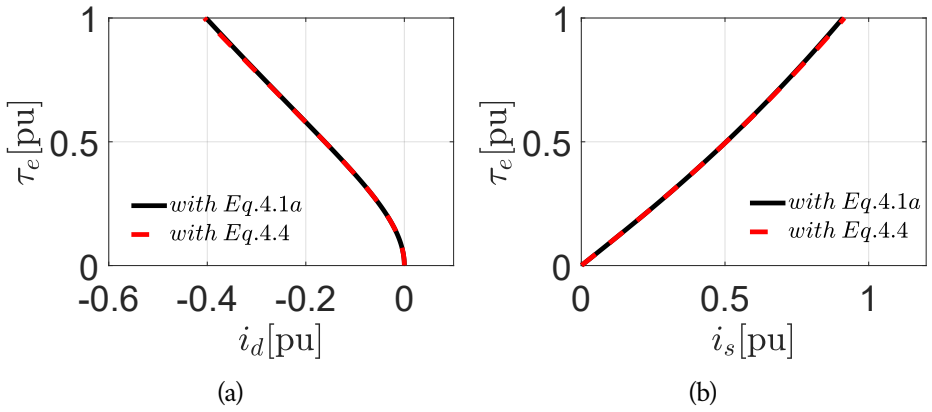

FIGURE 4.12. Comparison of computation formulae (4.1a) and (4.4), to realize the MTPA strategy: (a) $\tau_e(i_d^*)$ (b) $\tau_e(i_s^*)$.

4.4 INVESTIGATION USING THE FPGA-BASED REAL-TIME SIMULATOR

In this section, the same ERTS employed in Chapter 3 is used to investigate the RPEM dynamics and the cross-coupling among $\underline{\hat{\theta}}$ and between $\underline{\hat{\theta}}$ and $\hat{\vartheta}$. Figure 3.10 illustrates the ERTS design layout. The drive data are as given in Table 4.1. The machine inductances in the ERTS machine model are independent of the stator currents, and thus the corresponding rated load values are applied. IGBT switching frequency, f_{sw}, is 4 kHz. The processor sampling time, T_{samp}, is equivalent to the PWM double-update sampling time-step. Two-level VSI with asymmetrical modulation and 3rd harmonic injection is used to drive the machine.

4.4.1 *Investigation of MTPA Functions*

Figure 4.12 (a) and (b) illustrate the comparisons of (4.1a) and (4.4) w.r.t. $\tau_e(i_d^*)$ and $\tau_e(i_s^*)$ respectively. It appears that the proposed expression in (4.4) renders almost the same τ_e as the expression in (4.1a), and thus can be applied, without compromising the MTPA-targets, across the operating range.

4.4.2 *Cross-coupling between $\hat{\psi}_m$ and $\hat{r}_s$-Adaptations*

An exclusiveness of sensitive speed regions was evident from *Remark 1* and *Remark 2* in section 4.3.3 regarding $\hat{\psi}_m$ and $\hat{r}_s$. In this section, it is investigated, how these parameter adaptations behave when both of them are erroneous, given their cross-coupling. It's worth noting that in a typical IPMSM, in per unit values, $\psi_m \gg r_s$, $r_s \ll 1$. Henceforth, $\delta\psi_m$ can influence heavily upon the $\hat{r}_s$, if both or only $\hat{r}_s$ is adapted.

Analytical expressions can be derived from (4.11) as below, to investigate different scenarios:

Case 1: $\delta\psi_m$ and $\delta r_s \neq 0$ and only $\hat{r}_s$ adapts

Thus, $\hat{r}_s$ adapts until $\epsilon_d \rightarrow 0$, then (4.11) becomes:

$$\hat{r}_s = r_s + \frac{\hat{n}^2 \cdot \hat{x}_q}{\left(\hat{r}_s \cdot i_d + \hat{n} \cdot \hat{x}_q \cdot i_q\right)} \cdot \delta\psi_m \tag{4.25}$$

Accordingly, it is seen that, unless $n = 0$ or $\delta\psi_m = 0$, $\hat{r}_s$ can be penalized due to even a small percentage of $\hat{\psi}_m$-errors, and this penalty increases when the speed increases. With this background, it becomes mandatory to cut off the $\hat{r}_s$-tracking beyond a certain rotor speed. In view of the magnitude decay of $\Psi_{21,22}$, the upper limit for $\hat{r}_s$-tracking is chosen to be $n_{lim} = 0.1\ pu$. To illustrate the worth of such a gain-scheduler, a scenario with simultaneous error is simulated and results are plotted in Figure 4.13. An initial error of 10% is introduced on both machine parameters simultaneously, at a rotor speed of 0.5 pu and $\tau_{e,l} = 0.5\,pu$. In Figure 4.13(a), both parameters are attempted to be tracked whereas in Figure 4.13(b), only $\hat{\psi}_m$ is tracked. It is seen that in the first case, $\hat{r}_s$ is severely penalized owing to the $\delta\psi_m$ errors, which results in $\hat{r}_s$ saturating in $-\hat{r}_{s,lim}$, and the degradation in position estimation (higher $\delta\vartheta$). Consequently, $\hat{\psi}_m$ sustains a steady-state error. Conversely, in Figure 4.13(b), $\hat{\psi}_m$ shows good tracking despite the sustained δr_s, owing to the gain-scheduler that prevented $\hat{r}_s$ from correction. Thus, a gain-scheduler to constrain $\hat{r}_s$ adaptation only within a -0.1 to 0.1 pu speed range is suggested. From the perspective of sensorless control, the precision of the stator resistance matters when the rotor approaches the standstill, and thus such a choice can be justified. Conversely, the impact of δr_s on $\hat{\psi}_m$ is often negligible due to the same asymmetry in the magnitudes, which was seen in Figure 4.13(b) and analyzed next.

Case 2: $\delta\psi_m$ and $\delta r_s \neq 0$ and only $\hat{\psi}_m$ adapts

Thus, $\hat{\psi}_m$ adapts until $\epsilon_{d,q} \rightarrow 0$, then (4.11) becomes:

$$\begin{aligned}
\hat{\psi}_m &= \psi_m + \frac{\left(\hat{r}_s \cdot i_d + \hat{n} \cdot \hat{x}_q \cdot i_q\right)}{\hat{n}^2 \cdot \hat{x}_q} \cdot \delta r_s \\
\hat{\psi}_m &= \psi_m + \frac{\left(\hat{n} \cdot \hat{x}_q \cdot i_d - \hat{r}_s \cdot i_q\right)}{\hat{n}^2 \cdot \hat{x}_q} \cdot \delta r_s
\end{aligned} \tag{4.26}$$

From (4.26),it is seen that, unless $n << 1$, $\hat{\psi}_m$ cannot be significantly impacted by δr_s. However, $n << 1$ is a speed region where $\hat{\psi}_m$-related prediction gradient, i.e., Ψ_{11} is anyway weak as noted in the previous section. Consequently, a potential penalty induced by δr_s will be attenuated too, to allow simultaneous identification with minimum repercussions.

The question remains, whether to restrict $\hat{\psi}_m$-tracking to higher speeds or should $\hat{\psi}_m$ be allowed to adapt in the zone where $\hat{r}_s$-sensitivity dominates. To facilitate the parallel adaptation, (4.20) is modified as below, such that ϵ_d and ϵ_q are dedicated to $\hat{\psi}_m$

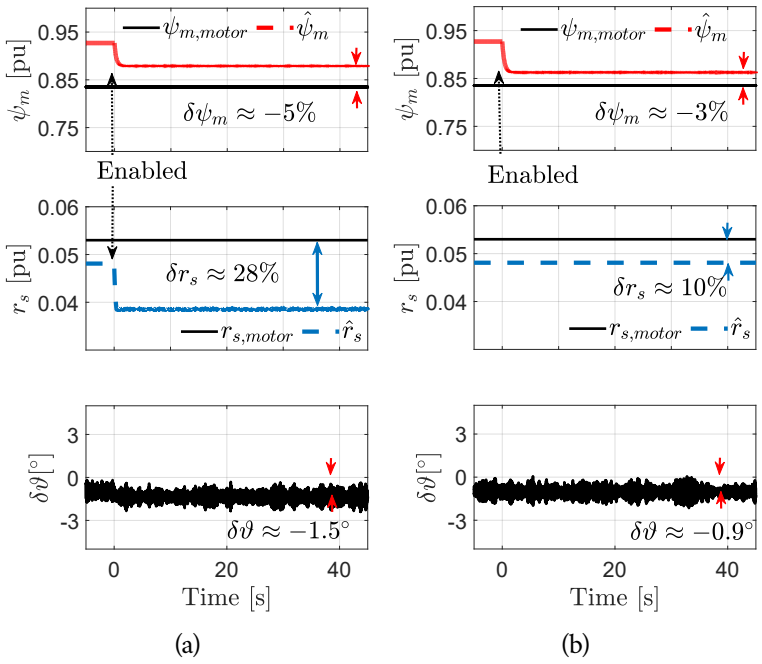

Figure 4.13. Position error and parameters when both $\hat{\psi}_m$ and $\hat{r}_s$ are erroneous by 10% at n = 0.5 pu, $\tau_{el} = 0.5$ (a) simultaneous parameter adaptation (b) preferred solution: only $\hat{\psi}_m$ adapts.

and $\hat{r}_s$ respectively.

$$\hat{r}_s[k] = \hat{r}_s[k-1] + \frac{\gamma_{0,Lk}}{r[k]} \left(\Psi_{22}[k] \cdot \epsilon_q[k]\right) \tag{4.27}$$

This modification is motivated by the fact that Ψ_{12} is anyway weak to disregard L_{12} in (4.19), that leaves ϵ_q redundant w.r.t. $\hat{\psi}_m$-adaptation. On the other hand, Ψ_{22} is substantial enough to adapt $\hat{r}_s$. Additionally, as noted in *Remark 4*, Ψ_{21} changes its sign near zero speed, which can render oscillatory adaptation due to noise, and thus, resorting only to $L_{22} \cdot \epsilon_q$ can be justified. Nevertheless, an alternative experiment can be designed to identify $\hat{r}_s$ at zero speed, only with i_d-injection, that can be useful during commissioning or non-operational modes of the drive, with the use of the following algorithm:

$$\hat{r}_s[k] = \hat{r}_s[k-1] + \frac{\gamma_{0,Lk}}{r[k]} \left(\Psi_{21}[k] \cdot \epsilon_d[k]\right) \tag{4.28}$$

Investigation of simultaneous error scenario is carried out at 0.05 pu rotor speed and $\tau_{e,l} = 0.5\ pu$, again with a 10% initial error in each model parameter. The results of only $\hat{r}_s$ adaptation is Figure 4.14(a) and $\hat{r}_s$, $\hat{\psi}_m$ simultaneous adaptation is in Figure 4.14(b). In this parallel adaptation, (4.19) and (4.27) are applied for the respective adaptations. Figure 4.14(b) shows that $\hat{\psi}_m$ begins to adapt rapidly in the correct direction. $\hat{r}_s$ adaption, in the meantime, is quite slow to sustain the same initial error after about

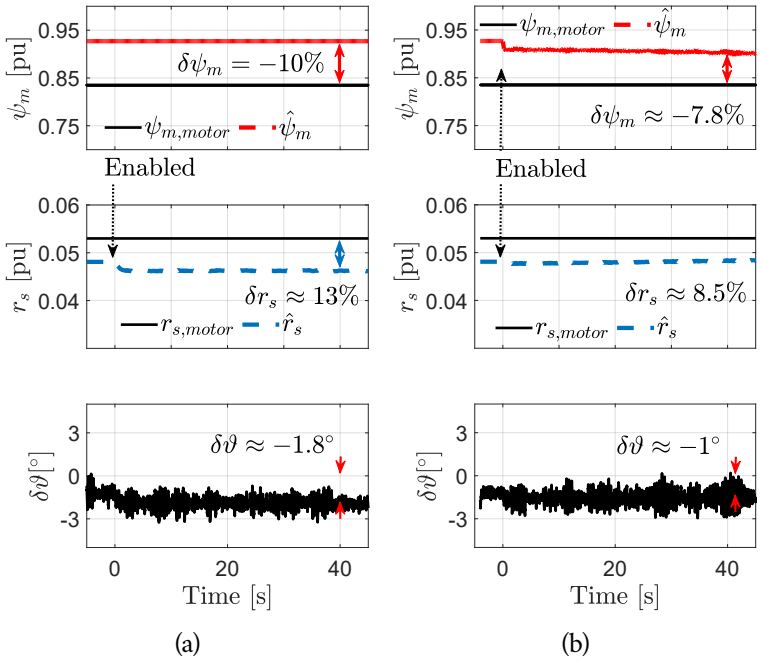

FIGURE 4.14. Position error and parameters when both $\hat{\psi}_m$ and $\hat{r}_s$ are erroneous by 10% at n = 0.05 pu, $\tau_{el} = 0.5$, and $r[k] = r_n$ (a) only $\hat{r}_s$ adapts (b) preferred solution: simultaneous parameter adaptation.

1 minute. In the former case in Figure 4.14(a), owing to the restriction of $\hat{\psi}_m$, $\hat{r}_s$ is degraded which results in deteriorating the observer performance compared to the parallel adaptation. The same phenomenon was evident in much smaller rotor speeds too, thus it is preferred to allow ψ_m-adaptation across the full speed range (with denominator limitations near standstill), during which L_{11} will naturally be weak when the rotor approaches the standstill, and be zero at the zero speed. Thus, a gain-scheduling scheme can be proposed as illustrated in Figure 4.15. In the same time, targeting the above scenarios, an analytical expression can be developed to compute $\delta\underline{\theta}$ as below:

Case 3: $\delta\psi_m$ and $\delta r_s \neq 0$ and both $\hat{\psi}_m$, $\hat{r}_s$ adapt
$\epsilon_d \rightarrow 0$, but $\delta\psi_m$ and $\delta r_s \neq 0$, then (4.11) becomes:

$$\delta\psi_m = \frac{(-\hat{r}_s \cdot i_d - \hat{n} \cdot \hat{x}_q \cdot i_q)}{\hat{n}^2 \cdot \hat{x}_q} \cdot \delta r_s \tag{4.29}$$

$\epsilon_q \rightarrow 0$, but δr_s and $\delta\psi_m \neq 0$, (4.11) becomes:

$$\delta r_s = \frac{(\hat{n} \cdot \hat{r}_s)}{(\hat{n} \cdot \hat{x}_d \cdot i_d - \hat{r}_s \cdot i_q)} \cdot \delta\psi_m \tag{4.30}$$

The respective $\delta\underline{\theta}$ values seen in the simulation results in relation to Figure 4.13 and Figure 4.14 can also be obtained using (4.29) and (4.30).

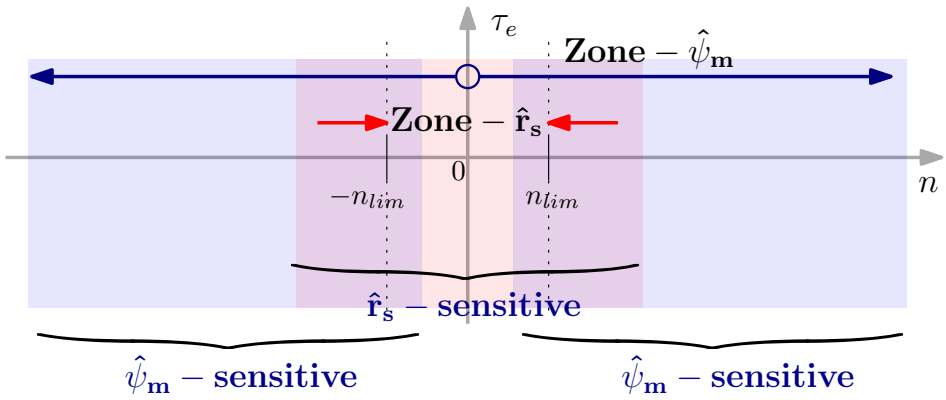

Figure 4.15. Gain-scheduling scheme to prevent undue $\hat{r}_s$-adaptation in the speeds beyond $|n_{lim}|$.

The impact of δx_d and δx_q on online tracking of these temperature-sensitive parameters is disclosed in Chapter 6. Accordingly, no-load and zero-speed conditions eliminate the influence from the inductances on $\hat{\psi}_m$ and $\hat{r}_s$ -identifications respectively, and thus these operating points become the best choices for the respective identification runs, during machine start-up (if possible) or commissioning.

4.4.3 *Impact of Hessian Choices*

In this section, the simultaneous tracking behaviors of $\hat{\psi}_m$ and $\hat{r}_s$ are assessed upon the choice of different $r[k]$ solutions from (3.29). Simulation runs showed that the impact of Hessians cannot significantly compensate for the largely erroneous $\hat{r}_s$ adaptations due to $\delta\psi_m$ in the higher speeds. Therefore, while maintaining the proposed gain-scheduling scheme, this discussion is limited to the parallel adaptation in the low-speed region, i.e., between $-n_{lim}$ and $+n_{lim}$. Figure 4.16 shows the related real-time simulation results at 0.05 pu speed and 0.5 load torque. In Figure 4.16(a), SGA is formulated using either $r[k] = r_n[k]$ or (3.29b) and (3.29c) for $\hat{\psi}_m$ and $\hat{r}_s$, respectively. It appears that opposing to the full trace, the traces with selective prediction gradients yield faster tracking. This phenomenon is further accentuated in Figure 4.16(b). Here, the trace for $\hat{r}_s$-tracking is limited to $r[k] = r_{rq}[k]$, which further amplifies the $\hat{r}_s$ estimation gains. Consequently, $\hat{\psi}_m$-tracking too becomes faster. In both figures, it is seen that the choice of traces with selective prediction gains appears to be more favorable than the trace with all prediction gradients. This difference in tracking can be attributed to the difference in the denominator behaviors noted in section 4.3.3.

According to the findings so far, the optimal stochastic gradient algorithms for

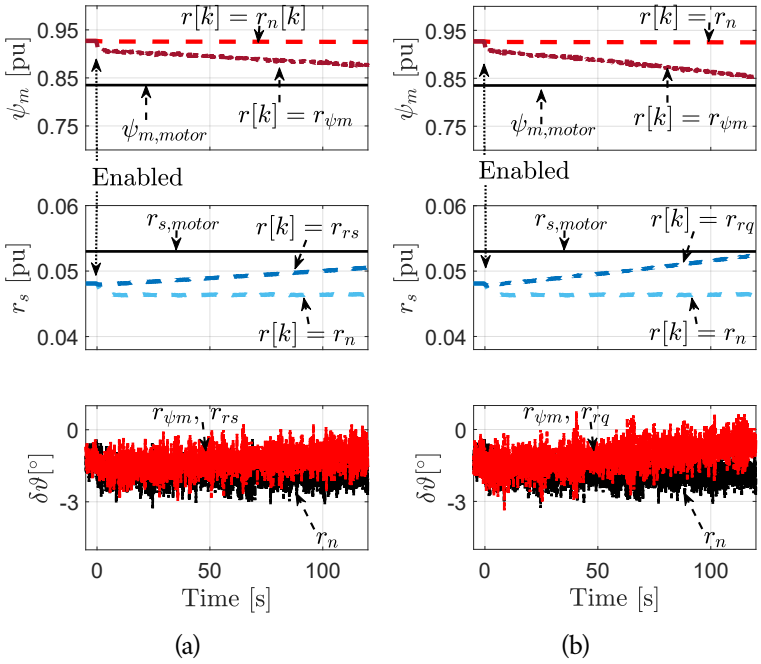

Figure 4.16. Simultaneous adaptation of $\hat{\psi}_m$ and $\hat{r}_s$ when both are erroneous by 10% at n = 0.05 pu, $\tau_{el} = 0.5$: (a) when SGA is formulated using $r[k] = r_n[k]$ vs. when using (3.29b) and (3.29c) for $\hat{\psi}_m$ and $\hat{r}_s$ respectively, (b) when SGA is formulated using $r[k] = r_n[k]$ vs. when using (3.29b) and (3.29e) for $\hat{\psi}_m$ and $\hat{r}_s$, respectively.

online identification of $\hat{\psi}_m$ and $\hat{r}_s$ become:

$$\hat{\psi}_m[k] = \hat{\psi}_m[k-1] + \frac{\gamma_{0,Lk}}{r_{\psi m}[k]} \left(\Psi_{11}[k] \cdot \epsilon_d[k]\right) \tag{4.31}$$

$$\hat{r}_s[k] = \hat{r}_s[k-1] + \frac{\gamma_{0,Lk}}{r_{rq}[k]} \left(\Psi_{22}[k] \cdot \epsilon_q[k]\right) \tag{4.32}$$

4.4.4 *Impact of the Observer on the Parameter Estimator*

In this section, the influence of the $\delta\vartheta$ on the performance and stability of the online parameter estimation is assessed. A steady-state electrical angle of 10° is added to the output of the $\hat{\vartheta}$ and removed at one point. Figure 4.17 (a) presents the performance at higher speeds. $\delta\vartheta$ influences $\hat{\psi}_m$ significantly. As soon as the angle injection is disabled, $\hat{\psi}_m$ adapts correctly and the observer yields no error. Figure 4.17 (b) presents the case at 0.05 pu speed, during which, only $\hat{r}_s$-tracking is allowed for the ease of inspection. Here, in addition to the injected error, an additional angle error is induced by the δr_s, which was originally caused by the injected 10° angle. As soon as it is removed, both $\delta\vartheta$ and δr_s get eliminated.

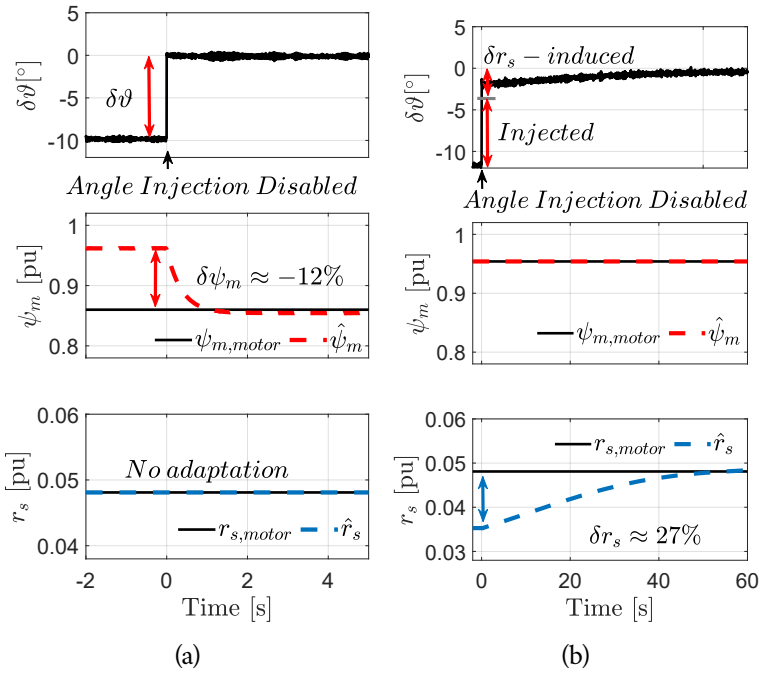

Figure 4.17. Influence from the position estimation error at $\tau_{el} = 0.5$ (a) at 0.3 pu speed, only $\hat{\psi}_m$ adapts. (b) At 0.05 speed, only $\hat{r}_s$ adapts.

4.5 Experimental Validation

The results and discussion of the experimental validation are given in this section. Experiments are conducted using a 3 kW IPMSM laboratory prototype shown in Figure 3.14, of which the data is given in Table 4.1. The SoC that houses the ERTS is used to drive the experimental prototype with the same control/estimation algorithms, and f_{sw}, T_{samp} configurations. However, one notable difference in this setup is that the nonlinearities in the machine inductances and VSI are accounted for, in the drive software program. The offline identified inductances-current mapping given in Figure 4.10 is used in real-time to update $\hat{x}_d$ and $\hat{x}_q$. The VSI-nonlinearity and dead-time effect compensation is performed according to [44].

4.5.1 Steady-State and Dynamic Performances

Figure 4.18 and Figure 4.19 correspond to different test cases when the drive is in the mechanical steady-state, yet electrical parameters are initially off-tuned and then tuned online. Figure 4.18 (a) and (b) display the performance during very low speeds, 0.01 and 0.02 pu respectively at 0.5 and 0.8 pu $\tau_{e,l}$. $\hat{r}_s$ was initially wrong and subsequently, at the 0-second point, the online adaptation scheme is enabled. At 0.01 pu speed, the

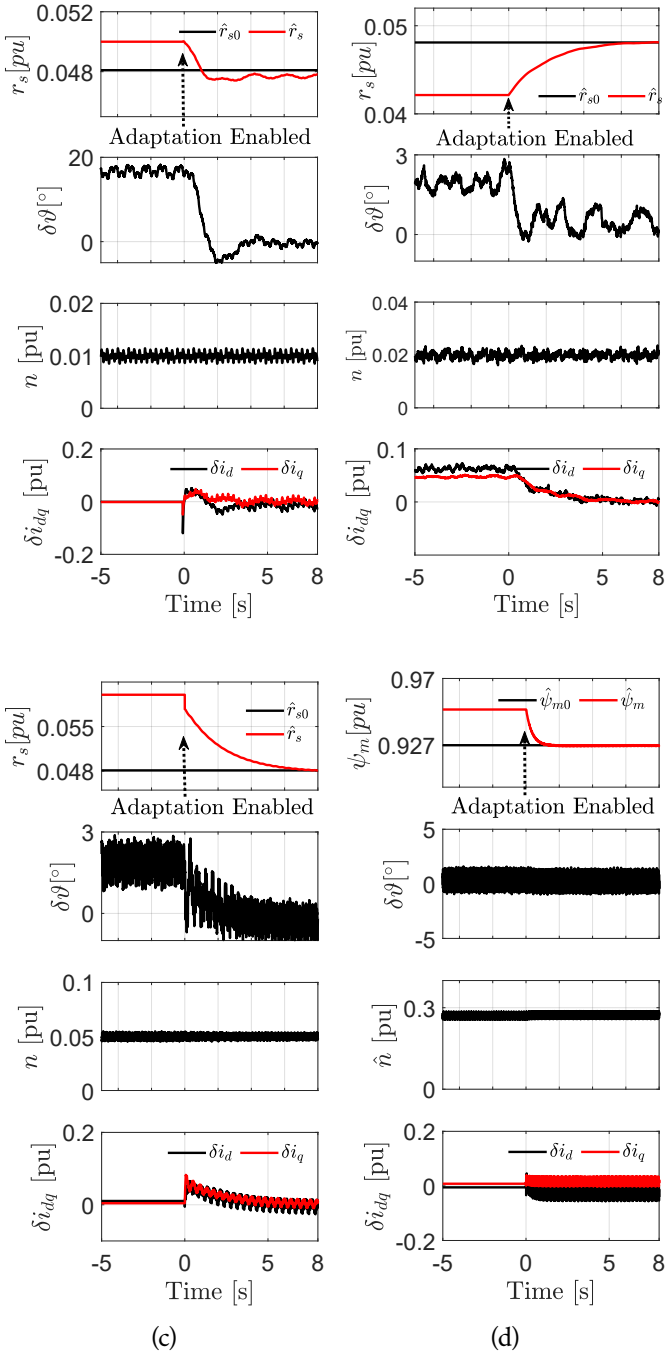

FIGURE 4.18. Experimental validations of the sensorless IPMSM drive before and after enabling the $\hat{r}_s$ adaptation (a) with $\tau_{e,l}$ = 0.5 pu, n^* = 0.01 pu (b) with $\tau_{e,l}$ = 0.8 pu, n^* = 0.02 pu (c) with $\tau_{e,l}$ = 0.5 pu, n^* = 0.05 pu (d) $\hat{\psi}_m$ adaptation with $\tau_{e,l}$ = 0.8 pu, n^* = 0.3 pu.

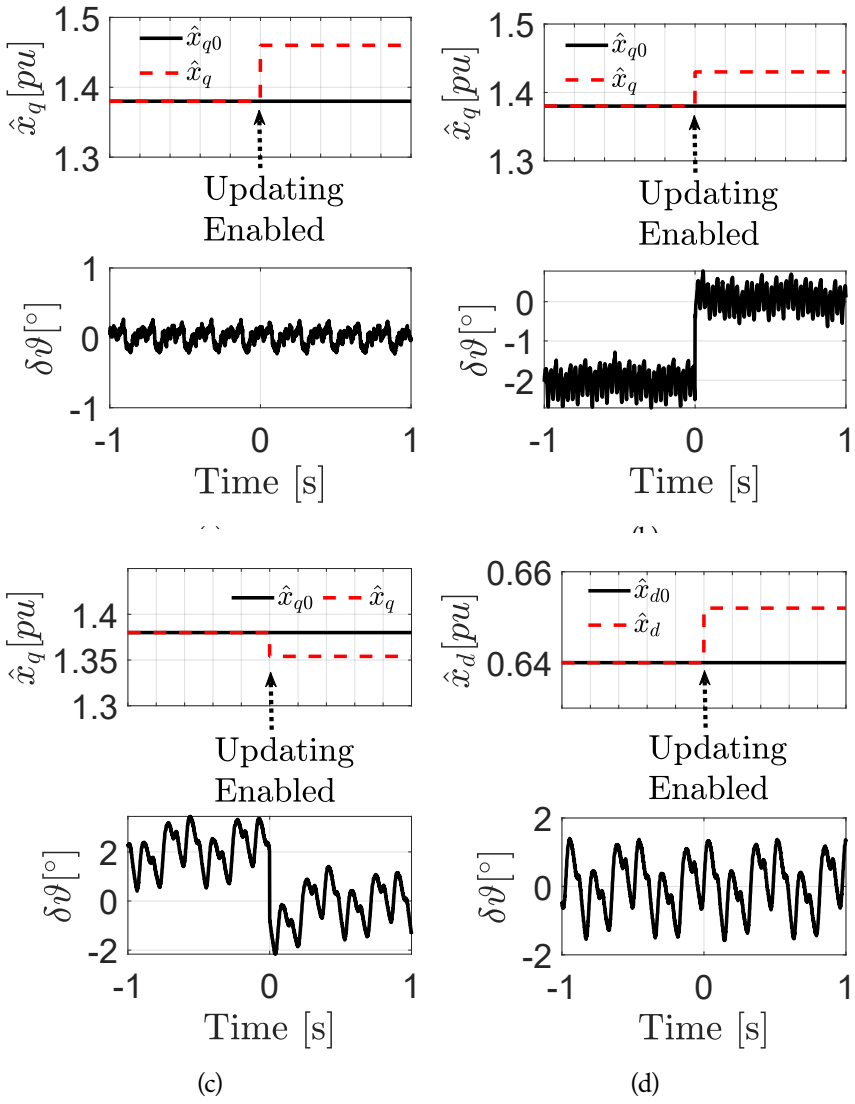

Figure 4.19. Experimental validations of the sensorless IPMSM drive before and after enabling the online updating of the $\hat{x}_q$ (a) with $\tau_{e,l}$ = 0 pu, n^* = 0.3 pu (b) with $\tau_{e,l}$ = 0.4 pu, n^* = 0.1 pu (c) with $\tau_{e,l}$ = 0.8 pu, n^* = 0.02 pu (d) $\hat{x}_d$ updating with $\tau_{e,l}$ = 0.8 pu, n^* = 0.02 pu.

improvement in $\delta\vartheta$ is dramatic, from about 20° to nearly 0°, owing to the accurate online adaptation of $\hat{r}_s$ and the accurate updating of $\hat{x}_q$. Figure 4.18 (c) again demonstrates the performance before and after the $\hat{r}_s$ adaptation, at 0.05 pu speed, in which, $\delta\vartheta$-improvement is evident. Figure 4.18 (d) shows the performance improvement at 0.3 pu speed when $\hat{\psi}_m$ is identified online, during which, $\delta\vartheta$ is not affected, due to the reliance only of $\mathscr{M}_u$ in the observer.

Similarly, Figure 4.19 (a), (b), and (c) demonstrate the assistance the active flux

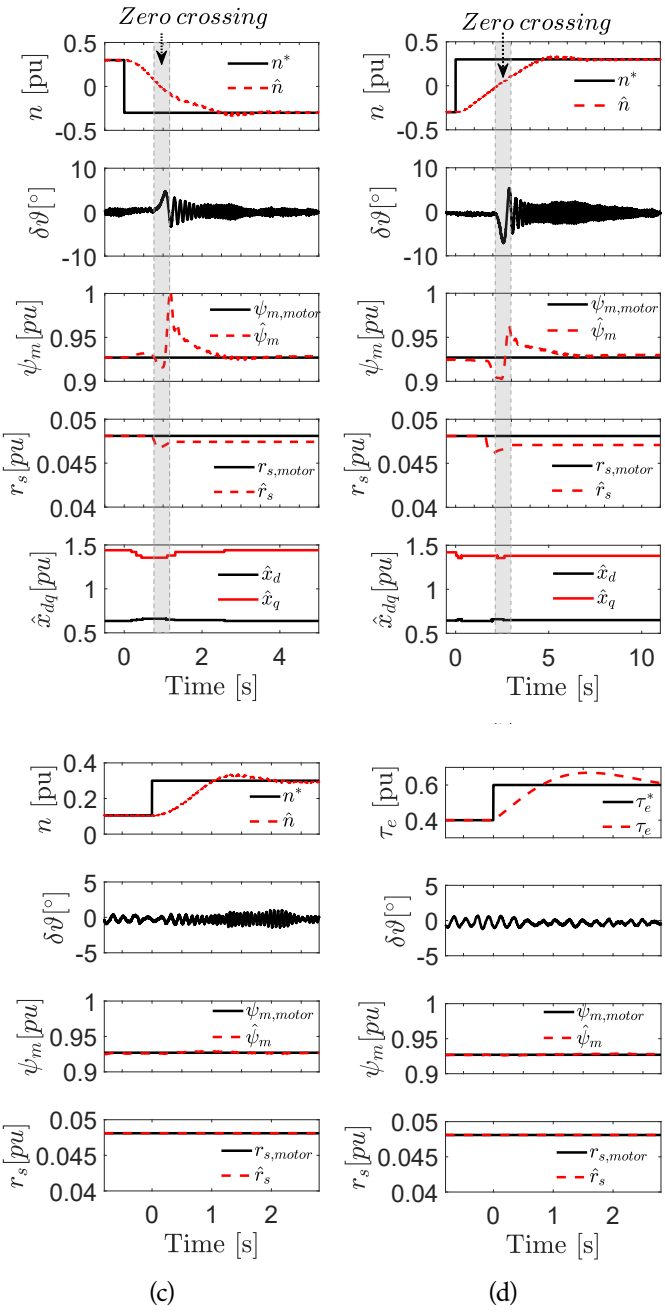

FIGURE 4.20. Dynamic performance of the sensorless IPMSM drive: speed reversal (a) from 0.3 to -0.3 pu at $\tau_{e,l}$ = 0 pu (b) speed reversal from -0.3 to +0.3 pu at $\tau_{e,l}$ = 0.5 pu (c) speed step change from 0.1 to 0.3 pu at $\tau_{e,l}$ = 0.5 pu (d) Load-torque step change from 0.4 to 0.6 pu at n^* = 0.2 pu.

observer receives, by updating $\hat{x}_q$, in contrast to the nameplate value, $\hat{x}_{q0}$. In the same way, Figure 4.19(d) illustrates the impact from $\hat{x}_d$-updating in contrast to its nameplate value $\hat{x}_{d0}$. During no-load (Figure 4.19(a)), $\hat{x}_q$-updating has no impact on the position estimation as then $\underline{\psi}_T = \underline{\psi}_s$. In the subsequent cases where $\underline{i}_s \neq 0$, the state estimation improvement is evident. The impact of from $\hat{x}_d$-updating also has no impact on the position estimation accuracy, as seen in the last figure. All in all, these results succeed to validate the proposed offline experiment method to identify x_d and x_q.

The performance and stability of the proposed scheme under mechanical dynamic conditions are investigated next. Figure 4.20 (a) and (b) correspond to speed reversal at no-load and 0.5 load-torque. In both cases, position estimation is excellent across the speed range, except during zero crossing, during which $\delta\vartheta$ increases momentarily. As soon the back EMF signal is strong enough, the observer recovers to render accurate estimations. These figures also present the traces of all electrical parameters. Both $\hat{\psi}_m$ and $\hat{r}_s$ track their physical counterparts accurately, including during the period of simultaneous adaptation. Figure 4.20 (c) and (d) correspond to the speed-step and load-torque step, respectively. In essence, the proposed sensorless scheme shows acceptable performance and stability during the mechanical dynamic conditions.

4.5.2 *Summary of Identification Methods and Validation Results*

The summary of parameter identification algorithms disclosed in this chapter is tabulated in Table 4.2, along with the necessary and sufficient conditions for identification and relevant drive modes of operation.

TABLE 4.2. Summary of experiments, their necessary and sufficient conditions, and drive modes of operation for parameter identification under the proposed scheme.

Parameter	Conditions	Algorithm
During drive operation		
$\hat{\psi}_m$	$n \neq 0$ $\delta x_d, \delta x_q \approx 0$	Eq. (4.31)
$\hat{r}_s$	$\lvert n \rvert < n_{lim}$ $i_q \neq 0$ $\delta x_d, \delta x_q \approx 0$	Eq. (4.32)
$\hat{x}_d$	$\underline{i}_s \neq 0$ $\delta\psi_m, \delta r_s \approx 0$	Eq. (4.21)
$\hat{x}_q$	$\underline{i}_s \neq 0$ $\delta\psi_m, \delta r_s \approx 0$	Eq. (4.22)
During commissioning/offline		
$\hat{r}_s$	$i_d \neq 0$	Eq. (4.28)
Offline		
$\hat{x}_{d,q}$	Section 4.3.6	Eq. (4.24)

The overall position estimation accuracy of the proposed combined scheme is summarized in Table 4.3. The results demonstrate that the proposed method renders commendable accuracy in the position estimation that can be attributed to the real-time updating of IPMSM electric parameters. The contribution from $\hat{x}_q$-updating

Table 4.3. Active flux observer performance comparison with and without the online parameter updating in different operating regions.

Operating range	Max. $\delta\vartheta$ No updating	Max. $\delta\vartheta$ With updating
When δr_s = 75 - 100%		
At 0.01 - 0.05 pu speed range	$> 15°$	$< 2°$
At 0.05 - 0.1 pu speed range	$\sim 2°$	$< 0.5°$
At 0.1 and above	$> 1°$	$\sim 0°$
When δx_q = ~5%		
At full load	$\sim 2°$	$\sim 0°$
Processor execution speed	~5 μs	~9.5 μs

is noticeable across the full-speed range, and $\hat{r}_s$-adaptation is of great assistance at lower speeds. The convergence speeds are within a few seconds for both $\hat{\psi}_m$ and $\hat{r}_s$, irrespective of n or $\tau_{e,l}$. Such speed of tracking is acceptable in consideration of the large thermal capacity that prevents sudden changes of these temperature-sensitive parameters. On the other hand, the inductance updating occurs at a delay only of T_{samp}. The execution time of the proposed combined scheme in the ARM processor is ~9 μs, whereas the position estimation alone takes ~4 μs. Unless the applications are bound to use low-cost processors or with very high rotor speeds, the additional time taken by the OPE can be conveniently accommodated in most of the industrial drives that employ IGBT-based inverters.

4.6 Conclusion and Summary

This chapter proposed a method to augment the sensorless control of three-phase IPMSM drives by combining a novel online parameter adaptation scheme that incorporates an open-loop current predictor. The inherent sensitivity of the open-loop predictor to the model parameters was capitalized by adopting prediction error gradients-based SGA to compute the estimation gains. The physical meanings behind the choices of estimation gains were disclosed. After assessing the possible Hessian formulations, among other alternatives, modifications to the general algorithm were proposed to supplement the simultaneous adaptation of $\hat{\psi}_m$ and $\hat{r}_s$. Algorithms to identify inductances online are developed by deriving the steady-state expressions of the respective prediction gradients. This chapter also disclosed an offline method to identify $\hat{L}_d$, $\hat{L}_q$ experimentally with the aid of the same predictor. The resulting inductance-current mapping was in acceptable agreement with those obtained from the FEM. The FPGA-based real-time simulations demonstrated the proposed algorithm modifications enhanced the feasibility of simultaneous adaptation during the low-speed region. In the experimental validations, R_s and Ψ_m were identified online whereas the offline identified $\hat{L}_d$, and $\hat{L}_q$ were updated online using a LUT in the processor. The proposed sensorless scheme yielded remarkable improvement in position estimation, particularly in the very low-speed range, in the presence of

varying parameters and various load conditions. The results also reflected that the sustained very low-speed operations are viable with the proposed method without test signal injection. Therefore, this scheme can be a desirable solution for a multitude of industrial applications that do not have persistent operations at and around the rotor standstill.

4.7 References

[1] Tayfun Gundogdu, Zi-Qiang Zhu, and Ching Chuen Chan. Comparative study of permanent magnet, conventional, and advanced induction machines for traction applications. *World Electric Vehicle Journal* (2022). doi: 10.3390. Cited on page/s 63.

[2] Joachim Holtz. Acquisition of position error and magnet polarity for sensorless control of PM synchronous machines. *IEEE Transactions on Industry Applications* **44** (4), 1172–1180 (2008). ISSN 00939994. doi: 10.1109/TIA.2008.921418. Cited on page/s 63.

[3] Cesar José Volpato Filho, Dianxun Xiao, Rodrigo Padilha Vieira, and Ali Emadi. Observers for high-speed sensorless PMSM drives : design methods , tuning challenges and future trends. *IEEE Access* (2021). Cited on page/s 64.

[4] Gaolin Wang, Maria Valla, and Jorge Solsona. Position sensorless permanent magnet synchronous machine drives - A review. *IEEE Transactions on Industrial Electronics* **67** (7), 5830–5842 (2020). ISSN 15579948. doi: 10.1109/TIE.2019.2955409. Cited on page/s 64.

[5] Gaolin Wang, Guoqiang Zhang, and Dianguo Xu. Saliency-tracking-based sensorless control for PMSM drives. In *Position Sensorless Control Techniques for Permanent Magnet Synchronous Machine Drives* chapter 3, pages 37–80. Springer, Singapore Singapore (2020). ISBN 9789811500503. doi: 10.1007/978-981-15-0050-3{_}3. Cited on page/s 64.

[6] Zhendong Zhang. Sensorless back EMF based control of synchronous PM and reluctance motor drives - a review. *IEEE Transactions on Power Electronics* **37** (9), 10290–10305 (2022). ISSN 19410107. doi: 10.1109/TPEL.2022.3162963. Cited on page/s 64.

[7] Marko Hinkkanen, Seppo E Saarakkala, Hafiz Asad, Ali Awan, M Eemeli, and Toni Tuovinen. Observers for sensorless synchronous motor drives : framework for design and analysis. *IEEE Transactions on Industriy Applications* **54** (6), 6090–6100 (2018). Cited on page/s 64.

[8] Shigeo Morimoto, Keisuke Kawamoto, Masayuki Sanada, and Yoji Takeda. Sensorless control strategy for salient-pole PMSM based on extended EMF in rotating reference frame. *IEEE Transactions on Industry Applications* **38** (4), 1054–1061 (2002). ISSN 00939994. doi: 10.1109/TIA.2002.800777. Cited on page/s 64.

[9] Ion Boldea, Mihaela Codruta Paicu, and Gheorghe Daniel Andreescu. Active flux concept for motion-sensorless unified AC drives. *IEEE Transactions on Power Electronics* **23** (5), 2612–2618 (2008). ISSN 08858993. doi: 10.1109/TPEL.2008.2002394. Cited on page/s 64, 69, 70.

[10] Silverio Bolognani, Ludovico Ortombina, Fabio Tinazzi, and Mauro Zigliotto. Model sensitivity of fundamental-frequency-based position estimators for sensorless PM and Reluctance synchronous motor drives. *Ieee Transactions on Industrial Electronics* **65** (1), 77–85 (2018). Cited on page/s 64, 71.

[11] Jorge Lara, Jianhong Xu, and Ambrish Chandra. Effects of rotor position error in the performance of field-oriented-controlled PMSM drives for electric vehicle traction applications. *IEEE Transactions on Industrial Electronics* **63** (8), 4738–4751 (2016). Cited on page/s 64.

[12] Toni Tuovinen, Marko Hinkkanen, Lennart Harnefors, and Jorma Luomi. Comparison of a reduced-order observer and a full-order observer for sensorless synchronous motor drives. *IEEE Transactions on Industry Applications* **48** (6), 1959–1967 (2012). doi: 10.1109/TIA.2012.2226200. Cited on page/s 64.

[13] Jun Hu and Bin Wu. New integration algorithms for estimating motor flux over a wide speed range.

IEEE Transactions on Power Electronics **13** (5), 969–977 (1998). ISSN 08858993. doi: 10.1109/63.712323. Cited on page/s 64, 71.

[14] Yukinori Inoue, Yasunori Kawaguchi, Shigeo Morimoto, and Masayuki Sanada. Performance improvement of sensorless IPMSM drives in a low-speed region using online parameter identification. *IEEE Transactions on Industry Applications* **47** (2), 798–804 (2011). ISSN 00939994. doi: 10.1109/TIA.2010.2101994. Cited on page/s 64.

[15] Oliver Wallscheid. Thermal monitoring of electric motors: state-of-the-art review and future challenges. *IEEE Open Journal of Industry Applications* **2** (June), 204–223 (2021). doi: 10.1109/ojia.2021.3091870. Cited on page/s 64.

[16] M.C. Paicu, I. Boldea, G.-D. Andreescu, and F. Blaabjerg. Very low speed performance of active flux based sensorless control: interior permanent magnet synchronous motor vector control versus direct torque and flux control. *IET Electric Power Applications* **3** (6), 551 (2009). ISSN 17518660. doi: 10.1049/iet-epa.2008.0290. URL http://digital-library.theiet.org/content/journals/10.1049/iet-epa.2008.0290. Cited on page/s 64, 69, 70.

[17] Chun Wu, Yuwei Zhao, and Mingxuan Sun. Enhancing low-speed sensorless control of PMSM using phase voltage measurements and online multiple parameter identification. *IEEE Transactions on Power Electronics* **35** (10), 10700–10710 (2020). ISSN 19410107. doi: 10.1109/TPEL.2020.2978200. Cited on page/s 64.

[18] Antti Piippo, Marko Hinkkanen, and Jorma Luomi. Adaptation of motor parameters in sensorless PMSM drives. *IEEE Transactions on Industry Applications* **45** (1), 203–212 (2009). ISSN 00939994. doi: 10.1109/TIA.2008.2009614. Cited on page/s 64, 65.

[19] Shinji Ichikawa, Mutuwo Tomita, Shinji Doki, and Shigeru Okuma. Sensorless control of permanent-magnet synchronous motors using online parameter identification based on system identification theory. *IEEE Transactions on Industrial Electronics* **53** (2), 363–372 (2006). ISSN 02780046. doi: 10.1109/TIE.2006.870875. Cited on page/s 64, 65.

[20] Shigeo Morimoto, Masayuki Sanada, and Yoji Takeda. Mechanical sensorless drives of IPMSM with online parameter identification. *IEEE Transactions on Industry Applications* **42** (5), 1241–1248 (2006). ISSN 00939994. doi: 10.1109/TIA.2006.880840. Cited on page/s 64, 65.

[21] Yukinori Inoue, Koji Yamada, Shigeo Morimoto, and Masayuki Sanada. Effectiveness of voltage error compensation and parameter identification for model-based sensorless control of IPMSM. *IEEE Transactions on Industry Applications* **45** (1), 213–221 (2009). ISSN 00939994. doi: 10.1109/TIA.2008.2009617. Cited on page/s 64, 65.

[22] Yukinori Inoue, Yasunori Kawaguchi, Shigeo Morimoto, and Masayuki Sanada. Performance improvement of sensorless IPMSM drives in a low-speed region using online parameter identification. *IEEE Transactions on Industry Applications* **47** (2), 798–804 (2011). ISSN 00939994. doi: 10.1109/TIA.2010.2101994. Cited on page/s 64, 65.

[23] Yu Yao, Yunkai Huang, Fei Peng, and Jianning Dong. Position sensorless drive and online parameter estimation for surface-mounted PMSMs based on adaptive full-state feedback control. *IEEE Transactions on Power Electronics* **35** (7), 7341–7355 (2020). ISSN 19410107. doi: 10.1109/TPEL.2019.2957058. Cited on page/s 64.

[24] Qiwei Wang, Gaolin Wang, Nannan Zhao, Guoqiang Zhang, Qingwen Cui, and Dianguo Xu. An impedance model-based multiparameter identification method of PMSM for both offline and online conditions. *IEEE Transactions on Power Electronics* **36** (1), 727–738 (2021). ISSN 19410107. doi: 10.1109/TPEL.2020.3000896. Cited on page/s 64.

[25] Xinyue Li and Ralph Kennel. General formulation of kalman-filter-based online parameter identification methods for VSI-fed PMSM. *IEEE Transactions on Industrial Electronics* **68** (4), 2856–2864 (2021). ISSN 15579948. doi: 10.1109/TIE.2020.2977568. Cited on page/s 65.

[26] R. Van Der Merwe and E. A. Wan. The square-root unscented Kalman filter for state and parameter-estimation. *ICASSP, IEEE International Conference on Acoustics, Speech and Signal Processing - Proceedings* **6**, 3461–3464 (2001). ISSN 15206149. doi: 10.1109/icassp.2001.940586. Cited on page/s 65.

[27] Muhammad Saad Rafaq, Francis Mwasilu, Jinuk Kim, Han Ho Choi, and Jin Woo Jung. Online parameter identification for model-based sensorless control of interior permanent magnet syn-

chronous machine. *IEEE Transactions on Power Electronics* **32** (6), 4631–4643 (2017). ISSN 08858993. doi: 10.1109/TPEL.2016.2598731. Cited on page/s 65.

[28] Sai Shiva Badini and Vimlesh Verma. A new stator resistance estimation technique for vector-controlled PMSM drive. *IEEE Transactions on Industry Applications* **56** (6), 6536–6545 (2020). ISSN 19399367. doi: 10.1109/TIA.2020.3025265. Cited on page/s 65.

[29] Shigeo Morimoto, Masayuki Sanada, and Yoji Takeda. Wide-speed operation of interior permanent magnet synchronous motors with high-performance current regulator. *IEEE Transactions on Industry Applications* **30** (4), 920–926 (1994). Cited on page/s 65.

[30] Aravinda Perera and Roy Nilsen. A Sensorless Control Method for IPMSM with an Open-Loop Predictor for Online Parameter Identification. In *23rd International Conference on Electrical Machines and Systems, ICEMS* pages 1983–1988 Hamamatsu, Japan (2020). IEEE. Cited on page/s 65.

[31] Roy Nilsen. Electric Drives Compendium TET4120. Trondheim (2022). Cited on page/s 69.

[32] Sorin Cristian Agarlita, Ion Boldea, and Frede Blaabjerg. High-frequency-injection-assisted 'active-flux'-based sensorless vector control of reluctance synchronous motors, with experiments from zero speed. *IEEE Transactions on Industry Applications* **48** (6), 1931–1939 (2012). ISSN 00939994. doi: 10.1109/TIA.2012.2226133. Cited on page/s 69, 70.

[33] Abebe Teklu Woldegiorgis, Xinglai Ge, Wang Huiming, and Yun Zuo. An Active Flux Estimation in the Estimated Reference Frame for Sensorless Control of IPMSM. *IEEE Transactions on Power Electronics* **37** (8), 9047–9060 (8 2022). Cited on page/s 70.

[34] F. Bauer and H. D. Heining. Quick response space vector control for a high power three-level-inverter drive system. *Archiv für Elektrotechnik* **74** (1), 53–59 (1990). ISSN 00039039. doi: 10.1007/BF01573231. Cited on page/s 70, 71, 72.

[35] Tom Fagernes Nestli and Roy Nilsen. Evaluation and comparison of predictor models for rotor flux calculation in induction motors. In *PESC Record - IEEE Annual Power Electronics Specialists Conference* volume 1 pages 729–737 (1994). ISBN 0780318595. doi: 10.1109/pesc.1994.349657. Cited on page/s 71.

[36] M.S. Fadali and A Visioli. Digital Control Engineering, Analysis and Design. Elsevier Inc. Oxford, UK 2nd edition (2013). Cited on page/s 71.

[37] Marko Hinkkanen, Toni Tuovinen, and Lennart Harnefors. A combined position and stator-resistance observer for salient PMSM drives : design and stability analysis. *IEEE Transactions on Power Electronics* **27** (2), 601–609 (2012). doi: 10.1109/TPEL.2011.2118232. Cited on page/s 72.

[38] Lennart Ljung and Torsten Soderstrom. Theory and Practice of Recursive Identification. The MIT Press Cambridge, Massachusetts 2nd edition (1985). ISBN 0-262-12095-X. Cited on page/s 72, 74.

[39] Pavel Vaclavek, Petr Blaha, and Ivo Herman. AC drive observability analysis. *IEEE Transactions on Industrial Electronics* **60** (8), 3047–3059 (2013). ISSN 02780046. doi: 10.1109/TIE.2012.2203775. Cited on page/s 73.

[40] Aravinda Perera, Roy Nilsen, and Thomas Haugan. Investigation of open-loop predictor implementation methods for online parameter estimation of IPMSM. In *PCIM Europe 2022* Nuremberg, Germany (2022). Cited on page/s 73.

[41] Aravinda Perera and Roy Nilsen. Recursive prediction error gradient-based algorithms and framework to identify PMSM parameters online. *IEEE Transactions on Industry Applications* page 11 (2022). doi: 10.1109/TIA.2022.3219041. Cited on page/s 73, 74.

[42] Miguel Velez-Reyes, Kazuaki Minami, and George C. Verghese. Recursive speed and parameter estimation for induction machines. In *IAS Annual Meeting (IEEE Industry Applications Society)* number pt 1 pages 607–611 (1989). doi: 10.1109/ias.1989.96712. Cited on page/s 77.

[43] Samuel J. Underwood and Iqbal Husain. Online parameter estimation and adaptive control of permanent-magnet synchronous machines. *IEEE Transactions on Industrial Electronics* **57** (7), 2435–2443 (2010). ISSN 02780046. doi: 10.1109/TIE.2009.2036029. Cited on page/s 77.

[44] Peter Weichbold and Thomas von Raumer. Influence of dead time effects of PWM-VSI on current control. In IEEE, editor, *EPE* page 8 Graz (2001). Cited on page/s 86.

Chapter 5

System-on-Chip-based Real-Time Simulator for Drives

Abstract

This chapter presents a modular and easily reusable Zynq System-on-Chip (SoC)-based Embedded Real-Time Simulator (ERTS) aimed at rapid prototyping of electric drives. The power hardware components of the drive including the voltage source converters (VSC) are programmed in the field programmable gate array (FPGA) fabric of the SoC to achieve real-time emulation. The control algorithms of the electric motor drive are programmed in the on-chip ARM processor, which can be used to drive either the physical or emulated hardware. The ERTS is scaled in the per-unit system to enhance reusability irrespective of the hardware ratings. The architectures and schematics of different partitions of the ERTS are illustrated. The simulator is demonstrated using a position sensorless IPMSM drive and compared against offline simulation for performance.

5.1 Introduction

5.1.1 Motivation

In the process of developing electric motor drive systems, personal computer (PC)-based offline simulation methods are extensively used, in which, the common practice is to run the control system in discrete- and the power components in continuous-mode to emulate a physical motor drive as closely as possible. The type of the solver and the size of the simulation time step (h) of these simulation environments determine the stability and precision of the simulation. When the switching frequency increases in the kilohertz scale, h needs to be shrunk below microsecond-level to precisely capture the switching transients [1]. One of the main challenges with smaller h in PC-based simulations is that the execution time becomes excessively elongated, particularly when simulating computationally intensive systems. Ref [2] reports that the time consumed by detailed offline simulation can be as much as 20,000 times more than by a real-time simulator for power electronic applications.

The digital real-time simulation (DRTS) technologies [3] that can solve the model equations taking a time-step which is equal to the real-world clock, are able to yield real-time results emulating the physical systems. SoC-based emulation, which falls into the ERTS category, is one such method that exploits the inherent parallelism in its FPGA fabric in computing dynamic mathematical models. Implementation of all or parts of the components of the motor drive in the SoC platform makes hardware-in-the-loop (HIL) scenarios possible to evaluate all or certain components of the physical system non-destructively and cost-effectively. At the same time, owing to the on-chip processor(s) in the SoC that can execute the actual control software, the software-in-the-loop (SIL) also becomes able to validate control software while not having access to the actual hardware or experimental setup. In this manner, ERTS can dramatically reduce the time-to-market and development costs of electric drives. Having both FPGA and processors in the same package along with other hardware resources makes SoCs an easily customizable yet compact tool with high data fidelity [4]. The cost of a modern SoC is just a fraction of the commercially available DRTS technologies and the space requirement, too, is negligible compared to its counterparts, which allows a MW-scale motor drive system to be emulated in a pocket-size digital electronic card.

5.1.2 Literature Review, Research Gaps, and Contribution

Consequently, ERTS is emerging as an essential tool in the electric drive development process, although details about their implementation are not prevalent. An approach to realize the electric drives in the FPGA, including the control system, is elaborated in [5] and [6]. Authors in [7] employ an SoC to implement a doubly-fed induction generator and its control either by fully hardware or fully software and evaluate the pros and cons. In [8], an ERTS is developed for a modular multilevel converter and control in which the plant is emulated in the processor. Zynq SoC has been employed only to implement the motor drive control algorithm in [9] in which the FPGA is used for Pulse-Width Modulation (PWM) and interrupt generation. A comprehensive ERTS investigation is available in [1], although its application is not focused on electric drives. An IPMSM drive is simulated in [10], where two discrete FPGA and DSP chips have been employed instead of a SoC.

This chapter aims to present a design method for a modularized, scalable, reconfigurable, and easily programmable ERTS for electric drives using a state-of-the-art SoC. The proposed simulator effectively exploits the processor system and FPGA of the SoC to emulate a range of industrial electric drives. The ERTS is demonstrated by implementing a sensorless IPMSM drive discussed in Chapter 4. In addition to the ERTS architecture and implementation, the real-time results are compared with offline simulations for numerical precision and execution time.

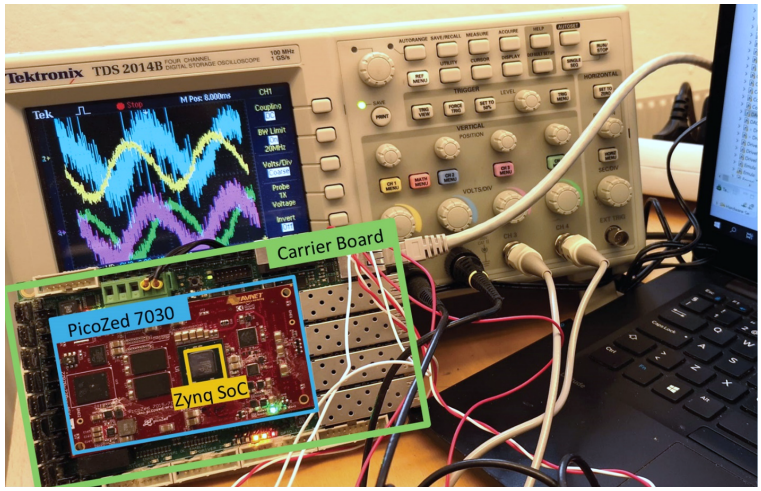

Figure 5.1. Embedded Real-Time Simulator Hardware and test/debugging setup.

5.2 ERTS Overview and Architecture

5.2.1 Hardware

PicoZed7030 from Avnet is used as the System-on-Module (SoM) that contains the Zynq 7030 SoC. This SoC houses two units of ARM Cortex -A9 processors and an FPGA section. An application-specific carrier board is used to access the communication physical layers and input/output of the SoM. The carrier board also contains high-speed analog-to-digital converter (ADC) and digital-to-analog converter (DAC) chips. See Figure 5.1 for an overview of the hardware.

5.2.2 ERTS Architecture

The proposed ERTS, illustrated in Figure 5.2, contains three main components: 1) the processor software program, 2) Generic Intellectual Property-(IP) Cores (GIPC), and 3) the Hardware Emulator, (HWE). This three-part ERTS allows individual development of each part and test with the use of already validated remaining parts. Also, such partitioning maximizes the reusability of the common components, ensures uniformity across simulations, minimizes design and simulation failures, and helps diagnose faults or design errors rapidly. Also, by retaining much of the ERTS modularized, the proposed simulator can rapidly be modified to emulate different motor types and designs, converters, or mechanical loads. The proposed simulator is also designed using the per-unit system, which makes its main components common across machines, loads, and converters irrespective of their ratings. The six-phase drive counterpart is illustrated in Figure 6.7.

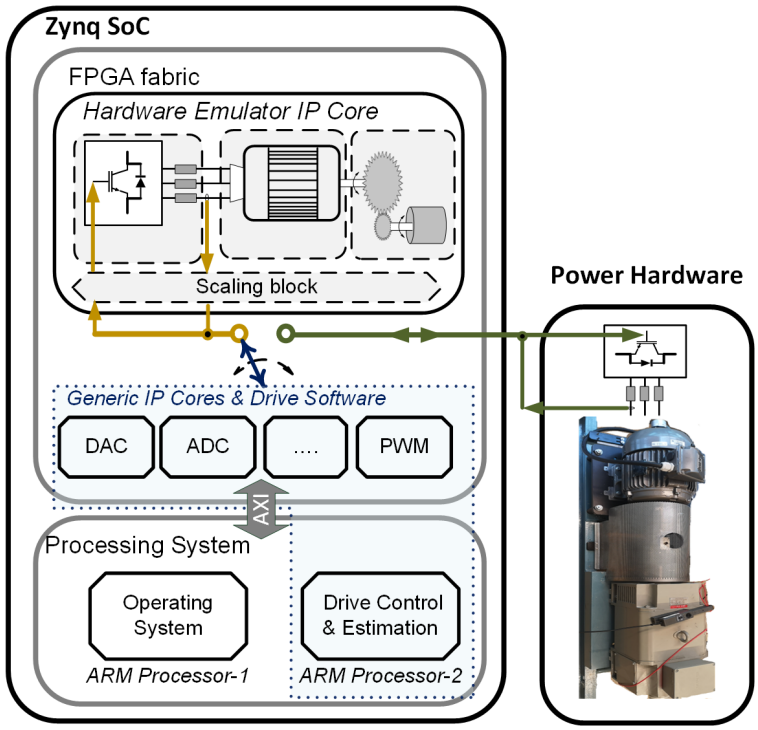

FIGURE 5.2. Design layout of the proposed SoC-Based Embedded Real-Time Simulator (ERTS), in which, the software and firmware are targeted to drive either the hardware emulator models or the actual power hardware.

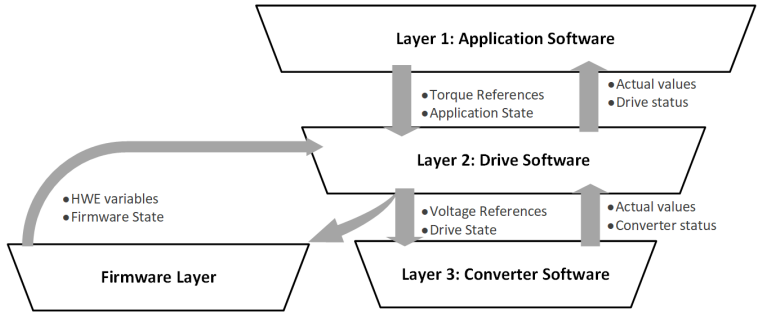

FIGURE 5.3. Software/firmware stack of the ERTS that shows its modularized architecture.

5.2.3 Processor Software Architecture

This part contains the per-unit scaling, reference frame transformations, MTPA and flux-weakening strategies, field-oriented control algorithms, reference voltage-vector calculations, the motor flux models, and active flux observer algorithms given in (4.5) and (4.6), among others. These are programmed in the processor of the SoC, with the aim of achieving iterative programmability, ease of expandability, and performance tuning with the help of a high-level programming language. The processor software program is modularized into 4 different layers as given in Figure 5.3, where states and references are cascaded only between the neighboring layers. To ensure modularity and structure, the C++ programming language is chosen to exploit its object-oriented programming capabilities.

5.2.4 IP Cores of Concern

Generic IP cores of the ERTS contain a set of building blocks programmed on the FPGA fabric of the SoC and are applicable for a wide range of electric drives and other power electronic applications. These include PWM and interrupt generation IP core, ADC-receiver, DAC, digital filters, and the fastest protection schemes. These IP cores are accessible to both the physical power hardware as well as the hardware emulation.

Hardware emulator IP core is the entity in the FPGA fabric that contains the digital replication of the power hardware of the electric drive. The emulator encompasses two units of 2-level VSCs to facilitate multiphase machines or separately excited machines, the rotating machine model, the mechanical load model, and the digital replication of the analog front end, known as the scaling block in this context. The emulator is designed in the per-unit system and it is parameterizable from the application software, thus this IP Core can remain unchanged when simulating different electric drives. The scaling block ensures that the generic IP cores will not see a difference between the physical hardware and the emulator during exchange of variables.

The Simulink library, Xilinx System Generator (XSG), a vendor-specific schematic approach is chosen to program the hardware emulator in the FPGA fabric, which will eventually convert the schematics to a preferred hardware descriptive language and also generate drivers for the IP cores. The basic combinatory and sequential building blocks offered by the System Generator library within the Matlab/Simulink environment ease the FPGA programming of rather complex models [6]. Also, since the FPGA program is already in the Matlab environment with XSG, the program can be fairly quickly ported to other digital real-time simulators such as OPAL-RT.

The AXI interface in the SoC is 32-bit, therefore the ERTS word length is kept at 32-bits (with the exception of integrators/accumulators which are 64-bit to ensure higher precision) for the convenience of data exchange with the on-chip processor. For real-time simulation, the 32-bit fixed-point representation guarantees higher numerical precision and demands less internal resources over the 32-bit floating point

TABLE 5.1. Clock settings in the proposed ERTS

Clock	Frequency	Time step
FPGA clock	100 MHz	T_{FPGA} = 10 ns
Processor interrupt cycle	8 kHz	T_{samp} = 125 μs
Solver clock	1 MHz	T_{step} = 1 μs

representation [6, 8, 11]. The per-unit scaling of the emulator further enhances the numerical precision such that its rated voltages and currents become 1 unit, and thus the range is minimized to maximize the number of precision bits of the 32-bit fixed-point format. Applied precision is 32.28 which means, 28 bits are retained for precision having a resolution of 3.725 x 10-9. While leaving the most significant bit to represent the sign, the chosen precision offers a range between +7.99 to -8 which is sufficient when a per-unit system is concerned.

5.2.5 ERTS Clock Settings

Three different clock cycles, as tabulated in Table 5.1, are utilized to represent the physical motor drive system as closely as possible in the ERTS. The subcomponents that require the fastest processing speeds, like the GIPC and converter block in the emulator, take advantage of the FPGA clock. The processor interrupts that is twice the speed of the PWM sets the processor interrupt cycle, which is sufficient for the application software. Solver-clock is used in the solver of the discretized rotating machine and mechanical load models in the hardware emulation. The ratio between the T_{step} to the mechanical time constant determines the stability of the discrete system, which is preferred to be as small as possible. T_{step} will also determine the integration intervals, and thus the shorter integration intervals will yield more precise results. Instead of applying the fast FPGA clock, a much slower solver clock is used to slow down the processing speed of the rotating machine and the mechanical load realizations in the FPGA fabric with the aim of emulating their real-world sluggishness in the digital hardware. Such processing speed reduction without compromising the numerical precision and stability will reduce the required number of bits in the integrator/accumulator and help reduce the power consumption, and heat generation from the SoC.

5.2.6 Discretization

$$s = \frac{z-1}{T_{step}} \tag{5.1}$$

$$s = \frac{2}{T_{samp}} \cdot \left(\frac{1+z^{-1}}{1-z^{-1}} \right) \tag{5.2}$$

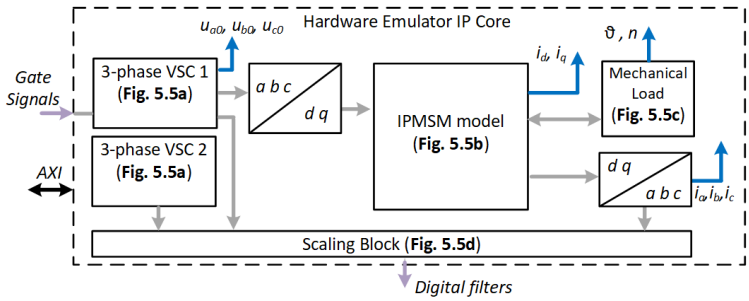

FIGURE 5.4. Overview of the Hardware Emulator (HWE) IP core.

In codifying the emulation models in the FPGA fabric, the Euler method (5.1) is applied as it is sufficiently precise. When control compensation schemes are concerned, mainly the proportional-integral (PI) compensation is applied, and it is implemented in the processor software using the trapezoidal method (5.2) due to the ease of implementation and reasonable performance.

5.3 HARDWARE EMULATOR DEVELOPMENT

5.3.1 Overview

The overview of the Hardware Emulator IP core is as illustrated in Figure 5.4. Apart from the motor model, its remaining subcomponents can be ported across different AC- or DC-motor types. The different colors of the arrows refer to where the respective data is carried to/from. Black arrows to/from the processor; gray arrows within the same IP Core; and purple to/from the other IP cores. The blue-arrowed data can be viewed from an oscilloscope using the DAC. The development of the main subcomponents is unveiled subsequently where some of the subcircuits are omitted to simplify the illustration. Pre/post -transformation blocks in Figure 5.4 are the digital implementation of Park- and Clarke-transformations, for which CORDIC functions were used.

5.3.2 Converter Implementation

The voltage source converters are modeled using the switching function model [12] and its schematic is presented in Figure 5.5(a). Accordingly, the gate signals are supplied from the modulator IP core, which resides outside the hardware emulator IP core, yet inside the FPGA fabric. The converter logic is as follows: during the dead time, if the current is positive, choose the ground DC-rail. In the same instance, if the current is negative, choose the positive DC-rail. During the other times, choose the gate signal command.

5.3.3 IPMSM Implementation

The schematic is found in Figure 5.5(b) in which the motor model assumes sinusoidal flux distribution in the stator, no cross-coupling between the d- and q- axes, thus no secondary saliencies apart from the rotor-geometric saliency. IPMSM model, when discretized, becomes:

$$\begin{aligned} i_d[k+1] &= i_d[k] \cdot \left(1 - T_{step} \cdot \frac{\omega_n \cdot r_s}{x_d}\right) + T_{step} \cdot \left(\frac{\omega_n}{x_d}\right) \cdot \left(u_d\,[k] + n[k] \cdot x_q \cdot i_q[k]\right) \\ i_q[k+1] &= i_q[k] \cdot \left(1 - T_{step} \cdot \frac{\omega_n \cdot r_s}{x_q}\right) + T_{step} \cdot \left(\frac{\omega_n}{x_q}\right) \cdot \left(u_q\,[k] - n[k] \cdot x_d \cdot i_d[k]\right. \\ &\qquad \left. - n[k] \cdot \psi_m\right) \end{aligned} \tag{5.3}$$

The electrical parameters and constants are passed from the application software program during the initialization of the simulator. In principle, any of the intermediate- or boundary-digital signals can be passed to the processor or DAC to be monitored using an oscilloscope.

5.3.4 Mechanical Load Implementation

The mechanical load is modeled as follows and it is illustrated in Figure 5.5(c):

$$\begin{aligned} n[k+1] &= n[k] + \frac{T_{step}}{T_m} \cdot (\tau_e[k] - \tau_L[k]) \\ \tau_L &= k_n \cdot sign(n) \cdot n^2 + \tau_{L,extern}\,, \qquad T_m = \frac{J \cdot \Omega^2}{S_n} \end{aligned} \tag{5.4}$$

5.3.5 Scaling Block

$$variable\_per\_bit = variable_{pu} \cdot \frac{K_{AFE} \cdot K_{base}}{K_{trans} \cdot K_{RAW}} \tag{5.5}$$

The scaling block as in Figure 5.5(d) ensures the currents and voltages from the emulator passed to the GIPC (for digital filtering and multiplexing) contain the identical volts-per-bit and amperes-per-bit resolution of those obtained from the physical hardware. Owing to this identicality, neither the GIPC nor the application software will notice a difference between the hardware emulator and physical hardware. With respect to the gains of each block given in Figure 5.5(d), one can find the gains for the scaling block using (5.5) which is common for both voltages and currents. Since the emulator is designed in per-unit scale, but the GIPC is scaled for SI values, the $variable_{pu}$ i.e., $u(t)$, $i(t)$ must be multiplied by the base values K_{base} in addition, as seen in the formula.

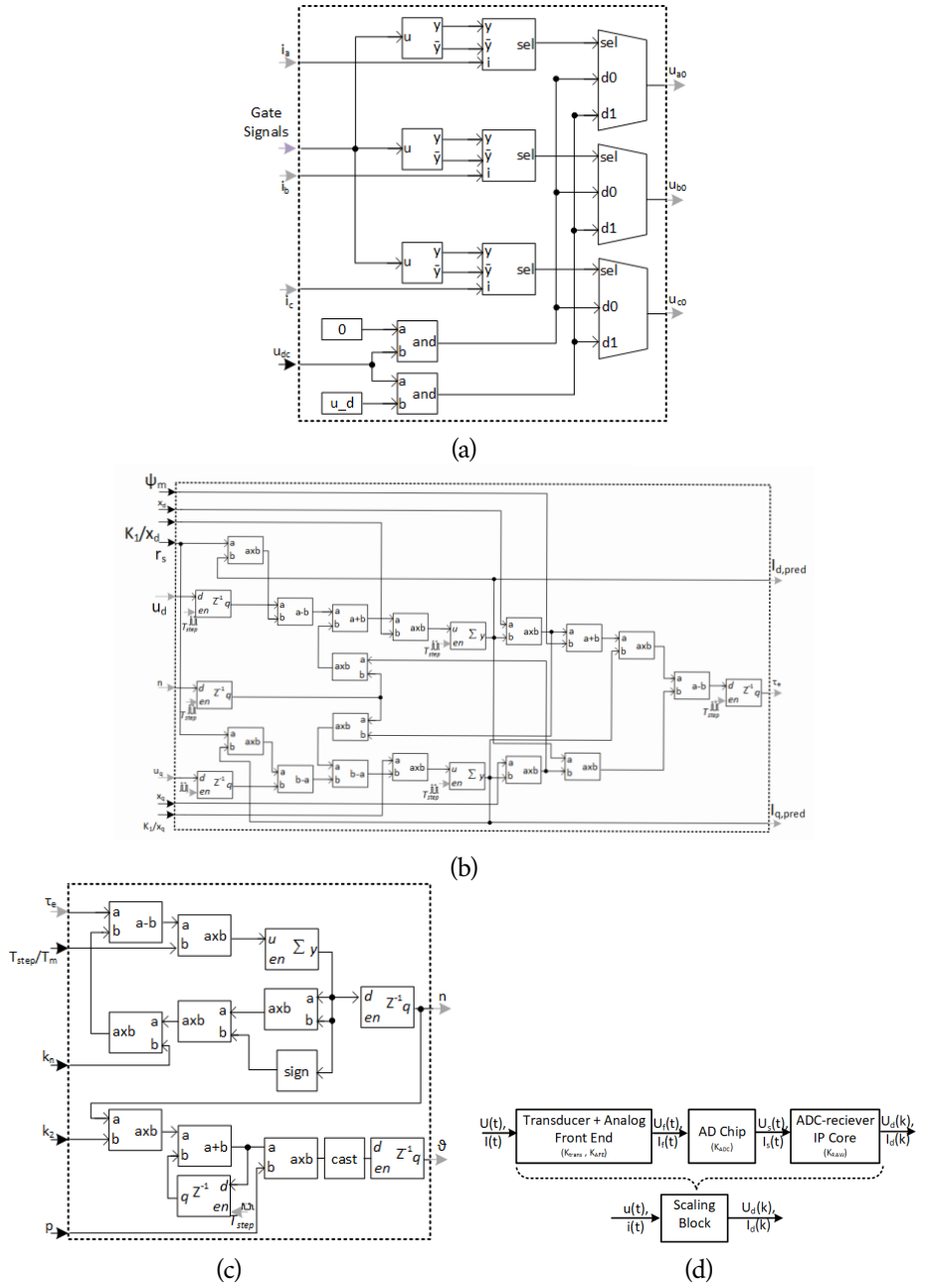

FIGURE 5.5. Xilinx System Generator schematic program of (a) Voltage Source Converter, (b) IPMSM, (c) mechanical load model, (d) scaling block.

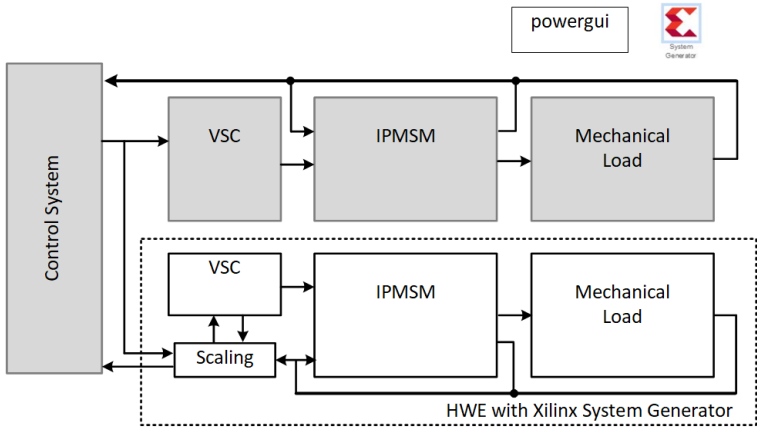

FIGURE 5.6. IPMSM drive co-simulation: Simulink floating point double precision model (gray blocks) in parallel with XSG fixed-point, 32.28-precision model (white blocks) using common floating-point control logic.

TABLE 5.2. Resource utilization of the Hardware Emulator IP Ccore

Resources	Used	% of the Total
Slice Look-Up Tables	4937	6.3%
Slice registers	5634	3.6%
Block RAMs	0	0% (total 265)
Block DSPs	0	0% (total 400)

5.3.6 Development Procedure

The Matlab development environment can be exploited not only to design the hardware emulation models but also to identify the satisfactory fixed-point precisions, and ranges, and test the closed-loop performance using the floating-point drive controller. As shown in Figure 5.6, both the Xilinx System Generator model, as well as the Simulink models, can be run in parallel to identify the numerical errors, thus fine-tune the fixed-point precisions. Once the models are ready for synthesis, they can be exported to the Vivado-integrated development environment where the final synthesis and bitstream generation is performed. Table 5.2 presents the internal FPGA resources utilized by the hardware emulator. The bitstream is then linked to the Xilinx Software Development Kit (SDK) for target-oriented application software and firmware development.

5.4 VALIDATION AND LIMITATIONS

ERTS validation is conducted in two stages: first, against the offline simulation, i.e., double-precision floating-point Matlab/Simulink simulation, and secondly, against laboratory prototypes. Ref [13] contains the first stage of validation results and [11],

Chapter 4 and Chapter 7 indirectly exhibit the validation of ERTS against the power hardware.

The ERTS performance is analyzed with respect to the execution time of a given simulation run and the numerical precision. For a 1-second simulation run of the IPMSM drive, the ERTS consumed just the run-time of 1 second while the offline method took ~ 550 seconds, which demonstrates a remarkable time saving with the ERTS. The numerical precision of the ERTS is evaluated using the root-mean-square (rms) error with reference to the offline simulation variable (with double-precision floating-point). The steady-state rms errors for d- and q- axes currents were calculated to be 7.16×10^{-4} and 3.67×10^{-4}, respectively, in per-unit.

Some of the notable limitations of the proposed ERTS with respect to a physical electric drive: VSC is modeled using the switching function model in the hardware emulator, which may not accurately represent the converter during the regenerative modes [5]. The emulated motor model does not include the secondary saliencies nor the saturation effects which limits its performance precision in certain operating ranges.

5.5 Conclusion and Summary

An inexpensive, modular, portable, and rapidly reusable Embedded Real-Time Simulator targeted for electric motor drives was presented in this chapter. Both the software and hardware architectures of the simulator and the detailed design method of the hardware emulation were discussed. The internal resource utilization of the FPGA is kept at a minimum in designing the real-time emulation. The overall simulation is significantly accelerated in the given sensorless control application at the expense of negligible numerical error. Such a simulator can be an effective tool in developing and debugging real drive software without having the access to the power components, which can be useful in modern-day remote work circumstances. The ability to rapidly prototype electric drive concepts with this simulator can significantly accelerate the product development process. The simulator sets the basis to expand its model behavior as closely as possible to the real-world systems and to include diagnosis and prognosis of faults in the drives to develop towards a real-time digital twin. This ERTS is extended to emulate the six-phase drives, of which the details and results are outlined in Chapter 6 and Chapter 7.

5.6 References

[1] Mohamed Dagbagi, Asma Hemdani, Lahoucine Idkhajine, Mohamed Wissem Naouar, Eric Monmasson, and Ilhem Slama-Belkhodja. ADC-Based Embedded Real-Time Simulator of a Power Converter Implemented in a Low-Cost FPGA: Application to a Fault-Tolerant Control of a Grid-Connected Voltage-Source Rectifier. *IEEE Transactions on Industrial Electronics* **63** (2), 1179–1190 (2016). ISSN 02780046. doi: 10.1109/TIE.2015.2491883. Cited on page/s 95, 96.

[2] Alberto Sanchez, Angel De Castro, and Javier Garrido. A comparison of simulation and hardware-in-the-loop alternatives for digital control of power converters. *IEEE Transactions on Industrial Informatics* **8** (3), 491–500 (2012). ISSN 15513203. doi: 10.1109/TII.2012.2192281. Cited on page/s 95.

[3] M. D. Omar Faruque, *et al.* Real-Time Simulation Technologies for Power Systems Design, Testing, and Analysis. *IEEE Power and Energy Technology Systems Journal* **2** (2), 63–73 (2015). ISSN 2332-7707. doi: 10.1109/jpets.2015.2427370. Cited on page/s 96.

[4] Louise Crockett, Ross Elliot, Martin Enderwitz, and Robert Stewart. The Zynq Book. Strathclyde Academic Media Glasgow 1 edition (2014). Cited on page/s 96.

[5] Gustavo G. Parma and Venkata Dinavahi. Real-time digital hardware simulation of power electronics and drives. *IEEE Transactions on Power Delivery* **22** (2), 1235–1246 (2007). ISSN 08858977. doi: 10.1109/TPWRD.2007.893620. Cited on page/s 96, 105.

[6] Nariman Roshandel Tavana and Venkata Dinavahi. A General Framework for FPGA-Based Real-Time Emulation of Electrical Machines for HIL Applications. *IEEE Transactions on Industrial Electronics* **62** (4), 2041–2053 (2015). ISSN 02780046. doi: 10.1109/TIE.2014.2361314. Cited on page/s 96, 99, 100.

[7] Daniel Tormo, Lahoucine Idkhajine, Eric Monmasson, Vidal-Albalate Ricardo, and R. Blasco-Gimenez. Embedded real-time simulators for electromechanical and power electronic systems using system-on-chip devices. *Mathematics and Computers in Simulation* (158), 326–343 (2019). Cited on page/s 96.

[8] Mattia Ricco, Marius Gheorghe, Laszlo Mathe, and Remus Teodorescu. System-on-Chip Implementation of Embedded Real-Time Simulator for Modular Multilevel Converters. In *ECCE 2017- IEEE Energy Conversion Congress and Exposition, Proceedings* pages 1500–1505 (2017). ISBN 9781509029983. Cited on page/s 96, 100.

[9] Danyal Mohammadi, Luka Daoud, Nader Rafla, and Said Ahmed-Zaid. Zynq-based SoC implementation of an induction machine control algorithm. *Midwest Symposium on Circuits and Systems* **0** (October), 16–19 (2016). ISSN 15483746. doi: 10.1109/MWSCAS.2016.7870150. Cited on page/s 96.

[10] Eisenhawer De M Fernandes, Denis R Huller, Alexandre C Oliveira, and Welflen R N Santos. Real-time simulator of interior permanent-magnet synchronous motor based on FPGA devices. In *Brazilian Power Electronic Conference (COBEP)* pages 11–16 (2017). ISBN 9781509062485. doi: 10.1109. Cited on page/s 96.

[11] Aravinda Perera and Roy Nilsen. Recursive prediction error gradient-based algorithms and framework to identify PMSM parameters online. *IEEE Transactions on Industry Applications* page 11 (2022). doi: 10.1109/TIA.2022.3219041. Cited on page/s 100, 104.

[12] H Jin. Behavior-Mode Simulation of Power Electronic Circuits. *IEEE TRANSACTIONS ON POWER ELECTRONICS* **12** (3), 1149–1154 (1997). ISSN 00262692. doi: 10.1016/s0026-2692(97)80962-7. Cited on page/s 101.

[13] Aravinda Perera, Roy Nilsen, Thomas Haugan, and Kjell Ljøkelsøy. A design method of an embedded real-time simulator for electric drives using low-cost system-on-chip platform. In *PCIM Europe digital days* Nuremberg, Germany (2021). Cited on page/s 104.

Part III

SIX-PHASE DRIVES

PART III

Chapter 6

Control and Parameter Estimation of Six-Phase IPMSM Drives

Abstract

Six-phase IPMSM drives with dual three-phase configurations offer unique merits that make them attractive for reliability-critical applications. Online identification of machine parameters, i.e., permanent magnet flux linkage Ψ_m, stator resistance R_s, and inductances can enhance the drive's performance. Full-order model-based open-loop predictor currents and their sensitivities were exploited for three-phase IPMSM identification in Chapter 3. The same approach is investigated for the six-phase IPMSM drive in this chapter. Single Synchronous Reference Frame-based modeling and current control are adopted for robust performance. Stochastic Gradient Algorithm (SGA) is used to compute the gain matrix that computes the parameter updates when discrepancies exist between the physical and model parameters. The concept is validated by demonstrating Ψ_m, R_s online tracking, and the influences from wrong inductances are analyzed analytically and with the aid of an Embedded Real-Time Simulator. Results show satisfactory convergence speeds and asymptotic behavior.

6.1 Introduction

SIX-phase electric machines arranged with dual three-phase stator winding configurations [1] possess unique features to make them attractive for a multitude of modern-day applications. Excellent fault tolerance, thus improved system availability, better power, and thermal distribution, lesser harmonic content in the DC-link, and electromagnetic torque are desirable attributes in DTP machines, to name a few [2, 3]. The advantages proliferate when IPMSM is arranged in the DTP configuration, which will combine its superior properties over other machine types [4] to reinforce the drive's reliability, power density, and efficiency. Thus, DTP IPMSM drives emerge to be an appealing choice in a wide range of mission-critical applications.

The accurate information of the electrical parameters of the machine, i.e. Ψ_m, R_s and d- and q- axis inductances L_d, L_q and stator leakage inductance $L_{s\sigma}$ are essential,

to achieve precise torque/speed control and predetermined control targets such as Maximum Torque Per Ampere (MTPA). When model-based control algorithms are concerned, for example, in position-sensorless control, model predictive control, direct torque control, or a combination of these, the performance relies on the accuracy of the parameters used to construct the machine model. The machine parameters also imply the aging and condition of the drive. The challenge is, however, that the datasheet parameters are often given for rated operation obtained under nominal conditions which can exclude a substantial range of operating points. As a result, the parameter identification methods as reviewed in [5] have gained interest. Due to the well-known rank deficiency problem [6] that prohibits from simultaneous identification of all parameters, either two time-scaled techniques [7] or incorporation of signal injection methods are used. In practice, using an offline method to identify the inductances is adequate, thus the real-time inductances can be calculated using a look-up table in relation to the measured stator currents. Conversely, the temperature influenced Ψ_m and R_s are essential to be tracked online to guarantee the drive's operational reliability [8].

6.1.1 Literature Review, Research Gaps, and Contribution

Among the recent research work dedicated to multiphase machine identification, Recursive Least Squares (RLS) method is adopted in [9] to identify inductances and Ψ_m during operation and R_s during standstill in dual three-phase IPMSM, which may, however, lead to temperature affected performance degradation, particularly at lower speeds, due to the absence of online R_s identification. RLS-based identification is attempted to be improved in [10] with the aid of signal injection by accounting for the VSI nonlinearity. The multiparameter estimation method is proposed in [11] based on improved machine models using redundant measurements, which is not ideal for online identification. The $\boldsymbol{\Psi}^T$-based Recursive Prediction Error Method (RPEM) presented in Chapter 3 is yet to be investigated with regard to multiphase machines, to the author's best of knowledge. Thus, it is attempted to address this gap by investigating the same for dual three-phase IPMSM identification.

This chapter extends the online identification scheme presented in Chapter 3 to identify temperature-sensitive parameters of dual three-phase IPMSM. The Vector Space Decomposition-based Single Synchronous Reference Frame (SSRF)-oriented machine model and current control is applied, and thus the flux models applied for three-phase IPMSM identification can be directly reused. The theoretical basis is developed to show the possibility of identifying Ψ_m, R_s, L_d, L_q, and $L_{s\sigma}$, and their interdependencies are discussed. Subsequently, the method is demonstrated by identifying Ψ_m and R_s online with the aid of SGA for gain-matrix computation. Online updating of the inductances using the corresponding offline estimates is assumed and their impact on $\hat{\Psi}_m$ and $\hat{R}_s$ are investigated both analytically and with dynamic simulations. Industrial embedded controller-based Embedded Real-Time Simulator (ERTS) is used

to conduct the experimental validation.

6.2 Dynamic Model and Control

6.2.1 Machine Model

The transformation matrix for the winding group 1 (see Figure 6.1), which yields $d_1 - q_1 - 0_1$:

$$\mathbf{T}^{\mathbf{r}}_{\mathbf{ss1}}(\vartheta) = \frac{2}{3}\begin{bmatrix} \cos(\vartheta) & \cos\left(\vartheta - \frac{2\pi}{3}\right) & \cos\left(\vartheta - \frac{4\pi}{3}\right) \\ -\sin(\vartheta) & -\sin\left(\vartheta - \frac{2\pi}{3}\right) & -\sin\left(\vartheta - \frac{4\pi}{3}\right) \\ \frac{1}{2} & \frac{1}{2} & \frac{1}{2} \end{bmatrix}$$

The complete transformation matrix for the winding group 1 and 2:

$$\mathbf{T}^{\mathbf{r}}_{\mathbf{ss}}(\vartheta) = \begin{bmatrix} \mathbf{T}^{\mathbf{r}}_{\mathbf{ss1}}(\vartheta) & \mathbf{0} \\ \mathbf{0} & \mathbf{T}^{\mathbf{r}}_{\mathbf{ss1}}(\vartheta - \vartheta_s) \end{bmatrix} \tag{6.1}$$

$$\begin{bmatrix} u_d \\ u_q \\ u_{z1} \\ u_{z2} \\ u_{01} \\ u_{02} \end{bmatrix} = r_s \begin{bmatrix} i_d \\ i_q \\ i_{z1} \\ i_{z2} \\ i_{01} \\ i_{02} \end{bmatrix} + \frac{1}{\omega_n} \begin{bmatrix} \dot{\psi}_d \\ \dot{\psi}_q \\ \dot{\psi}_{z1} \\ \dot{\psi}_{z2} \\ \dot{\psi}_{01} \\ \dot{\psi}_{02} \end{bmatrix} + n \begin{bmatrix} -\psi_q \\ \psi_d \\ \psi_{z2} \\ -\psi_{z1} \\ 0 \\ 0 \end{bmatrix} \tag{6.2}$$

$$\begin{aligned} \psi_d &= x_d \cdot i_d + \psi_m & \psi_q &= x_q \cdot i_q & \psi_{z1} &= x_{s\sigma} \cdot i_{z1} \\ \psi_{z2} &= x_{s\sigma} \cdot i_{z2} & \psi_{01} &= x_{s\sigma} \cdot i_{01} & \psi_{02} &= x_{s\sigma} \cdot i_{02} \\ x_d &= x_{md} + x_{s\sigma} & x_q &= x_{mq} + x_{s\sigma} \end{aligned}$$

$$\begin{aligned} f_d &= \frac{f_{d1} + f_{d2}}{2}, & f_q &= \frac{f_{q1} + f_{q2}}{2} \\ f_{z1} &= \frac{f_{d1} - f_{d2}}{2}, & f_{z2} &= \frac{f_{q2} - f_{q1}}{2} \end{aligned} \tag{6.3a}$$

$$\begin{aligned} f_{d1} &= f_d + f_{z1}, & f_{q1} &= f_q - f_{z2} \\ f_{d2} &= f_d - f_{z1}, & f_{q2} &= f_q + f_{z2} \end{aligned} \tag{6.3b}$$

Figure 6.1 illustrates the winding arrangement of the machine of interest, in which the two sets of three-phase winding groups are $a_1 - b_1 - c_1$ and $a_2 - b_2 - c_2$ and the displacement angle, $\vartheta_s = 30°$ is the spatial shift between the groups. To construct the machine model in the ERTS, Single Synchronous Reference Frame (SSRF) approach is used. The method in [12] is employed to transform the six stator winding phases into three orthogonal subspaces, namely, $d-q$, z_1-z_2, 0_1-0_2, which yields an SSRF-based

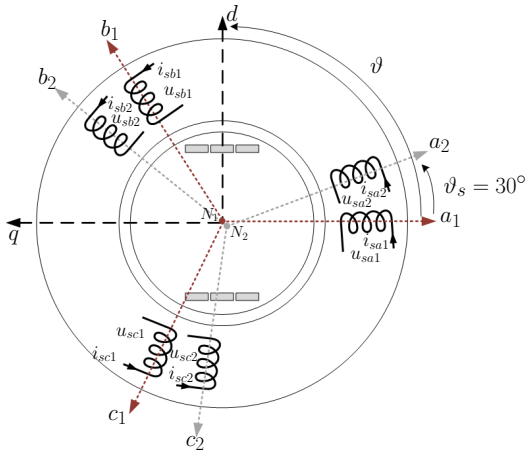

Figure 6.1. Simplified winding arrangement of dual three-phase, asymmetric IPMSM with isolated neutral points, N_1, N_2.

machine model. The amplitude invariant transformation matrix, $\mathbf{T}^r_{ss}$ is given in (6.1), using which the stator-oriented quantities can be transformed into rotor-oriented counterparts as in $\underline{f}^r_s = \mathbf{T}^r_{ss}(\vartheta) \cdot \underline{f}^s_s$, where f could be either voltage, current or flux linkage. Thus, the SSRF-oriented machine model can be presented as in (6.2). Here, $u,\ i,\ \psi,\ x,\ \omega_n$ are voltage, current, flux linkage, reactance, and nominal rotational frequency respectively. ϑ is the electrical angle of the mechanical rotor position ϑ_{mech} whose relationship with ϑ is given by $\vartheta = p \cdot \vartheta_{mech}$ where p is the number of pole pairs. Per unit electrical speed is denoted by n. Throughout this chapter, the superscript and subscript denote the reference frame and the location of the quantity (s-stator, r-rotor, m-magnet) respectively. The notation $\hat{}$ and superscript * indicate the estimated and the reference -quantities respectively. Provided that the sum of stator currents is zero in each isolated three-phase group, the 0-systems are not excited, and can then be omitted from the model. Close inspection of (6.1) will reveal that, when comparing row 1 with row 3 and row 2 with 4, the relationship between the SSRF and DSRF can be obtained as given in (6.3a) which can be processed to obtain (6.3b).

6.2.2 Drive Vector Control

The current vector-controlled dual three-phase IPMSM drive enhanced by the Online Parameter Estimator (OPE) is presented in Figure 6.2. Two units of classical 3-phase VSIs are supplied by separate dc-link capacitors, in which the voltages $u_{dc1,2}$ are measured and used to estimate the respective stator winding voltages $\hat{\underline{u}}_{s1,2}$. The stator winding currents are directly measured at the output of the inverters. Stator quantities are subsequently transformed using $\mathbf{T}^r_{ss}$ to obtain the SSRF counterparts, which are fed into the OPE.

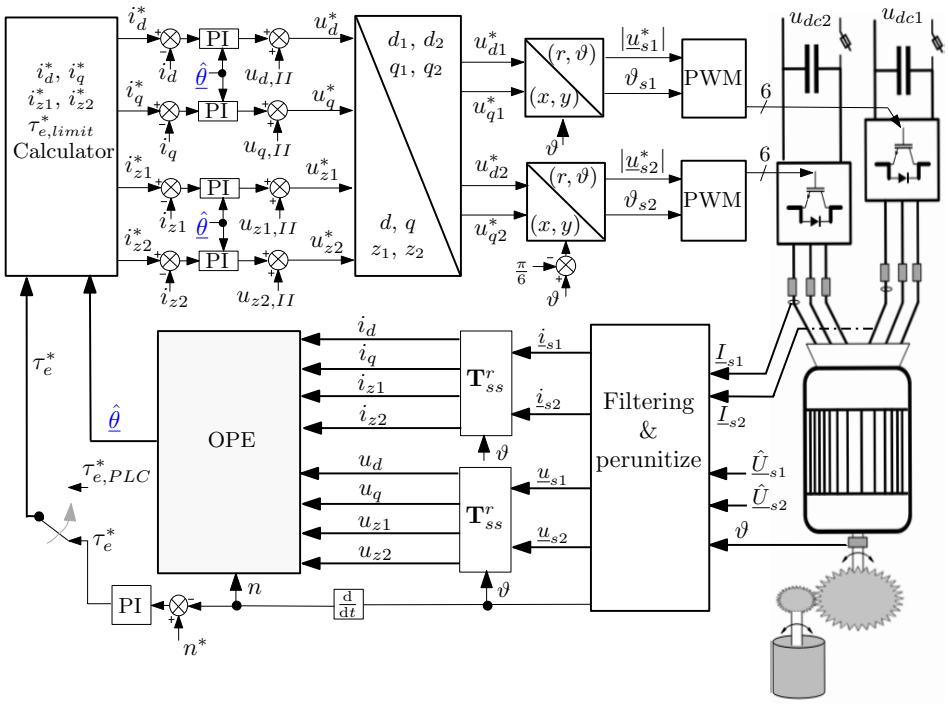

FIGURE 6.2. Dual three-phase IPMSM drive with SSRF-based and decoupled current control enhanced by the proposed Online Parameter Estimator (OPE).

$$i_d^* = \frac{\frac{\hat{\psi}_m}{3} - \sqrt[3]{\left(\frac{\hat{\psi}_m}{3}\right)^3 + \frac{\left(\hat{x}_q - \hat{x}_d\right)^2 \cdot \left(\tau_e^*\right)^2}{3 \cdot \hat{\psi}_m}}}{\hat{x}_q - \hat{x}_d}$$
$$i_q^* = \frac{\tau_e^*}{\hat{\psi}_m - \left(\hat{x}_q - \hat{x}_d\right) \cdot i_d^*} \tag{6.4}$$

$$u_{d,II} = -n \cdot x_q \cdot i_q, \quad u_{q,II} = -n \cdot x_d \cdot i_d + n \cdot \psi_m$$
$$u_{z1,II} = n \cdot x_\sigma \cdot i_{z2}, \quad u_{z2,II} = -n \cdot x_\sigma \cdot i_{z1} \tag{6.5}$$

Based on the given torque command τ_e^* either from the Programmable Logic Controller (PLC) or from the speed controller, i_d^*, i_q^* are calculated to fulfill either MTPA using (6.4) or the field-weakening strategy at high-speed operations. $i_{z1,2}^*$ can be set to zero assuming equal torque sharing between the VSI units. However, $i_{z1,2}^*$ can become nonzero if the two VSIs have different torque-limiters due to the possible differences among their respective dc-link voltage-, power-, or current- limitations. The resulting current errors are compensated using Proportional-Integral (PI) controllers. The cross-coupling between the $d - q$ quantities is evident in the (6.2) which can be tackled

by a simple and well-proven method known as decoupled current control [13]. The coupling terms as given in the (6.5) are fed forward to make the compensation more efficient and accurate. Thereby, $u_d^*, u_q^*, u_{z1}^*, u_{z2}^*$ in the SSRF are obtained. In order to split these quantities between the two VSIs, expressions in (6.3b) are employed, thereafter, the quantities are processed to obtain the voltage vector and fed into the dedicated Pulse Width Modulators (PWM). For the same reasons mentioned before, $u_{01},\ u_{02}$ are assumed zero.

6.2.3 Current Control and Modulation

The current control can imitate the classical three-phase drives by having dedicated current control for each VSI, as discussed in [14, 15], and thus each three-phase group will be referred to its own $d-q$ frame resulting in Double Synchronous Reference Frame (DSRF) current control [13]. Alternatively, SSRF-based current control, in which, a set of fictitious $d-q-z$ currents are computed and controlled, evidently has no direct control of the physical VSI currents, unlike the former, and therefore, unequal torque-limitations can be challenging. However, due to the natural elimination of coupling inductances between the two winding groups, SSRF current control has been claimed to be more robust in dynamic operations [13, 16], henceforth it is applied in this research work. Out of the several modulation strategies [17], the classical sinusoidal PWM with 3rd harmonic injection is applied.

6.3 Recursive Prediction Error Method for Six-Phase Drives

6.3.1 Overview of RPEM

The RPEM is introduced in Chapter 3 and its general expression in discrete form is given in (3.2). For the dual three-phase IPMSM, $\hat{\underline{\theta}}$ becomes as follows, with the same meanings of notations as in previous chapters:

$$\begin{aligned} \hat{\underline{\theta}} &= \begin{bmatrix} \hat{\psi}_m & \hat{r}_s & \hat{x}_d & \hat{x}_q & \hat{x}_{s\sigma} \end{bmatrix}^T,\ \hat{\underline{\theta}} \in D_{\mathscr{M}},\ D_{\mathscr{M}} \in D_s \\ D_{\mathscr{M}} &= \left\{ \hat{\underline{\theta}}_{min} \leq \hat{\underline{\theta}} \leq \hat{\underline{\theta}}_{max} \right\} \end{aligned} \tag{6.6}$$

Figure 6.3 illustrates the structure of the OPE. The predictor is designed with the Full-Order Model, $\mathscr{M}_{u\theta}$, given in (3.3). $\mathscr{M}_{u\theta}$ is modeled using the SSRF quantities, targeting several advantages. Firstly, with SSRF orientation, the model becomes identical to that of a three-phase machine, and thus the already developed functions and algorithms become directly applicable. The stability of the predictor in the continuous and discrete-time domains is discussed in Chapter 3 and A.3, which conclude that the trapezoidal rule-based implementation in the DSP offers stable prediction across the full speed range.

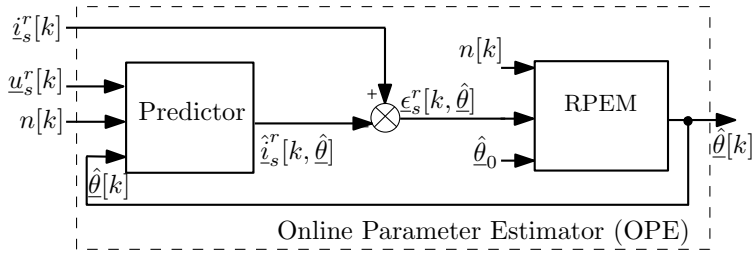

FIGURE 6.3. Block diagram of the adopted open-loop Online Parameter Estimator.

6.3.2 *Prediction Error Analysis*

The prediction error $\underline{\epsilon} = \underline{i}_s^r - \hat{\underline{i}}_s^r$, in steady-state, becomes:

$$
\begin{aligned}
\epsilon_d = (-)&\left(\frac{n^2\cdot\hat{x}_q}{\hat{r}_s^2+n^2\cdot\hat{x}_d\cdot\hat{x}_q}\right)\delta\psi_m\\
&-\left(\frac{\hat{r}_s}{\hat{r}_s^2+n^2\cdot\hat{x}_d\cdot\hat{x}_q}\cdot i_d+\frac{n\cdot\hat{x}_q}{\hat{r}_s^2+n^2\cdot\hat{x}_d\cdot\hat{x}_q}\cdot i_q\right)\delta r_s\\
&-\left(\frac{n^2\hat{x}_q}{\hat{r}_s^2+n^2\cdot\hat{x}_d\cdot\hat{x}_q}\cdot i_d\right)\delta x_d\\
&+\left(\frac{n\cdot\hat{r}_s}{\hat{r}_s^2+n^2\cdot\hat{x}_d\cdot\hat{x}_q}\cdot i_q\right)\delta x_q\\
\epsilon_q = &-\frac{n\cdot\hat{r}_s}{\hat{r}_s^2+n^2\cdot\hat{x}_d\cdot\hat{x}_q}\delta\psi_m\\
&-\left(\frac{\hat{r}_s}{\hat{r}_s^2+n^2\cdot\hat{x}_d\cdot\hat{x}_q}\cdot i_q-\frac{n\cdot\hat{x}_d}{\hat{r}_s^2+n^2\cdot\hat{x}_d\cdot\hat{x}_q}\cdot i_d\right)\delta r_s\\
&-\left(\frac{n\cdot\hat{r}_s}{\hat{r}_s^2+n^2\cdot\hat{x}_d\cdot\hat{x}_q}\cdot i_d\right)\delta x_d\\
&-\left(\frac{n^2\cdot\hat{x}_d}{\hat{r}_s^2+n^2\cdot\hat{x}_d\cdot\hat{x}_q}\cdot i_q\right)\delta x_q\\
\delta\psi_m = \psi_m-\hat{\psi}_m,&\qquad \delta r_s = r_s-\hat{r}_s\\
\delta x_d = x_d-\hat{x}_d,&\qquad \delta x_q = x_q-\hat{x}_q
\end{aligned}
\tag{6.7}
$$

This expression has become identical to that of three-phase IPMSM (3.9), attributing to the use of SSRF-oriented quantities. $\underline{\epsilon}$ carries parametric error information into the RPEM and this expression shows the sensitivity of each parametric error and parametric inter-dependencies. Analysis w.r.t. $\delta\psi_m$, δr_s have been presented in Chapter 3. Thus, let's analyse the $\underline{\epsilon}$ sensitivity in relation to $\delta x_d,\ \delta x_q$, assuming $\delta\psi_m,\ \delta r_s = 0$.

At standstill, neither ϵ_d or ϵ_q carry information w.r.t. $\delta x_d,\ \delta x_q$, thus identification is not possible, despite the stator excitation. Beyond standstill, $\hat{x}_d$ and $\hat{x}_q$ identifications are dependent, among others, on i_d and i_q respectively and prediction errors become

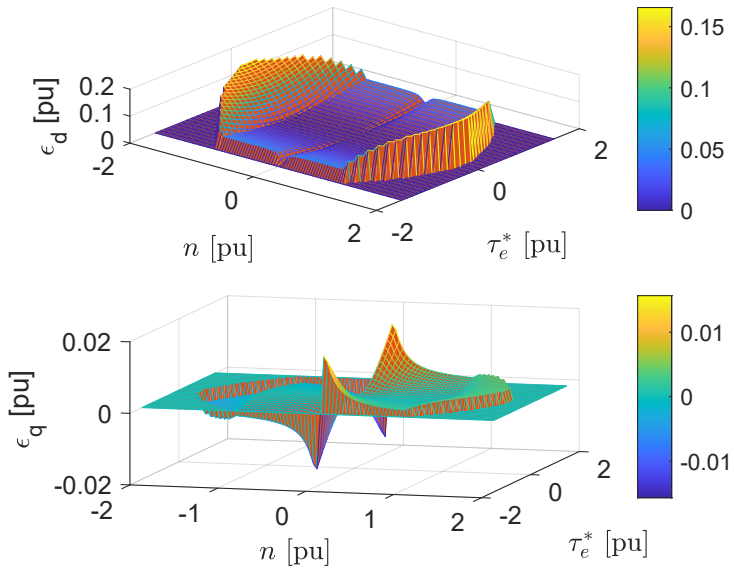

Figure 6.4. Prediction error in steady-state in four-quadrant speed-torque plane when $\hat{x}_d$ is 10% smaller than x_d.

richer with inductance error information when rotor speed and torque increase. When $\hat{x}_d$-identification is concerned, ϵ_d is expected to be more rich-conditioned in the high speed-region than ϵ_q because typically $x_q >> r_s$ (per-unit quantities). This advantage will be weakened in the lower speeds owing to the n^2-term in ϵ_d-numerator w.r.t. δx_d. Conversely, ϵ_q is expected to be richer with δx_q information at higher speeds due to the similar differences in the numerators compared to the ϵ_d. These phenomena become evident in Figure 6.4 and Figure 6.5 in which 10% lower $\hat{x}_d$ and $\hat{x}_q$ are assumed for a dual three-phase machine with data in Table 6.1.

Furthermore, the identification of $\hat{x}_{s\sigma}$ becomes possible by injecting nonzero z-plane currents. A new set of prediction errors emerges under these conditions as below:

$$\begin{aligned}
\epsilon_{z1} &= \left(\frac{-n^2 \cdot \hat{x}_\sigma}{\hat{r}_s^2 + n^2 \cdot \hat{x}_{s\sigma}^2} \cdot i_{z1} + \frac{n \cdot \hat{r}_s}{\hat{r}_s^2 + n^2 \cdot \hat{x}_{s\sigma}^2} \cdot i_{z2} \right) \delta x_{s\sigma} \\
&\quad - \left(\frac{\hat{r}_s}{\hat{r}_s^2 + n^2 \cdot \hat{x}_{s\sigma}^2} \cdot i_{z1} + \frac{n \cdot \hat{x}_{s\sigma}}{\hat{r}_s^2 + n^2 \cdot \hat{x}_{s\sigma}^2} \cdot i_{z2} \right) \delta r_s \\
\epsilon_{z2} &= \left(\frac{-n \cdot \hat{r}_s}{\hat{r}_s^2 + n^2 \cdot \hat{x}_{s\sigma}^2} \cdot i_{z1} - \frac{n^2 \cdot \hat{x}_\sigma}{\hat{r}_s^2 + n^2 \cdot \hat{x}_{s\sigma}^2} \cdot i_{z2} \right) \delta x_{s\sigma} \\
&\quad + \left(\frac{n \cdot \hat{x}_{s\sigma}}{\hat{r}_s^2 + n^2 \cdot \hat{x}_{s\sigma}^2} \cdot i_{z1} - \frac{\hat{r}_s}{\hat{r}_s^2 + n^2 \cdot \hat{x}_{s\sigma}^2} \cdot i_{z2} \right) \delta r_s \\
\delta x_{s\sigma} &= x_{s\sigma} - \hat{x}_\sigma
\end{aligned} \tag{6.8}$$

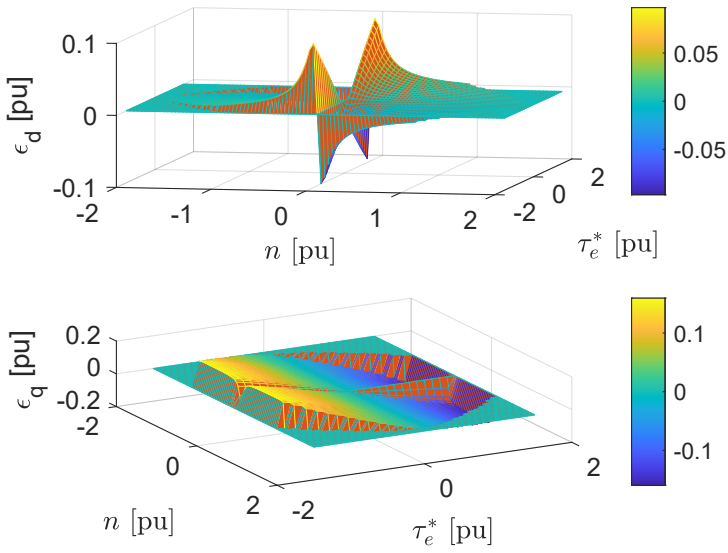

Figure 6.5. Prediction error in steady-state in four-quadrant speed-torque plane when $\hat{x}_q$ is 10% smaller than x_q.

Eq. (6.8) appears to be carrying information of not only $\delta x_{s\sigma}$, but also δr_s, yielding an additional method to identify $\hat{r}_s$. It is later shown in the section 6.4.1 that injection of i_{z1} has no influence on the torque production (unless the VSI reaches the current limit), thus utilization of i_{z1} can be useful in many ways. Provided that i_{z1}-injection is chosen, ϵ_{z1} can offer a fairly stronger input signal to RPEM in the high-speed region compared to ϵ_{z2} attributing to the fact that $x_{s\sigma} > r_s$ (per-unit quantities).

6.3.3 *Prediction-Gradients-Based Gain Computation*

$\boldsymbol{\Psi}^T$ is defined in Chapter 3 and it can be generally expressed as in (3.11). The subsequent expressions for dynamic $\boldsymbol{\Psi}^T$ w.r.t. $\hat{\psi}_m$, $\hat{r}_s$, $\hat{x}_d$, and $\hat{x}_q$ given in (3.12), (3.13), (3.14), and (3.15) are directly applicable to dual three-phase IPMSM identification with SSRF-oriented $\mathscr{M}_{u\theta}$-based predictor. Consequently, the corresponding steady-state $\boldsymbol{\Psi}^T$ expressions given in (4.15a), (4.15b), (4.16a), (4.16b), (4.17a), (4.17b), (4.18a), and (4.18b) also become applicable in this scope of research. The steady-state expressions of $\boldsymbol{\Psi}^T$ for $\hat{x}_d$ and $\hat{x}_q$ are plotted in Figure 6.6.

Given the oscillatory behavior, sensitivity to noise, and potential current sensor nonidealities, it is learned in section 3.5.1 that the choice of steady-state-$\boldsymbol{\Psi}^T$ is usually sufficient for satisfactory tracking. Accordingly, $\mathbf{L}$ can be computed using (6.9) in which $r[k]$ is the scalar Hessian and γ_0 is the gain-sequence which can be viewed as

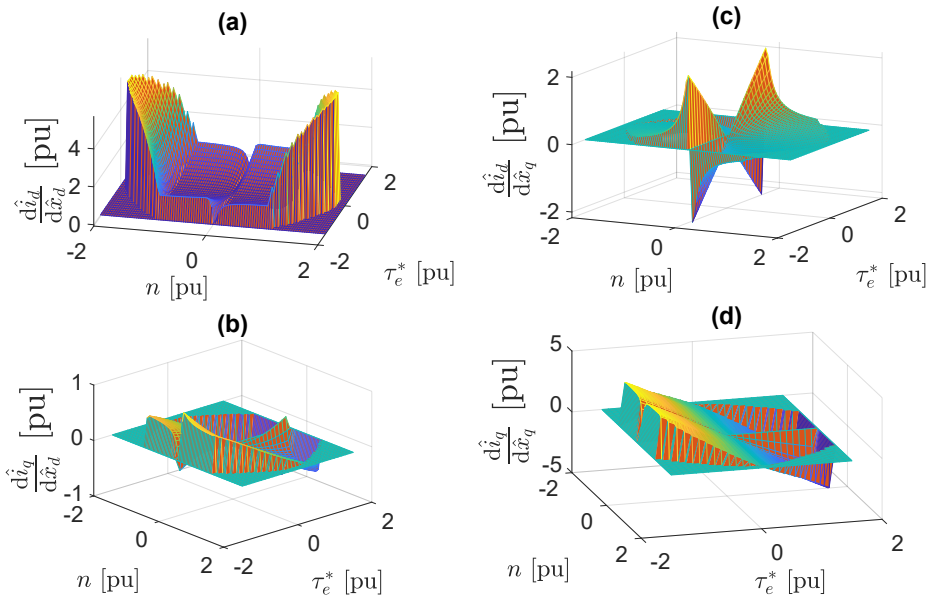

Figure 6.6. Prediction Gradient in steady-state in four-quadrant speed-torque plane (a) $\hat{i}_d$ w.r.t. $\hat{x}_d$ (b) $\hat{i}_q$ w.r.t. $\hat{x}_d$ (c) $\hat{i}_d$ w.r.t. $\hat{x}_q$ (d) $\hat{i}_q$ w.r.t. $\hat{x}_q$.

scaling and filtering quantities and their details are outlined in [18, 19].

$$\underline{\hat{\theta}}[k] = \underline{\hat{\theta}}[k-1] + \mathbf{L}[k] \cdot \underline{\epsilon}_s^r[k], \quad \mathbf{L}[k] = \gamma_{0,Lk} \frac{1}{r[k]} \mathbf{\Psi}[k]$$
$$r[k] = r[k-1] + \gamma_{0,rk} \left(tr \left\{ \mathbf{\Psi}[k] \cdot \mathbf{\Psi}^T[k] \right\} - r[k-1] \right) \tag{6.9}$$

6.4 Real-Time Simulation-Based Analysis and Results

In this section, the proposed online identification method of dual three-phase IPMSM is attempted to validate using a Xilinx Zynq System on Chip-based ERTS. Assuming the model inductances are updated online using the offline identifications, the concept is demonstrated by adapting $\hat{\psi}_m$ and $\hat{r}_s$ online. The overview of the ERTS is illustrated in Figure 6.7 and the associated hardware is presented in Figure 5.1. The power hardware components of the drive are programmed in the Field-Programmable Gate Array (FPGA) fabric of the SoC to achieve real-time emulation at a time-step of 1 μs. The digital filters and the PWM generators are programmed in separate entities in the on-chip FPGA at a time-step of 10 ns. The control, state- and parameter-estimation algorithms and likewise relatively slower processes are programmed in the on-chip processor at the PWM double-update time-step of 125 μs. The latter two programs are targeted also to control a physical hardware drive system. Ref

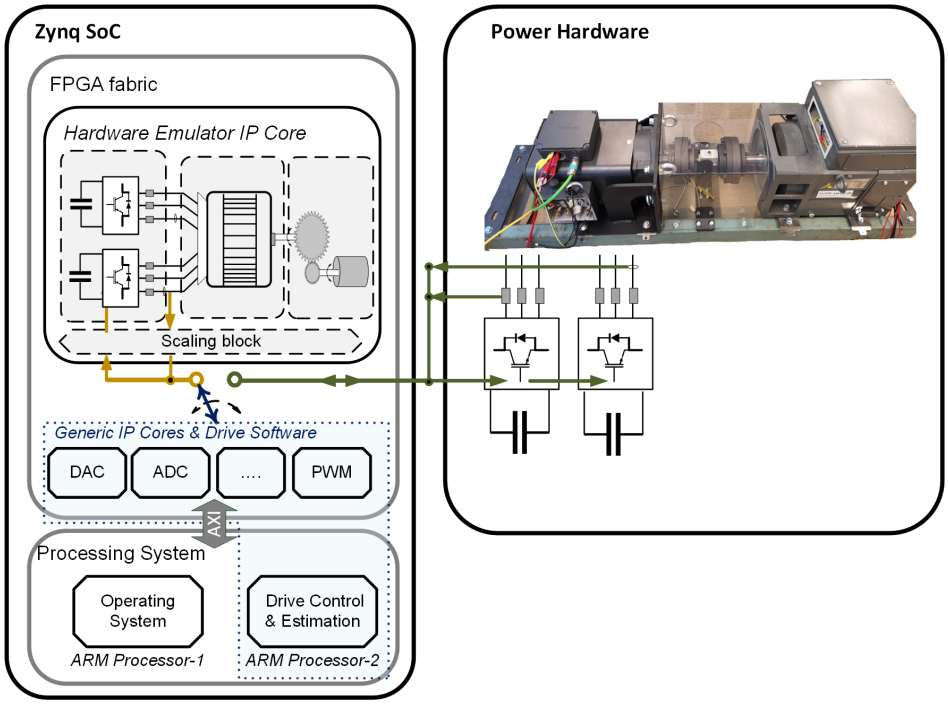

FIGURE 6.7. Overview of the Embedded Real-Time Simulator designed for simulation and implementation of the Field Oriented Control of dual three-phase IPMSM Drive.

[20] discloses the design details of a similar ERTS. Two separate two-level VSIs with asymmetrical modulation and 3rd harmonic injection are used to drive the machine. A simple speed-dependent gain-scheduler as presented in Chapter 3 is applied to restrain the $\hat{r}_s$-adaptation between -20 to 20 rpm and $\hat{\psi}_m$-adaptation beyond |200| rpm. A modified gain-scheduler that facilitates simultaneous adaptation of DTP IPMSM drives is presented in Chapter 7. Table 6.1 tabulates the experimental plant data.

TABLE 6.1. Parameters of the Experimental Plant

Symbol	Parameter	Value (SI)	Value (pu)
U_n	IPMSM Rated Voltage	336 V	1
I_n	IPMSM Rated Current	11.5 A	1
N_n	IPMSM Rated Speed	2000 rpm	1
T_n	IPMSM Rated Torque	63.8 Nm	1
p	IPMSM Number of pole-pairs	3	-
R_s	Stator Resistance	0.273 Ω	0.016
Ψ_m	Permanent magnet flux linkage	0.287 Wb	0.929
L_d	IPMSM d-axis inductance	7 mH	0.261
L_q	IPMSM q-axis inductance	12 mH	0.447
L_σ	IPMSM leakage inductance	2.7 mH	0.100
U_{dc}	DC bus voltage	220 V	0.655
f_{sw}	Power device switching frequency	4 kHz	-
T_{samp}	Sampling period	125 μs	-

6.4.1 Vector Control Performance

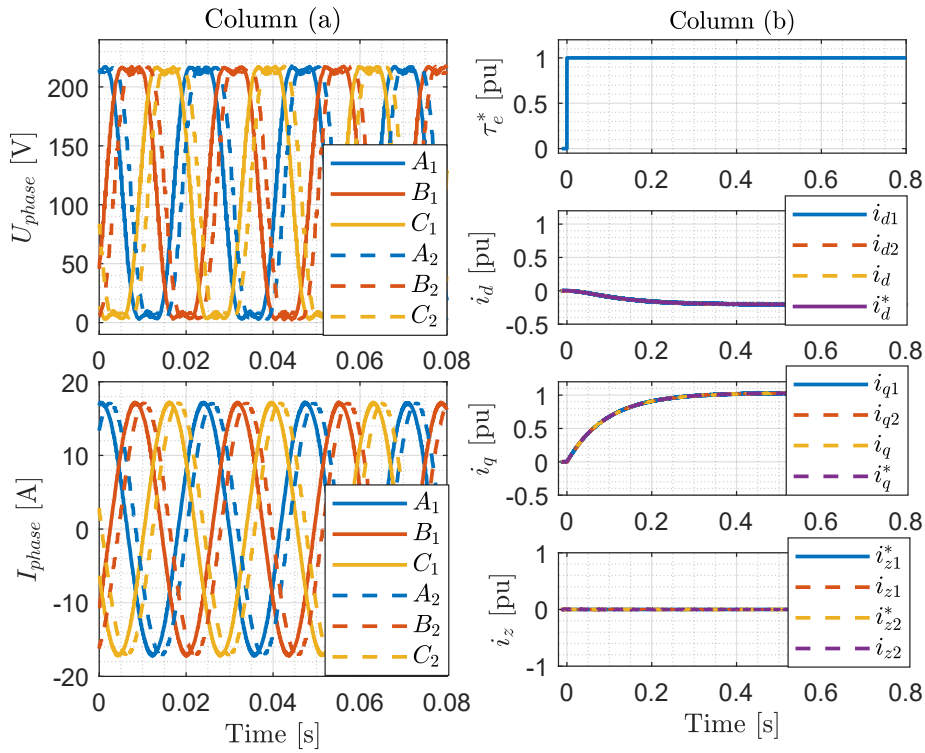

FIGURE 6.8. Field oriented control of the drive with SSRF current control when $i_{z1,2}^* = 0$. Column (a) phase voltages and currents at rated torque Column. (b) i_d, i_q, i_z at $\tau_{e,ref}$ step-change from 0 to 1 pu.

This section begins with a demonstration of the performance of the current vector controlled-drive during zero and nonzero z-axis excitation. Figure 6.8 corresponds to the case when $i_{z1,2}^* = 0$ in which column (a) shows the stator voltages and currents and column (b) gives insight to d, q, z-reference, and actual currents and the behavior of the respective controllers when τ^* step-changes from 0 to 1 pu. i_{d1}, i_{q1} are VSI-1 output currents after applying (6.1) and i_{d2}, i_{q2} are them for VSI-2. When these quantities are processed using (6.3a), i_d and i_q are obtained. Under this condition, equal torque sharing is seen between the two VSIs and the resulting current references conform to the MTPA strategy. Figure 6.9 demonstrates the behavior when z-currents are injected to the stator at 0 s when the machine is already loaded with 0.5 pu τ_{el}. Figure 6.9 column (a) corresponds to a case when a step-change of i_{z1}^* from 0 to 0.4 pu. This shows, firstly, the step-change does not influence i_{z2}^* in steady-state, apart from the transient under-dip of i_{z2}^* due to the coupling between $z1 - z2$ via L_σ. As a result, $u_{z2} \neq 0$. Conforming to (6.3a), i_{d1}, i_{d2} become ~0.4 and ~-0.4 pu such that $i_{z1} = 0.4$.

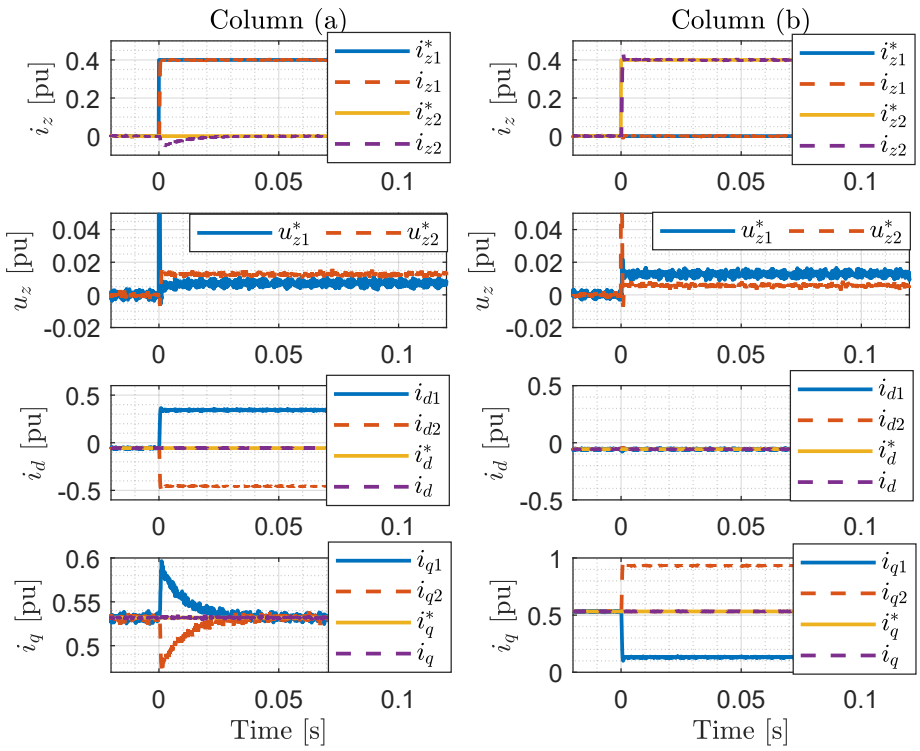

FIGURE 6.9. Field oriented control of the drive with SSRF current control at $\tau^*_e = 0.5pu$ (a) when i^*_{z1} step-change from 0 to 0.4 pu (b) when i^*_{z2} step-change from 0 to 0.4 pu.

Interestingly, i_{q1}, i_{q2}, apart from the transient over/under-shoot, settles at its reference value to make no change in the torque sharing between the VSI. Thus, the injection of i_{z1}-currents, at least periodically, can be used for the identification of r_s and x_σ. On the contrary, when $i_{z2} = 0.4$, as shown in column (b) of Figure 6.9, $i_{q1} \neq i_{q2}$, thus torque sharing becomes disturbed, thus may not be a solution for online identification. However, in both these cases, i^*_d, i^*_q, so are i_d, i_q not affected by $i_{z1,2}$ injection, which means the resultant torque production from the drive is undisturbed.

6.4.2 *Dynamics of Recursive Prediction Error Method*

In this section, the dynamic behaviors of predicted currents, prediction- errors $\epsilon_{d,q}$, error-gradients $\boldsymbol{\Psi}^T$, and Hessian functions are investigated. Figure 6.10 presents the dynamics at a -8% step-change of the motor PM flux $\psi_{m,mot}$ to simulate an effect due to the rotor temperature rise. A step reduction of the $\psi_{m,mot}$, an unlikely scenario, is simulated in order to identify the stability and the tracking speed of the proposed method. Figure 6.10(a) illustrates adaptation of $\hat{\psi}_m$. Figure 6.10(b) shows the currents and the respective predicted quantities and Figure 6.10(c) shows how the respective

prediction-error transients at the invoked parameter discrepancy at 0 s, yet are gradually driven to zero, in order to end the $\hat{\psi}_m$-adaptation. The prediction gradients, $\mathbf{\Psi}^T$ are plotted in Figure 6.10(d). It is evident that Ψ_{12} is relatively much smaller than Ψ_{11}, thus contributes very little in the **L**-computation. At the same time Ψ_{11} is settled at -3.84 which corresponds to $\frac{(-)1}{x_d}$. Note that, in the meantime, Ψ_{21} and Ψ_{22} are of comparable sizes to Ψ_{11}. What is also interesting is that because Ψ_{21} and Ψ_{22} are current-dependent and their dynamic states variants have been applied, small ripples are evident in them which is not noticed in the Ψ_{11} and Ψ_{12} because the latter contain their steady-state variants. Such oscillatory behavior is expected with dynamic variants as discussed in section 3.5.1. Figure 6.10(e) contains two alternatives for the scalar hessian that can be adopted. r_n corresponds to the scalar hessian as per (16) in [19]. However, one can eliminate Ψ_{21} and Ψ_{22} from the formula to obtain a smaller hessian, $r_{\psi m}$ which can yield a larger L_{11} and L_{12}. Thus, it is $r_{\psi m}$ that is adopted in this chapter. The choice of Hessians is elaborated in Chapter 3 and Chapter 4.

6.4.3 Online Parameter Adaptation

Online tracking performances of $\hat{\psi}_m$ and $\hat{r}_s$ using $\mathbf{\Psi}^T$-based SGA and RPEM at different speeds and loads will be investigated in this section. $\gamma_{0,rk}$, $\gamma_{0,Lk}$ values for $\hat{\psi}_m$-tracking are 6.25×10^{-4}, 3.25×10^{-4} and the same for $\hat{r}_s$-tracking are 6.25×10^{-4}, 1.25×10^{-4} respectively. Figure 6.11(a),(b) illustrate $\hat{\psi}_m$-adaptation at -8% step-change in the respective motor parameter, ψ_{mot}, while keeping $\delta r_s, \delta x_d, \delta x_q = 0$. In Figure 6.11(a), the adaptation is evaluated at different rotor speeds while keeping $\tau_{e,l}$ constant at 0.4 pu. When n increases, Ψ_{11} converges to $\sim \frac{1}{x_d}$ as per the respective steady-state $\mathbf{\Psi}^T$ shown in Chapter 3. This means that, here, the tracking speed becomes nearly independent from the rotor speed. The tracking performances at different load torques, when the rotor speed is kept constant are plotted in Figure 6.11(b). As the Ψ_{11}, Ψ_{12} are independent of loads, the convergence performances show indifference across different $\tau_{e,l}$. It can be summarized that with SGA, $\hat{\psi}_m$-adaptation is stable, sufficiently quick, and nearly or fully insensitive to speed (beyond very low speeds) and load variations. Figure 6.11- (c) and (d) are intended to show the influence of the wrong inductance estimates on the $\hat{\psi}_m$. Figure 6.11(c) corresponds to the steady-state $\hat{\psi}_m$ performance when $\delta x_d = 10\%$. It turns out that, irrespective of the rotor speed, $\hat{\psi}_m$ is fairly insensitive to δx_d as long as $\tau_{e,l}$ is small. This behaviour conforms to (6.7) in which, it is i_d and n will determine the influence from δx_d on $\hat{\psi}_m$. Similarly, when the impact from δx_q is considered in Figure 6.11(d), it appears that the influence increases with increasing rotor speed. When (6.7) is referred, it is seen that the influence of δx_q in ϵ_q-expression intensifies with higher speed, which can explain the observations. In general, this leads to an important conclusion that irrespective of the value of $\delta x_d, \delta x_q$, the accuracy of $\hat{\psi}_m$-identification can be improved when it is performed at no-load conditions.

The results of a similar study w.r.t. $\hat{r}_s$ online adaptation is shown in Figure 6.12. The adaptation performance at constant $\tau_{e,l}$ of 0.8 pu, while at different speeds is plotted in

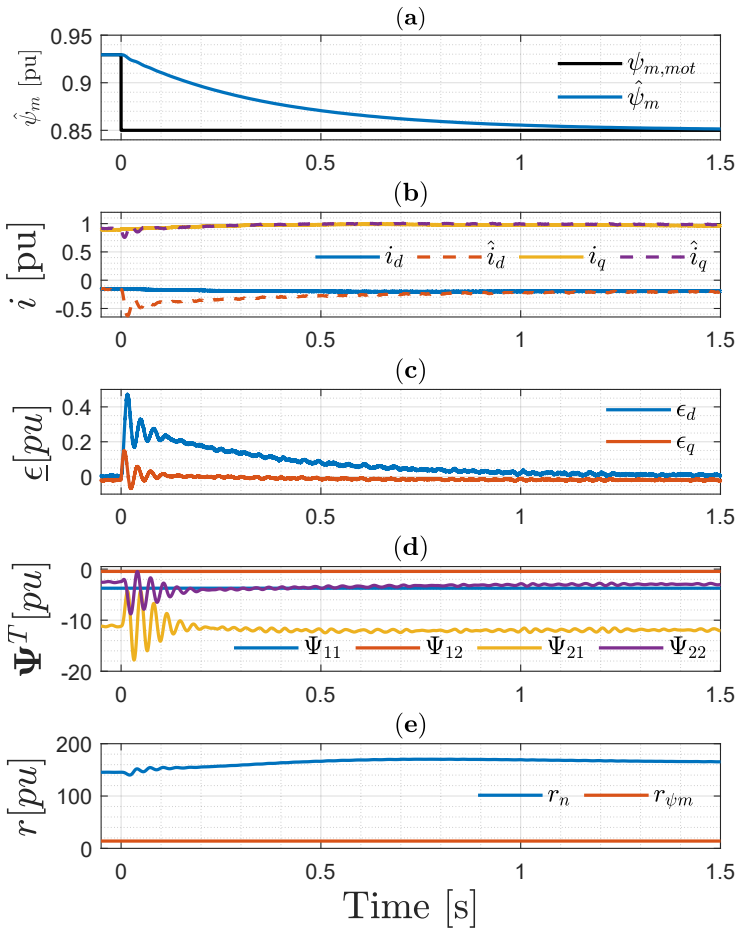

FIGURE 6.10. RPEM dynamics w.r.t. ψ_m-adaptation of the drive at 0.3 pu speed and 0.4 pu load-torque (a) $\hat{\psi}_m$ (b) actual and predicted currents (c) prediction-errors (d) prediction gradients (e) Hessians.

Figure 6.12(a). As expected, $\hat{r}_s$ online tracking is possible irrespective of the rotor speed including at standstill, as long as either or both i_d or i_q are nonzero. This indicates that at standstill no-load conditions, $\hat{r}_s$ identification is still possible with RPEM with the aid of injected i_d. Also, it is worth noting that the tracking speed is $\underline{i}_s$-dependent, and this dependence is evident in Figure 6.12(b). In Figure 6.12- (c) and (d), 10% of δx_d and δx_q are introduced to investigate their influence on the asymptotic behavior of $\hat{r}_s$. In both cases, it is observed that as long as the rotor is at a standstill, the inductance errors do not impact $\hat{r}_s$. This indicates an operating point where $\hat{r}_s$-identification can be performed more accurately.

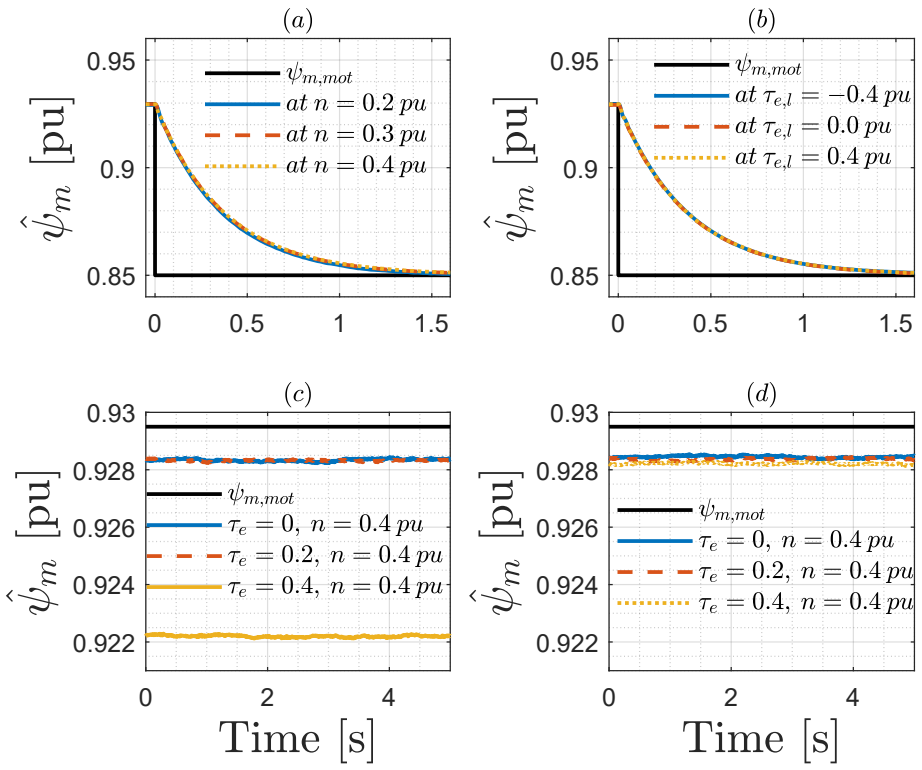

Figure 6.11. SGA based $\hat{\psi}_m$ adaptation of the drive (a) at different rotor speeds, while $\tau_{e,l} = 0.4$ pu (b) at different load torques, while $n = 0.3$ pu. Steady-state $\hat{\psi}_m$ behaviour at different torques and speeds when (c) $\delta x_d = 10\%$ (d) $\delta x_q = 10\%$.

6.5 Conclusion and Summary

This chapter proposed a recursive prediction error and gradients-based method for online identification of dual three-phase IPMSM. The method capitalizes on the sensitivity of the predicted currents to the model parameters. The prediction gradients are used to compute the gain matrix of the stochastic gradient algorithm. SSRF-based full-order model is adopted for its inherent robust performance and direct reuse of three-phase machine identification models. The theoretical basis is developed to explain the underlying physical inter-dependencies among the parametric errors and methods to identify d-, q- and leakage inductances are discussed. Eventually, the concept is demonstrated by tracking Ψ_m and R_s online with and without inductance errors which revealed the effects and operating points that can eliminate the impact of erroneous model inductances. Overall, the proposed method offers reasonable convergence speeds and stable tracking of temperature-sensitive motor parameters, which contributes to improving the performance of the multiphase electric drive. The

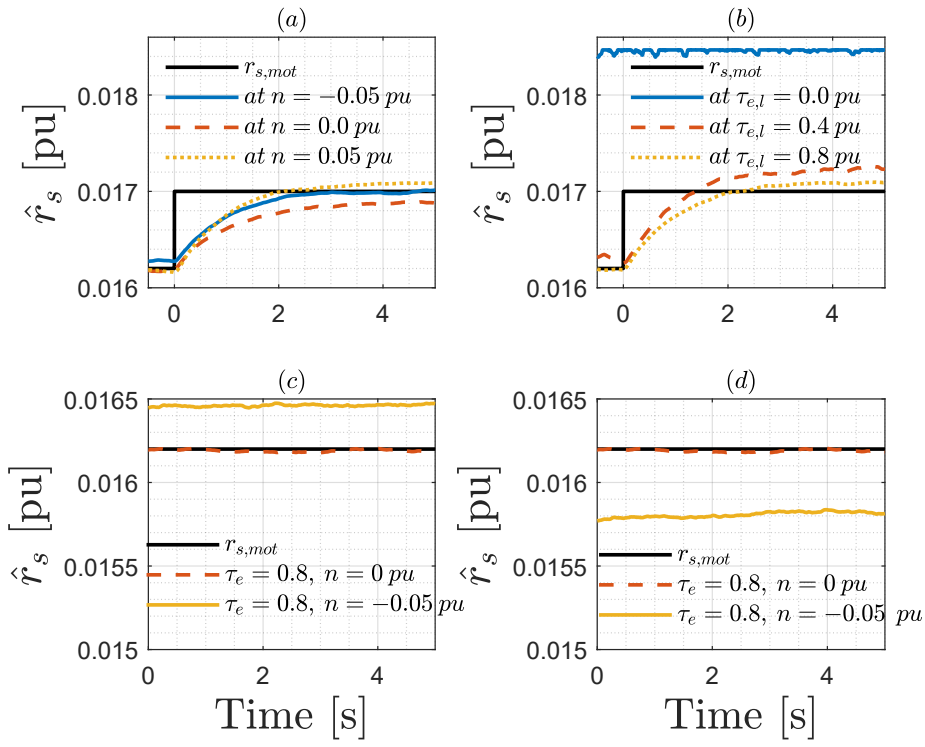

Figure 6.12. SGA based $\hat{r}_s$ adaptation of the drive (a) at different rotor speeds, while $\tau_{e,l} = 0.8$ pu (b) at different load torques, while $n = 0.005$ pu. Steady-state $\hat{r}_s$ behaviour at different torques and speeds when (c) $\delta x_d = 10\%$ (d) $\delta x_q = 10\%$.

validations using a laboratory prototype are given in the next chapter, which will also demonstrate how to capitalize on this concept in six-phase sensorless drives.

6.6 References

[1] Hang Seng Che, Mario J. Duran, Emil Levi, Martin Jones, Wooi Ping Hew, and Nasrudin Abd Rahim. Postfault operation of an asymmetrical six-phase induction machine with single and two isolated neutral points. *IEEE Transactions on Power Electronics* **29** (10), 5406–5416 (2014). ISSN 08858993. doi: 10.1109/TPEL.2013.2293195. Cited on page/s 109.

[2] Ahmed Salem and Mehdi Narimani. A Review on multiphase drives for automotive traction applications. *IEEE Transactions on Transportation Electrification* **5** (4), 1329–1348 (2019). ISSN 23327782. doi: 10.1109/TTE.2019.2956355. Cited on page/s 109.

[3] Emil Levi. Advances in converter control and innovative exploitation of additional degrees of freedom for multiphase machines. *IEEE Transactions on Industrial Electronics* **63** (1), 433–448 (2016). ISSN 02780046. doi: 10.1109/TIE.2015.2434999. Cited on page/s 109.

[4] Tayfun Gundogdu, Zi-Qiang Zhu, and Ching Chuen Chan. Comparative study of permanent magnet, conventional, and advanced induction machines for traction applications. *World Electric Vehicle Journal* (2022). doi: 10.3390. Cited on page/s 109.

[5] Z. Q. Zhu, Dawei Liang, and Kan Liu. Online parameter estimation for permanent magnet synchronous machines : an overview. *IEEE Access* **9**, 59059–59084 (2021). doi: 10.1109/ACCESS.2021.3072959. Cited on page/s 110.

[6] Pavel Vaclavek, Petr Blaha, and Ivo Herman. AC drive observability analysis. *IEEE Transactions on Industrial Electronics* **60** (8), 3047–3059 (2013). ISSN 02780046. doi: 10.1109/TIE.2012.2203775. Cited on page/s 110.

[7] Samuel J. Underwood and Iqbal Husain. Online parameter estimation and adaptive control of permanent-magnet synchronous machines. *IEEE Transactions on Industrial Electronics* **57** (7), 2435–2443 (2010). ISSN 02780046. doi: 10.1109/TIE.2009.2036029. Cited on page/s 110.

[8] Oliver Wallscheid. Thermal monitoring of electric motors: state-of-the-art review and future challenges. *IEEE Open Journal of Industry Applications* **2** (June), 204–223 (2021). doi: 10.1109/ojia.2021.3091870. Cited on page/s 110.

[9] Samuli Kallio, Jussi Karttunen, Pasi Peltoniemi, Pertti Silventoinen, and Olli Pyrhönen. Online estimation of double-star IPM machine parameters using RLS algorithm. *IEEE Transactions on Industrial Electronics* **61** (9), 4519–4530 (2014). ISSN 02780046. doi: 10.1109/TIE.2013.2290761. Cited on page/s 110.

[10] Ze Li, Guodong Feng, Chunyan Lai, Debmalya Banerjee, Wenlong Li, and Narayan C. Kar. Current injection-based multi-parameter estimation for dual three-phase IPMSM considering VSI nonlinearity. *IEEE Transactions on Transportation Electrification* **5** (2), 405–415 (2019). ISSN 23327782. doi: 10.1109/TTE.2019.2913270. Cited on page/s 110.

[11] Chunyan Lai, Guodong Feng, Ze Li, and Narayan C. Kar. Computation-Efficient Decoupled Multiparameter Estimation of PMSMs from Massive Redundant Measurements. *IEEE Transactions on Power Electronics* **35** (10), 10729–10740 (2020). ISSN 19410107. doi: 10.1109/TPEL.2020.2980315. Cited on page/s 110.

[12] Yifan Zhao and T A Lipo. Space vector PWM control of dual three-phase induction machine using vector space decomposition. *IEEE Transactions on Industry Applications* **31** (5) (1995). Cited on page/s 111.

[13] Nebrom Berihu Araya. Modelling and Control of Six-Phase Induction Motor Drive, M.Sc. Thesis. Norwegian University of Science and Technology, Trondheim (2012). Cited on page/s 114.

[14] Radu Bojoi, Mario Lazzari, Francesco Profumo, and Alberto Tenconi. Digital field-oriented control for dual three-phase induction motor drives. *IEEE Transactions on Industry Applications* **39** (3), 752–760 (2003). ISSN 00939994. doi: 10.1109/TIA.2003.811790. Cited on page/s 114.

[15] J. Karttunen, S. Kallio, P. Peltoniemi, P. Silventoinen, and O. Pyrhönen. Dual three-phase permanent magnet synchronous machine supplied by two independent voltage source inverters. *SPEEDAM 2012 - 21st International Symposium on Power Electronics, Electrical Drives, Automation and Motion* pages 741–747 (2012). doi: 10.1109/SPEEDAM.2012.6264448. Cited on page/s 114.

[16] Yashan Hu, Z. Q. Zhu, and Milijana Odavic. Comparison of Two-Individual Current Control and Vector Space Decomposition Control for Dual Three-Phase PMSM. *IEEE Transactions on Industry Applications* **53** (5), 4483–4492 (2017). ISSN 00939994. doi: 10.1109/TIA.2017.2703682. Cited on page/s 114.

[17] Ziqiang Zhu, Shensheng Wang, Bo Shao, Luocheng Yan, Peilin Xu, and Yuan Ren. Advances in dual-three-phase permanent magnet synchronous machines and control techniques. *Energies* **14** (7508) (2021). Cited on page/s 114.

[18] Lennart Ljung and Torsten Soderstrom. Theory and Practice of Recursive Identification. The MIT Press Cambridge, Massachusetts 2nd edition (1985). ISBN 0-262-12095-X. Cited on page/s 118.

[19] Aravinda Perera and Roy Nilsen. A framework and an open-loop method to identify PMSM parameters online. In *23rd International Conference on Electrical Machines and Systems, ICEMS* pages 1945–1950 Hamamatsu, Japan (2020). IEEE. Cited on page/s 118, 122.

[20] Aravinda Perera, Roy Nilsen, Thomas Haugan, and Kjell Ljøkelsøy. A design method of an embedded real-time simulator for electric drives using low-cost system-on-chip platform. In *PCIM Europe digital days* Nuremberg, Germany (2021). Cited on page/s 119.

Chapter 7

Enhanced Position Sensorless Control of Six-Phase Drives

Abstract

This chapter incorporates the open-loop predictor-based scheme proposed in previous chapter to identify all electric parameters, with the aim of enhancing the performance of sensorless Dual Three-Phase (DTP) IPMSM drives. Active Flux (AF) -based observer is employed to estimate the rotor position and speed. The online estimator identifies the temperature-sensitive parameters, i.e., permanent magnet flux linkage Ψ_m and stator winding resistance R_s. Methods are proposed to identify inductances including the stator leakage inductance ($L_{s\sigma}$), based on the same open-loop predictor. The combined observer and identification scheme is investigated using a Field Programmable Gate Array (FPGA)-based Real-Time Simulator, for the cross-coupling among the estimates, thereby, a modification to the general algorithm is proposed for simultaneous adaptation of Ψ_m and R_s. The experimental validations are conducted in 12 kW laboratory prototype, in which the proposed schemes are programmed using the C++ programming language in the industrial control platform previously presented. Results show that, by incorporating the proposed schemes, the observer is made more stable, precise, and robust to parameter variations as compared to the observer without parameter adaptation. Under the proposed scheme, the steady-state average rotor position error reported is below 2° and could reach speeds as low as 1%.

7.1 Introduction

7.1.1 Literature Review

ADVANTAGES of DTP IPMSM drives in medium voltage applications were mentioned in Chapter 6. In the meantime, the motivation behind the use of position sensorless drives and various methods to realize them have been reviewed in Chapter 4.

One drawback of such state observers used in sensorless control is their performance reliance on the precision of the machine parameters in the flux models (hereafter known as the model parameters). R_s and Ψ_m are temperature dependent whereas d,q -axes inductances, L_d, L_q, can vary due to the electromagnetic saturation and cross-coupling. In DTP machines, additionally, $L_{s\sigma}$ becomes a prominent parameter owing to its potential influence on the current control [1] and observer performance. The impact of remaining model parameters on the FE-based position estimation is discussed in [2, 3], and the discrepancies can lead to poor torque/speed control, reduced efficiency, increased torque ripples, and instability that can lead to faults [4]. Full-order observers are claimed to show more robustness to parameter variations over their reduced-order counterparts [5]. In this line of work, a range of modifications [6, 7] have been proposed lately to improve the classical MRAS-type observers, however, with the price of increased design complexity. Nonetheless, the performance of a simpler observer assisted by online parameter adaptation can emulate such complex types [8, 9], to obviate the need for tedious observer designing and tuning. Moreover, online parameter tracking can offer supplementary features like machine condition monitoring, and stator/rotor temperature tracking, a more reliable, less expensive, and much less cumbersome approach than sensor-based temperature monitoring. [10].

Consequently, online parameter adaptation has gained attention. Among the recent literature focused on multiphase drives, Recursive Least Squares (RLS) method is adopted in [11] to identify inductances and Ψ_m during operation and R_s during standstill in DTP IPMSM, which may, however, lead to temperature-affected performance degradation, particularly at lower speeds, due to the absence of online R_s identification. RLS-based identification is attempted to be improved in [12] with the aid of SI by accounting for the Voltage Source Inverters (VSI) nonlinearity. The multi-parameter estimation method is proposed in [13] based on improved machine models using redundant measurements, which is not ideal for online identification. The influence on the position estimation of DTP PMSM from the parameter deviation is attempted to mitigate in [14], using SI schemes. Additionally, the parameter identification schemes focusing on the three-phase machines have been reviewed in Chapter 4.

7.1.2 Research Gaps and Contribution

As noted, various model-based identification schemes have been proposed to augment reduced-order observers, in connection to three-phase drives. However, the author is unaware of similar literature dedicated to sensorless DTP drives. Besides, the set of algorithms proposed in Chapter 3 for three-phase IPMSM identification is yet to be validated in connection to DTP IPMSM identification and sensorless control, despite seeming to be promising as seen in the previous chapter. These gaps are attempted to address in this chapter, with the purpose of realizing relatively simple state estimation without compromising the performance due to observer simplicity or the injection of test signals.

In this chapter, the main contribution is to extend the Recursive Prediction Error Method (RPEM) along with the open-loop predictor to identify all electric parameters, with the aim of enhancing the sensorless DTP IPMSM drive. AF observer is chosen due to its prevalence, and relative ease of design, although, it is believed that any observer that relies on model parameters can fit into the proposed combined scheme. The Online Parameter Estimator (OPE) operates in parallel to the state observer and employs an open-loop model as opposed to the (closed-loop) observer. OPE is, hence, expected to be more sensitive to model parameter discrepancies. R_s and Ψ_m are identified online with the use of $\boldsymbol{\Psi}^T$-based Stochastic Gradient Algorithm (SGA), and to facilitate their simultaneous adaptation, minor modifications to the original method are proposed herein. For $L_{s\sigma}$ identification, the corresponding $\boldsymbol{\Psi}^T$ are developed and it is shown how SGA can be adopted in the cause. An alternative method known as the Physical Interpretative Method (PhyInt) is also developed and implemented for $L_{s\sigma}$ identification. An experimental method using the open-loop predictor is proposed to identify $L_{d,q}$. The method is aimed to improve sensorless control, particularly at very low speeds and saturation regions without the help of additional sensors or modification to the hardware or test signals, thus potential performance degradation is prevented. The Single Synchronous Reference Frame (SSRF)-oriented machine model and current control is applied in the flux models to harness the performance advantage over the DSRF-oriented approach [1]. The preliminary identification results shown in Chapter 6, offline identified parameters, and methods in combination with the AF observer are validated using the DTP laboratory prototype.

7.2 Dynamic Model and Control of DTP IPMSM

7.2.1 Machine Model

As same as in the previous chapter, the asymmetric winding configuration that has a displacement angle, $\vartheta_s = 30^\circ$ between the two three-phase groups $a_1 - b_1 - c_1$ and $a_2 - b_2 - c_2$, is chosen in this scope of work (see Figure 6.1), although the proposed methods are not limited to this configuration.

Six stator phases are transformed into three orthogonal subspaces, namely, $d - q,\ z_1 - z_2,\ 0_1 - 0_2$, which yields the SSRF-based machine model of interest. The transformation is performed sequentially, using the first principles as shown below

and their applications are illustrated in Figure 7.1.

$$\begin{bmatrix} f_{\alpha_m} \\ f_{\beta_m} \end{bmatrix} = \begin{bmatrix} f_{a_m} \\ \frac{1}{\sqrt{3}} \cdot (f_{b_m} - f_{c_m}) \end{bmatrix}, \qquad m = 1, 2 \tag{7.1}$$

$$f_{s_2} = \sqrt{f_{\alpha_2}^2 + f_{\beta_2}^2}, \qquad \delta_2 = \operatorname{atan2}\left(\frac{f_{\beta_2}}{f_{\alpha_2}}\right)$$

$$\begin{bmatrix} f_\alpha \\ f_\beta \end{bmatrix} = 0.5 \cdot \begin{bmatrix} f_{\alpha_1} + f_{s_2} \cdot \cos(\delta_2 + \vartheta_s) \\ f_{\beta_1} + f_{s_2} \cdot \sin(\delta_2 + \vartheta_s) \end{bmatrix} \tag{7.2}$$

$$\begin{bmatrix} f_{d_1} \\ f_{q_1} \\ f_{d_2} \\ f_{q_2} \end{bmatrix} = \begin{bmatrix} f_{\alpha_1} \cdot \cos(\hat{\vartheta}) + f_{\beta_1} \cdot \sin(\hat{\vartheta}) \\ -f_{\alpha_1} \cdot \sin(\hat{\vartheta}) + f_{\beta_1} \cdot \cos(\hat{\vartheta}) \\ f_{\alpha_2} \cdot \cos(\hat{\vartheta} - \vartheta_s) + f_{\beta_2} \cdot \sin(\hat{\vartheta} - \vartheta_s) \\ -f_{\alpha_2} \cdot \sin(\hat{\vartheta} - \vartheta_s) + f_{\beta_2} \cdot \cos(\hat{\vartheta} - \vartheta_s) \end{bmatrix} \tag{7.3}$$

In the context of Figure 7.1, f in (7.1)-(7.5) denotes either voltages or currents but can be flux linkages too. Therein, the SSRF-oriented DTP IPMSM model can be presented as follows:

$$\begin{bmatrix} u_d \\ u_q \\ u_{z1} \\ u_{z2} \\ u_{01} \\ u_{02} \end{bmatrix} = r_s \begin{bmatrix} i_d \\ i_q \\ i_{z1} \\ i_{z2} \\ i_{01} \\ i_{02} \end{bmatrix} + \frac{1}{\omega_n} \begin{bmatrix} \dot{\psi}_d \\ \dot{\psi}_q \\ \dot{\psi}_{z1} \\ \dot{\psi}_{z2} \\ \dot{\psi}_{01} \\ \dot{\psi}_{02} \end{bmatrix} + n \begin{bmatrix} -\psi_q \\ \psi_d \\ \psi_{z2} \\ -\psi_{z1} \\ 0 \\ 0 \end{bmatrix} \tag{7.4}$$

$$\begin{aligned} \psi_d &= x_d \cdot i_d + \psi_m & \psi_q &= x_q \cdot i_q & \psi_{z1} &= x_{s\sigma} \cdot i_{z1} \\ \psi_{z2} &= x_{s\sigma} \cdot i_{z2} & \psi_{01} &= x_{s\sigma} \cdot i_{01} & \psi_{02} &= x_{s\sigma} \cdot i_{02} \\ x_d &= x_{md} + x_{s\sigma} & x_q &= x_{mq} + x_{s\sigma} \end{aligned}$$

All the notations follow the same meanings given in Chapter 6. Provided that the sum of stator currents is zero in each isolated three-phase group, the 0-systems are not excited, and can then be omitted from the model. The relationship between the SSRF and DSRF quantities can be presented as given below:

$$\begin{aligned} f_d &= \frac{f_{d1} + f_{d2}}{2}, & f_q &= \frac{f_{q1} + f_{q2}}{2} \\ f_{z1} &= \frac{f_{d1} - f_{d2}}{2}, & f_{z2} &= \frac{f_{q2} - f_{q1}}{2} \end{aligned} \tag{7.5a}$$

$$\begin{aligned} f_{d1} &= f_d + f_{z1}, & f_{q1} &= f_q - f_{z2} \\ f_{d2} &= f_d - f_{z1}, & f_{q2} &= f_q + f_{z2} \end{aligned} \tag{7.5b}$$

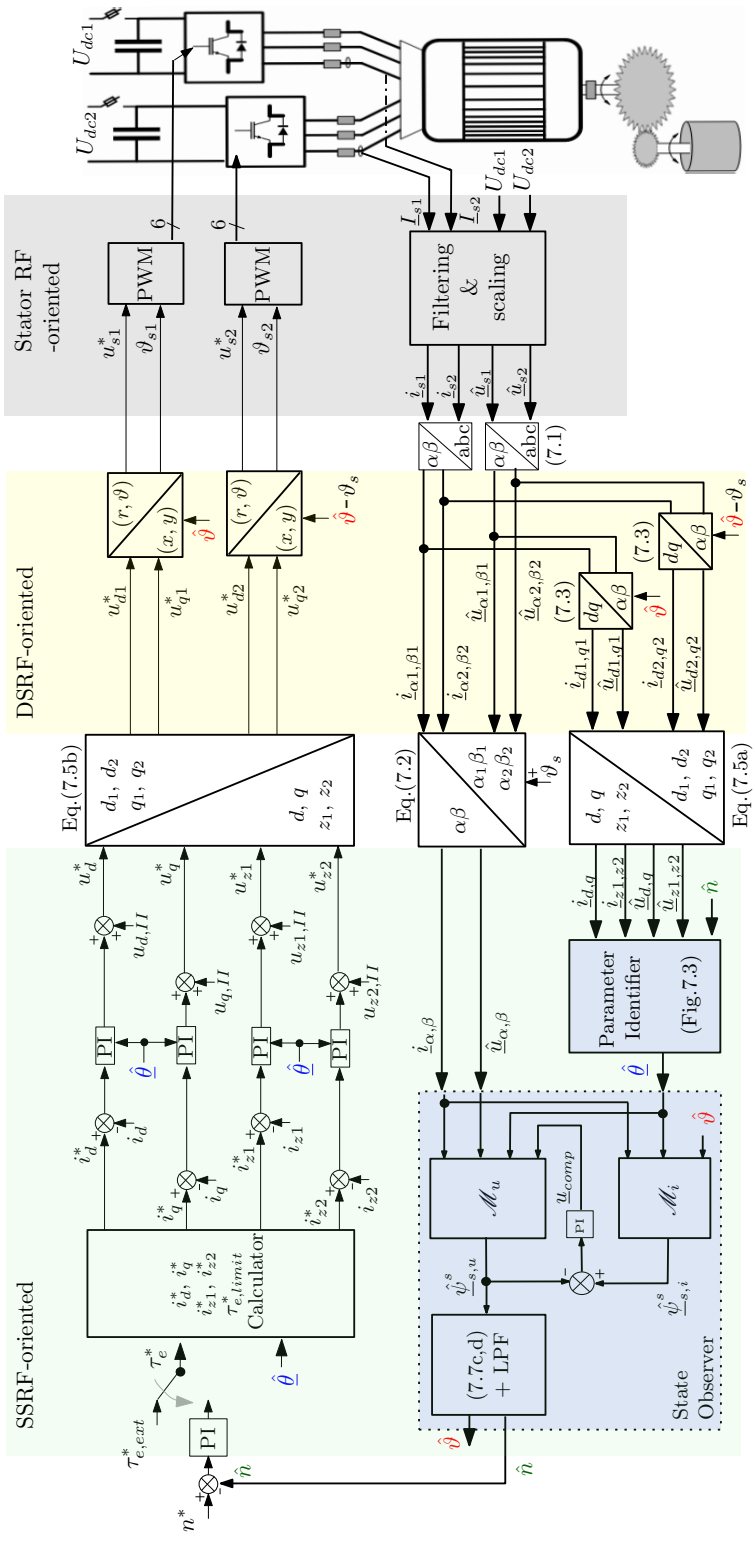

FIGURE 7.1. Block diagram of the vector-controlled, sensorless DTP IPMSM drive with SSRF-oriented and decoupled current control. State observer and parameter identifier are shaded in blue.

7.2.2 Drive Vector Control

Vector-controlled DTP IPMSM drive is illustrated in Figure 7.1. Two units of classical three-phase VSI are supplied by separate dc-link capacitors, in which the voltages $u_{dc1,2}$ are measured and used to estimate the respective stator winding voltages $\hat{\underline{u}}_{s1,2}$. The stator winding currents are directly measured at the output of the inverters. Stator quantities are subsequently transformed to obtain the SSRF counterparts, which are fed into the Parameter Identifier. Based on the torque command τ_e^* either from an external source or from the speed controller, i_d^*, i_q^* are calculated to fulfill either MTPA strategy or the field-weakening strategy at high-speed operations. $i_{z1,2}^*$ can be set to zero, assuming equal torque sharing between the VSI units. However, $i_{z1,2}^*$ can become nonzero if the two VSIs have different torque-limiters due to the possible differences among their respective dc-link voltage-, power- or current- limitations. The resulting current errors are compensated using Proportional-Integral (PI) controllers. As it is evident in Figure 7.1, the drive employs an SSRF-oriented current control over alternative approaches [15, 16] to eliminate the influence from the coupling between the winding sets, thus to enhance the dynamic performance [1].

$$\begin{aligned} u_{d,II} &= -n \cdot x_q \cdot i_q, & u_{q,II} &= n \cdot x_d \cdot i_d + n \cdot \psi_m \\ u_{z1,II} &= n \cdot x_{s\sigma} \cdot i_{z2}, & u_{z2,II} &= -n \cdot x_{s\sigma} \cdot i_{z1} \end{aligned} \tag{7.6}$$

The cross-coupling between the $d-q$ quantities can be compensated by using the decoupled current control. The coupling terms as given in the (7.6) are fed forward to make the compensation more efficient and accurate. Thereby, $u_d^*, u_q^*, u_{z1}^*, u_{z2}^*$ in the SSRF are obtained. In order to split these quantities between the two VSIs, expressions in (7.5b) are employed, thereafter, the quantities are processed to obtain the voltage vector and fed into the dedicated Pulse Width Modulators (PWM). For the same reasons mentioned before, u_{01}, u_{02} are assumed zero.

7.3 Sensorless Control Scheme

This section encapsulates the sensorless control scheme that is comprised of the AF-based state observer and the proposed open-loop model-based parameter identification.

7.3.1 Active Flux Observer for State Estimation

The classical AF observer is adopted for rotor position and speed estimation in this chapter. The AF concept is disclosed in [17] and the design and tuning details for such MRAS-type observers are unveiled in [18–20]. Owing to the use of SSRF, the flux models and tuning methods of an AF observer for DTP drives do not differ from those

of a three-phase drive presented in Chapter 4. Thus, only for the sake of completeness, related key formulae are presented below, in which $\underline{\psi}_T$ denotes the AF vector.

$$\psi_T = \psi_m - (x_q - x_d) \cdot i_d \tag{7.7a}$$

$$\underline{\psi}_T = \underline{\psi}_s - x_q \cdot \underline{i}_s \tag{7.7b}$$

$$\hat{\vartheta} = \text{atan2}\left(\frac{\psi^s_{T,\beta}}{\psi^s_{T,\alpha}}\right) \tag{7.7c}$$

$$\hat{n} = \frac{\psi^s_{T,\alpha}[k-1] \cdot \psi^s_{T,\beta}[k] - \psi^s_{T,\beta}[k-1] \cdot \psi^s_{T,\alpha}[k]}{T_{samp} \cdot \left(\psi^{s2}_{T,\alpha}[k] + \psi^{s2}_{T,\beta}[k]\right)} \tag{7.7d}$$

$$\hat{\underline{\psi}}^s_{s,u} = \omega_n \cdot \int \left(\underline{u}^s_s - r_s \cdot \underline{i}_s + \underline{u}_{comp}\right) \cdot dt \tag{7.8a}$$

$$\hat{\underline{\psi}}^r_{s,i} = \mathbf{x}^r_s \cdot \underline{i}^r_s + \underline{\psi}^r_m \tag{7.8b}$$

Figure 7.2 illustrates the phasor diagram in this context. As seen, under SSRF strategy, single $\underline{\psi}_T$ is formulated which is located in the d-axis of the rotor, thus identifying the phase of $\underline{\psi}_T$ will tell us the rotor position w.r.t. the machine a-axis, same as in the three-phase case. $\hat{\vartheta}$ and $\hat{n}$ can be calculated using the components of $\underline{\psi}_T$ using (7.7c) and (7.7d) [21] or alternatively, a Phase-Locked Loop (PLL) [17, 18]. The latter approach can provide some filtering, and thus can be favourable in some applications. These computation methods, however, fall out of the scope of this chapter in which the implementation relies on (7.7c) and (7.7d) along with a 1st order Low Pass Filter (LPF) with a time constant of 3 ms to eliminate the ripple in $\hat{n}$, that yields $\hat{n}_{filt}$.

The observer analysis and design criteria presented in Chapter 4 remain valid in this context. Chapter 4 also revealed the impact of mistuned model parameters on the observer performance. That impact is applicable in DTP drives-associated observers, which provides the motivation to develop schemes for parameter identification of sensorless DTP drives.

7.3.2 *Online Method for ψ_m, r_s Identification*

The online identification methods presented in Chapter 6 are followed in this chapter, i.e., $\mathbf{\Psi}^T$-based RPEM is adopted to identify ψ_m and r_s online. The generalized RPEM, in the discrete form of a pure integrator, becomes:

$$\underline{\hat{\theta}}[k] = \left[\underline{\hat{\theta}}[k-1] + \mathbf{L}[k, \underline{\hat{\theta}}] \cdot \underline{\epsilon}[k, \underline{\hat{\theta}}]\right]_{D_{\mathscr{M}}} \tag{7.9}$$

$$\begin{aligned} \underline{\hat{\theta}} &= \left[\hat{\psi}_m \quad \hat{r}_s \quad \hat{x}_d \quad \hat{x}_q \quad \hat{x}_{s\sigma}\right]^T,\ \underline{\hat{\theta}} \in D_{\mathscr{M}},\ D_{\mathscr{M}} \in D_s \\ D_{\mathscr{M}} &= \left\{\underline{\hat{\theta}}_{min} \le \underline{\hat{\theta}} \le \underline{\hat{\theta}}_{max}\right\} \end{aligned} \tag{7.10}$$

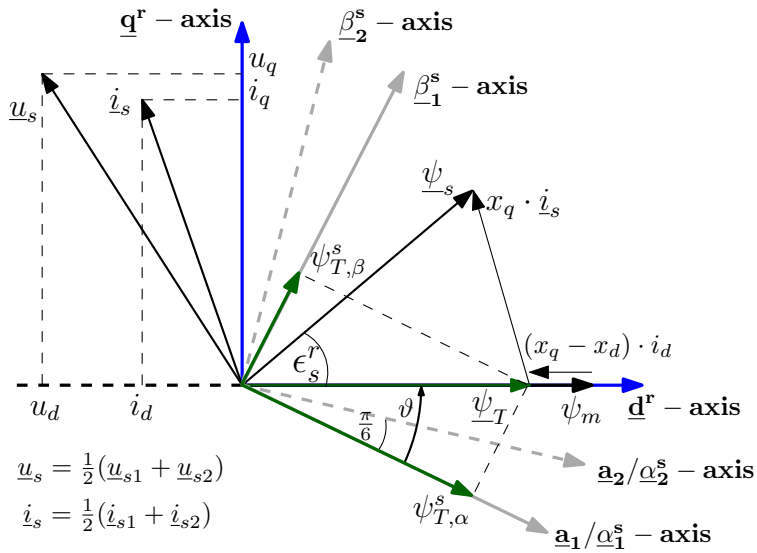

Figure 7.2. Phasor diagram of DTP IPMSM to highlight the Active Flux Vector in SSRF and its application in position estimation.

The meanings of the notations are as same as what is given in Chapter 6. To circumvent this challenge without compromising the performance, $\hat{\psi}_m$ and $\hat{r}_s$ are identified online and the remaining parameters are identified offline and updated in real-time. Figure 7.3 illustrates the structure of the Parameter Identifier in the proposed scheme.

$$\begin{aligned}\frac{\mathbf{x}_s^r(\underline{i}_s)}{\omega_n}\frac{\mathrm{d}\hat{\underline{i}}_s^r(t,\hat{\underline{\theta}})}{\mathrm{d}t} &= \underline{u}_s^r(t) - \hat{r}_s(t)\cdot\hat{\underline{i}}_s^r(t,\hat{\underline{\theta}}) \\ &\quad -\mathbf{j}\cdot\hat{n}(t,\hat{\underline{\theta}})\cdot\mathbf{x}_s^r(\underline{i}_s)\cdot\hat{\underline{i}}_s^r(t,\hat{\underline{\theta}}) - \mathbf{j}\cdot\hat{n}(t,\hat{\underline{\theta}})\cdot\underline{\psi}_m^r(t)\end{aligned} \tag{7.11}$$

The predictor is designed with the Full-Order Model, $\mathscr{M}_{u\theta}$ given in (7.11), that yields $\hat{\underline{i}}_s^r$. The stability of the predictor in the continuous and discrete-time domains is discussed in [22], which concludes that the trapezoidal rule-based implementation in the DSP offers stable prediction across the full speed range. $\underline{\epsilon}$ becomes $\underline{\epsilon} = \underline{i}_s^r - \hat{\underline{i}}_s^r$ for which a simplified expression in steady-state can be obtained as below, w.r.t. $\hat{\psi}_m$, $\hat{r}_s$ where $\delta\underline{\theta} = \underline{\theta} - \hat{\underline{\theta}}$.

$$\begin{aligned}\epsilon_d &= -\left(\frac{\hat{n}^2\cdot\hat{x}_q}{\hat{r}_s^2+\hat{n}^2\cdot\hat{x}_d\cdot\hat{x}_q}\right)\delta\psi_m \\ &\quad -\left(\frac{\hat{r}_s}{\hat{r}_s^2+\hat{n}^2\cdot\hat{x}_d\cdot\hat{x}_q}\cdot i_d + \frac{\hat{n}\cdot\hat{x}_q}{\hat{r}_s^2+\hat{n}^2\cdot\hat{x}_d\cdot\hat{x}_q}\cdot i_q\right)\delta r_s \\ \epsilon_q &= -\left(\frac{\hat{n}\cdot\hat{r}_s}{\hat{r}_s^2+\hat{n}^2\cdot\hat{x}_d\cdot\hat{x}_q}\right)\delta\psi_m \\ &\quad -\left(\frac{\hat{r}_s}{\hat{r}_s^2+\hat{n}^2\cdot\hat{x}_d\cdot\hat{x}_q}\cdot i_q - \frac{\hat{n}\cdot\hat{x}_d}{\hat{r}_s^2+\hat{n}^2\cdot\hat{x}_d\cdot\hat{x}_q}\cdot i_d\right)\delta r_s\end{aligned} \tag{7.12}$$

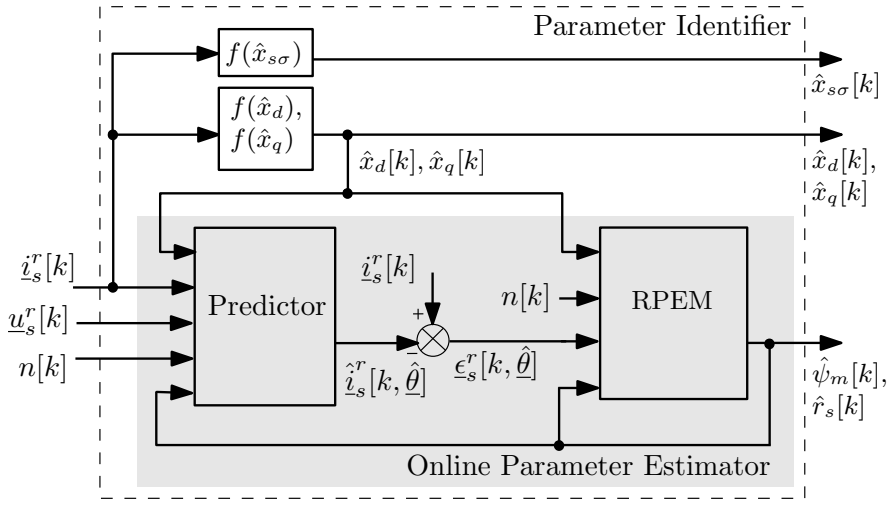

FIGURE 7.3. Detailed block diagram of the Parameter Identifier shown in Figure 7.1 that incorporates the Online Parameter Estimator with open-loop predictor.

Here, it is assumed that δx_d and δx_q are eliminated in real-time by using the offline identified values. The full expression is disclosed in Chapter 3. Eq. (7.12) provides insight into the inter-dependencies among the rotor speed, loading and parameter discrepancies. $\underline{\epsilon}$ is also the quantity that carries parametric error information into the RPEM, thus when $\delta\underline{\theta}$ reaches zero, the updating of the model parameter naturally stops. The updating of the model parameter will be weakened (or stopped) also when the drive is in an operating region, where $\underline{\epsilon}$ is not sensitive for the particular $\delta\underline{\theta}$. For example, at a standstill or very low speeds, $\underline{\epsilon}$ is null or poorly conditioned w.r.t. $\delta\psi_m$-information, thus not suitable for $\hat{\psi}_m$-adaptation in the very low-speed region. Similarly, at no- or smaller- stator current conditions, $\hat{r}_s$-adaptation becomes impossible or poor.

$$\mathbf{L}[k] = \gamma_{0,Lk} \frac{1}{r[k]} \boldsymbol{\Psi}[k] \tag{7.13}$$
$$r[k] = r[k-1] + \gamma_{0,rk} \left(tr\left\{ \boldsymbol{\Psi}[k] \cdot \boldsymbol{\Psi}^T[k] \right\} - r[k-1] \right)$$

$$\Psi : \frac{\mathrm{d}}{\mathrm{d}\hat{\underline{\theta}}} \left(\frac{\mathrm{d}\hat{\underline{i}}_s^r(t, \hat{\underline{\theta}}))}{\mathrm{d}t} \right) = \frac{\mathrm{d}}{\mathrm{d}t} \left(\frac{\mathrm{d}\hat{\underline{i}}_s^r(t, \hat{\underline{\theta}}))}{\mathrm{d}\hat{\underline{\theta}}} \right) \tag{7.14}$$
$$= \frac{\mathrm{d}}{\mathrm{d}\hat{\underline{\theta}}} \left(\underline{f}_{-c} \left(t, \hat{\underline{i}}_s^r(t, \hat{\underline{\theta}}), \underline{u}_s^r(t), n(t); \hat{\underline{\theta}} \right) \right)$$

The other main component in (7.9) is $\mathbf{L}$ that can be computed using a few different algorithms, out of which the Stochastic Gradient Algorithm (SGA) appears to be the optimal choice from the perspective of temperature-sensitive parameter identification

[22]. SGA can be expressed as in (7.13) [23]. r[k] is the Hessian function that provides filtering against the potential oscillations in $\boldsymbol{\Psi}^T$. Gain-sequences $\gamma_{0,Lk}$, $\gamma_{0,rk}$ are time-constants in the respective integral and filtering actions. The centerpiece of SGA is $\boldsymbol{\Psi}^T$ of which the generalized dynamic form can be expressed as in (7.14), of which $\underline{f}_c$ is a function equivalent to the right-hand side of (7.11).

$$\Psi_{11}: \frac{\mathrm{d}\hat{i}_d}{\mathrm{d}\hat{\psi}_m} = -\frac{\hat{n}^2 \cdot \hat{x}_q}{\hat{r}_s^2 + \hat{n}^2 \cdot \hat{x}_q \cdot \hat{x}_d} \tag{7.15a}$$

$$\Psi_{12}: \frac{\mathrm{d}\hat{i}_q}{\mathrm{d}\hat{\psi}_m} = -\frac{n \cdot \hat{r}_s}{\hat{r}_s^2 + n^2 \cdot \hat{x}_q \cdot \hat{x}_d} \tag{7.15b}$$

$$\Psi_{21}: \frac{\mathrm{d}\hat{i}_d}{\mathrm{d}\hat{r}_s} = -\frac{\hat{r}_s \cdot \hat{i}_d}{\hat{r}_s^2 + \hat{n}^2 \cdot \hat{x}_q \cdot \hat{x}_d} - \frac{\hat{n} \cdot \hat{x}_q \cdot \hat{i}_q}{\hat{r}_s^2 + \hat{n}^2 \cdot \hat{x}_q \cdot \hat{x}_d} \tag{7.16a}$$

$$\Psi_{22}: \frac{\mathrm{d}\hat{i}_q}{\mathrm{d}\hat{r}_s} = -\frac{\hat{r}_s \cdot \hat{i}_q}{\hat{r}_s^2 + \hat{n}^2 \cdot \hat{x}_q \cdot \hat{x}_d} + \frac{\hat{n} \cdot \hat{x}_d \cdot \hat{i}_d}{\hat{r}_s^2 + \hat{n}^2 \cdot \hat{x}_q \cdot \hat{x}_d} \tag{7.16b}$$

The dynamic forms of the $\boldsymbol{\Psi}^T$ w.r.t. $\hat{\psi}_m$ and $\hat{r}_s$ are presented in [22]. The corresponding steady-state $\boldsymbol{\Psi}^T$ forms can be derived by equalizing the left hand side of their dynamic forms to zero. The final derivations are given in (7.15) and (7.16) w.r.t. $\hat{\psi}_m$ and $\hat{r}_s$.

In order to elaborate on the behaviors of the prediction gradients, they are visualized in Figure 7.4. It is evident from Figure 7.4(a) that Ψ_{11} is clearly more sensitive than Ψ_{12} w.r.t. $\hat{\psi}_m$. Additionally, Ψ_{11} becomes a stronger signal beyond low speeds. In contrast, $\Psi_{21,22}$ in Figure 7.4(b) are stronger in the low-speed region. By applying the significant prediction gradient elements into (7.9), the specific algorithms to identify temperature-sensitive parameters online can be developed as follows.

$$\hat{\psi}_m[k] = \hat{\psi}_m[k-1] + \frac{\gamma_{0,Lk}}{r[k]} \left(\Psi_{11}[k] \cdot \epsilon_d[k]\right) \tag{7.17}$$

$$\hat{r}_s[k] = \hat{r}_s[k-1] + \frac{\gamma_{0,Lk}}{r[k]} \left(\Psi_{21}[k] \cdot \epsilon_d[k] + \Psi_{22}[k] \cdot \epsilon_q[k]\right) \tag{7.18}$$

7.3.3 *Experimental Method for x_d, x_q Identification*

In this section, an intuitive experimental method is presented to identify the SSRF-oriented $\hat{x}_d, \hat{x}_q$. The proposed experiment, also, is premised on the $\mathscr{M}_{u\theta}$-based open-loop predictor in (7.11). The method assumes $\hat{\psi}_m$, $\hat{r}_s$ are correctly tuned, thus $\delta\psi_m, \delta r_s = 0$. To prevent the influence of temperature-affected variations, the tests must be performed in short runs at regular intervals. It must be ensured that no error in the rotor position/speed acquisition. To improve the accuracy of the identification, DTP IPMSM drive to be operated in the torque mode whereas the load drive in the speed mode. Under this configuration, the friction and other mechanical losses will be served of

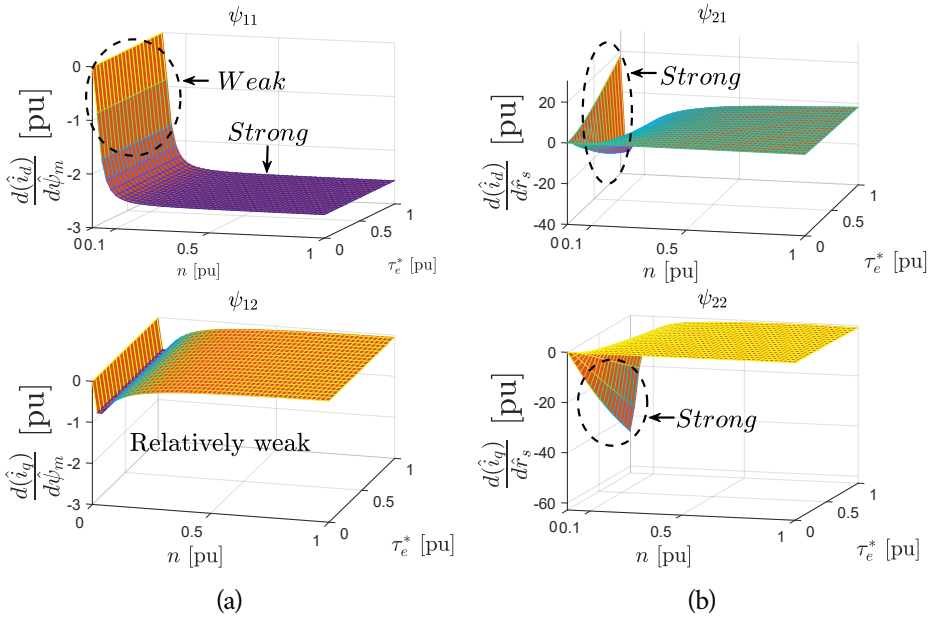

FIGURE 7.4. Steady-state prediction gradients in the speed-torque plane w.r.t. (a) $\hat{\psi}_m$ (b) $\hat{r}_s$.

by the load drive, or can be neglected, thus the stator currents in the DTP IPMSM can be assumed only for the production of the commanded torque. When the above assumptions are held true and the inductances are correctly identified, the following expressions become valid in steady-state.

$$
\begin{aligned}
u_d &= \underbrace{r_s \cdot i_d - n \cdot x_q \cdot i_q}_{\text{Physical}} = \underbrace{\hat{r}_s \cdot \hat{i}_d - n \cdot \hat{x}_q \cdot \hat{i}_q}_{\text{Model}} \\
u_q &= \underbrace{r_s \cdot i_q + n \cdot x_d \cdot i_d + n \cdot \psi_m}_{\text{Physical}} \\
&= \underbrace{\hat{r}_s \cdot \hat{i}_q + n \cdot \hat{x}_d \cdot \hat{i}_d + n \cdot \hat{\psi}_m}_{\text{Model}}
\end{aligned}
\tag{7.19}
$$

Under these conditions, when there exist differences in actual and predicted currents, i.e. $i_d - \hat{i}_d = \delta i_d \neq 0$ and/or $i_q - \hat{i}_q = \delta i_q \neq 0$, the following expressions can be derived by neglecting the voltage drops across the resistances because $r_s << x_{d,q}$ in per-unit.

$$
\delta i_d = \frac{u_q - n \cdot \psi_m}{n \cdot x_q \cdot \hat{x}_q}(\hat{x}_d - x_d), \;\; \delta i_q = \frac{u_d}{n \cdot x_q \cdot \hat{x}_q}(x_q - \hat{x}_q) \tag{7.20}
$$

Eq. (7.20) tells us that, under the given conditions, if the model inductances are correctly tuned, then $\delta i_{d,q}$ will be driven to zero. Subsequently, the analytical functions

are developed as below to represent the identified inductance-current relationships, assuming the MTPA control strategy.

$$\begin{aligned}\hat{x}_q(i_q) &= \begin{cases} -0.0535 \cdot |i_q| + 1.089; & |i_q| \le 0.55\ pu \\ -0.25 \cdot |i_q| + 1.2063; & |i_q| > 0.55\ pu \end{cases} \\ \hat{x}_d(i_d) &= -0.1622 \cdot i_d + 0.33; \qquad i_d < 0\ pu \end{aligned} \tag{7.21}$$

Alternatively, one can also develop higher-order functions to fit the identified data. These functions are programmed in the processor, to update $\hat{x}_d,\ \hat{x}_q$ in real-time in accordance with the measured current.

7.3.4 *Experimental Method for $x_{s\sigma}$ Identification*

Similar to (7.12), an analytical expression can be developed as below with the aid of z-axis quantities, to include $\hat{x}_{s\sigma}$, speed, and loading.

$$\begin{aligned}\epsilon_{z1} &= \left(\frac{-n^2 \cdot \hat{x}_{s\sigma}}{\hat{r}_s^2 + n^2 \cdot \hat{x}_{s\sigma}^2} \cdot i_{z1} + \frac{n \cdot \hat{r}_s}{\hat{r}_s^2 + n^2 \cdot \hat{x}_{s\sigma}^2} \cdot i_{z2}\right)\delta x_{s\sigma} \\ &\quad - \left(\frac{\hat{r}_s}{\hat{r}_s^2 + n^2 \cdot \hat{x}_{s\sigma}^2} \cdot i_{z1} + \frac{n \cdot \hat{x}_{s\sigma}}{\hat{r}_s^2 + n^2 \cdot \hat{x}_{s\sigma}^2} \cdot i_{z2}\right)\delta r_s \\ \epsilon_{z2} &= \left(\frac{-n \cdot \hat{r}_s}{\hat{r}_s^2 + n^2 \cdot \hat{x}_{s\sigma}^2} \cdot i_{z1} - \frac{n^2 \cdot \hat{x}_{s\sigma}}{\hat{r}_s^2 + n^2 \cdot \hat{x}_{s\sigma}^2} \cdot i_{z2}\right)\delta x_{s\sigma} \\ &\quad + \left(\frac{n \cdot \hat{x}_{s\sigma}}{\hat{r}_s^2 + n^2 \cdot \hat{x}_{s\sigma}^2} \cdot i_{z1} - \frac{\hat{r}_s}{\hat{r}_s^2 + n^2 \cdot \hat{x}_{s\sigma}^2} \cdot i_{z2}\right)\delta r_s \\ \delta x_{s\sigma} &= x_{s\sigma} - \hat{x}_{s\sigma} \end{aligned} \tag{7.22}$$

This expression helps us design an experiment to identify $x_{s\sigma}$. By providing the following test conditions: $i_{z1}^* \neq 0,\ i_{z2}^* = 0,\ n \neq 0,\ (preferably\ |n| >> 0),\ \delta r_s = 0$, (7.22) can be simplified as below:

$$\begin{aligned}\epsilon_{z1} &= \left(\frac{-n^2 \cdot \hat{x}_{s\sigma}}{\hat{r}_s^2 + n^2 \cdot \hat{x}_{s\sigma}^2} \cdot i_{z1}\right)\delta x_{s\sigma} \\ \epsilon_{z2} &= \left(\frac{-n \cdot \hat{r}_s}{\hat{r}_s^2 + n^2 \cdot \hat{x}_{s\sigma}^2} \cdot i_{z1}\right)\delta x_{s\sigma} \end{aligned} \tag{7.23}$$

When the test machine is rotated at a known speed, (7.23) provides us with a simpler expression for the prediction error that is enriched with $\delta x_{s\sigma}$. It is also possible to develop the prediction gradients w.r.t. $\hat{x}_{s\sigma}$, by following the same general form given

in (7.14). The resulting prediction gradients become as follows:

$$\Psi_{z1}: \frac{\mathrm{d}\left(\frac{\mathrm{d}\hat{i}_{z1}}{\mathrm{d}\hat{x}_{s\sigma}}\right)}{\mathrm{d}t} = \frac{\omega_n}{\hat{x}_{s\sigma}}\left(-\hat{r}_s \cdot \frac{\mathrm{d}\hat{i}_{z1}}{\mathrm{d}\hat{x}_{s\sigma}} + \hat{x}_{s\sigma} \cdot n \cdot \frac{\mathrm{d}\hat{i}_{z2}}{\mathrm{d}\hat{x}_{s\sigma}} + \frac{\hat{r}_s}{\hat{x}_{s\sigma}} \cdot \hat{i}_{z1} - \frac{u_{z1}}{\hat{x}_{s\sigma}}\right) \tag{7.24}$$

$$\Psi_{z2}: \frac{\mathrm{d}\left(\frac{\mathrm{d}\hat{i}_{z2}}{\mathrm{d}\hat{x}_{s\sigma}}\right)}{\mathrm{d}t} = \frac{\omega_n}{\hat{x}_{s\sigma}}\left(-\hat{r}_s \cdot \frac{\mathrm{d}\hat{i}_{z2}}{\mathrm{d}\hat{x}_{s\sigma}} - \hat{x}_{s\sigma} \cdot n \cdot \frac{\mathrm{d}\hat{i}_{z1}}{\mathrm{d}\hat{x}_{s\sigma}} + \frac{\hat{r}_s}{\hat{x}_{s\sigma}} \cdot \hat{i}_{z2} - \frac{u_{z2}}{\hat{x}_{s\sigma}}\right) \tag{7.25}$$

By applying the Ψ_{z1}, Ψ_{z2} : into (7.13), the following expression can be derived, to identify $\hat{x}_{s\sigma}$ experimentally.

$$\hat{x}_{s\sigma}[k] = \hat{x}_{s\sigma}[k-1] + \frac{\gamma_{0,Lk}}{r[k]}\left(\Psi_{z1}[k] \cdot \epsilon_{z1}[k] + \Psi_{z2}[k] \cdot \epsilon_{z1}[k]\right) \tag{7.26}$$

Alternatively, one can adopt a simpler algorithm known as the physically interpretative method [22] with the following expression, for which $\mathbf{L}$ can be computed without the prediction gradients as shown below:

$$\begin{aligned} L_{z1} &= \gamma_{0,Lk}\left(\frac{\hat{r}_s^2 + n^2 \cdot \hat{x}_{s\sigma}^2}{-n^2 \cdot \hat{x}_{s\sigma} \cdot i_{z1}}\right) \\ L_{z2} &= \gamma_{0,Lk}\left(\frac{\hat{r}_s^2 + n^2 \cdot \hat{x}_{s\sigma}^2}{-n \cdot \hat{r}_s \cdot i_{z1}}\right), \qquad i_{z1}, n \neq 0 \\ \hat{x}_{s\sigma}[k] &= \hat{x}_{s\sigma}[k-1] + L_{z1}[k] \cdot \epsilon_{z1}[k] + L_{z2}[k] \cdot \epsilon_{z2}[k] \end{aligned} \tag{7.27}$$

However, it can be shown that, (7.26) becomes (7.27) in steady-state, when the respective $r[k]$ are computed with the use of only the corresponding prediction gradient.

7.4 Real-Time Simulation-Based Analysis

In this section, the Embedded Real-Time Simulator (ERTS) developed in relation to Chapter 6 is employed to investigate the RPEM dynamics and the cross-coupling among $\underline{\hat{\theta}}$ and between $\underline{\hat{\theta}}$ and $\hat{\vartheta}$. Figure 6.7 illustrates the ERTS design layout. Accordingly, the ERTS is programmed in the Xilinx Zynq SoC-based PicoZed System-on-Module (SoM). The power hardware components of the DTP IPMSM drive are programmed in the FPGA fabric of the SoC to achieve real-time emulation at an integration time-step of 1

μs and a computational clock speed of 100 MHz. The proposed estimation algorithms, drive software and likewise, relatively slower processes are programmed in the on-chip ARM processor using the C++ programming language. The drive data are given in Table 7.1. The machine inductances in the ERTS machine model are independent of the stator currents, thus the corresponding rated load values are applied. The processor sampling time is equivalent to the PWM double-update sampling time step. Two units of two-level VSI with asymmetrical modulation and 3rd harmonic injection are used to drive the machine.

TABLE 7.1. Parameters of the DTP IPMSM and drive.

Symbol	Parameter	Value (SI)	Value (pu)
U_n	Rated Voltage	336 V	1.0
I_n	Rated Current	11.5 A	1.0
N_n	Rated Speed	2000 rpm	1.0
T_n	Rated Torque	63.8 Nm	-
p	Number of pole-pairs	3	-
$^*R_s$	Stator Resistance	0.296 Ω	0.0175
Ψ_m	Permanent magnet flux linkage	0.287 Wb	0.954
L_d	d-axis inductance (rated load)	10.4 mH	0.39
L_q	q-axis inductance (rated load)	26.5 mH	0.985
$L_{s\sigma}$	Stator leakage inductance	2.7 mH	0.100
U_{dc}	DC bus voltage	220 V	0.655
f_{sw}	Power device switching frequency	4 kHz	-
T_{samp}	Sampling period	125 μs	-

$^*R_s$, with cable resistance, becomes 0.337 Ω (0.02 pu), which is used as the basis for identification.

7.4.1 Prediction Gradient and Online Tracking behaviour

The respective elements of $\mathbf{\Psi}^T$ are investigated in different speed regions as plotted in Figure 7.5, as they are the main components in the corresponding estimation gains, hence can explain the tracking behaviors at different speeds.

Figure 7.5(a) shows the ψ_m-tracking at a step change under different speeds. Since the respective estimation gains (7.15) are independent of the stator currents, these tests are conducted at no-load. It is evident that at lower speeds, ψ_m-tracking becomes poor owing to the near-zero prediction gradients. When the speed is beyond very low speeds, Ψ_{11} becomes substantial to provide stable and precise tracking. This speed dependence in the prediction gradients, thus tracking, corroborates Figure 7.4(a), in which it is seen that Ψ_{11} becomes stronger beyond 0.05-0.1 pu rotor speeds whereas Ψ_{12} is relatively weak across the speed range.

Similarly, r_s-tracking dependence on the rotor speed is assessed in Figure 7.5(b). Unlike the previous discussion, r_s-tracking gains are load-dependent, thus tested under 0.5 pu load-torque ($\tau_{e,l}$). Opposing to the previous discussion, tracking becomes faster and more precise when the rotor speeds approach the standstill. The corresponding

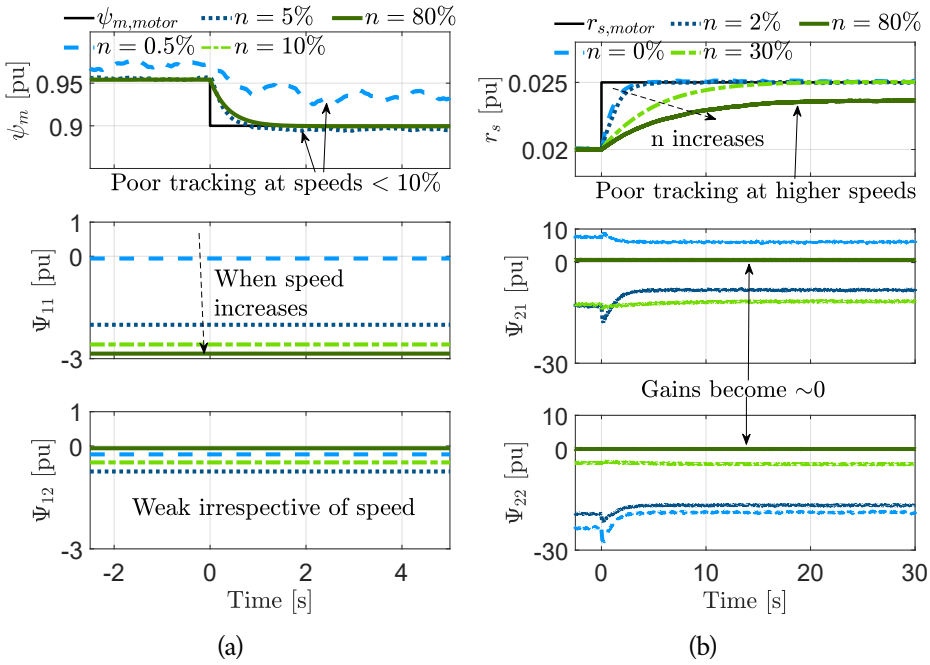

FIGURE 7.5. Adaptation performance upon a step change in one machine parameter in different speed regions and the respective prediction gradients (a) $\hat{\psi}_m$ with no-load (b) $\hat{r}_s$ with 0.5 pu load-torque.

prediction gradients become nearly negligible in the higher speed regions to make the r_s tracking unfeasible. Tracking at higher speeds can be further degraded when the loading is smaller. These outcomes are hinted by Figure 7.4(b), in which it is noticed that $\Psi_{21,22}$ are stronger around zero speed provided that some stator current is present. In summary, the following remarks can be drawn:

Remark 1: ψ_m-tracking is becoming more effective when the rotor speed departs from the standstill.

Remark 2: r_s-tracking is becoming more effective when the rotor speed approaches the low-speed region.

7.4.2 *Cross-Coupling Among the Estimated Parameters*

Under this exclusiveness in the speed regions of better sensitivity, it is interesting to examine the tracking performance when both ψ_m and r_s vary in the same time. It's worth noting that in a typical DTP IPMSM, in per unit values, $\psi_m \gg r_s$, $r_s \ll 1$. Hence, $\delta\psi_m$ can influence heavily upon the $\hat{r}_s$, if both or only $\hat{r}_s$ is adapted. Analytical expressions can be derived from (7.12) as below, to investigate different scenarios:

Case 1: $\delta\psi_m,\ \delta r_s \neq 0$ *and only* $\hat{r}_s$ *adapts*

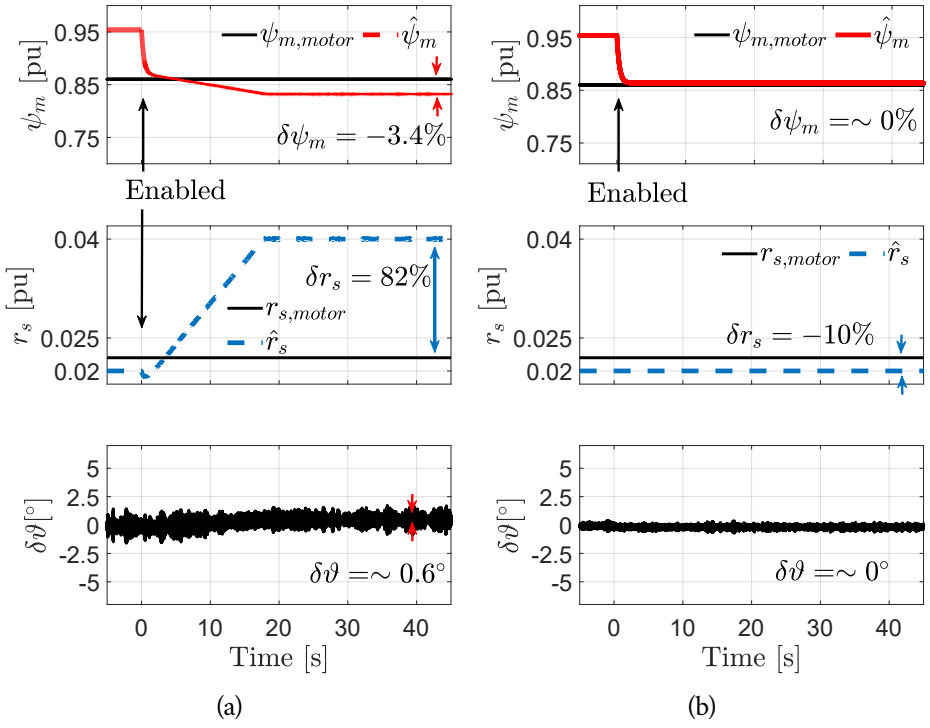

FIGURE 7.6. Position error and parameters when both $\hat{\psi}_m$ and $\hat{r}_s$ are erroneous by 10% at n = 0.5 pu, $\tau_{el} = 0.5$ (a) simultaneous parameter adaptation (b) preferred solution: only $\hat{\psi}_m$ adapts.

Thus, $\hat{r}_s$ adapts until $\epsilon_d \rightarrow 0$, then (7.12) becomes:

$$\hat{r}_s = r_s + \frac{\hat{n}^2 \cdot \hat{x}_q}{\left(\hat{r}_s \cdot i_d + \hat{n} \cdot \hat{x}_q \cdot i_q\right)} \cdot \delta\psi_m \tag{7.28}$$

Accordingly, it is seen that, unless $n = 0$ or $\delta\psi_m = 0$, $\hat{r}_s$ can be penalized due to even a small percentage of $\hat{\psi}_m$-errors and this penalty increases when the speed increases. With this background, it becomes mandatory to cut-off the $\hat{r}_s$-tracking beyond a certain rotor speed. In view of the magnitude decay of $\Psi_{21,22}$, the upper limit for $\hat{r}_s$-tracking is chosen to be $n_{lim} = 0.1\ pu$. To illustrate the worth of such a gain-scheduler, a scenario with simultaneous error is simulated and results are plotted Figure 7.6. An initial error of 10% is introduced on both machine parameters simultaneously, at a rotor speed of 0.5 pu and $\tau_{e,l} = 0.5\ pu$. In Figure 7.6(a), both parameters are attempted to be tracked whereas in Figure 7.6(b), only $\hat{\psi}_m$ is tracked. It is seen that in the first case, $\hat{r}_s$ is severely penalized owing to the $\delta\psi_m$ errors, that results in $\hat{r}_s$ saturating in $\hat{r}_{s,lim}$, and the degradation in position estimation (higher $\delta\vartheta$). Consequently, $\hat{\psi}_m$ sustains a steady-state error. Conversely, in Figure 7.6(b), $\hat{\psi}_m$ shows good tracking despite the sustained δr_s, owing to the gain-scheduler that prevented $\hat{r}_s$ from correction. Thus, a gain-scheduler to constrain $\hat{r}_s$ adaptation only within a -0.1 to 0.1 pu speed range

is adopted. From the perspective of sensorless control, the precision of the stator resistance matters when the rotor approaches the standstill, thus such a choice can be justified. Conversely, the impact from δr_s on $\hat{\psi}_m$ is often negligible due to the same asymmetry in the magnitudes, which was seen in Figure 7.6(b) and analyzed next.

Case 2: $\delta\psi_m$ = $\delta r_s \neq 0$ and only $\hat{\psi}_m$ adapts

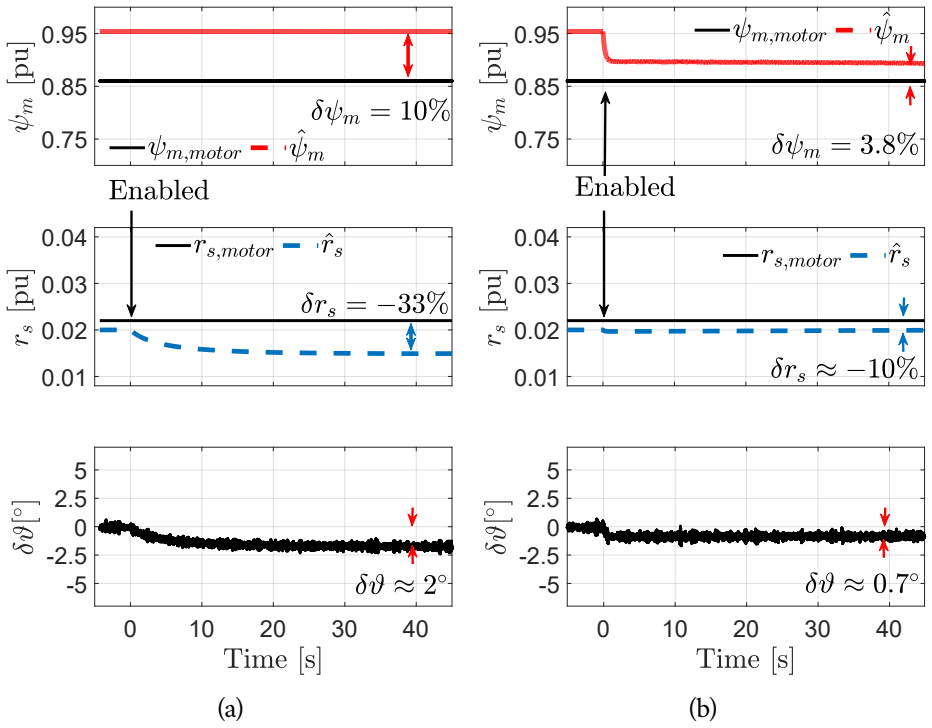

FIGURE 7.7. Position error and parameters when both $\hat{\psi}_m$ and $\hat{r}_s$ are erroneous by 10% at n = 0.05 pu, $\tau_{el} = 0.5$ (a) only $\hat{r}_s$ adapts (b) preferred solution: simultaneous parameter adaptation.

Thus, $\hat{\psi}_m$ adapts until $\epsilon_{d,q} \rightarrow 0$, then(7.12) becomes:

$$\hat{\psi}_m = \psi_m + \frac{\left(\hat{r}_s \cdot i_d + \hat{n} \cdot \hat{x}_q \cdot i_q\right)}{\hat{n}^2 \cdot \hat{x}_q} \cdot \delta r_s$$
$$\hat{\psi}_m = \psi_m + \frac{\left(\hat{n} \cdot \hat{x}_q \cdot i_d - \hat{r}_s \cdot i_q\right)}{\hat{n}^2 \cdot \hat{x}_q} \cdot \delta r_s \tag{7.29}$$

From (7.29), it is evident that, unless $n << 1$, $\hat{\psi}_m$ cannot be significantly impacted by δr_s. However, $n << 1$ is a speed region where $\hat{\psi}_m$-related prediction gradient, i.e., Ψ_{11} is anyway weak as noted in the previous section. Consequently, a potential penalty induced by δr_s will be attenuated too, to allow simultaneous identification with minimum repercussions.

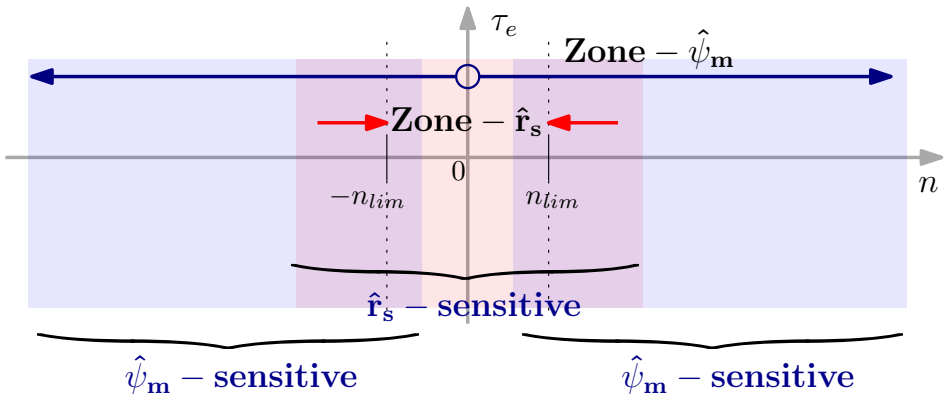

FIGURE 7.8. Gain-scheduling scheme to prevent undue $\hat{r}_s$-adaptation in the speeds beyond $|n_{lim}|$.

The question remains, whether the $\hat{\psi}_m$-tracking should be restricted only to higher speeds, or should $\hat{\psi}_m$ be allowed to adapt in the zone where $\hat{r}_s$-sensitivity dominates. To facilitate the parallel adaptation, (7.18) is slightly modified as below, such that ϵ_d and ϵ_q are dedicated to $\hat{\psi}_m$ and $\hat{r}_s$ respectively.

$$\hat{r}_s[k] = \hat{r}_s[k-1] + \frac{\gamma_{0,Lk}}{r[k]} \left(\Psi_{22}[k] \cdot \epsilon_q[k]\right) \tag{7.30}$$

This modification is motivated by the fact that Ψ_{12} is anyway weak such that L_{12} is eliminated, that leaves ϵ_q redundant w.r.t. $\hat{\psi}_m$-adaptation. On the other hand, Ψ_{22} is substantial enough to adapt $\hat{r}_s$. Additionally, it is noted in Figure 7.5 that, Ψ_{21} changes its sign near zero speed, which can render oscillatory adaptation due to noise, thus, resorting only to $L_{22} \cdot \epsilon_q$ can be justified. Albeit, an alternative experiment can be designed to identify $\hat{r}_s$ at zero speed, only with i_d-injection, that can be useful during commissioning or non-operational modes of the drive, with the use of the following algorithm:

$$\hat{r}_s[k] = \hat{r}_s[k-1] + \frac{\gamma_{0,Lk}}{r[k]} \left(\Psi_{21}[k] \cdot \epsilon_d[k]\right) \tag{7.31}$$

Investigation of simultaneous error scenario is carried out at 0.05 pu rotor speed and $\tau_{e,l} = 0.5\,pu$, again with a 10% initial error in each model parameter. The results of only $\hat{r}_s$ adaptation is presented in Figure 7.7(a) and $\hat{r}_s$, $\hat{\psi}_m$ simultaneous adaptation is in Figure 7.7(b). In this parallel adaptation, (7.15) and (7.30) are applied for the respective adaptations. Figure 7.7(b) shows that $\hat{\psi}_m$ adapts rapidly in the correct direction and settles with a steady-state error. $\hat{r}_s$ adaption, in the meantime, is quite slow to sustain the same initial error after about 1 minute. In the former in Figure 7.7(a), owing to the restriction of $\hat{\psi}_m$, $\hat{r}_s$ is degraded which results in deteriorating the observer performance compared to the parallel adaptation. The same phenomenon was evident in much smaller rotor speeds too, thus it is preferred to allow ψ_m-adaptation across the full speed range, during which L_{11} will naturally be weak when the rotor approaches

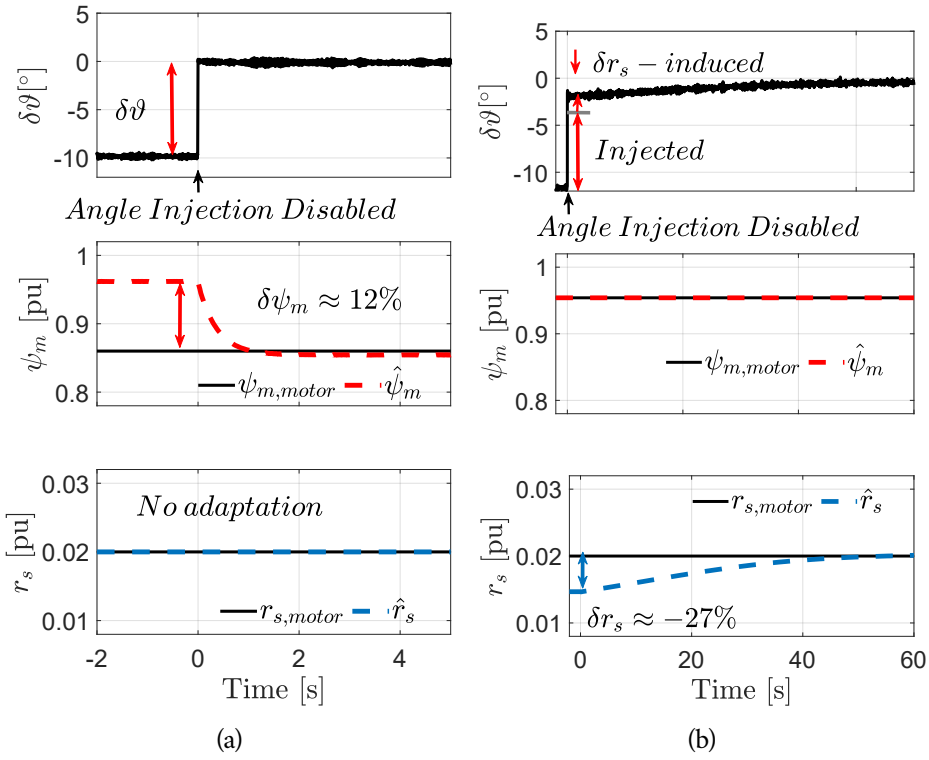

FIGURE 7.9. Influence from the position estimation error at $\tau_{el} = 0.5$ (a) at 0.3 pu speed, only $\hat{\psi}_m$ adapts. (b) at 0.05 speed, only $\hat{r}_s$ adapts.

the standstill, and be zero at the zero speed. Thus, a gain-scheduling scheme can be proposed as illustrated in Figure 7.8. In the same time, targeting the above scenarios, an analytical expression can be developed to compute $\delta\underline{\theta}$ as below:

Case 3: $\delta\psi_m,\ \delta r_s \neq 0$ *and both* $\hat{\psi}_m$, $\hat{r}_s$ *adapt*
$\epsilon_d \rightarrow 0$, but $\delta\psi_m,\ \delta r_s \neq 0$, then(7.12) becomes:

$$\delta\psi_m = \frac{(-\hat{r}_s \cdot i_d - \hat{n} \cdot \hat{x}_q \cdot i_q)}{\hat{n}^2 \cdot \hat{x}_q} \cdot \delta r_s \tag{7.32}$$

$\epsilon_q \rightarrow 0$, but $\delta r_s,\ \delta\psi_m \neq 0$,then (7.12) becomes:

$$\delta r_s = \frac{(\hat{n} \cdot \hat{r}_s)}{(\hat{n} \cdot \hat{x}_d \cdot i_d - \hat{r}_s \cdot i_q)} \cdot \delta\psi_m \tag{7.33}$$

The respective $\delta\underline{\theta}$ values seen in the simulation results in relation to Figure 7.6 and Figure 7.7 can also be obtained using (7.32) and (7.33).

The impact from δx_d and δx_q on the online tracking are disclosed in Chapter 6, which reveals that no-load and zero-speed conditions eliminate the cross-coupling

from the remaining electrical parameters when $\hat{\psi}_m$ and $\hat{r}_s$ -identifications are concerned.

7.4.3 *Influence from the Observer on the Estimator*

In this section, the influence of the $\delta\vartheta$ on the parameter estimation performance and stability is assessed. A steady-state electrical angle error of 10° is added to the output of the $\hat{\vartheta}$ and removed at one point. Figure 7.9 (a) presents the performance at higher speeds. $\delta\vartheta$ influences $\hat{\psi}_m$ significantly. As soon as the angle injection is disabled, $\hat{\psi}_m$ adapts correctly and the observer yields no error. Figure 7.9 (b) presents the case at 0.05 pu speed, during which, only $\hat{r}_s$-tracking is allowed for the ease of inspection. Here, in addition to the injected error, an additional angle error is induced by the δr_s, which was originally caused by the injected 10° angle. As soon as it is removed, both $\delta\vartheta$ and δr_s get eliminated.

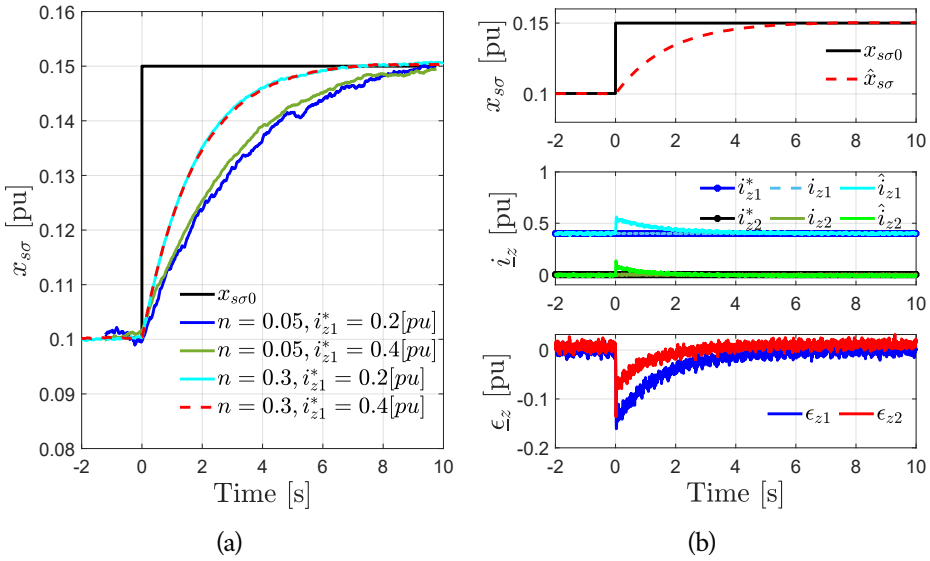

Figure 7.10. Real-time simulation of the identification of $\hat{x}_{s\sigma}$ of the DTP IPMSM (a) at different speeds and i_{z1} (b) behaviours of $\underline{i}_z$ and $\underline{\epsilon}_z$ during $\hat{x}_{s\sigma}$ when n = 0.3, i_{z1} = 0.4 pu.

7.4.4 $x_{s\sigma}$-*Identification*

Figure 7.10 illustrates the real-time simulation results of $\hat{x}_{s\sigma}$-identification. How the convergence speeds of $\hat{x}_{s\sigma}$ are influenced by the rotor speed and i_{z1} is seen in Figure 7.10 (a). It is evident that the rotor speed influences more than the magnitude of i_{z1} in the tracking speed, that can be attributed to the $\hat{n}^2$-terms in the numerators in the respective gains as seen in (7.27). Figure 7.10(b) shows the behaviour of $\underline{i}_z$ and $\underline{\epsilon}_z$ during

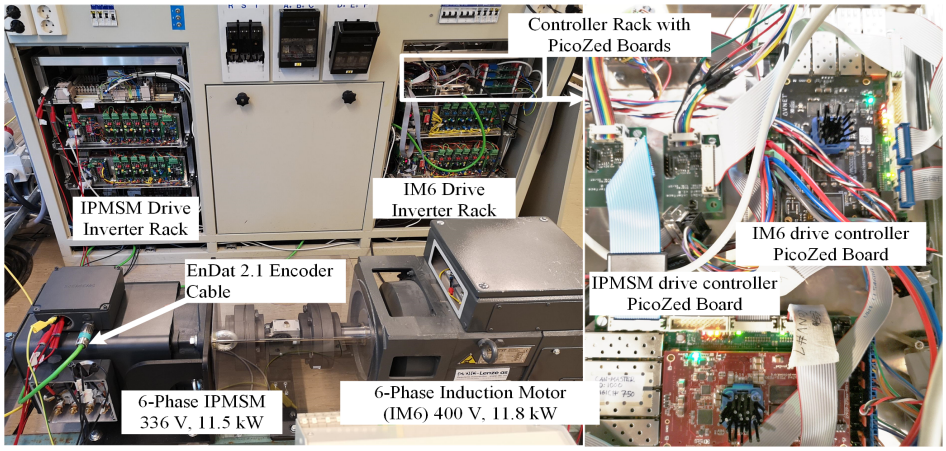

FIGURE 7.11. Experimental setup having DTP IPMSM as the drive machine and DTP induction machine (IM6) as the load machine mounted on the same shaft. PicoZed System-on-Module that embeds the Xilinx Zynq SoC is used to program the control algorithms for each machine.

the adaptation. i_{z2}^* is kept at 0 while i_{z1}^* is injected. When the adaption routine is called at 0 second-point, $\underline{\epsilon}_z$ becomes transiently large due to the off-tuned $\hat{x}_{s\sigma}$, and when $\hat{x}_{s\sigma}$ is well-tuned, $\underline{\epsilon}_z = 0$.

7.5 EXPERIMENTAL VALIDATION

Experiments were conducted on a laboratory prototype which is shown in Figure 7.11. The setup is composed of a DTP IPMSM and a DTP induction machine of which the data are given in Table 7.1. The same control platform hardware and software/estimation algorithms in the ERTS are used to the setup with the same configurations including the scaling and sampling. However, one notable difference here is that the nonlinearities in the inductances and the VSI are accounted for, in these experiments. That is, (7.21) is used here to adapt inductances in real-time, and the VSI nonlinearities including the dead-time effects are corrected using the methods in [24]. A gain-scheduling scheme is implemented to constrain $\hat{r}_s$-adaptation within $|n_{lim}| = 0.1\ pu$.

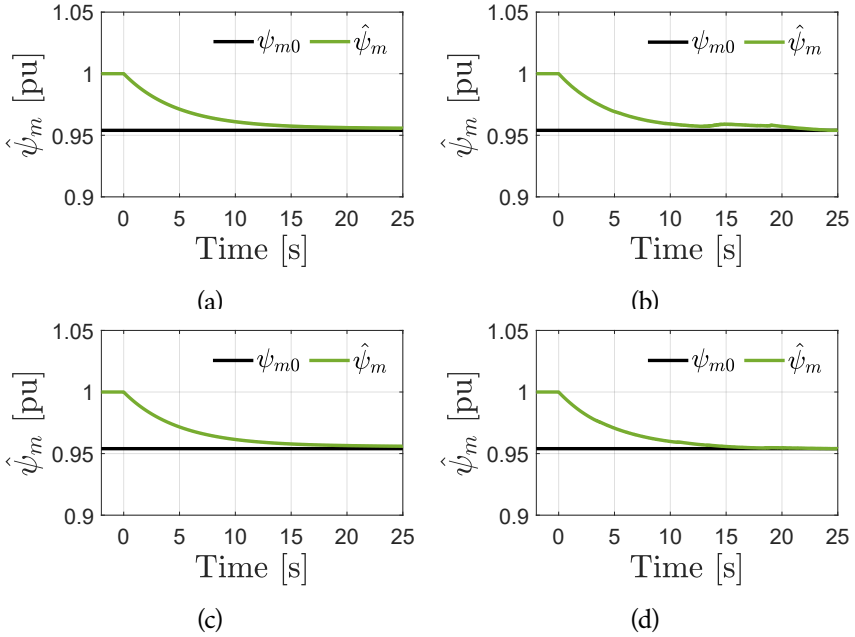

Figure 7.12. Experimental validations of the online adaptation of $\hat{\psi}_m$ of the DTP-IPMSM at (a) n = 0.15 pu, $\tau_{e,l}$ = 0 pu (b) n = 0.15 pu, $\tau_{e,l}$ = 0.5 pu (c) n = 0.3 pu, $\tau_{e,l}$ = 0 pu (d) n = 0.3 pu, $\tau_{e,l}$ = 0.5 pu.

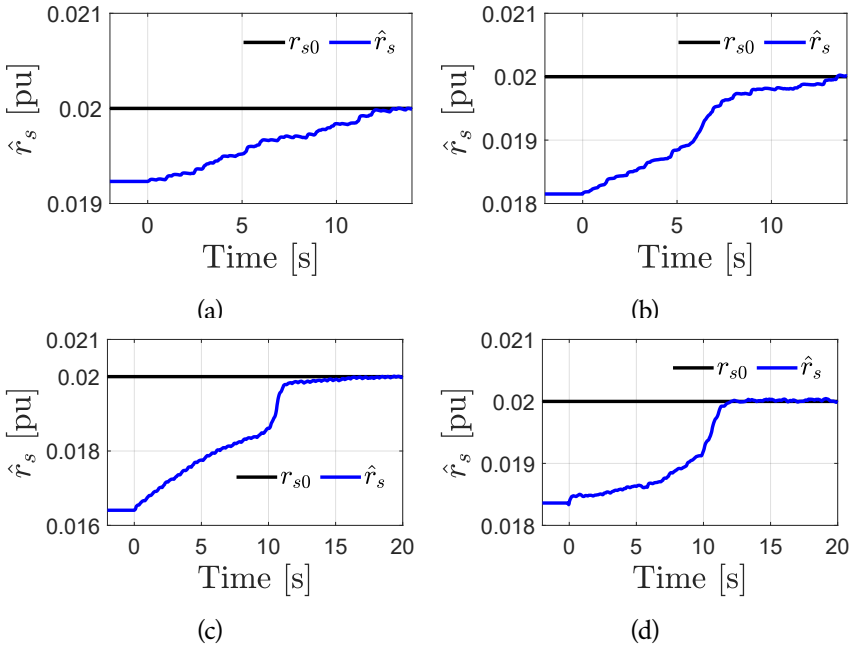

Figure 7.13. Experimental validations of the online identification of $\hat{r}_s$ of the DTP-IPMSM at (a) n = 0 pu, $\tau_{e,l}$ = 0.2 pu (b) n = 0 pu, $\tau_{e,l}$ = 0.5 pu (c) n = 0.01 pu, $\tau_{e,l}$ = 0.2 pu (d) n = 0.01 pu, $\tau_{e,l}$ = 0.8 pu.

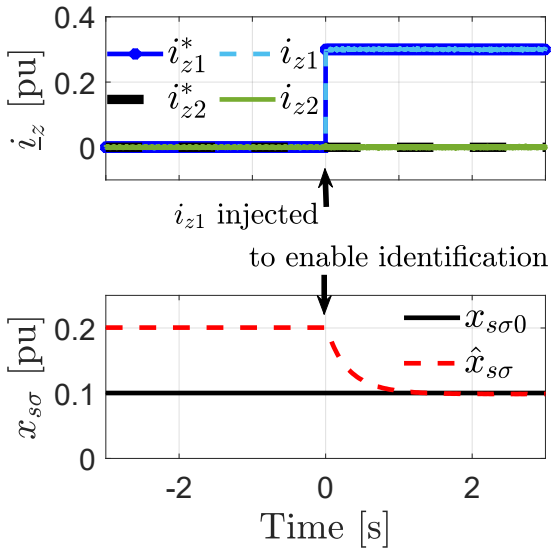

FIGURE 7.14. Experimental validations of the identification of $\hat{x}_{s\sigma}$ of the DTP IPMSM at n = 0.1 pu and i_{z1} = 0.3 pu.

7.5.1 Parameter Identification

Here, the results of $\hat{\psi}_m$, $\hat{r}_m$ and $\hat{x}_{s\sigma}$ -identifications are presented and discussed. The experimental results of the online tracking performances of $\hat{\psi}_m$ and $\hat{r}_s$ at different speeds and loads are shown in Figure 7.12 and Figure 7.13. $\gamma_{0,rk}$, $\gamma_{0,Lk}$ values for $\hat{\psi}_m$-tracking are 6.25×10^{-4}, 3.25×10^{-5} and the same for $\hat{r}_s$-tracking are 6.25×10^{-4}, 6.25×10^{-4} respectively. Initially, the model parameter of concern is wrongly tuned, and when the adaptation is enabled, the model parameter correctly identifies the machine parameter. Figure 7.12 -(a) and (c) demonstrate that the $\hat{\psi}_m$-identification is possible at no-load. Similarly, $\hat{r}_s$-tracking is possible even at standstill, as long as loading is present, as seen in Figure 7.13 (a) and (b). Although a step-change is unlikely for such parameters, it has been tested to investigate the stability of the OPE. For the convergence of both these temperature-sensitive parameters at this step-change, it has taken about 10 - 15 s. Given the thermal capacity, this tracking speed seems reasonable.

Figure 7.14 shows the experimental validation of the $\hat{x}_{s\sigma}$-identification. Enabling of the adaptation is triggered with the injection of i_{z1} that results in a fairly rapid $\hat{x}_{s\sigma}$ convergence with good asymptotic behaviour.

7.5.2 Sensorless Control

In this section, the performance of the AF observer is investigated when the parameter identifier is initially disabled and then enabled, such that to witness the targeted per-

formance enhancements in steady-state. As it was evident from section 7.4 that $\delta\psi_m$ has nearly no influence on $\delta\vartheta$, our primary focus is on the influence from δr_s. Figure 7.15 and Figure 7.16 correspond to these experiments. The drive is in the mechanical steady-state, yet $\hat{r}_s$ is initially off-tuned and then tuned online with the aid of the OPE. Initial $\hat{r}_s$ is about 50% lower than the physical r_s, under which, $\delta\vartheta$ can be as high as 20°, particularly near standstill. Similarly, Figure 7.17 (a) and (b) demonstrate the assistance the AF observer receives by updating $\hat{x}_q$ opposing to the nameplate value $\hat{x}_{q0}$. These experiments also validate the experimental method using the open-loop predictor proposed in Section 7.3.3. In general, the effectiveness of the Parameter Identifier assisted AF observer is evident in the laboratory experiments and the steady-state performances are satisfactory, even at very low speeds near rotor standstill.

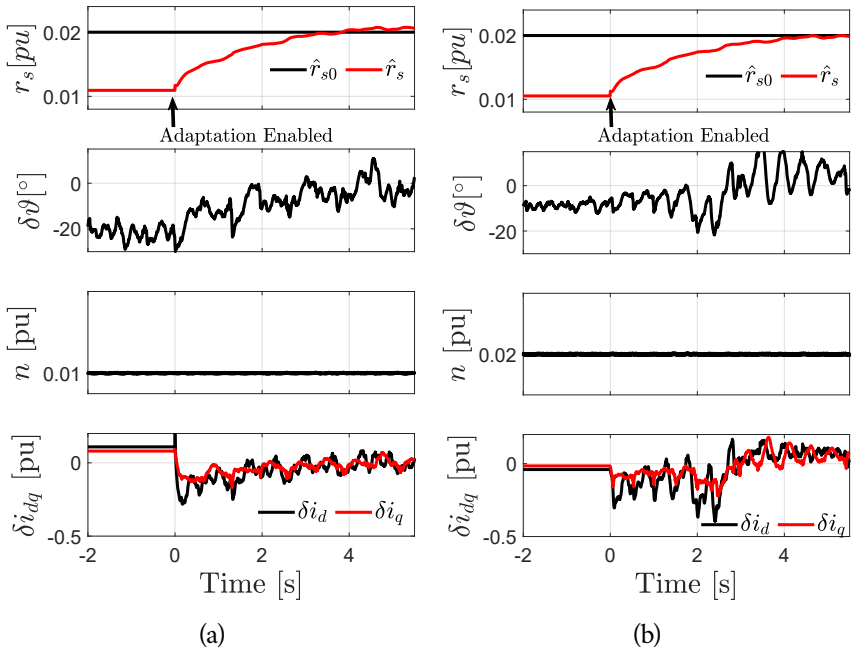

Figure 7.15. Experimental validations of the sensorless DTP IPMSM drive before and after enabling the $\hat{r}_s$ adaptation at the following load-torque and speed conditions: (a) $\tau_{e,l}$ = 0.5 pu, n^* = 0.01 pu (b) $\tau_{e,l}$ = 0.5 pu, n^* = 0.02 pu.

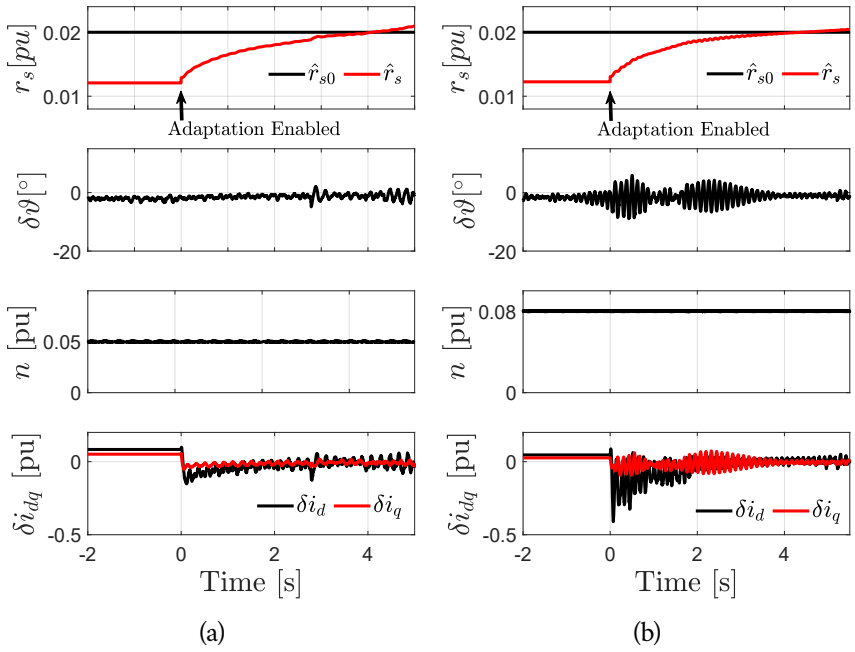

FIGURE 7.16. Experimental validations of the sensorless DTP IPMSM drive before and after enabling the $\hat{r}_s$ adaptation at the following load-torque and speed conditions: (a) $\tau_{e,l}$ = 0.8 pu, n^* = 0.05 pu (b) $\tau_{e,l}$ = 0.8 pu, n^* = 0.08 pu.

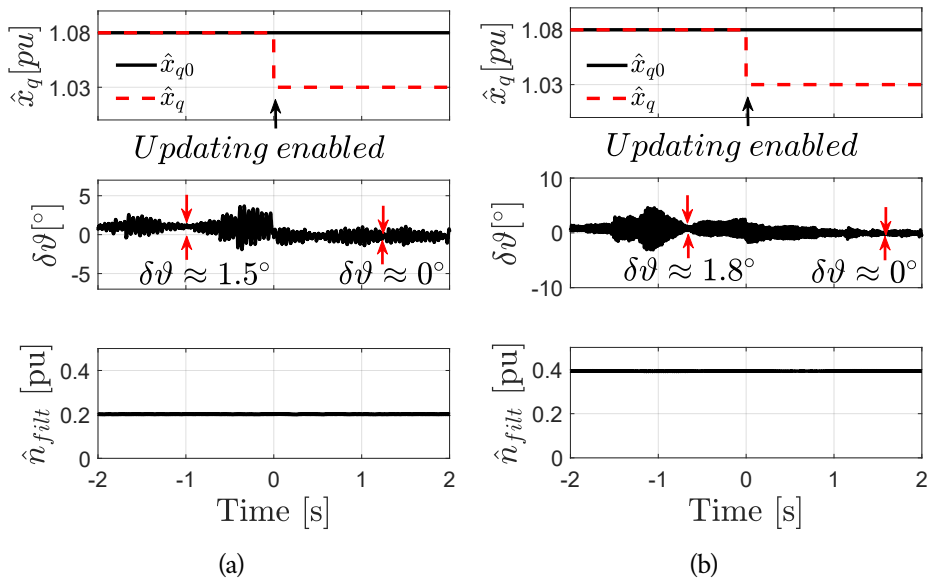

FIGURE 7.17. Experimental validations of the sensorless DTP IPMSM drive before and after enabling the $\hat{x}_q$ updating at the following load-torque and speed conditions: (a) $\tau_{e,l}$ = 0.8 pu, n^* = 0.2 pu (b) $\tau_{e,l}$ = 0.8 pu, n^* = 0.4 pu.

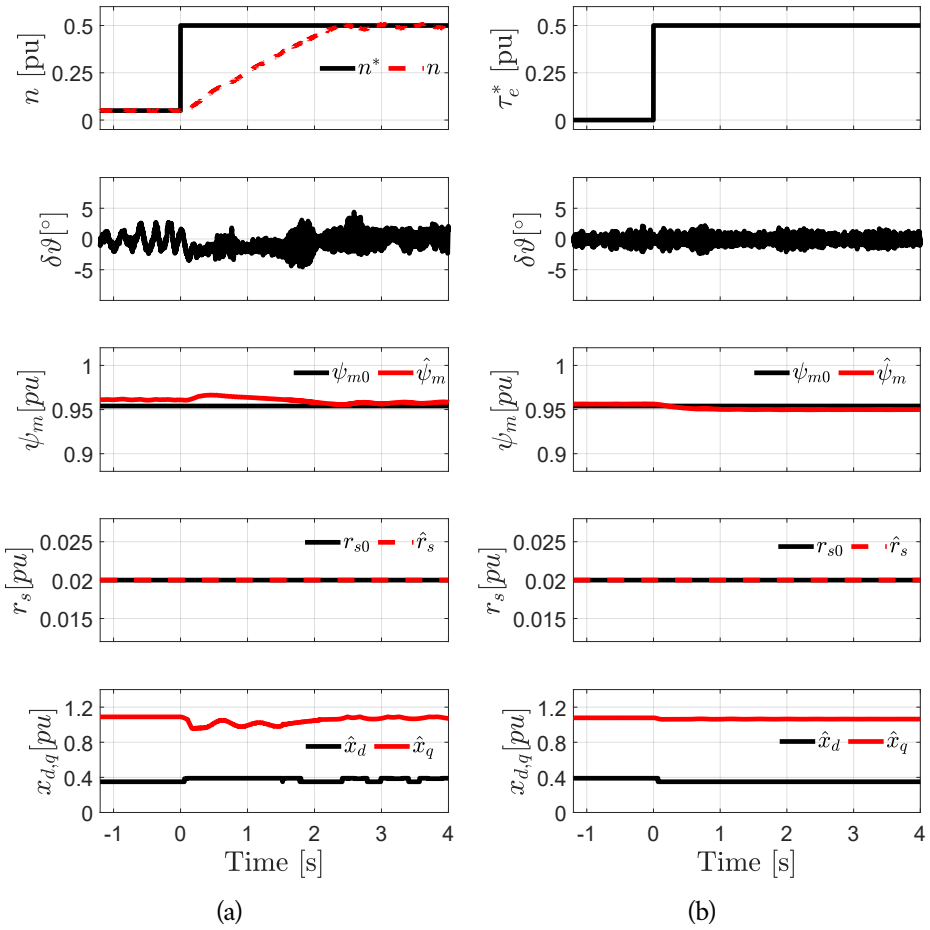

FIGURE 7.18. Sensorless control performance (a) Speed step-change from 0.05 to 0.5 pu at no-load (b) Load step-change from 0 to 0.5 pu at 0.2 pu speed.

The performance and stability of the proposed scheme in dynamic conditions is investigated next. Figure 7.18(a) corresponds to a speed step-change from the lower speed region to mid-speeds, at no-load. The online parameter adaptation is enabled across the experiment. $\hat{\psi}_m$ exhibits reasonable convergence when the rotor stops accelerating. At no-load, $\hat{r}_s$ remains at its initial value because its estimation gains are load-dependent. $\hat{x}_{d,q}$ are updated as per their analytical functions. Similarly, the response at a load step-change is seen in Figure 7.18(b). $\hat{\psi}_m$ along with $\hat{x}_{d,q}$ display reasonable tracking that results in very good observer performance. An event of speed reversal is shown in Figure 7.19 under loaded conditions. The online parameter tracking shows satisfactory performance and stability to maintain the observer performance error at a minimum.

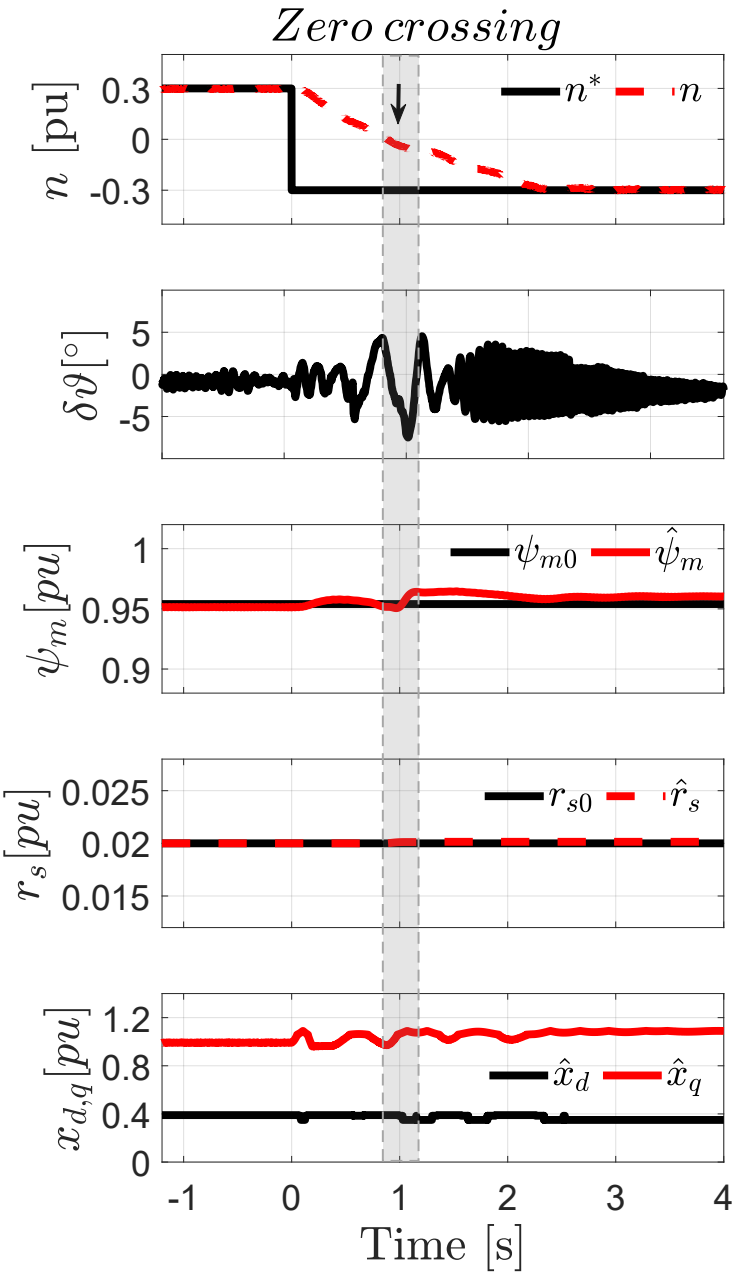

Figure 7.19. State estimation and simultaneous parameter adaptation at a speed reversal from +0.3 to -0.3 pu at $\tau_{e,l}$ = 0.5 pu.

7.5.3 Summary of Identification Methods and Validation Results

Table 7.2 summarizes the identification methods proposed herein. Accordingly, a comprehensive identification scheme is achievable to estimate all DTP IPMSM parameters.

TABLE 7.2. Summary of experiments, their necessary and sufficient conditions, and drive modes of operation for parameter identification under the proposed scheme.

Parameter	Conditions	Algorithm
During drive operation		
$\hat{\psi}_m$	$n \neq 0$	Eq. (7.17)
$\hat{r}_s$	$\lvert n \rvert < n_{lim}$ $i_q \neq 0$	Eq. (7.30)
During commissioning/offline		
$\hat{x}_{s\sigma}$	$i_{z1}, n \neq 0$	Eq. (7.27)
$\hat{r}_s$	$i_d \neq 0$	Eq. (7.31)
Offline		
$\hat{x}_{d,q}$	Section 7.3.3	Eq. (7.21)

TABLE 7.3. Active flux observer performance comparison with and without the online parameter identification (OPI) in different operating regions.

Max $\delta\vartheta$	Max. $\delta\vartheta$ No OPI	Max. $\delta\vartheta$ With OPI
When δr_s = 75 - 100%		
At 0.01 - 0.05 pu speed range	$\sim 20^\circ$	$< 2^\circ$
At 0.05 - 0.1 pu speed range	$\sim 2^\circ$	$< 0.5^\circ$
At 0.1 and above	$< 1^\circ$	$\sim 0^\circ$
When δx_q = ~5%		
At full load	2°	$\sim 0^\circ$
Algorithms processing time	~5 μs	~9.5 μs

The steady-state $\delta\vartheta$ across different loads and speeds of the DTP IPMSM drive with the proposed scheme is presented in Figure 7.20. It is seen that the position estimation accuracy is very good in the rotor speeds beyond 0.05 pu, irrespective of the loading of the machine. The effectiveness of the proposed scheme is manifested in the speeds below 0.05 pu rotor speeds. Despite the estimation degrades in the very low speeds, the highest average error reported is below 2° in steady-state. Table 7.3 summarizes the results of the AF observer with and without the parameter identification. The enhancement becomes more and more evident when the rotor speed reaches a standstill. The table also shows the execution times between the methods when the said SoC is in use. The enhanced method requires about 4.5 μs more processing time in the given Zynq SoC, owing to the additional routines for parameter adaptation. Unless cost-sensitive applications or resource-stringent processors are used, typical IGBT-based drives can afford to bare this additional processing time.

7.6 CONCLUSION AND SUMMARY

This chapter proposed a method to enhance the sensorless control of DTP IPMSM drives by combining a novel online parameter adaptation scheme that incorporates an open-loop predictor. Identification schemes and appropriate algorithms are proposed to identify all electric parameters, including $\hat{x}_{s\sigma}$, by revealing the physical meanings

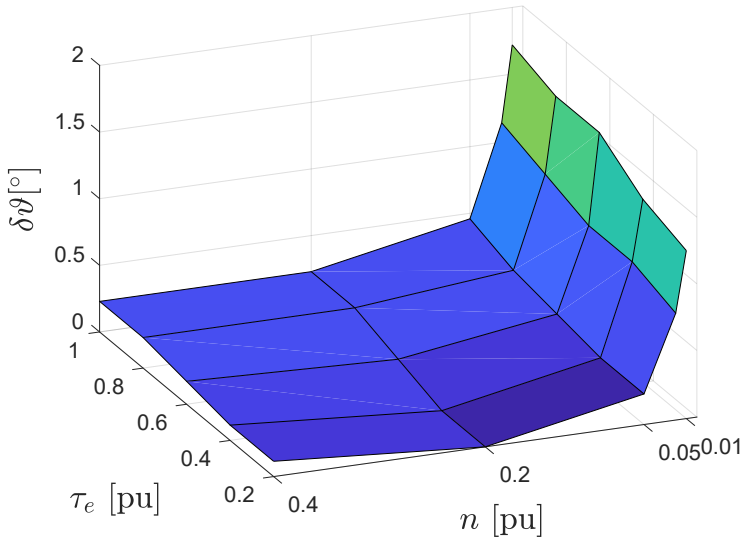

Figure 7.20. Experimental steady-state position error of the enhanced sensorless control scheme across different loads and speeds.

behind the choices for estimation gains. Temperature sensitive R_s and Ψ_m are chosen to identify online with the use of $\boldsymbol{\Psi}^T$-based stochastic gradient algorithm. The prediction gradients are developed to identify inductances as well, to facilitate online identification. Albeit, to circumvent the rank deficiency, they are identified offline and updated in real-time. Single Synchronous Reference Frame-oriented flux models and vector control are adopted in the drive. The cross-coupling among the state and parameter -estimators was analyzed and proposed a modification that facilitated simultaneous identification of R_s and Ψ_m to minimize the impact from their inherent coupling. Experimental validations confirmed the effectiveness of the proposed open-loop-based estimation scheme, which resulted in commendable observer performance both in steady-state and dynamic conditions. The position estimation improvement was evident particularly in the low-speed range even in the presence of varying parameters, that enabled stable operation at rotor speeds as low as 1%. The feasibility of realizing sensorless control at very low speeds without signal injection schemes can make the proposed method a desirable solution for a variety of industrial applications that do not require persistent operations around the rotor standstill.

7.7 References

[1] Yashan Hu, Z. Q. Zhu, and Milijana Odavic. Comparison of Two-Individual Current Control and Vector Space Decomposition Control for Dual Three-Phase PMSM. *IEEE Transactions on Industry Applications* **53** (5), 4483–4492 (2017). ISSN 00939994. doi: 10.1109/TIA.2017.2703682. Cited on page/s 128, 129, 132.

[2] Erik Capecchi, Paolo Guglielmi, Michele Pastorelli, and Alfredo Vagati. Position-Sensorless Control of the Transverse-laminated Synchronous Reluctance Motor. *IEEE Trans. on Industry Applications* **37** (6), 1768–1776 (2001). Cited on page/s 128.

[3] Silverio Bolognani, Ludovico Ortombina, Fabio Tinazzi, and Mauro Zigliotto. Model sensitivity of fundamental-frequency-based position estimators for sensorless PM and Reluctance synchronous motor drives. *Ieee Transactions on Industrial Electronics* **65** (1), 77–85 (2018). Cited on page/s 128.

[4] Jorge Lara, Jianhong Xu, and Ambrish Chandra. Effects of rotor position error in the performance of field-oriented-controlled PMSM drives for electric vehicle traction applications. *IEEE Transactions on Industrial Electronics* **63** (8), 4738–4751 (2016). Cited on page/s 128.

[5] Toni Tuovinen, Marko Hinkkanen, Lennart Harnefors, and Jorma Luomi. Comparison of a reduced-order observer and a full-order observer for sensorless synchronous motor drives. *IEEE Transactions on Industry Applications* **48** (6), 1959–1967 (2012). doi: 10.1109/TIA.2012.2226200. Cited on page/s 128.

[6] Andreas Andersson and Torbjorn Thiringer. Motion Sensorless IPMSM Control Using Linear Moving Horizon Estimation With Luenberger Observer State Feedback. *IEEE Transactions on Transportation Electrification* **4** (2), 464–473 (6 2018). Cited on page/s 128.

[7] Abebe Teklu Woldegiorgis, Xinglai Ge, Wang Huiming, and Yun Zuo. An Active Flux Estimation in the Estimated Reference Frame for Sensorless Control of IPMSM. *IEEE Transactions on Power Electronics* **37** (8), 9047–9060 (8 2022). Cited on page/s 128.

[8] Jun Hu and Bin Wu. New integration algorithms for estimating motor flux over a wide speed range. *IEEE Transactions on Power Electronics* **13** (5), 969–977 (1998). ISSN 08858993. doi: 10.1109/63.712323. Cited on page/s 128.

[9] Yukinori Inoue, Yasunori Kawaguchi, Shigeo Morimoto, and Masayuki Sanada. Performance improvement of sensorless IPMSM drives in a low-speed region using online parameter identification. *IEEE Transactions on Industry Applications* **47** (2), 798–804 (2011). ISSN 00939994. doi: 10.1109/TIA.2010.2101994. Cited on page/s 128.

[10] Oliver Wallscheid. Thermal monitoring of electric motors: state-of-the-art review and future challenges. *IEEE Open Journal of Industry Applications* **2** (June), 204–223 (2021). doi: 10.1109/ojia.2021.3091870. Cited on page/s 128.

[11] Samuli Kallio, Jussi Karttunen, Pasi Peltoniemi, Pertti Silventoinen, and Olli Pyrhönen. Online estimation of double-star IPM machine parameters using RLS algorithm. *IEEE Transactions on Industrial Electronics* **61** (9), 4519–4530 (2014). ISSN 02780046. doi: 10.1109/TIE.2013.2290761. Cited on page/s 128.

[12] Ze Li, Guodong Feng, Chunyan Lai, Debmalya Banerjee, Wenlong Li, and Narayan C. Kar. Current injection-based multi-parameter estimation for dual three-phase IPMSM considering VSI nonlinearity. *IEEE Transactions on Transportation Electrification* **5** (2), 405–415 (2019). ISSN 23327782. doi: 10.1109/TTE.2019.2913270. Cited on page/s 128.

[13] Chunyan Lai, Guodong Feng, Ze Li, and Narayan C. Kar. Computation-Efficient Decoupled Multiparameter Estimation of PMSMs from Massive Redundant Measurements. *IEEE Transactions on Power Electronics* **35** (10), 10729–10740 (2020). ISSN 19410107. doi: 10.1109/TPEL.2020.2980315. Cited on page/s 128.

[14] Tianyi Liu, Z Q Zhu, Ximeng Wu, Zhanyuan Wu, David A Stone, and Martin P Foster. A position error correction method for sensorless control of dual three-phase permanent magnet synchronous machines. *IEEE Transactions on Industry Applications* **58** (3), 3589–3601 (2022). Cited on page/s 128.

[15] Radu Bojoi, Mario Lazzari, Francesco Profumo, and Alberto Tenconi. Digital field-oriented control for dual three-phase induction motor drives. *IEEE Transactions on Industry Applications* **39** (3), 752–760 (2003). ISSN 00939994. doi: 10.1109/TIA.2003.811790. Cited on page/s 132.

[16] J. Karttunen, S. Kallio, P. Peltoniemi, P. Silventoinen, and O. Pyrhönen. Dual three-phase permanent magnet synchronous machine supplied by two independent voltage source inverters. *SPEEDAM 2012 - 21st International Symposium on Power Electronics, Electrical Drives, Automation and Motion* pages 741–747 (2012). doi: 10.1109/SPEEDAM.2012.6264448. Cited on page/s 132.

[17] Ion Boldea, Mihaela Codruta Paicu, and Gheorghe Daniel Andreescu. Active flux concept for

motion-sensorless unified AC drives. *IEEE Transactions on Power Electronics* **23** (5), 2612–2618 (2008). ISSN 08858993. doi: 10.1109/TPEL.2008.2002394. Cited on page/s 132, 133.

[18] Sorin Cristian Agarlita, Ion Boldea, and Frede Blaabjerg. High-frequency-injection-assisted 'active-flux'-based sensorless vector control of reluctance synchronous motors, with experiments from zero speed. *IEEE Transactions on Industry Applications* **48** (6), 1931–1939 (2012). ISSN 00939994. doi: 10.1109/TIA.2012.2226133. Cited on page/s 132, 133.

[19] Yue Zhao, Wei Qiao, and Long Wu. Improved Rotor Position and Speed Estimators for Sensorless Control of Interior Permanent-Magnet Synchronous Machines. *IEEE Journal of Emerging and Selected Topics in Power Electronics* **2** (3), 627–639 (9 2014). ISSN 2168-6777. doi: 10.1109/jestpe.2014.2298433. Cited on page/s 132.

[20] R. Cárdenas, R. Peña, J. Clare, G. Asher, and J. Proboste. MRAS observers for sensorless control of doubly-fed induction generators. *IEEE Transactions on Power Electronics* **23** (538 CP), 568–572 (5 2008). doi: 10.1049/cp:20080585. Cited on page/s 132.

[21] M.C. Paicu, I. Boldea, G.-D. Andreescu, and F. Blaabjerg. Very low speed performance of active flux based sensorless control: interior permanent magnet synchronous motor vector control versus direct torque and flux control. *IET Electric Power Applications* **3** (6), 551 (2009). ISSN 17518660. doi: 10.1049/iet-epa.2008.0290. URL http://digital-library.theiet.org/content/journals/10.1049/iet-epa.2008.0290. Cited on page/s 133.

[22] Aravinda Perera and Roy Nilsen. Recursive prediction error gradient-based algorithms and framework to identify PMSM parameters online. *IEEE Transactions on Industry Applications* page 11 (2022). doi: 10.1109/TIA.2022.3219041. Cited on page/s 134, 136, 139.

[23] Lennart Ljung and Torsten Soderstrom. Theory and Practice of Recursive Identification. The MIT Press Cambridge, Massachusetts 2nd edition (1985). ISBN 0-262-12095-X. Cited on page/s 136.

[24] Peter Weichbold and Thomas von Raumer. Influence of dead time effects of PWM-VSI on current control. In IEEE, editor, *EPE* page 8 Graz (2001). Cited on page/s 147.

Part IV

EPILOGUE

Chapter 8

Conclusions and Suggestions for Further Research

8.1 Conclusions

In this section, the initial research objectives are revisited to assess the extent of fulfillment by the overall research work. Subsequently, the key conclusions are drawn from the main results of the thesis.

8.1.1 On the Overall Solution

To recapitulate the main contributions from the thesis, electric drivetrains for deep-sea mining vehicles proposed herein were featured with the following solutions:

☑ Six-phase IPMSM drive in addition to the three-phase IPMSM drive, to enhance the overall system availability.
☑ Online adaptation of all electrical parameters of three-phase and six-phase IPMSM drives to enhance the position estimation, control performance, efficiency, and stability of the drive system.
☑ Enhancement of the state observer with online parameter adaptation to make the observer more stable, precise, and robust to parameter variations as compared to the observer without parameter adaptation.

In essence, an electric drivetrain with these experimentally validated features becomes a more robust and reliable solution to enable more productive and sustainable deep-sea mining technologies. With reference to the initial research proposition in Chapter 2, the thesis has accomplished in its goal of fulfilling the research objectives. Detailed conclusions of the above contributions will be outlined next.

8.1.2 Three-Phase and Six-Phase IPMSM Drives

Both three-phase and six-phase IPMSM drives were investigated. The classical current vector-controlled method is applied. SSRF orientation is adopted to develop the six-phase drive and flux models with the main aim of extracting the dynamic performance benefits over the DSRF-oriented control. Simulation and experimental validation

exhibited the viability and acceptable performance of the three-phase and six-phase IPMSM drives, by incorporating the parameter estimation schemes proposed herein.

8.1.3 On the Position Sensorless Control Schemes

A state-of-the-art position sensorless control scheme, namely Active Flux observer was adopted in this thesis for the rotor position estimation. The observer performance was significantly improved with the aid of a novel parameter adaptation scheme in real-time, which made the observer more robust against the temperature-affected and stator current-affected machine parameter variations. The temperature-sensitive parameters were identified online. The inductances were identified offline and updated online with the aid of either a Look-Up Table or an analytical function programmed in the processor. Laboratory experiments demonstrated improved performance of the sensorless control schemes that yielded average estimation errors below 3 electrical degrees in both drive systems in steady-state. Further, the flux observer could estimate the rotor position/speeds persistently at very low speeds, as low as 0.01 pu, which can also be attributed to the observer's improved stability.

8.1.4 On the Parameter Estimation Schemes

The core contribution from the research emerges under this category. Firstly, a structured and first principles-oriented framework for parameter estimation is disclosed that can encompass many of the model-based parameter estimation schemes. Secondly, the choice of an open-loop model was proven to be an effective method in machine parameter identification because of its inherent sensitivity to model parameter errors. The analytical function for the steady-state prediction error was a significant outcome of this research. This function could enlighten the designers about the interplay among the rotor speed, stator current, model parameters, and parametric errors. Thereby, the design of experimental methods was made more convenient. Thirdly, the adoption of prediction gradients-premised algorithms, namely the stochastic gradient algorithm and Gauss-Newton algorithm appeared to be a successful approach. The development and the sensitivities of the gradient functions and algorithm tuning methods were illustrated. The stochastic gradient algorithm offered better transient performance and the implementation is less tedious than the Gauss-Newton, thus it was chosen for online identification. Modification to the stochastic gradient algorithm were proposed w.r.t. Hessian formulation and dedication of prediction error components to optimize the simultaneous online adaptation of $\hat{\Psi}_m$ and $\hat{R}_s$. Real-time simulation and experimental validations demonstrated that the tracking was sufficiently quick to track temperature-sensitive parameters online, with acceptable asymptotic behavior.

8.2 Limitations and Alternative Approaches

In this section, the limitations of the proposed schemes are underlined along with possible alternative solutions to overcome them. Some of these limitations are known issues, although not evident in the scope of research.

The SSRF-oriented current control scheme for six-phase drives is associated with tediousness in developing torque limiters for each VSI. Proper implementation of torque-limiters is required if the two three-phase VSIs cannot share the power demand equally due to a potential inequality in either the dc-link voltages, power, or currents of the two VSIs. DSRF-premised current control, on the other hand, is more straightforward in this regard. Nonetheless, due to the appearance of the coupling inductance in the latter method, the current control during the transients should be either compromised or improved with extra design efforts.

Despite the relative simplicity and reasonable performance of the AF observer, its reliance on the parameters is a concern that this thesis attempts to address, with the aid of parameter adaptation. A few other concerns have also been reported in relation to the classical AF observer [1, 2]. Alternative observers that claim to either eliminate or reduce the impact of mistuned model parameters, can be worth investigating, however, at the price of increased design complexities.

The combined state and parameter estimation schemes proposed in this thesis require to be processed in parallel in the digital signal processor. This is resource-consuming and may not be appropriate for applications that employ digital signal processes with stringent resource allocations, i.e., often a low-cost processor for the electric drive. A scheme that estimates both state and parameters with the aid of the same model, and therefore, the same criterion function can be more resource-efficient, henceforth can be more appropriate in such cases. However, it is an unlikely scenario with regard to sophisticated deep-sea mining technologies.

8.3 Future Research

This section accumulates the areas of research associated with the scope of the thesis that has not or inadequately been investigated.

8.3.1 Load-profile oriented performance

A further step would be to identify how the proposed sensorless schemes perform at different load profiles in the DMV drives. It was shown in Chapter 2, that certain loads like rock cutting demand several zero-speed crossings within a short time span. Under such circumstances, the observer in cooperation with the parameter adaptation is required to respond quickly. The IGBT-junction temperature can rise fast, which can

influence the VSI voltage output, which in return can affect the flux models, unless, the VSI nonlinearities are well-compensated. This is a potential area for further research.

8.3.2 On the Position Sensorless Control Schemes

The adoption of signal injection-based saliency tracking could be introduced into the proposed scheme to make the sensorless control comprehensive and insensitive to stator resistance variations at and around the rotor standstill. The signal injection scheme can also be used as a reference model to tune the model-based observer during the transition from a very low to a low-speed region.

8.3.3 On the Parameter Estimation Schemes

It would be interesting to evaluate the comparative performance of the proposed estimation schemes against the widely known methods like the MRAS-, RLS-, and Kalman Filter-based methods.

An investigation of the simultaneous adaptability of $\hat{\psi}_m$ and $\hat{r}_s$, by designing the gain sequence to be speed, load and time adaptive, would also be an aspect for further research.

The use of the open-loop predictor implemented in the FPGA may allow the identification of all the electric parameters online, by using the two-paced identification approach, proposed by [3, 4]. This topic is yet to be investigated.

When the DTP machine identification is concerned, the injection of i_{z1} during operation, without hampering the torque production, can provide identification of $\hat{r}_s$, and thus $\hat{\psi}_m$ can be simultaneously identified using the $d-q$-quantities. There is scope to examine this topic.

8.3.4 On the Fault-Tolerance Schemes

Certain literature discusses the ability of a six-phase drive to operate with five or lesser phases in the event of a fault in one or several phases/IGBT bridge legs. Reconstruction of the flux models when the drive has less than six phases without compromising the performance of the proposed enhanced sensorless control scheme would be an intriguing topic to research further. This topic can be extended further to investigate the reconfigurability in the event of one or more current sensor failures.

8.4 References

[1] Abebe Teklu Woldegiorgis, Xinglai Ge, Wang Huiming, and Yun Zuo. An Active Flux Estimation in the Estimated Reference Frame for Sensorless Control of IPMSM. *IEEE Transactions on Power Electronics* **37** (8), 9047–9060 (8 2022). Cited on page/s 163.

[2] Sreejith R and Bhim Singh. Sensorless predictive current control of PMSM EV drive using DSOGI-FLL based sliding mode observer. *IEEE Transactions on Industrial Electronics* **68** (7), 5537–5547 (7 2021). Cited on page/s 163.

[3] Miguel Velez-Reyes, Kazuaki Minami, and George C. Verghese. Recursive speed and parameter estimation for induction machines. In *IAS Annual Meeting (IEEE Industry Applications Society)* number pt 1 pages 607–611 (1989). doi: 10.1109/ias.1989.96712. Cited on page/s 164.

[4] Samuel J. Underwood and Iqbal Husain. Online parameter estimation and adaptive control of permanent-magnet synchronous machines. *IEEE Transactions on Industrial Electronics* **57** (7), 2435–2443 (2010). ISSN 02780046. doi: 10.1109/TIE.2009.2036029. Cited on page/s 164.

Appendix A

Supplementary Information for Chapter 3

A.1 Derivation of Prediction Error Functions

Assuming the application of the same voltage for both the machine and model, the derivation begins with (3.8).
Thus,

$$\hat{i}_d = \frac{r_s \cdot i_d - n \cdot x_q \cdot i_q + n \cdot \hat{x}_q \cdot \hat{i}_q}{\hat{r}_s} \tag{1}$$

$$\hat{i}_q = \frac{r_s \cdot i_q + n \cdot (x_d \cdot i_d + \psi_m) - n \cdot (\hat{x}_d \cdot \hat{i}_d + \hat{\psi}_m)}{\hat{r}_s} \tag{2}$$

Substituting (2) into (1):

$$\begin{aligned} \hat{r}_s^2 \cdot \hat{i}_d = {} & \hat{r}_s \cdot r_s \cdot i_d - n \cdot \hat{r}_s \cdot x_q \cdot i_q + n \cdot \hat{x}_q \cdot r_s \cdot i_q \\ & + n^2 \cdot \hat{x}_q \cdot (x_d \cdot i_d + \psi_m) - n^2 \cdot \hat{x}_q \cdot (\hat{x}_d \cdot \hat{i}_d + \cdot \psi_m) \end{aligned}$$

By rearranging:

$$\begin{aligned} (\hat{r}_s^2 + n^2 \cdot \hat{x}_q \cdot \hat{x}_d) \cdot \hat{i}_d - {} & (\hat{r}_s \cdot r_s + n^2 \cdot \hat{x}_q \cdot x_d) \cdot i_d \\ = {} & (n \cdot \hat{x}_q \cdot r_s - n \cdot \hat{r}_s \cdot x_q) \cdot i_q + n^2 \cdot \hat{x}_q \cdot (\psi_m - \hat{\psi}_m) \end{aligned} \tag{3}$$

Substituting $r_s = \delta r_s + \hat{r}_s,\ x_d = \delta x_d + \hat{x}_d,\ \hat{i}_d = i_d - \epsilon_d$ into LHS of (3) and solving:

$$LHS = -\epsilon_d \cdot (\hat{r}_s^2 + n^2 \cdot \hat{x}_q \cdot \hat{x}_d) - \hat{r}_s \cdot i_d \cdot \delta r_s - n^2 \cdot \hat{x}_q \cdot i_d \cdot \delta x_d \tag{4}$$

Substituting $r_s = \delta r_s + \hat{r}_s,\ x_q = \delta x_q + \hat{x}_q,\ \psi_m = \delta\psi_m + \hat{\psi}_m$ into RHS of (3) and solving:

$$RHS = n \cdot \hat{x}_q \cdot i_q \cdot \delta r_s - n \cdot \hat{r}_s \cdot \delta x_q \cdot i_q + n^2 \cdot \hat{x}_q \cdot \delta\psi_m$$

$$\begin{aligned} LHS &= RHS \\ -\epsilon_d \cdot (\hat{r}_s^2 + n^2 \cdot \hat{x}_q \cdot \hat{x}_d) &= n^2 \cdot \hat{x}_q \cdot \delta\psi_m + (\hat{r}_s \cdot i_d + n \cdot \hat{x}_q \cdot i_q) \cdot \delta r_s + n^2 \cdot \hat{x}_q \cdot i_d \cdot \delta x_d \\ & \quad - n \cdot \hat{r}_s \cdot i_q \cdot \delta x_q \end{aligned} \tag{5}$$

By rearranging (5):

$$\begin{aligned}\epsilon_d = &-\left(\frac{n^2\cdot\hat{x}_q}{\hat{r}_s^2+n^2\cdot\hat{x}_d\cdot\hat{x}_q}\right)\delta\psi_m\\ &-\left(\frac{\hat{r}_s}{\hat{r}_s^2+n^2\cdot\hat{x}_d\cdot\hat{x}_q}\cdot i_d+\frac{n\cdot\hat{x}_q}{\hat{r}_s^2+n^2\cdot\hat{x}_d\cdot\hat{x}_q}\cdot i_q\right)\delta r_s\\ &-\left(\frac{n^2\hat{x}_q}{\hat{r}_s^2+n^2\cdot\hat{x}_d\cdot\hat{x}_q}\cdot i_d\right)\delta x_d\\ &+\left(\frac{n\cdot\hat{r}_s}{\hat{r}_s^2+n^2\cdot\hat{x}_d\cdot\hat{x}_q}\cdot i_q\right)\delta x_q\end{aligned}$$

By substituting (1) into (2) and following the same procedure, one can arrive at the equivalent expression for ϵ_q:

$$\begin{aligned}\epsilon_q = &-\left(\frac{n\cdot\hat{r}_s}{\hat{r}_s^2+n^2\cdot\hat{x}_d\cdot\hat{x}_q}\right)\delta\psi_m\\ &-\left(\frac{\hat{r}_s}{\hat{r}_s^2+n^2\cdot\hat{x}_d\cdot\hat{x}_q}\cdot i_q-\frac{n\cdot\hat{x}_d}{\hat{r}_s^2+n^2\cdot\hat{x}_d\cdot\hat{x}_q}\cdot i_d\right)\delta r_s\\ &-\left(\frac{n\cdot\hat{r}_s}{\hat{r}_s^2+n^2\cdot\hat{x}_d\cdot\hat{x}_q}\cdot i_d\right)\delta x_d\\ &-\left(\frac{n^2\cdot\hat{x}_d}{\hat{r}_s^2+n^2\cdot\hat{x}_d\cdot\hat{x}_q}\cdot i_q\right)\delta x_q\end{aligned}$$

A.2 Derivation of Prediction Gradient Functions

By writing (3.11) explicitly, in component form:

$$\frac{\mathrm{d}\left(\frac{\mathrm{d}\hat{i}_d}{\mathrm{d}\hat{\theta}}\right)}{\mathrm{d}t}=\underbrace{\frac{\mathrm{d}}{\mathrm{d}\hat{\theta}}\left(\frac{-\hat{r}_s\cdot\omega_n\cdot\hat{i}_d}{\hat{x}_d}\right)}_{d_1}+\underbrace{\frac{\mathrm{d}}{\mathrm{d}\hat{\theta}}\left(\frac{\omega_n\cdot u_d}{\hat{x}_d}\right)}_{d_2}+\underbrace{\frac{\mathrm{d}}{\mathrm{d}\hat{\theta}}\left(\frac{\hat{x}_q\cdot n\cdot\omega_n\cdot\hat{i}_q}{\hat{x}_d}\right)}_{d_3} \tag{6}$$

$$\frac{\mathrm{d}\left(\frac{\mathrm{d}\hat{i}_q}{\mathrm{d}\hat{\theta}}\right)}{\mathrm{d}t}=\underbrace{\frac{\mathrm{d}}{\mathrm{d}\hat{\theta}}\left(\frac{-\hat{r}_s\cdot\omega_n\cdot\hat{i}_q}{\hat{x}_q}\right)}_{q_1}+\underbrace{\frac{\mathrm{d}}{\mathrm{d}\hat{\theta}}\left(\frac{\omega_n\cdot u_q}{\hat{x}_q}\right)}_{q_2}+\underbrace{\frac{\mathrm{d}}{\mathrm{d}\hat{\theta}}\left(\frac{-\hat{x}_d\cdot n\cdot\omega_n\cdot\hat{i}_d}{\hat{x}_q}\right)}_{q_3}+\underbrace{\frac{\mathrm{d}}{\mathrm{d}\hat{\theta}}\left(\frac{-\hat{\psi}_m\cdot n\cdot\omega_n}{\hat{x}_q}\right)}_{q_4} \tag{7}$$

Now by partial derivation of d_1, d_2, and d_3 w.r.t. $\hat{\psi}_m$ one can derive (3.12a). Similarly, by partial derivation of q_1, q_2, q_3, and q_4 w.r.t. $\hat{\psi}_m$, one can arrive at (3.12b). By following the same procedure, the dynamic forms of the prediction gradients w.r.t. the other model parameters can also be derived.

A.3 Predictor stability details

In this section, the predictor's stability details are studied, giving emphasis to the discrete-time domain.

A.3.1 In Continuous Time-Domain

$\mathscr{M}_{u\theta}$ for three-phase IPMSM, in continuous time-domain:

$$\begin{aligned} \underline{u}_s^r &= \hat{r}_s \cdot \underline{i}_s^r + \frac{\mathbf{x}_s^r}{\omega_n} \cdot \frac{\mathrm{d}\underline{i}_s^r}{\mathrm{d}t} + \mathbf{j} \cdot n \cdot \mathbf{x}_s^r \cdot \underline{i}_s^r + \mathbf{j} \cdot n \cdot \underline{\hat{\psi}}_m^r \\ \underline{i}_s^r &= \mathbf{T}_{ss}^r(\vartheta) \cdot \underline{i}_s^s, \qquad \underline{u}_s^r = \mathbf{T}_{ss}^r(\vartheta) \cdot \underline{u}_s^s \end{aligned} \tag{8}$$

The system matrix, **A**, of the linearized system, and the eigenvalues ($\lambda_{1,2}$) of the model are presented in Chapter 3. For the ease of analysis, let (3.4b) be expressed as $\lambda_{1,2} = Real\ Part \pm j \cdot Imaginary\ Part$. The Real Part is machine impedance- and ω_n- dependent and higher R_s and/or ω_n will push the eigenvalues further into the stability region. In other words, the real part hints at necessary conditions such as $r_s, \omega_n \neq 0$ to guarantee stability in the continuous time domain.

The imaginary part, on the other hand, has a speed-dependent component, $(\omega_n \cdot n)^2$-term which is much larger than its speed-independent terms. Due to this dominance of $(\omega_n \cdot n)^2$-term, the eigenvalues can be approximated such as $\lambda_{1,2} \approx Real\,Part \pm j \cdot \omega_n \cdot n$. It is known that the imaginary part corresponds to the natural frequency of the system, thus it can be expected that the oscillation frequency of the predicted currents increases in proportion to the rotor speed.

A.3.2 In Discrete Time-Domain

To implement the predictor in a digital controller, (3.3) needs to be solved for currents and discretized, for which one can use an explicit numerical method like the Forward Euler Method (called Euler's method) or Runge-Kutta method or an implicit method like the trapezoidal rule. Despite the ease of computation, the explicit methods offer a limited stability region in the left half plane, unlike the implicit methods that offer stability, theoretically, in the entire left half plane. The predicted currents become as in (9) with Euler's method. The final expressions with the trapezoidal rule can be derived using (10), where $\underline{f}_c$ is a function of input variables to the $\mathscr{M}_{u\theta}$. Figure A.1 illustrates the behaviors of the eigenvalues in the $\lambda \cdot h$-plane, when discretized using the above two numerical methods and applying typical h-values corresponding to DSP-based (T_{samp}) and FPGA-based (T_{step}) implementations. Unlike in the case of the continuous time domain, this Figure illustrates that when $h = T_{samp}$, the eigenvalues can escape the stability region of Euler's method, at higher speeds, yet they are still within the stability region w.r.t. the trapezoidal rule (see Zoom-1). This potential instability with

the Euler's method can still be circumvented with a choice of narrower time-step like $h = T_{step}$ (see Zoom-2).

$$\begin{aligned}
\hat{i}_d[k] =& \hat{i}_d[k-1] \cdot \left[1 - h \cdot \left(\frac{\omega_n \cdot \hat{r}_s}{\hat{x}_d}\right)\right] \\
&+ \frac{h \cdot \omega_n}{\hat{x}_d}\Big(u_d[k-1] + n[k-1] \cdot \hat{x}_q \cdot \hat{i}_q[k-1]\Big) \\
\hat{i}_q[k] =& \hat{i}_q[k-1] \cdot \left[1 - h \cdot \left(\frac{\omega_n \cdot \hat{r}_s}{\hat{x}_q}\right)\right] \\
&+ \frac{h \cdot \omega_n}{\hat{x}_q} \cdot \Big(u_q[k-1] - n[k-1] \cdot \hat{x}_d \cdot \hat{i}_d[k-1] \\
&- n[k-1] \cdot \hat{\psi}_m[k-1]\Big)
\end{aligned} \tag{9}$$

$$\begin{aligned}
\underline{\hat{i}}_s^r[k, \underline{\hat{\theta}}] =& \underline{\hat{i}}_s^r[k-1, \underline{\hat{\theta}}] + \frac{h}{2} \cdot \underline{f}_c\left(\underline{\hat{i}}_s^r[k, \underline{\hat{\theta}}], \underline{u}_s^r[k], n[k]\right) \\
&+ \frac{h}{2} \cdot \underline{f}_c\left(\underline{\hat{i}}_s^r[k-1, \underline{\hat{\theta}}], \underline{u}_s^r[k-1], n[k-1]\right)
\end{aligned} \tag{10}$$

A.4 FPGA vs. DSP-Based Predictor Implementation

In the DSP, the predictor is implemented using the C++ programming language in the fastest interrupt routine, with $h = T_{samp} = 125\ \mu s$. In the FPGA, the predictor is programmed using a schematic language known as the Xilinx System Generator. The program looks as in Figure A.2 which has $h = T_{step} = 1\ \mu s$. The predictor still follows the same structure as in Figure 3.2. The resource utilization from the predictor intellectual property (IP): 1175 Look-Up Tables (1.5% of total) and 1786 slice registers (1.1% of total). The predictor is designed without the use of scarce internal FPGA resources such as the DSP blocks and Random Access Memory blocks. It is worth noting that, under the FPGA-based method, apart from the predictor, the rest of the OPE routines are programmed in the DSP.

A.4.1 Real-Time Simulation

In this section, the proposed implementation methods of the predictor are investigated using a Xilinx Zynq System on Chip-based ERTS. Assuming the model inductances are updated online using the offline identifications, the methods are demonstrated by adapting $\hat{\psi}_m$ and $\hat{r}_s$ online. The overview of the ERTS and the associated hardware as same given in Figure 5.2 and Figure 5.1. Table A.1 tabulates the experimental plant data.

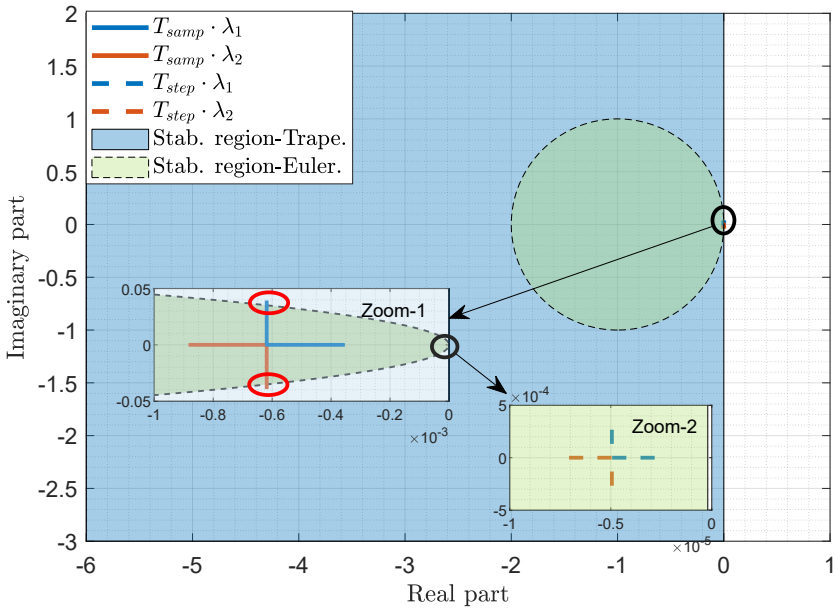

FIGURE A.1. Predictor eigenvalue trajectories and stability regions in $\lambda \cdot h$-plane when discretized using the trapezoidal rule and Euler's method. Zoom-1: Trajectories cross the Euler-stability region, yet within the region with the trapezoidal method, when $h = T_{samp}$. Zoom-2: Trajectories are within both stability regions, when $h = T_{step}$.

Stochastic gradient algorithm (3.18) is adopted for identification in which $\gamma_{0,rk}$, $\gamma_{0,Lk}$ values for $\hat{\psi}_m$-tracking are 6.25×10^{-4}, 3.25×10^{-4} and the same for $\hat{r}_s$-tracking are 6.25×10^{-4}, 1×10^{-4} respectively.

A.4.2 Predictor Behaviours Across the Speed Range

In this section, the steady-state behaviors of the different predictor implementations and the effect on the estimates will be evaluated, particularly at higher rotor speeds. To keep the discussion within the scope, only $\hat{\psi}_m$-adaptation is considered, assuming the other parameters are in agreement with their physical counterparts. The predicted currents, $\underline{\epsilon}_s^r$, update-terms ($\mathbf{L} \cdot \underline{\epsilon}_s^r$) and $\hat{\psi}_m$ are plotted in Figure A.3, in which Columns (a), (b) and (c) are dedicated to the rotor speeds 0.4, 0.6 and 0.8 pu respectively. One general observation is that irrespective of the discretization strategy, the DSP-based predictors result in oscillations. Close inspection reveals that the periods of these oscillations are approximately 35, 24, and 18 ms in the three different speeds, which result in the oscillation frequencies 28, 42, and 55 Hz respectively. If the respective rotor speeds along with the machine data are applied to (3.4b), it is obtained the same natural frequencies. Thus, it can be confirmed that the oscillation frequencies of the predictions are directly proportional to the rotor speed. The rotor-speed dependent

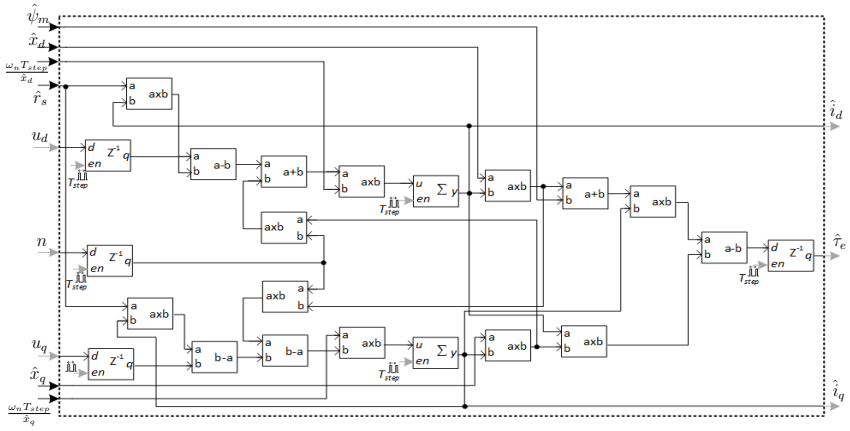

FIGURE A.2. Xilinx System Generator based-schematic program of the predictor, implemented in the FPGA.

TABLE A.1. Parameters of the Experimental Plant

Symbol	Parameter	Value (SI)
U_n	IPMSM Rated Voltage	220 V
I_n	IPMSM Rated Current	51 A
N_n	IPMSM Rated Speed	2100 rpm
T_n	IPMSM Rated Torque	88.4 Nm
p	IPMSM Number of pole-pairs	2
R_s	Stator Resistance	0.022 Ω
Ψ_m	Permanent magnet flux linkage	0.33 Wb
L_d	IPMSM d-axis inductance	2.26 mH
L_q	IPMSM q-axis inductance	5.66 mH
U_{dc}	DC bus voltage	280 V
f_{sw}	Power device switching frequency	4 kHz
T_{samp}	Sampling period	125 μs

oscillations are superimposed on the $\underline{\epsilon}$, so in the update-terms and inevitably, in $\hat{\psi}_m$, thus in the τ_e. As expected from the study in Section A.3.2, the Euler's method-based predictor implementation in the DSP (E-plots in Column (c)) displays an unstable behavior when $n = 0.8\ pu$. This suggests that Euler's method cannot guarantee stable estimations across the full-speed range, therefore, is not suitable for the cause. Despite the increasing oscillations, the trapezoidal rule-based predictor in the DSP yields stable predictions across the full-speed range. Opposing to the DSP-based methods, the FPGA-based predictor results in nearly no oscillations, thus yielding smooth and steady $\hat{\psi}_m$ irrespective of the rotor speed.

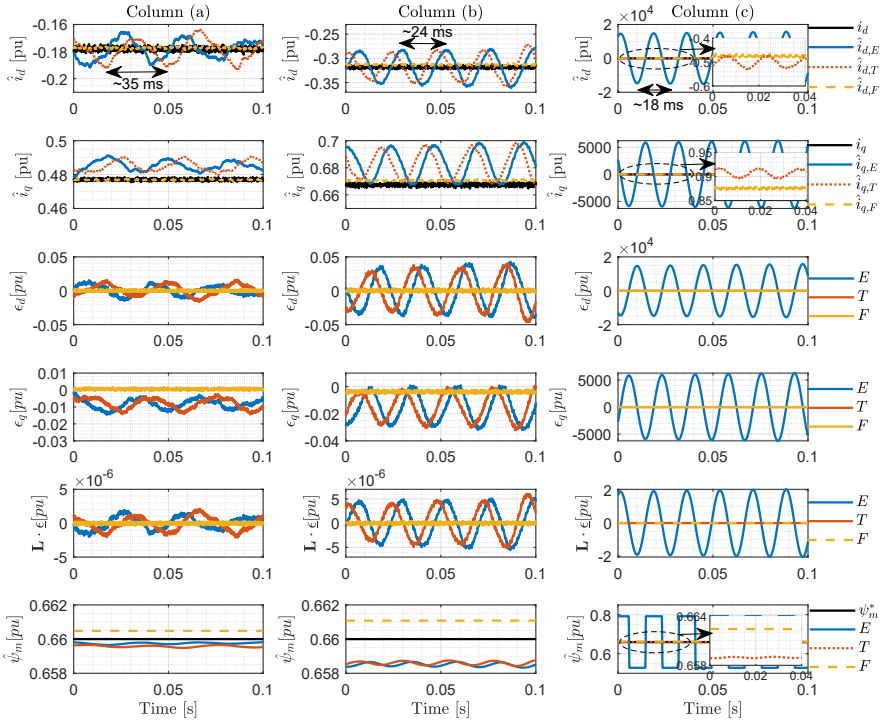

FIGURE A.3. The steady-state behavior of predicted currents $\hat{i}_{d,q}$, prediction errors $\epsilon_{d,q}$, update-terms $\mathrm{L} \cdot \underline{\epsilon}$ and $\hat{\psi}_m$ when the predictor is developed using Euler's Method in DSP (E), Trapezoidal Method in DSP (T) and Euler's Method in FPGA (F) at rotor speeds: Column-(a) $n = 0.4$, Column-(b) $n = 0.6$, Column-(c) $n = 0.8$.

A.4.3 Processor- vs. FPGA-Based Predictor

In this section, an investigation is carried out between the dynamic performances of the trapezoidal rule-based DSP predictor and the Euler-based FPGA predictor involving parameter adaptations. Approximately 10% step-changes of motor parameters r_s^*, ψ_m^* are introduced as in Figure A.4, although an unlikely scenario, to evaluate the stability and the convergence speeds of the corresponding approaches. Different $\gamma_{0,Lk}$ values have been used to vary the convergence speeds. Figure A.4 (a) and (b) present the adaptations of $\hat{r}_s$ at 0.05 pu rotor speed and 0.5 pu load-torque (τ_{el}) when the DSP and FPGA -based predictors are used respectively. When the FPGA-based predictor yields noise-free $\hat{r}_s$-tracking, the DSP-based approach displays noise-rich $\hat{r}_s$ and the smaller $\gamma_{0,Lk}$ enables better noise-filtering at the price of delayed convergence.

The same effect is seen in Figure A.4 (c) and (d) w.r.t. the ψ_m^*-adaptation at 0.8 pu rotor speed and 0.4 τ_{el}. It is interesting to note that at increased $\gamma_{0,Lk}$ (see plot(c) $3 \times \gamma_{0,Lk}$-case), ψ_m^*-adaptation becomes unstable, yet at lower values, smoother and stable tracking is achievable with DSP based predictor. However, the FPGA-based

predictor again performs well irrespective of the $\gamma_{0,Lk}$ values. On a side note, $\gamma_{0,Lk}$ can be an effective parameter to determine the tracking speed with a trade-off of noise sensitivity.

In general, for temperature-sensitive parameter tracking, the convergence speeds in the range of several seconds is sufficient, thus trapezoidal rule-based predictor implementation the DSP suffices such requirements. However, when the ^{T}-based RPEM is extended for online identification of the IPMSM inductances, which can rapidly change, the FPGA-based predictor can become a necessary approach.

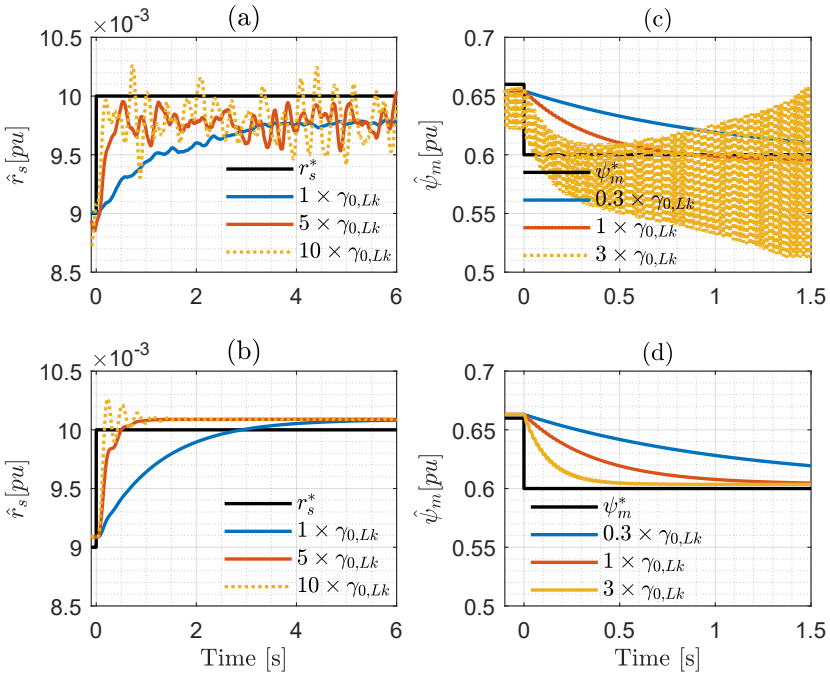

FIGURE A.4. The online parameter adaption performances across different values for $\gamma_{0,Lk}$, when the predictor is implemented using (a) Trapezoidal Method in the DSP for $\hat{r}_s$-tracking (b) Euler Method in the FPGA for $\hat{r}_s$-tracking (c) Trapezoidal Method in the DSP for $\hat{\psi}_m$-tracking (d) Euler Method in the FPGA for $\hat{\psi}_m$-tracking.

Appendix B

Supplementary Information for Chapter 6

B.1 Derivation of z-axis Prediction Error Functions

Assuming the application of the same voltage for both the machine and model, the derivation begins with:

$$i_{z2} \cdot r_s + n \cdot x_{s\sigma} \cdot i_{z1} = \hat{i}_{z2} \cdot \hat{r}_s + n \cdot \hat{x}_{s\sigma} \cdot \hat{i}_{z1} \tag{11}$$

$$i_{z1} \cdot r_s - n \cdot x_{s\sigma} \cdot i_{z2} = \hat{i}_{z1} \cdot \hat{r}_s - n \cdot \hat{x}_{s\sigma} \cdot \hat{i}_{z2} \tag{12}$$

From (11) :

$$\hat{i}_{z1} = \frac{i_{z2} \cdot r_s - \hat{i}_{z2} \cdot \hat{r}_s + n \cdot x_{s\sigma} \cdot i_{z1}}{n \cdot \hat{x}_{s\sigma}} \tag{13}$$

$$\epsilon_{z1} = i_{z1} - \hat{i}_{z1}$$

By substituting $\hat{i}_{z1}$ from (13) into (14) :

$$i_{z1} - \hat{i}_{z1} = \frac{n \cdot i_{z1} \cdot (\hat{x}_{s\sigma} - x_{s\sigma}) - i_{z2} \cdot r_s + \hat{i}_{z2} \cdot \hat{r}_s}{n \cdot \hat{x}_{s\sigma}} \tag{14}$$

After solving and rearranging:

$$n \cdot x_{s\sigma} \cdot i_{z1} - n \cdot \hat{x}_{s\sigma} \cdot \hat{i}_{z1} = -i_{z2} \cdot r_s + \hat{i}_{z2} \cdot \hat{r}_s \tag{15}$$

From (12) :

$$\hat{i}_{z2} = \frac{\hat{i}_{z1} \cdot \hat{r}_s - i_{z1} \cdot r_s + n \cdot x_{s\sigma} \cdot i_{z2}}{n \cdot \hat{x}_{s\sigma}} \tag{16}$$

By substituting $\hat{i}_{z2}$ from (16) into (15) and solving :

$$\begin{aligned} n^2 \cdot x_{s\sigma} \cdot \hat{x}_{s\sigma} \cdot i_{z1} - n^2 \cdot x_{s\sigma}^2 \cdot \hat{i}_{z1} &= -i_{z2} \cdot r_s \cdot n \cdot \hat{x}_{s\sigma} + n \cdot x_{s\sigma} \cdot i_{z2} \cdot \hat{r}_s \\ &\quad + \hat{i}_{z1} \cdot \hat{r}_s^2 - i_{z1} \cdot r_s \cdot \hat{r}_s \end{aligned} \tag{17}$$

By substituting $x_{s\sigma} = \delta x_{s\sigma} + \hat{x}_{s\sigma}$ and further solving:

$$\begin{aligned} n \cdot i_{z2} \cdot (\delta x_{s\sigma} \cdot \hat{r}_s - \hat{x}_{s\sigma} \cdot \delta r_s) &= i_{z1} \cdot (n^2 \cdot x_{s\sigma} \cdot \hat{x}_{s\sigma} + r_s \cdot \hat{r}_s) \\ &\quad - \hat{i}_{z1} \cdot (n^2 \cdot \hat{x}_{s\sigma}^2 + \hat{r}_s^2) \\ -\hat{i}_{z1} \cdot (n^2 \cdot \hat{x}_{s\sigma}^2 + \hat{r}_s^2) &= (n \cdot i_{z2} \cdot \hat{r}_s - n^2 \cdot \hat{x}_{s\sigma} \cdot i_{z1}) \cdot \delta x_{s\sigma} \\ &\quad - (\hat{r}_s \cdot i_{z1} + n \cdot \hat{x}_{s\sigma} \cdot i_{z2}) \cdot \delta r_s \\ &\quad - n^2 \cdot i_{z1} \cdot \hat{x}_{s\sigma}^2 - i_{z1} \cdot \hat{r}_s^2 \end{aligned} \tag{18}$$

By substituting $\hat{i}_{z1} = i_{z1} - \epsilon_{z1}$

$$\begin{aligned} \epsilon_{z1} \cdot (n^2 \cdot \hat{x}_{s\sigma}^2 + \hat{r}_s^2) &= (n \cdot i_{z2} \cdot \hat{r}_s - n^2 \cdot \hat{x}_{s\sigma} \cdot i_{z1}) \cdot \delta x_{s\sigma} \\ &\quad - (\hat{r}_s \cdot i_{z1} + n \cdot \hat{x}_{s\sigma} \cdot i_{z2}) \cdot \delta r_s \end{aligned} \tag{19}$$

After rearranging (19), one can derive an expression for ϵ_{z1} as:

$$\epsilon_{z1} = \left(\frac{-n^2 \cdot \hat{x}_\sigma}{\hat{r}_s^2 + n^2 \cdot \hat{x}_{s\sigma}^2} \cdot i_{z1} + \frac{n \cdot \hat{r}_s}{\hat{r}_s^2 + n^2 \cdot \hat{x}_{s\sigma}^2} \cdot i_{z2} \right) \delta x_{s\sigma} - \left(\frac{\hat{r}_s}{\hat{r}_s^2 + n^2 \cdot \hat{x}_{s\sigma}^2} \cdot i_{z1} + \frac{n \cdot \hat{x}_{s\sigma}}{\hat{r}_s^2 + n^2 \cdot \hat{x}_{s\sigma}^2} \cdot i_{z2} \right) \delta r_s$$

By following the same procedure, an expression for ϵ_{z2} can be derived as in:

$$\epsilon_{z2} = \left(\frac{-n \cdot \hat{r}_s}{\hat{r}_s^2 + n^2 \cdot \hat{x}_{s\sigma}^2} \cdot i_{z1} - \frac{n^2 \cdot \hat{x}_\sigma}{\hat{r}_s^2 + n^2 \cdot \hat{x}_{s\sigma}^2} \cdot i_{z2} \right) \delta x_{s\sigma} + \left(\frac{n \cdot \hat{x}_{s\sigma}}{\hat{r}_s^2 + n^2 \cdot \hat{x}_{s\sigma}^2} \cdot i_{z1} - \frac{\hat{r}_s}{\hat{r}_s^2 + n^2 \cdot \hat{x}_{s\sigma}^2} \cdot i_{z2} \right) \delta r_s$$

ISBN 978-82-326-7088-8 (printed ver.)
ISBN 978-82-326-7087-1 (electronic ver.)
ISSN 1503-8181 (printed ver.)
ISSN 2703-8084 (online ver.)

NTNU
Norwegian University of
Science and Technology